Investigation of Magnetostrictive $Fe_{1-x}Ga_x$ Bilayer Films and Devices

Debi Prasad Pattnaik

School of Physics and Astronomy

University of Nottingham

Thesis submitted for the degree of

Doctor of Philosophy

:March 2018:

Acknowledgements

As many of my friends and some very good colleagues know that, I am a modest fan of contemporary superheroes specially Batman and his allies, and firmly believe that they just do not exist in comics and science fiction. During my time as a PhD student in the Spintronics group, I have had many events which were no different that the adventures in the DC comics universe. In the past three years of my studies, I have worked with a team very similar to the justice league (or what we called the "spintronics league") which always motivated me and reminded me of this quote by Henri Ducard, " The training is nothing! The will is everything! The will to act".

So here I have tried to thank all those league members who have helped me during this adventure. I am very sorry if I have not mentioned anyone.

A big Thank You to:

My supervisors Dr Kevin Edmonds, and Dr Andrew Rushforth for accepting me into the Spintronics group and engaging me in new ideas everyday of the last three years I spent in the group. They have supported me throughout my thesis with their patience and vast knowledge whilst allowing me the space and environment to work in my own way. I loved our discussions on science and anything on everything.

Every result in this thesis was possible with the help of the collaborators specially Dr Stuart Cavill, Mr Christopher Love for the ferromagnetic resonance experiments, and Dr Maciek Sawicki for the SQUID magnetometry measurements and Dr. Jan Michalicka, Dr. Michal Urbanek and Dr. Martin Veis for the wonderful TEM images.

Dr. Ryan Beardsley, Dr. Peter Wadley, Dr. Mu Wang, Dr. Duncan Parkes, and Dr Bryn Howells for the great innovative ideas and helping me the experiments and discussions and bridging the cultural gap.

A sincere gratitude to Jas Chauhan and David Taylor for the cleanroom training and always helping me out in the fabrication process. Thanks to the people in mechanical and electronics workshop specially Andrew Stuart for helping me setup the electromagnet and the necessary electronics for it.

A very special acknowledgement goes out to all down at Room number C26 to make it an interesting place to work. With a special mention to Michal Gryzbowski for always helping me to stay positive and the not so delicious strawberry dumplings, and Carl Andrews for the humor and teaching me how not to live life in general. To all my colleagues, past and present members Mo Khah, Stuart Bowe, Vicky Hills, Mohammed Al Qayoudhi, Sonka Riemers, Syamashree Roy, Alex Lewis, Luke Barton, Ollie Amin and the cold atom and astro group for the pub trips. I am also thankful to my housemates Srikanth Reddy for the motivation and humor and care and Prasujya for not getting annoyed and displeased for my untimely humor and sarcastic talks.

The University of Nottingham's international office for their financial assistance and scholarship which helped me to secure the financial aspect of the PhD.

Finally, I would like to acknowledge my family who supported me through out the PhD. A special appreciation goes to Monica for all her love, patience and support.

To my life-coach, my father: because I owe it all to you. Many Thanks!

"Every son's first superhero is his father, and it is the same for me. For me, he is Superman and Batman combined."

Abstract

Magnetic memory technology, especially hard disk drives are the leading technology for storing data. Increasing demand for improved storage density, along with faster processing times and low power consumption, have led to the invention and exploration of more sophisticated technologies based on magnetism. In these state of the art technologies, the primary aim is to manipulate the magnetisation state of the material in order to store information. In the next generation of magnetic memory technologies, the manipulation of the magnetisation state by an external magnetic field has been replaced with electric current or electric field. More recently, the use of strain mediated magnetoelastic coupling to change the magnetisation has attracted a lot of interest for development of energy efficient logical processing and information storage devices. One method to demonstrate this is to use a hybrid piezoelectric/ferromagnetic device. A voltage across the piezoelectric transducer induces a mechanical strain in the ferromagnetic layer and results in the manipulation of the magnetic anisotropy via the inverse magnetostriction effect.

In this thesis, hybrid structures of a piezoelectric transducer and a magnetostrictive ferromagnet alloy of $Fe_{1-x}Ga_x$ have been used to investigate the strain manipulation and control of magnetisation. The Fe rich Fe-Ga alloy has demonstrated enhanced values of magnetostriction and has been shown to be very magnetically sensitive to strain both in bulk crystals and in thin film cases. Due to a very high magnetostriction value of $\frac{3}{2}\lambda_{100}$= 395 ppm, and no rare earth constituents, the material is a competitive candidate for strain mediated magnetic storage devices.

The investigations described in the thesis are on 5 nm bilayer films of $Fe_{1-x}Ga_x$ deposited on GaAs (001) substrates by the magnetron sputter deposition technique. The ferromagnetic layers were separated by either a Cu or Al spacer layer of thickness 5 nm or 10 nm. The grown ferromagnetic layers had different Ga concentration so that they demonstrate different magnetostriction value and the magnetisation reversal process in each layer will be unique and independent. SQUID magnetometry along with ferromagnetic resonance experiments and mathematical

modelling of minimising the free magnetic energy, revealed that there is a strong cubic magnetocrystalline anisotropy in the individual layers which was approximately equal for all the samples. The uniaxial anisotropy varied in each of the grown samples due to variation in the interface bonds between the substrate and the metallic stack. By modelling each of the layers to be independent, and solving at the switching field regions, the domain wall depinning energies for each layers have also been estimated. It is revealed that the domain wall depinning energies for the layers grown on the substrate is weaker than the layer grown on the metallic stacks.

Ferromagnetic resonance experiments along with mathematical modelling were also used to investigate the dynamic properties of these bilayer films. The role of magnetic anisotropies and spacer type and thickness on the magnetisation precession in terms of the resonance frequency, Gilbert damping and linewidth have been investigated. A narrow linewidth of 3.8 mT and 4.7 mT for the top and bottom layers with a low Gilbert damping value of approximately 0.015 and 0.019 have been obtained which makes these films a competitive candidate for applications of microwave spintronic devices.

An investigation of the effects of strain on the magnetisation reversal is described in chapter 4, by employing magnetotransport measurements on processed Hall bar devices mounted on piezoelectric transducers. The measured transport data containing contributions from the anisotropic magnetoresistance and giant magnetoresistance effects arising from distinct magnetisation reversal processes of each layer which were independent for each layer and dependent on the voltage-induced strain. This strain-mediated modification of the measured resistances was different for all the samples. The induced strain changed the switching fields of the individual layers and was found to be higher for the 5 nm Al spacer samples than the 5 nm Cu spacer samples. However, the 5 nm Cu sample demonstrated a higher giant magnetoresistance contribution to the measured longitudinal resistance.

Finally, the working parameters for a multi-level memory cell operated by voltage-induced strain and based on the layers studied in this thesis have been determined. The conceptualised device is an attractive candidate for high density magnetic information storage. The extension to more than one layer would increase the possible storage density by utilising the third spatial dimension to stack storage elements.

Contents

Chapter 1

Introduction and background theory

1.1 Introduction to spintronics

The demand for increased storage density[1, 2] and faster processing time [3, 4] has paved the way to more efficient and densely packed storage elements. A pronounced example in this field was the invention of the first spin electronic device employing giant magnetoresistance (GMR) in 1988 [5–7], which paved the way towards the emergence of a new branch of magnetism research called spintronics. [8, 9].

Spintronics or spin-electronics aims to simultaneously control and manipulate both the charge and spin of electrons in the same device[10]. As has been mentioned in the Nobel lecture by Albert Fert and Peter Grünberg [6, 7], GMR exploited the influence of the spin of the electron on the mobility of electrons as previously been suggested by Mott in 1936 [11]. What set off from the discovery of GMR effect was to develop and engineer magnetic multilayers with non- magnetic spacer layers with respective thickness of similar size to the mean free path of the conduction electrons. To exploit the multifunctionality of these structure various researches have been demonstrated which exploited the spin of the electron instead of the charge. These involve working towards perfecting the existent GMR technology by development of novel materials to obtain a higher and improved storage density with faster and efficient processing times and at the same time towards the manipulation and control of the spin polarised current which will build the foundation for designing new multifunctional devices capable of data storage and logical processing. These novel devices would then be integrated with the current traditional semiconductor logical and digital units. Thus research in this field aims at improv-

ing and revolutionising the magnetic storage memory architecture and the logical integration of the computing architecture.

Long before the discovery of the GMR effect, or using the spin of electrons for devices, William Thomson in 1850 discovered the dependence of a magnetic material's resistance on the direction of its magnetisation which came to be known as the anisotropic magnetoresistance [12]. With the launch of the first commercial magnetoresistive read head: IBM 9340 and 9345 using the AMR effect, it replaced the earlier bulky storage disc drives based on core memory and disk storage drives (IBM 1311). Increasing demand and competition for further improved storage volume showed the limitation of the AMR based memory devices which at that time were capable of storing under 5 MB of data, and the responsibility was passed onto developing devices based on the GMR effect. Traditional GMR with Fe/Cr multilayer followed by Co/Cu structures encouraged various other similar experiments and design of the spin valve sensors. A spin valve structure comprises a non-magnetic layer sandwiched between two ferromagnetic layers. One of the ferromagnetic layer is called the free layer and the other ferromagnet layer is pinned to an antiferromagnet layer by strong exchange coupling. Traditional spin valve sensors showed magnetoresistance value mathematically expressed as $\Delta R/R = (R_{AP} - R_P)/R_P$ where R_{AP} is the resistance in the antiparallel configuration and R_P is the resistance in parallel configuration, of about 6%. This new fundamental of spintronic technology was realised by the first commercial release of IBM Deskstar 16GP Titan in late 1997, which had a storage capacity of 16.8 GB. This was the first use of spin valve sensors in hard disk drives and redefined the memory integration architecture. Further discussion about the GMR effect will be done in the later sections of the thesis.

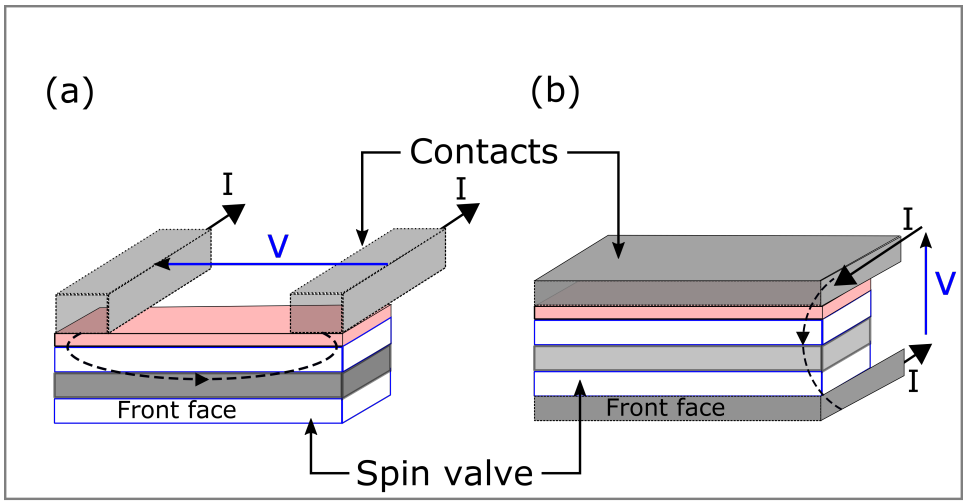

Figure 1.1: Schematic of spin valve read head sensor with (a) current in plane, and (b) current perpendicular to plane. In both the configurations, the recording medium traverses parallel to the front face of the sensor.

Fig.1.1 shows the schematic of the current in- plane and current perpendicular to plane spin valve sensor read head. When the magnetic bit stored as "1" passes very close to the sensor it affects the magnetisation of the free layer such that its magnetisation is parallel to the magnetisation of the fixed layer.Therefore the magnetoresistance of the sensor will change to lower value which will be read as "1" by the sensor. Conversely, if the hard disk has data stored as "0" then it aligns the magnetisation of the free layer to be in an antiparallel configuration with respect to the fixed layer, therefore the magnetoresistance is higher and less current passes through the sensor which will be interpreted as "0" by the sensor then. This is the fundamental principle of the spin valve based read sensor in hard disk drive heads[13].

Tunnelling magnetoresistance (TMR) which replaced the non-magnetic conducting layer with an insulator, thus creating a magnetic tunnel junction (MTJ) was proposed by Julliere et all in 1975[14]. In this multilayer arrangement, the spin current traversed from one layer to another by tunnelling with the spin of the electrons being conserved during the process. The practical implication of the TMR effect was realised in 1995 with the introduction of sophisticated deposition and fabrication techniques. MTJs with single crystal MgO barrier demonstrated magnetoresistance values up to two orders of magnitude higher than the existent GMR devices (~600%) [15] and had an immediate impact on the magnetic memory storage technology. The first TMR read head sensor was released by Seagate in

late 2004. This high magnetoresistance MTJ device based on the TMR effect is the basis of the development of the magnetic random access memory or MRAM [16, 17], a non-volatile memory element. A schematic representation of MRAM cell is shown in Fig. 1.2. MRAMs are basically an array of MTJs which individually store the binary operations "0" and "1". MRAM technology is a break through in storage technology and it combined features like non-volatile memory, faster processing times (5 ns for read/write operation) and high endurance. However it has a drawback of writing, as the conduction line has a limitation of current density due to the resistance of the insulating barrier. The other issue it suffers is the magnetisation induction was performed using external magnetic field applied spatially over the device dimension. This would produce stray fields and eddy effects.

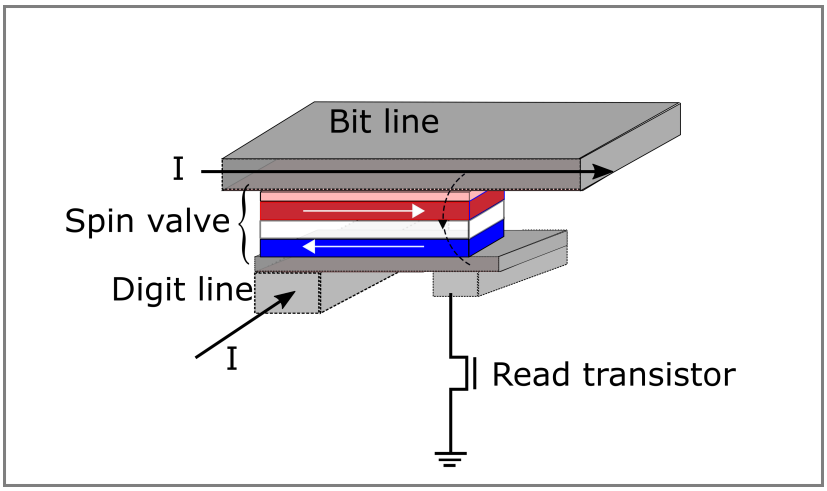

Figure 1.2: Schematic of a magnetic random access memory showing a conventional reading procedure.

Later advanced models of MRAMs used the "Spin- transfer- torque" (STT-MRAM)[18–20] which added the benefit of improved energy efficiency to the existing MRAM technology using spin valves. These STT- spin valves comprise a ferromagnetic layer which is thicker compared to the other ferromagnetic layer and a non- magnetic layer which separates these two magnetic layers. The GMR effect determines the magnetisation and electrical state of the structure. When a high density current is injected into the structure the magnetic layers will spin polarise the current. When the current passes through the first layer, the magnetisation of this layer filters the antiparallel spin with respect to the magnetisation. The polarised spin current when traverses to the second layer, the electrons orient towards the magnetisation. This difference in the spin orientation creates a torque

the effect of which which can be understood using the LLG equation (Eqn.1.26) discussed later in the chapter. The generated torque can then oppose the intrinsic damping of the free layer causing the magnetisation to continue precessing [21].

Besides being used as a memory storage device, STT-MRAMs can also be used as multifunctional logical devices to store code, informations and microcontrollers [22–24].

Before STT-MRAMs can be adopted in more advanced and commercial applications, there is still a need to overcome the problem of high writing current and eddy fields effects. The write current needs to be further reduced to allow more efficient device. That being said, STT-MRAMs are a very competitive candidate[25, 26] in the storage industry and have the potential to replace the NAND flash mass storage for stand alone memory units. Recently Parkin has demonstrated magnetic mass storage originating from the magnetic domain wall, which is known as the "racetrack memory"[4, 27], and prospects for much better functionality with faster processing time[28].

Table 1.1 lists some important aspects of some memory elements that are in operation and emerging . The values have been taken from Ref. [4, 29].

Feature	HDD	MRAM	NAND Flash	STT-MRAM	Racetrack
Non-volatile	Yes	Yes	Yes	Yes	Yes
Read time	5 ms	20 ns	$100 - 10^6$ ns	2-30 ns	10 ns
Write time	5 ms	20 ns	$100 - 10^6$ ns	2-30 ns	10 ns
Endurance	$> 10^{15}$	$> 10^{15}$	$> 10^5$	Unlimited	Unlimited
Write power	High	High	High	Medium	Medium
Density	Low	Medium	High	Medium	High
Standby power	High	Low	Low	Low	Low
Status	Current	Current	Current	Current	Emerging

Table 1.1: Comparison of current technology to emerging technology in improving the memory architecture.

Within the past few decades of the birth of spintronics novel, robust and efficient concepts and technologies have been developed and postulated which have revolutionised the magnetic memory storage industry. As time passes by more challenging and interesting research continues to develop in this field. The recent discovery of graphene based spintronics[30], molecular and organic spintronics[31, 32], antiferromagnetic spintronics[33–35], superconductors and the recent Nobel winning

topological matter[36] have made this field even more interesting and fascinating with tremendous potential for future research. With this we conclude the introduction to spintronics section, and in the next few sections introduce some processes and techniques which are exploited to control the magnetisation of the material, relevant to the work described in my thesis.

1.2 Manipulation and control of magnetisation

In the last section we discussed the emerging and existent storage technology utilising the manipulation and control of magnetisation to store digital information and perform logical operations. As such there have been numerous techniques to achieve control over the behaviour of the magnetic moments. The most common approach is to apply an external magnetic field, which however suffers the drawback of inducing stray effects due to spatial localisation limit, which could create distortions in the magnetisation process being investigated.

In this section we introduce three techniques namely (a) electric field control, (b) strain mediated control, and (c) magneto-acoustic techniques to modulate the magnetisation processes in magnetic materials.

1.2.1 Electric field control of magnetisation

The manipulation of magnetisation of a material by using electric fields had been conceived back in 1960s [37, 38], but due to unavailability of finding a viable material whose magnetic moments could be affected by electric field, the technique was not investigated further.

In most of the ferromagnetic materials, by applying a very large electric field there still is not any observable change in the magnetic properties without breaking down the insulator through which the field is applied. This is due to the field screening by the free electrons in metals. However applying an electric field to semiconductors changes the conductivity by altering the density of the electrons in the conduction and valence bands. Investigation into this led to the demonstration of manipulation of carrier concentration in a class of material known as the ferromagnetic semiconductors specially (In,Mn)As, and (Ga,Mn)As [39, 40],by electrical gating[41]. The first demonstration to change the magnetisation in ferromagnetic transition metals was observed for thin film layers of FePt and FePd [41, 42]. The manipulation in these films was achieved by changing the magnetic coercivity as a

function of voltage applied across an electrolytic cell system comprising the magnetic film grown on MgO substrate in a propylene carbonate electrolyte as depicted in Fig.1.3 which has been adapted from Ref. [42]. This paved the way to further investigation of the electric field effects in other materials like Fe(Co)/MgO system [43, 44]. In the Fe(Co)/MgO system it was observed that the electric field manipulated the magnetisation by changing the interface magnetic anisotropy, which was further investigated in MTJs [45, 46]. The investigation into the electric field manipulation in MTJ structures can be broadly classified into (a) electric field to change the coercive fields, and (b) using the electric field to realign the magnetic easy axis, thus inducing magnetisation precession about the new effective axis.

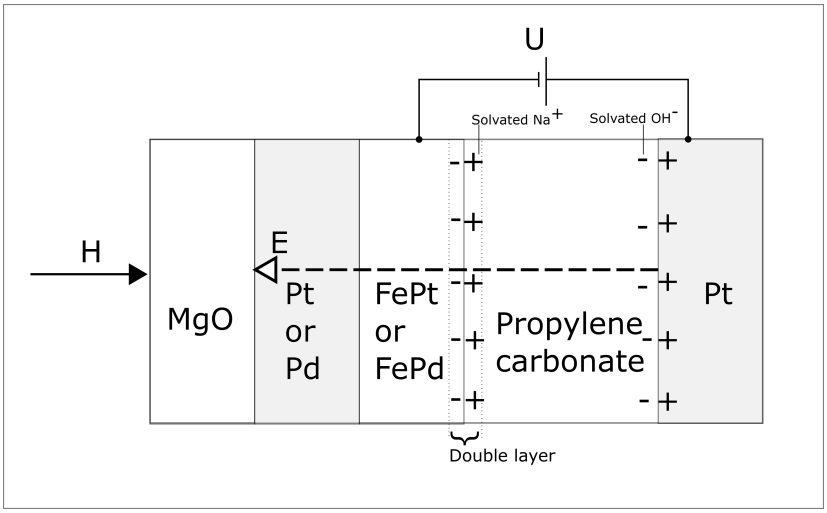

Figure 1.3: Schematic of the electrolytic cell containing the magnetic film (FePt or FePd) grown on MgO substrate. The magnetic film is under the influence of the external magnetic field H. The potential U creates an electric field E in the cell, which produces the electrolytic double layer at the sample surface. The change in coercivity is achieved by utilising this double electric layer at different potentials.

1.2.2 Strain control of magnetism

The strain control of magnetisation can be considered as an extension of the electric field manipulation of the magnetisation by influencing the magnetic anisotropy of the material. A part of this thesis describes the strain control of magnetisation in magnetic multilayer system.

Strain control of magnetisation utilises the multiferroic property of a material or a hybrid device via the strong cross coupling between the ferromagnet and ferroelectric order. There have been multiple approaches to couple the ferromagnetic

and ferroelectric properties which include sintering of particle composites [47], introduction of defects in crystal lattice and fabrication of the ferromagnetic devices on a ferroelectric substrate with or without a buffer layer [48]. The method used in this thesis involves bonding the ferromagnetic material ,grown on a GaAs substrate, onto a piezoelectric transducer using a binding glue (See Sec.2.2.4).

There have been numerous developments exploiting the magneto-elastic coupling effect in the ferromagnet/ferroelectric hybrid structure which includes strain mediated magnetic anisotropy manipulation in $CoFe_2O_4$/FeBaTiO_3 [49],Ni/BaTiO_3 [50],Terfenol-D/PbZr_{1-x}Ti_xO_3 [51] and many more which can be found in Ref. [52–55]. Even though these experiments were successful in demonstrating the electric field induced strain to influence the magnetisation, the efficiency was too low due to ferromagnet/ferroelectric mixing during the sintering process. To overcome this issue ferromagnetic and ferroelectric layers were separately prepared and connected together by physical techniques such as epoxy resin and polyvinyldene fluoride (PVDF) [56, 57]. Rushforth et al[58] demonstrated this technique to influence the magnetic anisotropy in the ferromagnetic semiconductor GaMnAs by bonding the GaAs over which the magnetic material was grown onto a piezoelectric transducer using epoxy resin. By applying a voltage across the transducer a tensile or compressive strain is generated depending on the sign of the voltage which gets transmitted to the magnetic layer and alters the magneto-elastic coupling energy and thereby the anisotropy direction. A schematic for this hybrid configuration is illustrated in Fig. 1.4 which shows the magnetic material bonded onto a piezoelectric transducer using epoxy glue.

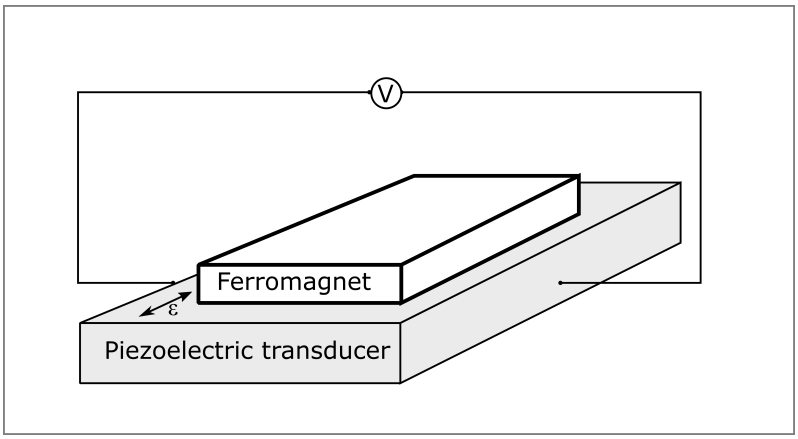

Figure 1.4: Schematic of the hybrid configuration for strain mediated control of magnetisation in a magnetic material bonded onto a piezoelectric transducer. By applying a voltage across the transducer a tensile or compressive strain is generated which is transmitted to the magnetic layer and alters the magneto-elastic energy term and thereby the magnetic anisotropy direction.

The configuration comprises two main components, (a) a piezoelectric material which produces a strain when subjected to an electric potential, and (b) a magnetic material which should be sensitive to this generated strain. This sensitivity parameter for the magnetic materials is known as the magnetostriction coefficient (λ) and relates the change in the length of the material under influence of external applied field. This magnetostrictive strain coefficient is related to the magnetoelastic coupling coefficient tensor(B) which is analogous of Young's modulus by

$$B \propto -c\lambda \tag{1.1}$$

where c is the elastic constant.

Rare earth elements and their alloys have shown naturally high values of magnetostriction coefficient in excess of 2000 ppm [59], with Terfenol-D being the highest. It is an alloy of terbium, dysprosium and iron and has the highest value of magnetostriction at room temperature. This efficient property has made its application in magneto-mechanical sensors, actuators, and transducers [60]. However this rare earth element alloy has its limitations and disadvantages such as the large negative impact on the environment, large economic costs, the non linear magnetisation hysteresis behaviour, low sensitivity to temperature, necessity to magnetise them for application purpose and the stoichiometric disproportion under strain [61]. A viable candidate to replace this rare earth alloy is galfenol- an alloy of iron and gallium with magnetostriction coefficient an order of magnitude higher than iron

at room temperature [62]. This alloy was first developed by Clark [63, 64] and is a very promising material for sensor and transducer/actuator applications [65, 66]. Galfenol has a magnetostriction value of $\sim$ 350 ppm under low magnetic field (0.01 T) and a low hysteresis behaviour. It shows a high tensile strength value ($\sim$ 500 MPa) [62, 67] and is not very sensitive to temperature variation, which signifies the endurance of the alloy. Even though the magnetostriction value is low compared to Terfenol-D, this high tensile strength value makes it a more stable and durable replacement for sensing applications in environments prone to shocks.

Table 1.2 lists the magnetostriction and saturation magnetisation values for some materials and alloys . It is now understood that galfenol shows a high magnetostriction value in bulk cases. For the purpose of using this alloy in storage architecture it must also show similar properties for thin film scenario. This has been demonstrated by Parkes [68] and will be discussed in more detail in Sec.1.3 which describes the origin of the magnetostriction and work performed on thin films of this material.

Material	M_s $(\times 10^6 Am^{-1})$	λ_{100} $(\times 10^{-6})$	λ_{111} $(\times 10^{-6})$
Fe[69]	1.712	30	-21
Ni[69, 70]	0.49	-46	-24
Co[69, 71]	1.431	-75	50
$Fe_{81}Ga_{19}$[64, 67]	1.386	395	15
$Fe_{20}Ni_{80}$[71, 72]	0.86	8	0
$Terfenol-D$[59, 73]	0.8	90	1640

Table 1.2: Summary of magnetostriction values and saturation magnetisation for some materials and their alloys

1.2.3 Acoustic methods to control magnetisation

Following from the previous discussion it is possible to change the direction of magnetisation via inverse magnetostriction effect or the Villari effect. In order to attain fast magnetisation switching (100 ps) rates comparable to existent technology, the strain which tunes the magnetic anisotropy should be of higher order of frequencies. One way to perform this is to apply a picosecond strain pulse to one edge of the magnetic material which then traverses through the magnetic layer. This has been reported for (Ga,Mn)As [74] and Ni [75] and for galfenol by Jager et al [76] where picosecond scale magnetisation precession was observed due to the excitation of

spin waves in the lattice of the galfenol film.

In order to achieve the tunability of magnetisation by ultra-fast strain, the experiment involves pumping a pulsed laser of about 100 fs step time to one edge of the sample and monitoring the probe pulse on the other edge of the magnetic sample. The optical pulse will generate a picosecond strain pulse that is transmitted through the substrate into the magnetic layer. Depending on the substrate crystal orientation ([001] or [311]) the strain pulse will be longitudinal or transverse [74, 77, 78]. If the frequency of this transmitted pulse matches to the precessional frequency of the magnetic moment resonance is achieved, and it imparts an out of plane component to the magnetisation precession (M_z in our case). If the amplitude of the acoustic generated strain exceeds a certain threshold value, the magnetisation would be forced to switch to minimise the energy. Fig. 1.5 highlights the schematic of this method to generate a pulsed strain to precession of the magnetisation.

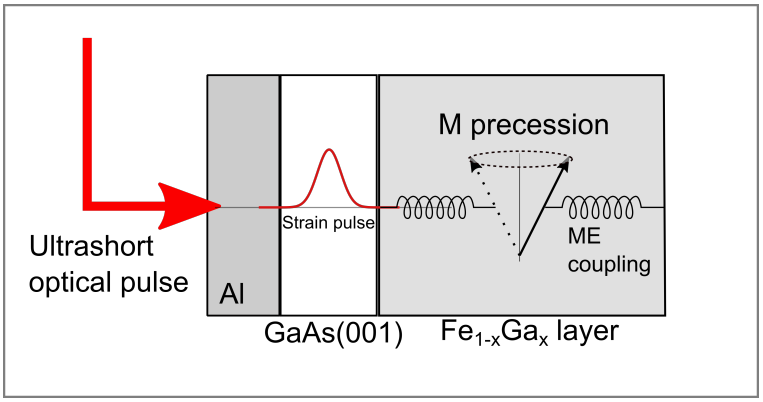

Figure 1.5: Schematic of an ultra fast acoustic method to manipulate the magnetisation precession. The ultra short optical pulse generates a picosecond strain pulse which results in a out of plane kick of the magnetisation vector followed by its precession about the effective field direction.

1.3 Galfenol for strain mediated spintronics

It has been outlined previously in Sec.1.2.2 that galfenol is a suitable and realistic candidate for strain mediated spintronics operations due to its high magnetostriction and tensile strength values. Previous works were based on the bulk properties of this alloy with different concentration of Ga [62, 64, 79], and sometimes substitution of other metals (Al, Cr, Ni, Va, Mo, Sn, Co, Rh) to improve the magnetostriction value [80, 81]. Hall had demonstrated that the magnetostriction of pure Fe can be raised by addition of slight amounts of transition metals [82]. This encouraged

to substitute the same elements to the binary alloy of $Fe_{1-x}Ga_x$ to see any change in the magnetostriction value . V and Cr additions were shown to increase the magnetostriction value and also the room temperature ductility. Further details on the doping of the alloy with other metals and the magneto-elastic property are reported in Ref.[80, 81, 83]

In order to be used in the memory storage architecture, $Fe_{1-x}Ga_x$ must also show the similar functionality in thin film or nano length scale situations. The work presented in this thesis involves studies on bilayer thin films of $Fe_{1-x}Ga_x$ to demonstrate strain mediated magnetisation effects and to propose a design for a future memory technology based on the magnetostriction effect in this alloy. This section is divided into two subsections, the first segment discusses the understanding of the origin of the magnetostriction in galfenol and the second part outlines some of the previous works performed on thin films of galfenol.

1.3.1 Magnetostriction in Fe-Ga

The magnetostriction property of this alloy has been shown to be dependent on the concentration of Ga [64], with the highest λ_{100} observed for 19% Ga concentration and ~28% Ga concentration. The origin of this peculiarity in magnetostriction has been a subject of discussion and numerous theories have been proposed. Sophisticated experimental techniques involving x ray studies and theoretical density functional theory calculations predicted that the origin is entirely intrinsic and structural [84–88]. Based on the work by Xing et al [89], the magnetostriction for the [100] crystal direction at different Ga concentration can be separated into four broad segments as shown in Fig. 1.6 with different colour regions.

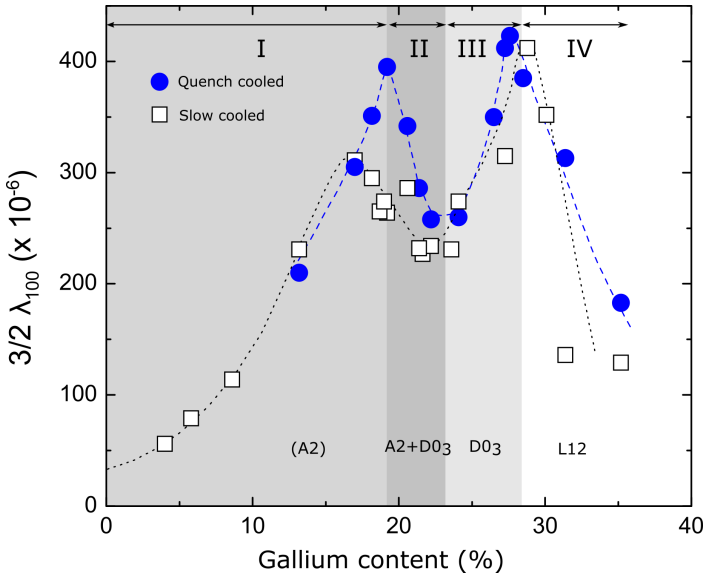

Figure 1.6: Magnetostriction coefficient along [100] direction for galfenol at different Ga%. The magnetostriction values have been divided into four different sections depending on the concentration of Ga and have been discussed in the text. The blue points are the values for quench cooled samples and the hollow squares are for slowly cooled samples.

In region (I) it is seen that as the gallium concentration is increased, the magnetostriction value also increases monotonically till it reaches the maximum at 19% Ga. This increase has been proposed to be due to the lattice transformation from a disordered A2 structure to a more ordered DO_3 structure (see Fig.1.7 (a) and (b,c)). The peak at 19% Ga concentration was explained by Cao [84, 90] and Ruffoni [91]. Their findings indicated that there was strong diffusion scattering in the $A2 + DO_3$ structure which would be due to the coherent nano precipitates that form within the A2 matrix. These nano precipitates are tetragonal DO_{22} crystal structure rather than cubic (Fig.1.7 (d)). The tetragonal nano precipitates cause a tetragonal distortion to the cubic A_2 structure, refelected as diffusive scattering, The relative structural density of these tetragonal domains along the {100} direction determine the magnetostriction.

Mechanisms proposed by Khachaturyan and Viehland [92], and Rao [93] attributed the magnetostriction to the nano-inclusions being cubic DO_3which under the influence of external field deform and rotate continuously to a tetragonal DO_{22} structure. Recent works by Cao [90], Rao [94], and He [95] have proposed that the Ga distribution remains unchanged, but the induced tetragonality of the A2 matrix rotates by small atomic displacements. This matrix exhibit vanishing structural

anisotropy.

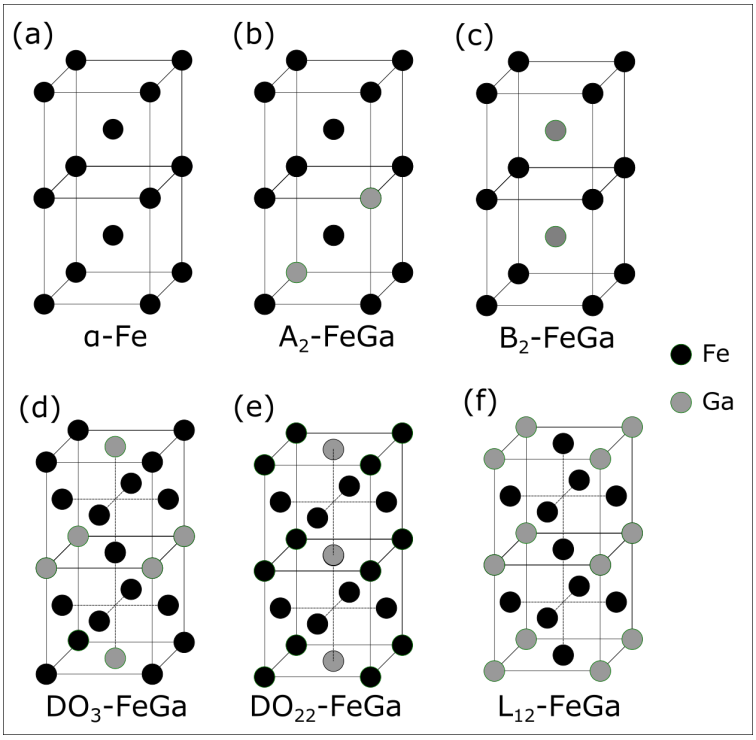

Figure 1.7: Crystal structures of Fe and $Fe_{1-x}Ga_x$. (a) is the body centred crystal structure of pure Fe. When Ga is substituted to Fe, the crystal structure is body centred. But the crystal can take two forms (b) Ga atoms are randomly distributed, (c) Ga occupy the body centred sites. At 19% Ga, it nano-precipitates to a (d) DO_3 structure and are distorted to a tetragonal phase (e) DO_{22} and appear like a fcc L_{12} structure (f).

According to their model, the minimum of the energy as a function of the tetragonal distortion corresponds to a purely cubic structure and there is a lower minimum in one direction, which corresponds to the tetragonal state. If an external field is applied along the tetragonal directions, this crystal is stabilised and it is possible to flip the tetragonal c-axis via a sequence of small atomic displacements due to vanishing structural anisotropy.

The second peak at 28% Ga concentration has been attributed to the lattice softening and lower lattice constants [96–98].

1.3.2 Demonstration of magnetostriction in thin films of Fe-Ga

In order to exploit the high magnetostriction value of galfenol for use in magnetic memory based technology, numerous works have been done on $Fe_{1-x}Ga_x$ films. Parkes[68, 99] utilised the inverse magnetostriction effect to determine the behaviour of the net magnetisation of epitaxial $Fe_{81}Ga_{19}$ films to an external strain produced by a piezoelectric transducer. For the strain manipulation of the magnetic moments he used a similar technique (see Ref. [58] and Sec.2.2.4) of bonding the magnetic material to a piezoelectric transducer using epoxy resin glue. He reported that $Fe_{81}Ga_{19}$ grown on $GaAs(001)$ substrate possesses cubic magnetocrytalline anisotropy which defines two distinct easy axes along the [100]/[010] crystal orientations. The magnetisation will be preferentially oriented along these axes in the absence of any external field. By applying a strain using the transducer, he demonstrated tuning of the magnetic easy axis of the sample. Fig.1.8 shows the magnetisation reversal field behaviour for the epitaxial $Fe_{81}Ga_{19}$ thin film for tensile strain along the [010] (positive voltages), and compressive strain along the [010] (negative voltages). It illustrates that by applying a strain, it is possible to manipulate the magnetocrytalline easy axis, and thus the magnetisation process in the material. The figure has been sourced from Ref. [68]

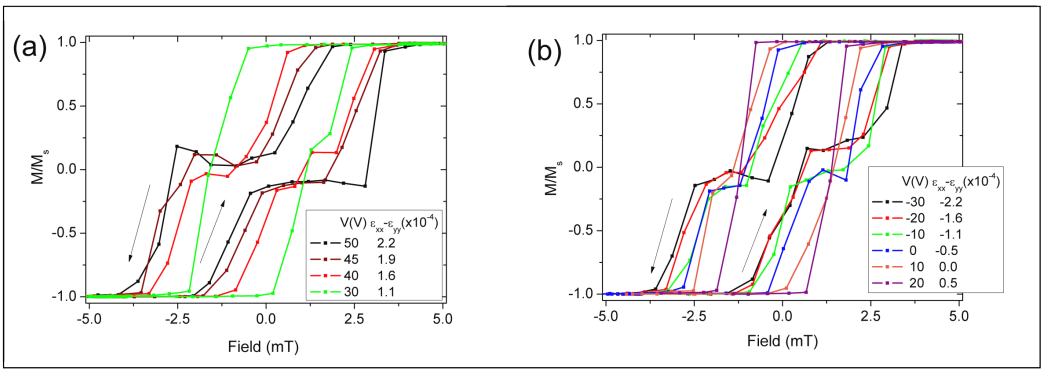

Figure 1.8: Magnetisation reversal loops for single layer of $Fe_{81}Ga_{19}$.(a) The field is applied along the [010] axis while the strain favours the same direction . (b) The field and strain both along the [100] direction. It is observed that the magnetic anisotropy is manipulated by applying a strain along these directions. (Source: Ref. [68])

Similar effects to change the magnetic easy axis have also been observed for

sputter grown samples [100] implying the usability of this material at more efficient costs and time. The values of the magneto-elastic coefficients for bulk , MBE, and sputter grown Fe-Ga samples are presented in Fig. 1.9 and have been adapted from Ref. [100, 101].

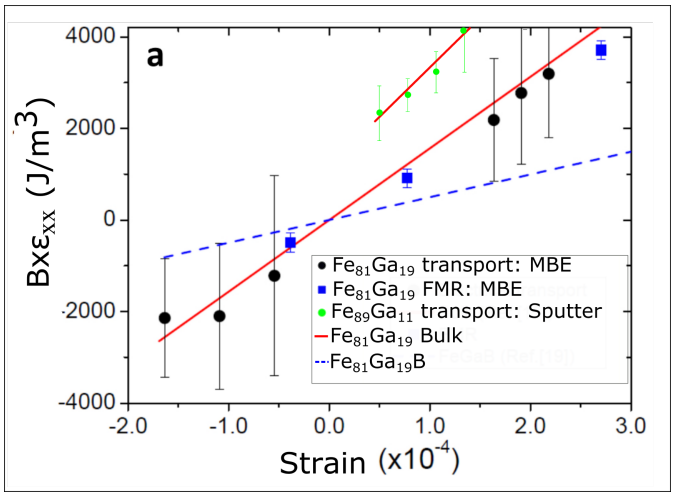

Figure 1.9: Variation of the magnetic free energy coefficient with different values of induced strain for Fe-Ga, Fe-Ga-B bulk and thin films grown by different techniques. The strain anisotropy was determined using electrical transport, ferromagnetic resonance techniques. (Source: Ref. [68, 100])

The high magnetostrictive property of galfenol has a high potential for applications such as non-volatile memory. It was demonstrated [99] that the magnetisation can be switched by 90° utilising the strain generated by the transducer, and without the aid of any extra external field thus minimising the effect of any eddy losses due to stray effects and Joule heating. The non-volatile nature for $Fe_{81}Ga_{19}$ has been shown in Fig.1.10 adapted from [99]. It shows that as the magnitude and the sign of the strain varies, it manipulates the effective magnetic anisotropy of the material and forces the switching of the magnetic material which shows a hysteresis behaviour.

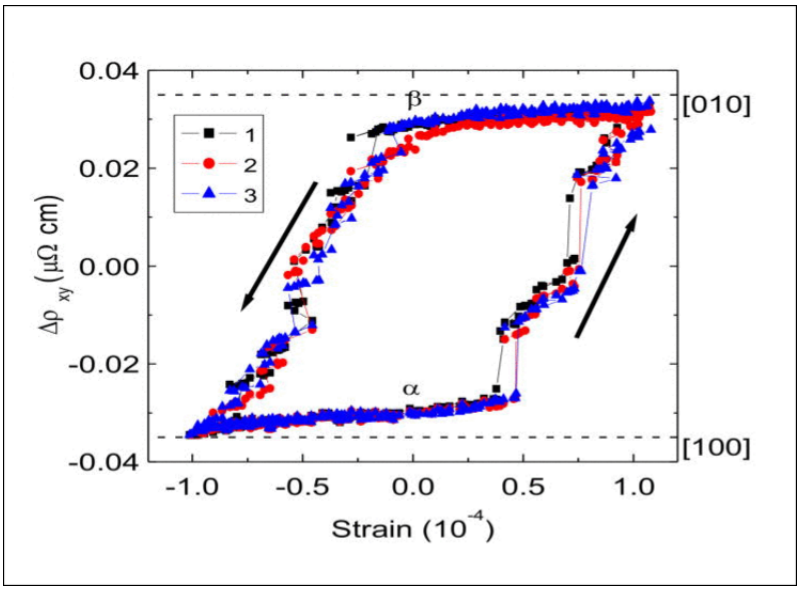

Figure 1.10: Non-volatile magnetisation switching mechanism demonstrated for $Fe_{81}Ga_{19}$ films. The magnetisation orientation has been obtained by electrical transport measurements which will be discussed in Sec.1.4.4 . (Source: Ref. [68])

The dynamic behaviour of the magnetisation in $Fe-Ga$ films has also been studied extensively. The behaviour of the ferromagnetic resonance linewidth and the damping parameters for different concentration of Ga in the alloy [102] and thickness of the film [103] have been studied. It has been concluded that the linewidths in this alloy are narrow with small values of intrinsic damping. The intrinsic damping or the Gilbert damping parameter has been found to be dependent on the concentration of Ga and suggesting different relaxation and scattering mechanisms (especially magnon scattering [104]) that govern the precession of the magnetic moments. The magnetisation dynamics has also been studied when the sample is under a compressive or tensile strain, and no change to the intrinsic damping has been observed. This is a good indication for the microwave device applications side, which would demand for much smaller devices where the extrinsic damping which is dependent on strain can be minimised at such length scales. However this independent behaviour is not well understood. In this thesis, we report the under-damping and over-damping of the Gilbert parameter for the multilayer $Fe_{1-x}Ga_x$ samples which will be discussed in detail in Ch.3. The variation of the linewidth for different Ga concentrations and strains have been shown in Fig.1.11, sourced from Ref.[101, 102].

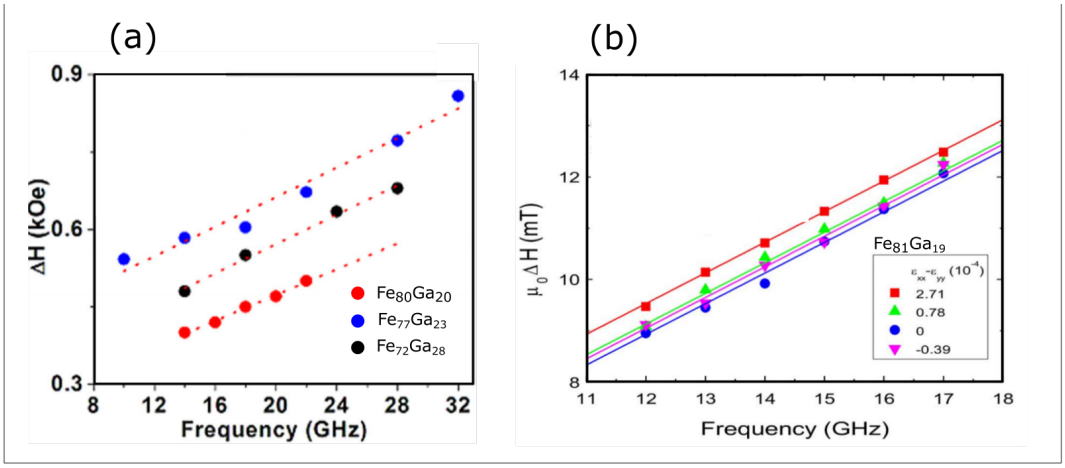

Figure 1.11: Magnetisation dynamics for $Fe_{1-x}Ga_x$ thin films studied by ferromagnetic resonance experiments. (a) The variation of linewidth and damping which is determined by the gradient, for different Ga%, (b) The enhancement of the extrinsic damping at different strain values for $Fe_{81}Ga_{19}$. (Source: Ref. [101, 102])

This combination of high magnetostriction parameter and narrow linewidth have encouraged research towards the spin wave generation from the lattice of the structure. The evolution of spin wave modes in Fe-Ga thin films and stripe domains have been studied with ultrafast laser Kerr spectrometry [76] and Brillouin light scattering experiments [105]. The lattice excitation towards out of plane magnetic anisotropy have been studied to understand in more details the mechanism of the damping process in this material.

As can be understood from the mentioned features of Fe-Ga, it is a capable candidate for use in the magnetic material based storage technology and microwave applications. The ability to use the magnetostriction to demonstrate non-volatile memory with fast processing times offers a possible solution to the high power consumption and writing problems in the present day MRAMs architecture. The motivation of this thesis is to continue the research on magnetostrictive multilayer films of galfenol and understand and control the magnetisation reversal process in each layer. The investigation involves employing experimental techniques such as magneto-optical effects, magneto-transport, SuperConducting Quantum Interference Device (SQUID) magnetometry, ferromagnetic resonance and mathematical calculations to investigate the magnetisation process in bilayer films of $Fe_{1-x}Ga_x$ of the same or different thicknesses. The intention is to design a strain controlled magnetic information storage device by utilising the multilayer for improved storage density. Fig.1.12 illustrates the schematic of an array of memory cells bonded

on a piezoelectric transducer. As the strain is varied, it affects the magnetisation differently in each layer due to difference in their magnetic anisotropy values and magnetostriction coefficient. This would lead to an independent magnetisation reversal process of the bilayer films causing variations in resistance as the strain is varied. Further details about the working of this memory cell using the anisotropy coefficients will be discussed in the later sections of this thesis.

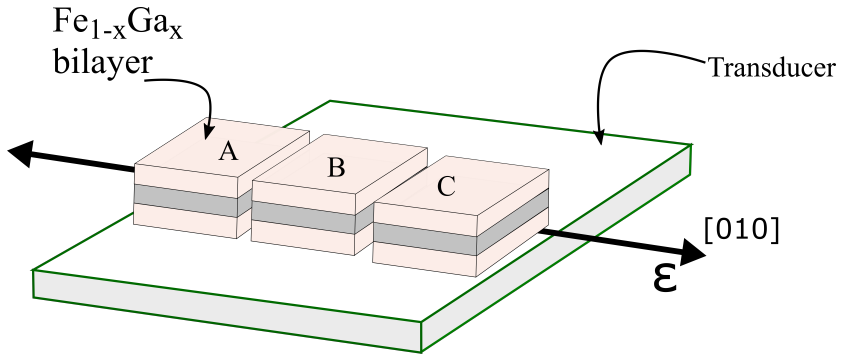

Figure 1.12: Design of a strain controlled memory element, in which the the extra layers improve the storage density. The magnetisation of each layer is manipulated by applying an external strain. The strain would cause independent switching of the magnetisation due to difference in anisotropy and magnetostriction constant for each layer.

The concept of having multilayer of different composition and thickness could pave design and ideas towards design of a spin torque based logical device which can be influenced and tuned by strain, thus minimising the stray effects.

1.4 Theory of magnetic materials

This section is intended to introduce the basic concepts of magnetism used in this thesis as well as most of the models used for the analysis and understanding of the experimental results.

1.4.1 Magnetic moment and magnetisation

Magnetic moment is the fundamental object of a magnetic material and quantitatively determines the strength of the magnetic material. Classically it is equivalent to a current loop or a magnetic dipole. In an atom it is associated with the electronic orbital angular momentum ($\overline{L}$), and its spin angular momentum ($\bar{S}$) and

represented as,

$$\bar{\mu}_L = -g_L \mu_B \frac{\bar{L}}{\hbar} \tag{1.2}$$

$$\bar{\mu}_S = -g_S \mu_B \frac{\bar{S}}{\hbar} \tag{1.3}$$

where g_L, g_S are the Lande g- factors with values 1 and 2 respectively and $\mu_B = |e|\hbar/2m$ is the Bohr magneton. The magnetisation is the measure of the net magnetic moment per unit volume (volume magnetisation) and expressed as Am^{-1} in SI units. Some materials posses a very strong magnetisation in the absence of any external field, and are in a spontaneously magnetised state. This class of materials are known as the ferromagnetic materials, and have regions of ordered magnetic moments . Weiss in 1907 proposed the molecular field theory in order to explain the spontaneous magnetisation of ferromagnets [69, 106]. He postulated that due to the mutual interaction between the magnetic moments, the moments prefer to be oriented relatively parallel or antiparallel to each other. This mutual interaction is due to an internal field - Weiss molecular field (H_w). The net internal field is therefore the vector sum of the Weiss field and the external field and is expressed as

$$H^i = H + H_w \tag{1.4}$$

The temperature dependence of the magnetisation state was predicted from this model (Curie Weiss model, see Eqn.1.5) and relates the phase change of the magnetisation expressed in terms of susceptibility (χ), from ferromagnetic state to a paramagnetic state at the critical temperature (T_c)

$$\chi = \frac{C}{T - T_c} \tag{1.5}$$

Even though this model predicted the magnetisation state it did not describe the origin of the internal field. Heisenberg in 1928 proposed that the exchange energy interaction between two neighbouring spins plays a crucial role in ferromagnetic state of magnetic material [107]. Mathematically the exchange energy is expressed as

$$E_{ex} = -2J_{ex} S_i S_j cos\phi \tag{1.6}$$

where J_{ex} is the exchange integral and ϕ is the angle between two adjacent spins S_i, and S_j. The exchange energy is minimised when the spins are parallel or antiparallel

depending on the sign of the exchange integral. This exchange energy theory was able to explain Weiss's postulate. However the limitation to explain the different ferromagnetism behaviour led to the development of the band theory which is based on the electronic configurations of the material, and coherently explains the magnetic and electric behaviour in metals, insulators and semiconductors. Band theory was first postulated by Stoner, Mott and Slater and is often referred as the collective electron theory[108, 109].

According to this theory, the Fermi energy for a ferromagnetic material lies in a region of overlapping 3d and 4s bands as shown in Fig. 1.13 . Assuming that the structures of the 3d and 4s bands do not change across the 3d series and so any differences in electronic structure are entirely due to changes in the Fermi energy (E_F)[69, 109].

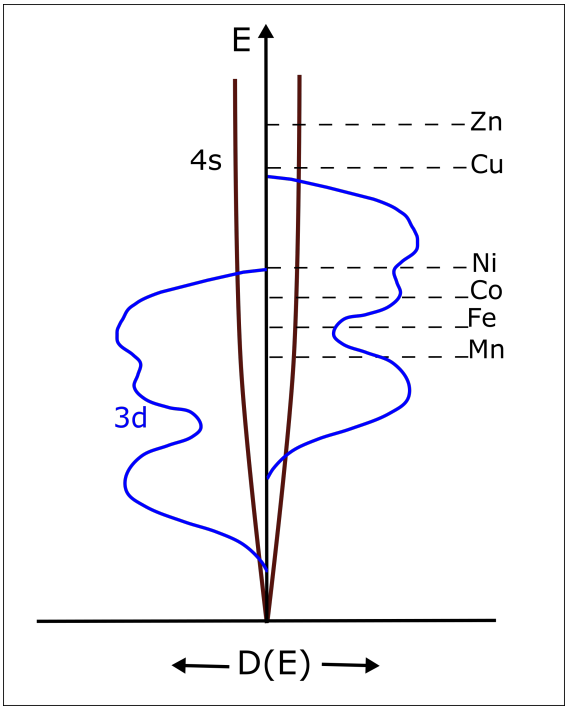

Figure 1.13: Schematic of the density of states for the 3d- and 4s- for different metals. The Fermi energy is represented by the dashed line.The positions of the Fermi levels (E_F) in Zn, Cu, Ni, Co, Fe, and Mn are shown for representation only. For a ferromagnetic material the E_F lies in a region of overlapping 3d and 4s bands. (Adapted from Ref. [69].)

Due to the exchange interaction (Eqn. 1.6) the energy of the 3d band for electrons with one spin direction relative to that with opposite spin is shifted . If the Fermi energy lies within the 3d band, then this shift in energy will cause more

electrons of the lower-energy spin direction and hence a spontaneous magnetic moment in the ground state. A schematic of this splitting for a transition metal is shown in Fig. 1.14.

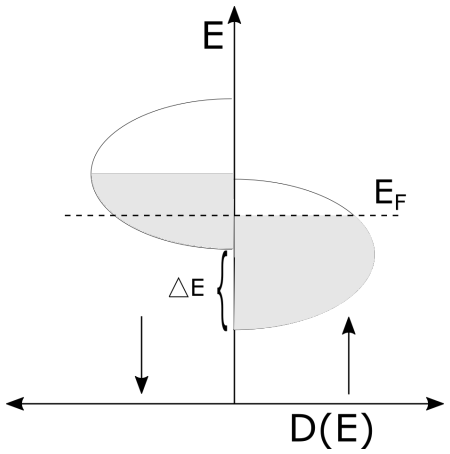

Figure 1.14: Schematic to show the d- band density of state for a ferromagnetic transition metals which shows the 3d- band splitting depending on the orientation of the electron's spin.

1.4.2 Magnetic energies and fields

The magnetisation of a magnetic material favours to point in a direction where the energy is minimum, and is known as the easy axis of the magnetisation[110]. The energy of the magnetisation state is dependent on the direction of the magnetisation with respect to the easy axis and is referred to as the magnetic anisotropy energy along a particular direction. The origin of this energy could be the sample geometry and shape, crystal symmetry, internal and external strain, atomic pair ordering, and dipolar interactions between spins[69, 107, 111].

The different energies that influence the magnetisation of a material have been discussed in this section. The intrinsic fields due to shape and anisotropy and how they interact with the external field to influence the magnetisation process is described here.

1.4.2.1 Demagnetising energy

Demagnetising fields are the fields that emanate from the surface of the magnetic material due to its magnetisation and pass through the volume of the sample. Consider a thin film of magnetic material with the magnetisation aligned perpendicular to the plane of the film (Fig. 1.15a). Magnetic poles are created on either sides

of the film. Following Maxwell's equation ($\nabla.\bar{B} = 0$), there is an internal field which is oriented opposite to the magnetisation and leads to a demagnetising field ($\nabla.\bar{H} = -\nabla.\bar{M}$). However when the magnetisation is in the plane of the sample (1.15b) , the generated demagnetising fields can be approximate to zero due to the long distance between the created poles. Therefore, to avoid the energy cost associated with the demagnetising field, the magnetisation prefers to orient in the plane of the sample.

The demagnetising energy is given as:

$$E_{dem} = -\frac{\mu_o}{2} \int_V \bar{M}.\bar{H}_{dem} dV \tag{1.7}$$

where V is the volume of the sample and the integration is performed over the volume of the film.

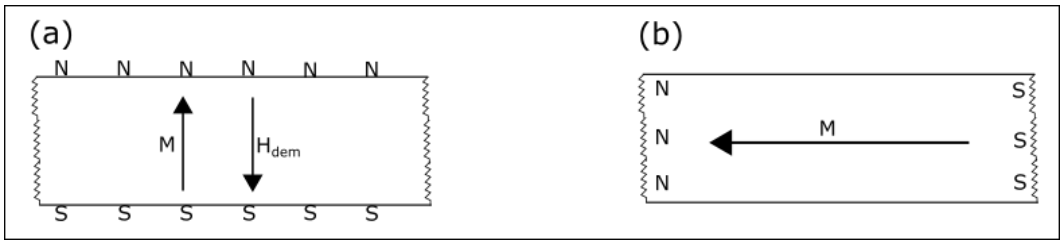

Figure 1.15: Cross sectional view of a magnetic thin film. (a) When the magnetisation is perpendicular to the film plane , demagnetising field H_{dem} is generated due to magnetic poles on the sides of the film. (b) When the magnetisation is in plane of the sample, the effect of H_{dem} can be approximated to be zero.

1.4.2.2 Zeeman energy

Zeeman energy term describes the interaction between the external magnetic field (H_{ext}) and the magnetisation density. This energy term is given as

$$E_{Zeeman} = -\mu_o \int_V \bar{M}.\bar{H}_{ext} dV \tag{1.8}$$

The Zeeman energy term tries to align the magnetisation along the direction of the applied external field.

1.4.2.3 Magnetocrystalline anisotropy energy

The magnetization prefers to be oriented along the easy axis, and the energy cost to orient it along the easy axis is determined by the magnetocrytalline anisotropy

energy, which is the change in the energy for a crystal upon rotation of the magnetization. In thin films the magnetocrytalline anisotropy is different from the bulk due to the symmetry breaking [110] and can be manipulated by changing the thickness and type of a material. This energy plays a decisive role in the orientation of the magnetisation by contributing to the free energy of the crystal. It has its origin from the relativistic corrections to the Hamiltonian which contributes to the symmetry breaking and invariance of the spin orbit coupling term and the dipole-dipole interaction term.

At the macroscopic level, the magnetocrystalline anisotropy energy can be explained phenomenologically by expressing the magnetisation unit vector in spherical coordinates as

$$E_{ani} = \int_V f(\bar{m})dV \tag{1.9}$$

where $f(\bar{m})$ is the free energy function of the system with the magnetisation vector $\bar{m} = \frac{M}{|M|}$ over the spherical coordinates,

$$m_x = sin\theta cos\phi$$

$$m_y = sin\theta sin\phi$$

$$m_z = cos\theta$$

The unit magnetisation vector can also be represented by the direction cosines as well as shown in the representation in Fig.1.16 such that $\alpha_1 = m_x$, $\alpha_2 = m_y$, and $\alpha_3 = m_z$.

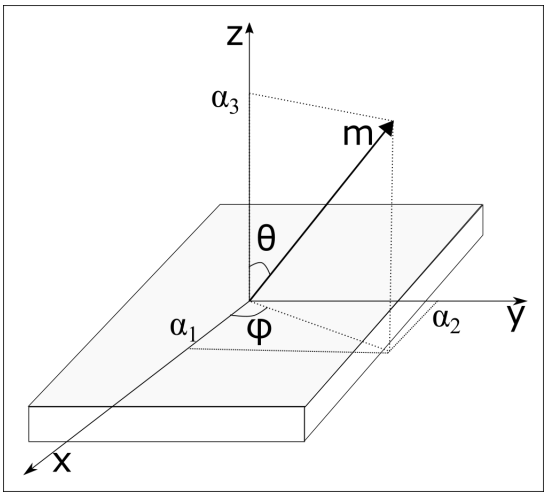

Figure 1.16: Definition of the direction cosines for magnetocrystalline anisotropy.

The magnetocrystalline energy per unit volume can then be expressed as a power series expansion of the components of the magnetisation as shown below for cubic systems as :[112]

$$E_{ani} = K_0 + K_1(\alpha_1^2\alpha_2^2 + \alpha_2^2\alpha_3^2 + \alpha_3^2\alpha_1^2) + K_2(\alpha_1^2\alpha_2^2\alpha_3^2) + K_3(\alpha_1^2\alpha_2^2 + \alpha_1^2\alpha_3^2 + \alpha_2^2\alpha_3^2) \quad (1.10)$$

where K_i are the magnetocrystalline anisotropy coefficients. Table 1.3 lists the typical values of K_1 and K_2 for several materials at 4.2K taken from Ref.[107].

Material	K_1 ($\times 10^4 Jm^{-3}$)	K_2 ($\times 10^4 Jm^{-3}$)
Fe	-1.8	5.2
Co	1.8	7
Ni	3	-12
Fe_3O_4	-0.9	-2

Table 1.3: Magnetocrystalline anisotropy coefficients for some materials at 4.2K.

For the samples described in this thesis it is known that for $Fe_{1-x}Ga_x$ grown on $GaAs$ has the weaker uniaxial anisotropy along the [110] and a stronger biaxial anisotropy along the [010]/[100] axes [113]. Therefore the net magnetocrystalline anisotropy energy to the lowest order can be represented as a superposition of a

biaxial anisotropy and uniaxial anisotropy[99, 101, 114]

$$E_{magnetocrystalline} = E_{uniaxial} + E_{cubic} \tag{1.11}$$

$$= K_1 sin^2(\phi - 45°) + \frac{K_2}{4} sin^2(2\phi)$$

where ϕ is the angle between the magnetisation vector ($\bar{m}$) and the easy axis along [010] axis.

SQUID MH loops showing the magnetisation along different crystal axis has been shown for one of the experimental sample (Sample S421) in Fig.1.17. It shows the magnetisation variation as the field is varied along three different crystal axis, [110], [1$\bar{1}$0], and [100] .

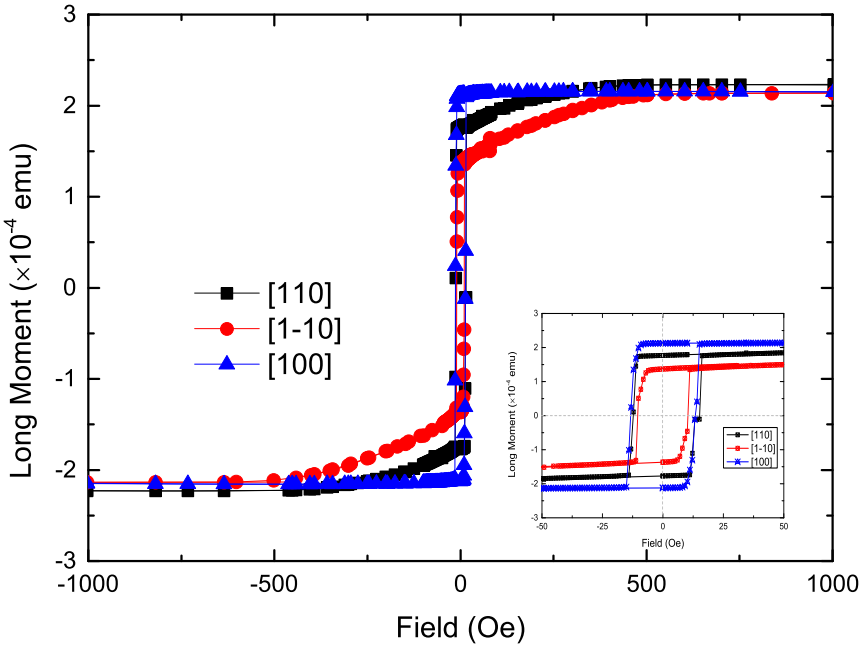

Figure 1.17: Magnetisation loop collected by SQUID on $Fe_{1-x}Ga_x$ bilayer structure along three different crystal axes, [110]: black, [1$\bar{1}$0]: red, and [100] : blue . Due to different magnetocrystalline uniaxial and cubic anisotropy the magnetisation is different for field swept along the axis. Th inset is the zoomed in MH loop for the different directions to define the remnance magnetisation and coercive field.

The calculated variation of the magnetocrystalline anisotropy energy with the angle of magnetisation about the easy axis is shown for zero external field in Fig.

1.18, using the values of anisotropies as $K_1 = 6.2\ kJ/m^3$ and $K_2 = 31.5\ kJ/m^3$. The two fold and four fold symmetries seen in the energy landscape correspond to the uniaxial anisotropy energy and cubic anisotropy energy terms.

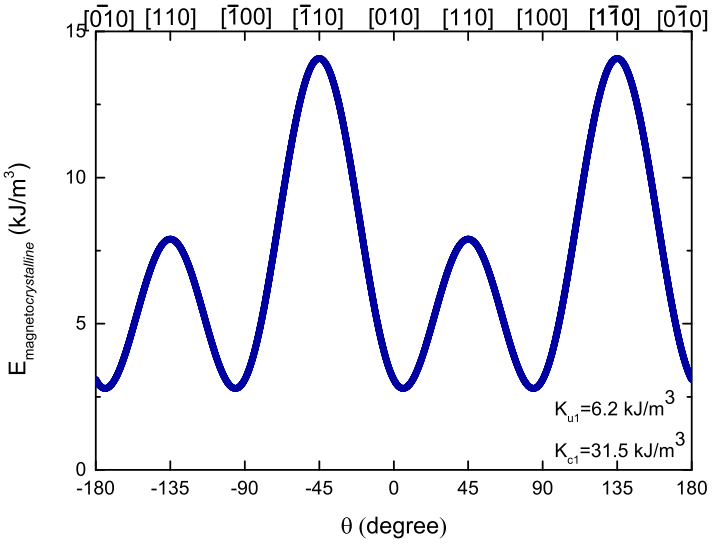

Figure 1.18: Variation of the magnetocrystalline anisotropy energy term with angle between the magnetisation and the easy axis along the [010]. The energy landscape has been modelled using the uniaxial anisotropy constant as 6.2 kJ/m^3 , and cubic anisotropy energy constant as 31.5 kJ/m^3.

1.4.2.4 Magnetoelastic anisotropy energy

When a stress is applied to a magnetic material it is subjected to a change in the crystal lattice which manifests as a change in the magnetic properties due to spin- orbit coupling. The energy which causes this change is called as the magnetoelastic anisotropy energy. Magnetoelastic energy depends on a constant called the magnetostrictive constant (λ), which can be positive or negative. The magnetostriction coefficient describes a change of length of the material in the direction of the field, while maintaining a constant volume. The coefficient at saturating field is denoted as λ.

$$\lambda = \frac{\triangle l}{l}$$

where l is the length of the material and $\triangle l$ is the change in length under the influence of the field.

The magnetostrictive coefficient is an anisotropic property and therefore varies for different crystal axis directions. For cubic crystals, the magnetostrictive constant is measured along the [100] and [111] directions. Details and values of the magnetostriction constants for different materials were discussed before in Sec. 1.2.2 when we described the strain control of magnetisation.

For cubic crystals, the magnetoelastic energy term is given by

$$E_{ME} = B_1 \left[\epsilon_{xx}(\alpha_1^2 - \frac{1}{3}) + \epsilon_{yy}(\alpha_2^2 - \frac{1}{3}) + \epsilon_{zz}(\alpha_3^2 - \frac{1}{3})\right] + B_2 \left[\epsilon_{xy}\alpha_1\alpha_2 + \epsilon_{yz}\alpha_2\alpha_3 + \epsilon_{xz}\alpha_1\alpha_3\right] \quad (1.12)$$

where B_1, and B_2 are the magnetoelastic coupling coefficients, α_1,α_2, α_3 are the direction cosines of magnetisation discussed in last section, and ϵ_{ij} with $i, j = x, y, z$ are the components of the strain tensor.

Eqn. 1.12 can be simplified to Eqn. 1.13 by taking in-plane magnetisation ($\alpha_3 = 0$) and assuming that the strain tensor components ϵ_{xy}, ϵ_{yz}, and ϵ_{xz} are small.

$$E_{ME} = B_1 \left[\epsilon_{xx}(\alpha_1^2 - \frac{1}{3}) + \epsilon_{yy}(\alpha_2^2 - \frac{1}{3}) + \epsilon_{zz}(\alpha_3^2 - \frac{1}{3})\right] \quad (1.13)$$

Following the formulation reported in ref. [68] [115][116], the magnetic coupling constant B_1 is given as

$$B_1 = \frac{3}{2}\lambda_{100}\left(c_{12} - c_{11}\right) \quad (1.14)$$

and the magnetoelastic energy is then given as

$$E_{ME} = \frac{3}{2}\lambda_{100}\left(c_{12} - c_{11}\right)\left(\epsilon_{xx} - \epsilon_{yy}\right) cos^2\phi \quad (1.15)$$

where ϕ is the angle between the magnetisation and the [010] axis and c_{ij} are the components of the elastic tensor.

The magnetostrictive property of the crystals is used to manipulate the magnetisation of the material by applying a strain. This is performed by the effect known as the Villari effect or the inverse magnetoelastic effect [107, 117] and is illustrated in Fig. 1.19 which shows the change in magnetisation of material due to a tensile strain for a magnetic material with positive λ (Fig. 1.19(a)) and negative λ (Fig. 1.19(b)). What this schematic describes is that when the sample is in the

demagnetised state the magnetisation prefers to be in domains to minimise the free energy. By applying a small stress, it will force the domain walls to move in such a way as to decrease the volume of the domains magnetised perpendicular to the direction of stress.

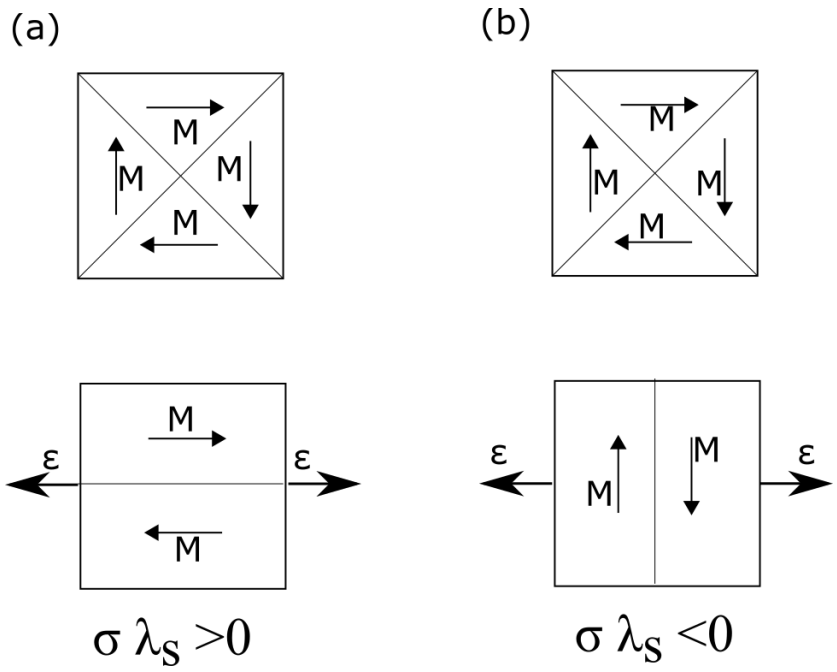

Figure 1.19: Demonstration of Villari effect. (a) Change in the magnetisation of the material with positive λ (b) Change in the magnetisation of the material with negative λ under tensile stress. The stress favours the magnetisation to orient along its direction for a positive λ and favours orthogonal orientation of magnetisation for negative λ.

The results discussed in this thesis are based on the measurements performed on thin films of $Fe_{1-x}Ga_x$ which have been reported to show exceptionally high magnetoelasticity along the [100] direction at different concentrations of Ga[64, 68]. For the experiments involving strain discussed in the thesis, the $Fe_{1-x}Ga_x$ multilayer films have been bonded to a piezoelectric transducer in such a way that the strain is along the [100]/[010] directions. The strain transmitted to each layer is different due to the attenuation through the volume of the sample, and there is no direct way to measure the strain in an individual layer. However, we have calibrated the approximate relative strain applied by the transducer to the whole structure, by removing the AMR and GMR contribution to the magneto resistance by keeping the sample at saturating fields and sweeping the piezoelectric voltage from a negative value to a positive and vice versa. The relation between

the resistivity and the strain have been calculated and described in Sec. 2.2.4. Calibrated strain values for some samples have been highlighted in Appendix B.

Using the measured strain values and Eqn. 1.15 it is possible to calculate the value of the magnetoelastic constants for the structure using the expressions given in Ref. [118, 119] which relates the effective switching field to the magnetoelastic coefficient and strain. The expression can be simplified as:

$$\left(\frac{\triangle H_{eff}}{\epsilon_{xx} - \epsilon_{yy}}\right) M_s = B \tag{1.16}$$

Here the fraction $\frac{\triangle H_{eff}}{\epsilon_{xx}-\epsilon_{yy}}$ is the change in switching field (H_{eff}) over the applied strain ($\epsilon_{xx}-\epsilon_{yy}$) , M_s is the saturation magnetisation in Am^{-1} and B is the magneto elastic coefficient which is equal to $\frac{3}{2}\lambda_{100}\left(c_{12} - c_{11}\right)$ and has energy units.

1.4.3 Magnetisation dynamics in ferromagnetic films

The effect of time varying magnetic fields in the frequency range of MHz and GHz on the magnetisation of the material to induce magnetisation precession is regarded as magnetisation dynamics[120]. In this section, the motion of magnetisation vector under the influence of time-varying field is explained. The background details of ferromagnetic resonance are also described as it is a method employed in some of the experimental measurements presented in this thesis.

1.4.3.1 Motion of magnetisation vector

The rate of the change of the angular momentum vector is related to the torque on the magnetic moment μ due to an external field H as:

$$\frac{d\bar{L}}{dt} = \mu_o \bar{\mu} \times \bar{H} \tag{1.17}$$

with $\mu_o = 4\pi 10^7 H/m$. The equation of the motion of a magnetic moment under the influence of an applied field is then expressed as[121]

$$\frac{d\bar{\mu}}{dt} = -\mu_o \gamma \bar{\mu} \times \bar{H} \tag{1.18}$$

The magnetic moment precesses around the external field with Larmor frequency given by

$$f_{Larmor} = |\frac{\gamma H}{2\pi}| \tag{1.19}$$

with $\gamma = 1.75 \times 10^{11} s^{-1} T^{-1}$ is the gyromagnetic ratio.

This equation of motion (Eqn. 1.18) is modified by the interaction of the magnetic precession with the crystal lattice, scattering, etc. Landau, Lifshitz and later Gilbert [122][123], proposed a continuum equation of the precession of the moment known as the $Landau - Lifshitz - Gilbert$ (LLG) equation and has the formula:

$$\frac{d\bar{m}}{dt} = -\frac{\gamma}{1+\alpha^2}\left(\bar{m} \times \bar{H}_{eff}\right) - \frac{\alpha\gamma}{(1+\alpha^2)M_s}\bar{m} \times (\bar{m} \times \bar{H}_{eff}) \tag{1.20}$$

where α is the phenomenological damping constant or the Gilbert damping parameter and has usual values <0.01, $\bar{H}_{eff}$ is the effective field taking into account the external field, anisotropy contributions, the rf field and is usually expressed as in Eqn.1.21.

$$\bar{H}_{eff} = \bar{H}_{ext} + \bar{H}_{ani} + \bar{h}_{MW} \tag{1.21}$$

The first term of the LLG equation (Eqn. 1.20) represents the precessional motion of the magnetisation vector. The second term represents the damping term, which pulls the magnetisation vector back towards the $\bar{H}_{eff}$ direction. The origin of the damping could be attributed to induction of eddy currents due to the precessional motion, phonon drag mechanism, spin flip scattering, magnon scattering [124, 125]. The solutions of this non linear equation determine the precession of the magnetisation about the new effective field axis $\bar{H}_{eff}$ which is the superposition of the external field and the magnetic anisotropy fields discussed previously. By solving the LLG equation the precessional motion of the magnetisation vector about an effective field direction calculated by using the values of anisotropies as $K_u = 6.2$ kJ/m^3 and $K_c = 31.5$ kJ/m^3 is shown in Fig. 1.20 . The in plane magnetic field when subjected to an external rf field perpendicular to the plane of the sample, kick starts the magnetisation to precess around the new effective field direction. The orange spiral line shows the trajectory motion of the moment represented by a black arrow at time $t = 0$. The trajectory was modelled by solving the LLG equation in MATLAB using the ode toolbox[126].

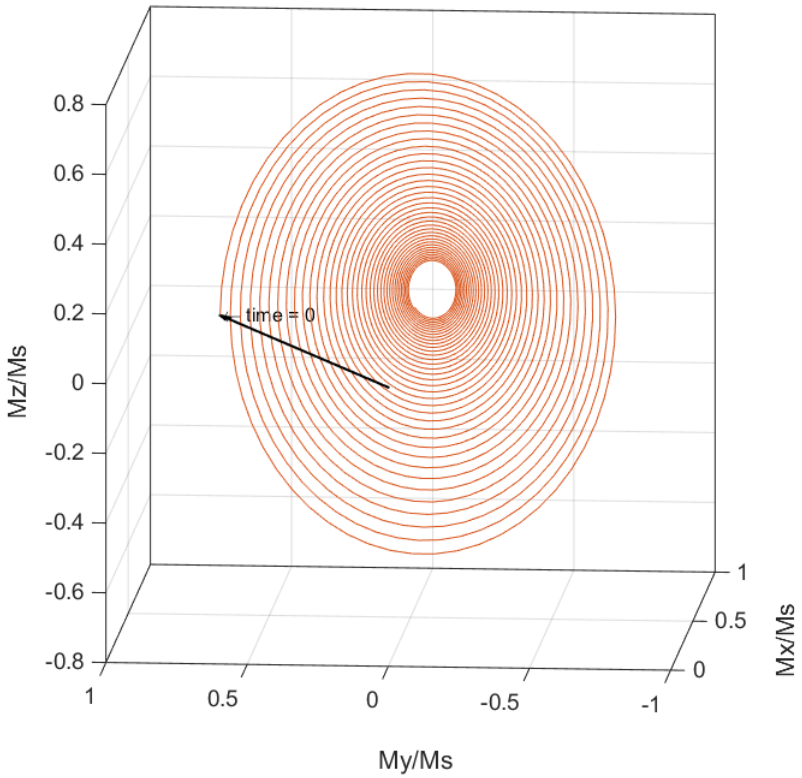

Figure 1.20: The precessional motion of the magnetisation vector for an effective field direction calculated by using the values of anisotropies as $K_{u1} = 6.2\ kJ/m^3$ and $K_{c1} = 31.5\ kJ/m^3$ and $\alpha = 0.01$ for a film of $Fe_{1-x}Ga_x$. The orange spiral line shows the trajectory motion of the moment represented by a black arrow at time $t = 0$.

1.4.3.2 Ferromagnetic resonance

Ferromagnetic resonance (FMR) is a well established and sensitive measurement technique [127] to characterise a magnetic material[128]. In this thesis, by performing angle, frequency, field dependent FMR measurements, the magnetic anisotropy constants, and saturation magnetisation for each layer in the multilayer film of $Fe_{1-x}Ga_x$ have been determined. In this section, a brief introduction to the physics of FMR is described. The FMR experimental set up and the mathematics of the extraction of the magnetic parameters will be discussed in the subsequent chapters.

In a FMR experiment, an alternating microwave field $\bar{h}(t)$ of frequency f excites the magnetisation vector $\bar{M}$. At the same time a d.c. magnetic field is applied which changes the precessional frequency of the magnetisation vector. The reson-

ance condition is found by either sweeping the microwave frequency f, or by varying the d.c. magnetic field [129][130][131]. When the precessional frequency matches to the microwave frequency, the magnetisation is defined to be in resonance [131][132], and the cone angle of the precessing magnetisation reaches a maximum. Experimentally this is observed as absorption of microwave power. The FMR spectrum is characterised by the peak centre related to the resonance condition and the linewidth which is related to the damping parameter.

The ferromagnetic resonance condition can be solved by following the Kittel approach [133] to FMR resonance condition [134][135], which is based on the geometries of the magnetic material and solving the LLG equation. However due to increasing complexity, Smit,Suhl and Beljers in 1955 [136] proposed their approach to ferromagnetic resonance conditions [137, 138] which is based on terms of the derivatives of the total free energy density of magnetisation.

In this thesis, the analysis to extract the magnetic parameters are based on the approach proposed by Smit,Suhl and Beljers, so the basic mathematics have been discussed in this section without much explanation to the mathematical derivation. The derivations have been lucidly explained in Ref.[139].

The equilibrium conditions when an external field H_{ext} is applied causing the magnetisation vector $\bar{M}$ to precess is given by the first derivative of the magnetic free energy with respect to the polar angles θ, and ϕ as shown in Fig. 1.21.

$$\frac{\partial E}{\partial \theta} = 0 \ \ and \ \ \frac{\partial E}{\partial \phi} = 0$$

Applying a microwave field of frequency f generates a small magnetic field $\bar{h}$. If $\bar{h}$ has a component normal to $\bar{m}$ it interacts with the magnetisation vector , and microwave energy is absorbed by the magnetic material itself [131].

Using the LLG equation without the damping term as it does not affect the resonance condition:

$$\frac{d\bar{m}}{dt} = -\gamma \left(\bar{m} \times \bar{H}_{eff}\right) \tag{1.22}$$

The vectors in the Eqn.1.22 can be represented in the local basis of orthonormal spherical vectors $\hat{r}$, $\hat{\theta}$, $\hat{\phi}$ determined by the magnetisation vector $\bar{m}$ such that $\bar{m} = m\hat{r}$. Therefore

$$\frac{d\bar{m}}{dt} = -\gamma(m\hat{r}) \times \left(H_r\hat{r} + H_\theta\hat{\theta} + H_\phi\hat{\phi}\right) \tag{1.23}$$

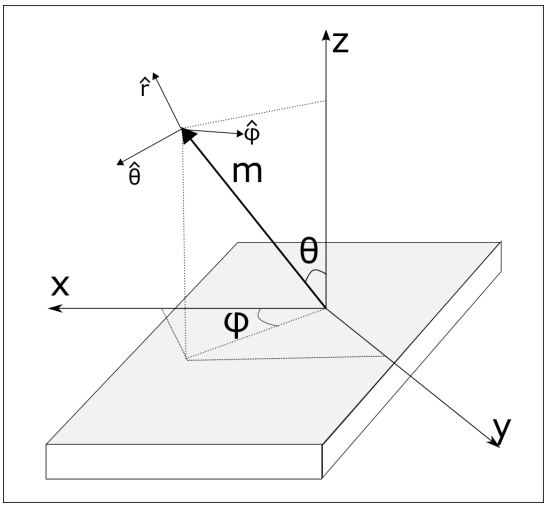

Figure 1.21: Local basis of spherical vectors $\hat{r}$, $\hat{\theta}$, $\hat{\phi}$ used to calculate the resonance condition using the Smit Suhl and Beljers approach

Eqn.1.23 can be written in matrix form as :

$$\begin{bmatrix} \frac{dm}{dt} \\ m\frac{d\theta}{dt} \\ msin\theta\frac{d\phi}{dt} \end{bmatrix} = -\gamma \begin{vmatrix} \hat{r} & \hat{\theta} & \hat{\phi} \\ m & 0 & 0 \\ H_r & H_\theta & H_\phi \end{vmatrix} \tag{1.24}$$

By determining the angles of magnetisation using the first derivatives of energy, Eqn. 1.24 yields the resonance frequency conditions which is known by the Smit Suhl Beljers equation [136] and is shown in Eqn. 1.25

$$\left(\frac{\omega_{res}}{\gamma}\right)^2 = \frac{1}{m^2 sin^2\theta}\left[\frac{\partial^2 E}{\partial\theta^2}\frac{\partial^2 E}{\partial\phi^2} - \left(\frac{\partial^2 E}{\partial\theta\partial\phi}\right)^2\right]\Bigg|_{\theta=\theta_{equ},\phi=\phi_{equ}} \tag{1.25}$$

The frequency linewidth was calculated by Vonsovoskii[140] as in Eqn. 1.26

$$\Delta\omega = \frac{\alpha\gamma}{m}\left[\frac{\partial^2 E}{\partial\theta^2} + \frac{1}{sin^2\theta}\frac{\partial^2 E}{\partial\phi^2}\right]\Bigg|_{\theta=\theta_{equ},\phi=\phi_{equ}} \tag{1.26}$$

1.4.4 Electrical transport properties in ferromagnetic films

In this section, the electrical transport effects in a magnetic material caused by the motion of electron charge are discussed. The basic observations and some important concepts and theories coupling the magnetism to the electrical effects (magneto-transport) have been described. The combination of the spin and charge have led to the discovery of interesting magnetoresistance effects which aid in the

understanding of the magnetisation process in these materials [141].

1.4.4.1 Electronic states and spin dependent transport in ferromagnetic metals

Magnetoresistance (MR) of a ferromagnetic material describes the dependence of the electrical resistivity on the external magnetic field (B) and is denoted as $(\triangle R(B)/R)$. It depends on the spin of the conduction electrons along with their diffusion length scale [11]. The electronic structure of a ferromagnetic transition metal comprises mainly the s- and d- orbitals as discussed previously (Sec.1.4.1) . The hybridisation of the s and d orbitals allows the free electrons to get scattered into more localised d states of the same energy. A large density of these d states at E_F enhances the probability of such scattering which results in decrease in relaxation time and suppression of the mobility and results in increased resistivity. The s-d scattering can be expressed in terms of the scattering potential (V_{scat}) and relaxation time (τ) as:[11, 107].

$$\frac{1}{\tau} = |V_{scat}|^2 N(E_F) \tag{1.27}$$

where$N(E_F)$ is the density of scattering states at Fermi energy level.

A schematic of the density of states for various metals is shown in Fig. 1.22 . The spin dependence of the electrical conductivity is governed by the density of the up spin and down spin electrons in d-band at the Fermi energy level[107]. Mott's two conduction channel model explained the difference in resistivity between the ferromagnetic and non- ferromagnetic transition of metals. He postulated that the spin direction of electrons are conserved during the scattering and the conduction processes, and resulting in two parallel conduction paths for the up spin and the down spin electrons. The resistivity of metal according to this model is given as:

$$\rho = \frac{\rho^{\uparrow}\rho^{\downarrow}}{\rho^{\uparrow} + \rho^{\downarrow}} \tag{1.28}$$

The fraction $\frac{\rho^{\downarrow}}{\rho^{\uparrow}}$ is known as the $\alpha-$parameter and was measured experimentally for different metals by Fert and Campbell who obtained the scattering within each spin band for various impurities [142], together with the temperature dependent scattering rates [107]. For the purpose of comparing the net resistivity Campbell and Fer t[143, 144] followed the Matthiessen's rule [145], which assumes that there is only one type of current carrier and the scattering mechanisms are independent

and for a finite temperature T, the resistivity is expressed as

$$\rho_m(T) = \rho(0) + \rho_h(T) \tag{1.29}$$

where $\rho(0)$ is the residual resistivity of the metal with impurities and $\rho_h(T)$ is the resistivity of the pure homogeneous metal at temperature T.

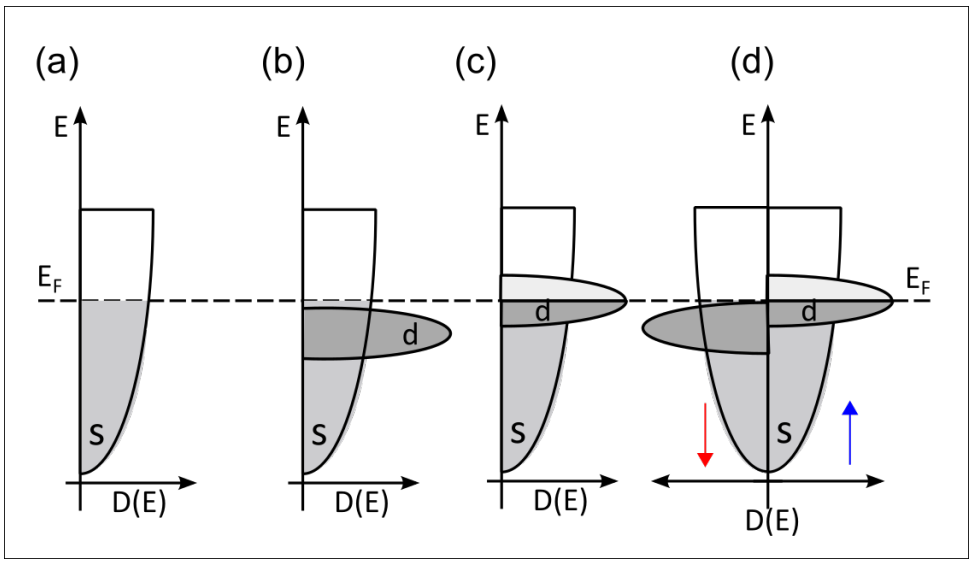

Figure 1.22: Representation of the density of states for various metals. (a) Alkali metals, (b) Noble metals, (c) Non-ferromagnetic metals, and (d) Ferromagnetic transition metals. (Image adapted from Ref. [107]).

The density of states in the d-band depends on the direction of the magnetisation through the spin-orbit coupling. This explains why resistivity, which depends on the density of states in the d-band, also depends on the direction of the magnetisation.

A phenomenological explanation of AMR is described followed by the more detailed explanation of the GMR effect

1.4.4.2 Anisotropic magnetoresistance

In the mid 1850's , William Thomson demonstrated the first evidence of a spintronic phenomenon [12] by observing that the resistance of a magnetic material (Fe and Ni for his experiment) depends on the angle between the applied magnetic field and the direction of the current flowing through the sample. Further research in this phenomenon have reported the occurrence of this magnetoresistance known as the anisotropic magnetoresistance (AMR) in $3d$ transition metals and their alloys[11,

146–148]. In spite of the time period of its existence and practical functionality, there is still a big gap in complete fundamental understanding of the origin of AMR. However a model describing the magnetoresistance based on the scattering mechanism of the up spin and down spin electrons was formulated by Campbell, Fert and Jaoul and called as the CFJ model [144, 149]. This model is based on Mott's two current model as discussed previously in section 1.1. Campbell, Fert, and Jaoul defined an expression for AMR as :

$$\frac{\Delta\rho(\theta)}{\rho} = \frac{\rho(\theta) - \rho_{\perp}}{\rho_{\perp}} \tag{1.30}$$

Here $\rho(\theta)$ is the resistivity at an angle θ and $\rho_{\perp}$ is the resistivity when the angle between the magnetisation and current is 90°.

AMR can be observed in the longitudinal resistance and transverse resistance depending on the component of the electric field parallel or perpendicular to the magnetisation respectively[68, 150] as shown in the Fig. 1.23. The in-plane electric field $\bar{E}$ can be decomposed to a component parallel ($E_{||}$), and component perpendicular ($E_{\perp}$) to the magnetisation ($\bar{M}$). Similarly the current density ($\bar{J}$) has two components as well , the parallel ($J_{||}$) and the perpendicular ($J_{\perp}$).

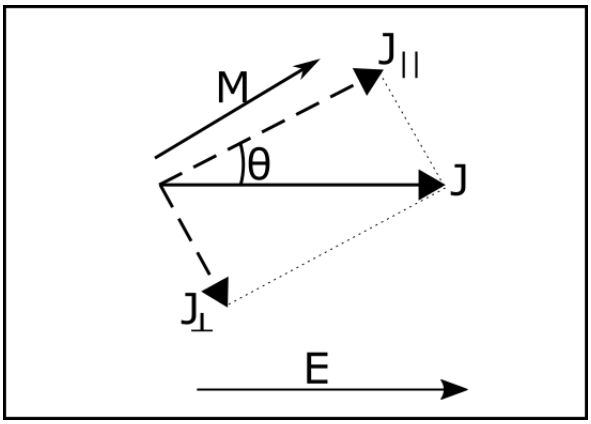

Figure 1.23: Phenomenological description of anisotropic magnetoresistance. The in-plane electric field has components parallel ($E_{||}$) and perpendicular ($E_{\perp}$) to the magnetisation vector ($\bar{M}$). The resistance of the magnetic material depends on the angle θ between the magnetisation and the direction of current.

$$E_{||} = \rho_{||} J_{||}$$

$$E_{\perp} = \rho_{\perp} J_{\perp}$$

where $E_{||} = |E|cos\theta$, $E_{\perp} = |E|sin\theta$ and $J_{||} = |J|cos\theta$, $J_{\perp} = |J|sin\theta$, and θ is the angle between the magnetisation and the direction of current.

As

$$E_x = E_{||}cos\theta + E_{\perp}sin\theta$$

$$= |J|(\rho_{||}cos^2\theta + \rho_{\perp}sin^2\theta)$$

and the longitudinal resistivity is given by:

$$\rho_{xx} = \rho_{||}cos^2\theta + \rho_{\perp}sin^2\theta \tag{1.31}$$

Similarly the transverse component can be derived as:

$$E_y = E_{||}sin\theta - E_{\perp}cos\theta$$

$$= |J|(\rho_{||}cos\theta sin\theta - \rho_{\perp}sin\theta cos\theta)$$

and the transverse resistivity is given by:

$$\rho_{xy} = \left(\rho_{||} - \rho_{\perp}\right) sin\theta cos\theta \tag{1.32}$$

1.4.4.3 Giant magnetoresistance

Baibich et al[151] in 1988 reported the MR ratio of the order 50% at 4.2 K in Fe/Cr multilayers in which the Fe layers were 3 nm to 6 nm thick, and Cr spacer with thickness varied between 0.9 nm to 6 nm and an in-plane current was applied along the {110} crystal direction as shown by the schematic in Fig. 1.24 (a). The Fe layers are antiferromagnetically coupled via the Cr spacer. The relative change in resistance at 4.2 K for different thickness of the Cr spacer was studied (shown in Fig. 1.24 (b)) and it was observed that that the magnitude of the MR was very high when the layers are thinner causing the antiferromagnetic coupling to be highest.

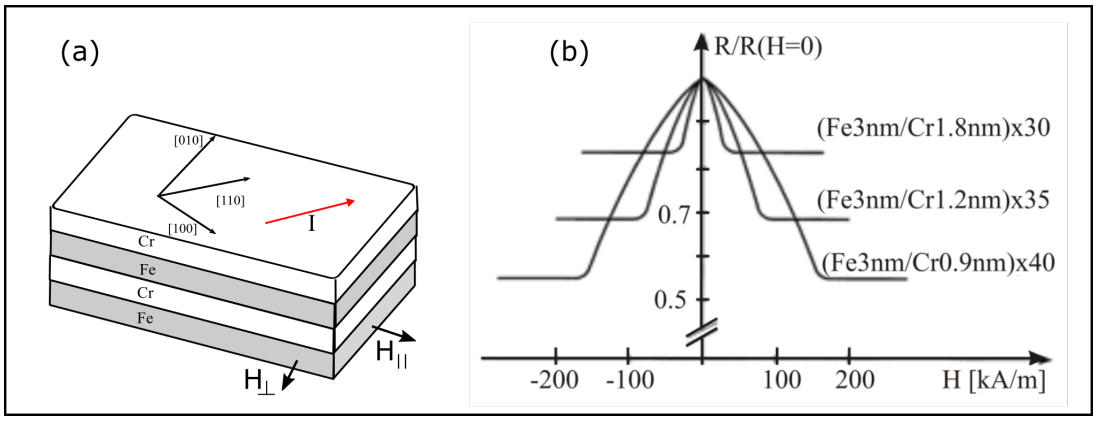

Figure 1.24: (a) Orientation of the current and field for Fe/Cr multilayers in GMR experiments by Baibich et al, (b) Relative change in resistance with field applied parallel to the direction of current for Fe/Cr multilayers with different thickness of the Cr spacer at 4.2 K. (Source: Ref.[151])

The GMR effect depends on the relative orientation of the magnetisation in each ferromagnetic layer, and is a manifestation of the scattering processes due to the relative spin orientation of the carrier at the ferromagnetic scattering sites. A simple interpretation of the effect is in the context of interface spin scattering by Mott's two current channel model, assuming that the scattering is localised[107]. In this ordinary classical interpretation the current is carried in parallel channels by the up spin and down spin electron. The spin polarised current can be in in-plane (CIP-) or perpendicular to the plane (CPP-) of the magnetic film. As previously mentioned , the resistivity for the up spin and down spin electrons are different with the $\rho^{\downarrow} > \rho^{\uparrow}$. When the charge carriers leave the first ferromagnetic layer and reach the non-magnetic layer there will be additional resistance due to scattering at the interface. Since the up and down spin have different density of states at the Fermi energy level, the resistivity within the ferromagnetic layers will be different for the two opposite spins, A schematic of a CIP-GMR and the CPP- GMR comprising two ferromagnetic layers separated by a non-magnetic layer is illustrated in Fig. 1.25. The representation is for the net magnetisation in the adjacent magnetic layers as (a) and (c) parallel , and (b) and (d) antiparallel to each other.

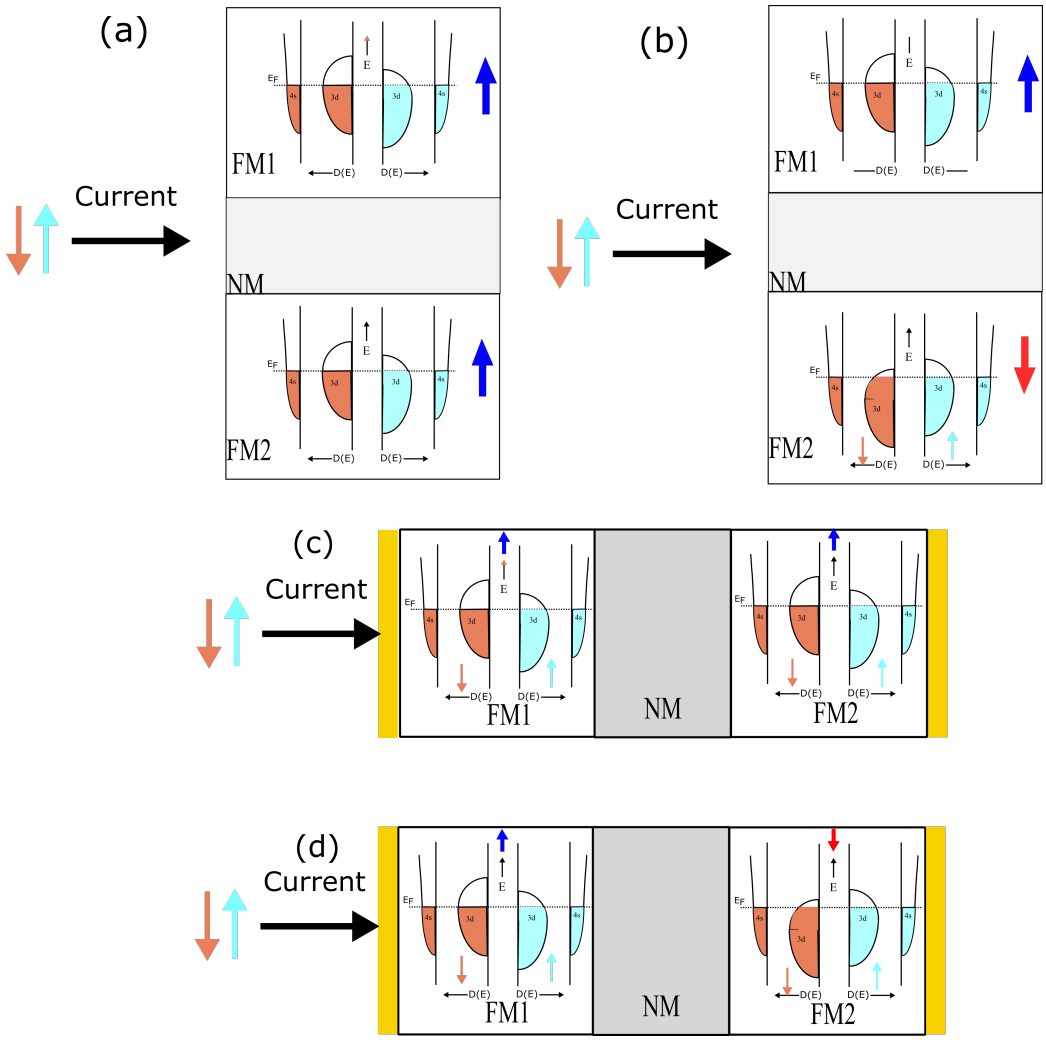

Figure 1.25: Schematic of the CIP- GMR effect with (a) parallel configuration of the magnetisations in adjacent layer, (b) magnetisations are antiparallel to each other in the adjacent ferromagnet layers, and CPP-GMR with magnetisations (c) parallel configuration, and (d) antiparallel configuration.

In this semi-classical model by Camley and Barnas[107, 152–154] for a CIP-multilayer structures it was proposed that when the ratio of the thickness of the non-magnetic spacer layer to the mean free path of the electrons increases, the MR ratio decreases. Levy, Zhang [155] along with experimental observations by Prat[156] proposed a unified theory to explain this taking into account the electron scattering in the ferromagnetic layer, additional scattering resistivity due to the roughness of the interface between the layers and the resistivity due to the magnetisation orientation in the adjacent layers. They described that when the thickness surpasses the mean free path, the scattering within the non-magnetic layer becomes more

significant compared to the scattering at the interface or in the bulk of the magnetic layer and postulated that due to this conduction electrons of a particular spin experiences a series of resistivity due to the non-magnetic and magnetic layers through which they pass.

$$R_{NM} = \frac{\rho_{NM} l_{NM}}{A_{NM}}$$

$$R_M^i = \frac{\rho_M^m l_M}{A_M}$$

where R_{NM} is the resistance due to the non-magnetic spacer and R_M^i is the resistance due to the magnetic layer for different spin orientations denoted by $i = \uparrow$ or $\downarrow$, and m is the magnetisation state of the multilayer (parallel or antiparallel) with respect to the spin of the electron. The magnetic and the non-magnetic layers are modelled to obtain the MR ratio and are shown in Fig. 1.26 for the parallel and antiparallel orientation.

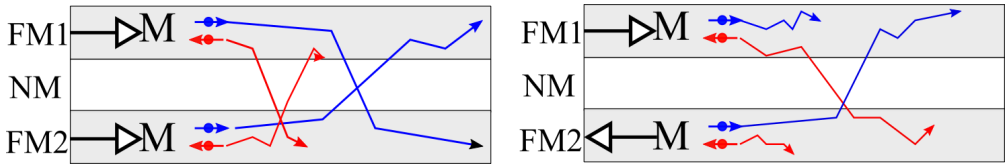

Figure 1.26: Representation of GMR effect with magnetic bilayers when the magnetisations are in parallel and antiparallel configuration. For parallel case, one spin polarisation of electrons will have longer scattering lengths in all layers. For antiparallel case, an electron will have short scattering length on one layer regardless its spin polarisation.

When the magnetisations are in parallel configuration, the equivalent resistance can be expressed as:

$$R_P = \frac{(\alpha - 1)(\beta - 1)}{(\alpha + \beta + 2)} \frac{\rho_{NM} l_{NM}}{A_M} \tag{1.33}$$

where $\alpha = \frac{\rho_M^{\downarrow}}{\rho_{NM}}$ and $\beta = \frac{\rho_M^{\uparrow}}{\rho_{NM}}$.

When the magnetisation in adjacent layers are antiferromagnetically configured the equivalent resistance is expressed as:

$$R_{AP} = (\alpha + \beta + 2) \frac{\rho_{NM} l_{NM}}{2} A_M \tag{1.34}$$

and therefore the GMR ratio is given as:

$$\frac{\Delta R}{R} = \frac{R_P - R_{AP}}{R_{AP}} = -\frac{(\alpha - \beta)^2}{(\alpha + \beta + 2\frac{l_{NM}}{l_M})^2} \tag{1.35}$$

For a CPP geometry the theory of the magnetoresistance was proposed by Valet and Fert[157] by taking into account the volume and interface spin dependent scattering. They derived a "spin diffusion type" equation for the spin accumulation around the interface with the non-magnetic layer which gives rise to an extra potential drop $\Delta V = Jr_s$,where J is the current density and $r_s$is the spin coupled interface resistance.

The advantage of the CPP GMR is that the conduction electrons pass through many interfaces while in CIP the transmission path is governed by the electric field direction. Due to this the MR is higher for a CPP configuration.

Phenomenological expressions to describe the GMR effect was proposed by Dieny[107, 158] in a variety of ferromagnetic/non-magnetic multilayer systems. He demonstrated that the in plane resistivity depends on the relative angle between the the magnetisation of the adjacent layers. His demonstrations with uncoupled $Ni_{81}Fe_{19}$, $Ni_{80}Co_{20}$, Ni ferromagnetic layers separated by Cu, Ag, Au non-magnetic layers led to the expression of GMR as a function of the angle between the magnetisation in the two sets of layer represented by ψ:

$$\frac{\triangle\rho(\psi)}{\rho} = \left(\frac{\triangle\rho}{\rho}\right)_{GMR} \frac{[1 - cos\psi]}{2} \tag{1.36}$$

We have used this analytical expression to model the GMR effect for the samples in this thesis, and will be discussed in next chapters.

1.4.5 Magneto-optical effects in ferromagnetic materials

The interaction of the magnetisation of a material with the polarisation of light was first observed by Faraday in 1846[159], where he observed rotation in the plane of polarisation of the transmitted light through a ferromagnetic material. Few years later in 1877 John Kerr[160] discovered a similar phenomenon in which the light reflected from a magnetic material underwent a change in plane of polarisation; and this phenomenon has been named as the *Magneto Optical Kerr Effect* ($MOKE$) in his honour. In this thesis, $MOKE$ has been used to probe the magnetisation in each layer of the bilayer structure and to study the magnetisation reversal process in a varying external magnetic field.

MOKE is a quantum mechanical effect[161] manifested due to the interaction between the spin polarisation of the electrons and the polarisation of the incident light. Various models have been proposed to explain the origin and also calculating the magneto optical response using the dielectric tensor and the Voigt material constant[162–164]. The dielectric displacement is related to the Voigt constant in the form:

$$D = \epsilon \left(E + iQ_V m \times E\right) \tag{1.37}$$

where ϵ is the dielectric tensor vector and Q_V is the Voigt constant and describes the magneto-optical rotation of the plane of polarisation of the light.

A classical explanation is described here to obtain a qualitative understanding of the effect. When a beam of polarised light is incident on a magnetic material, the electric field vector ($\bar{E}$) of the incident beam excites the electrons of the material and sets them to oscillate parallel to the $\bar{E}$ direction. Besides this, due to the Lorentz force interaction between the field and the magnetisation vector $\bar{M}$, there is an additional perpendicular component with respect to the magnetisation ($\bar{M}$) and the electric field ($\bar{E}$). This additional component superimposes to the regular reflected component and leads to the rotation of the polarisation of light.

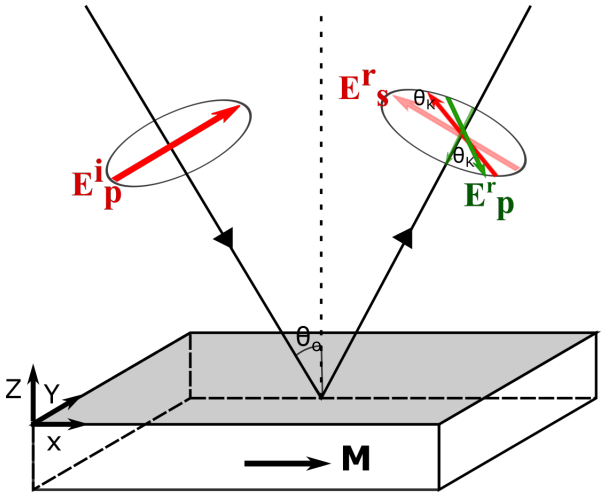

Figure 1.27: Representation of longitudinal MOKE configuration. The incident beam is $p-polarised$ and the electric field vector is denoted by E_p^i. The normal reflected beam has electric field vector represented as E_p^r and the Kerr component as E_s^r and θ_k is the Kerr angle.

Depending on the relative orientation of the plane of incidence, polarisation, and the magnetisation of the sample *MOKE* can be classified into three basic

categories. In the longitudinal $MOKE$, the magnetisation is in the plane of the sample and is parallel to the incidence plane. In transverse $MOKE$, the magnetisation is still in the plane of the sample but is perpendicular to the plane of incidence. In polar $MOKE$, the magnetisation is perpendicular to the sample plane but is parallel to the plane of incidence. In the work performed in the thesis, the longitudinal $MOKE$ configuration has been used, and a general schematic of the effect is shown in Fig. 1.27 which has been adapted from ref.[164]. In the representation, the incident beam is $p-polarised$ and the electric field vector is denoted by E_p^i. The normal reflected beam has electric field vector represented as E_p^r and the Kerr component as E_s^r . The reflected light has a rotated polarisation by θ_k from the incident light and an ellipticity ϵ_k. The complex Kerr angle is given as:

$$\phi_k = \theta_k + i\epsilon_k$$

and which is related to the dielectric tensor[164] of the material by:

$$\phi_k = \theta_k + i\epsilon_k = \frac{i\tilde{\epsilon}_{xy}}{\sqrt{\tilde{\epsilon}_{xx}}(1-\tilde{\epsilon}_{xx})}$$

where $\tilde{\epsilon}_{xx}$ and $\tilde{\epsilon}_{xy}$ are the diagonal and off diagonal elements of the dielectric tensor.

The magneto optical Kerr effect provides an ideal method for studying thin films magnetisation reversal. MOKE effect that investigates the magnetisation hysteresis loops are used to distinguish the magnetisation process in a multilayer structure and has been discussed in the later sections of the thesis.

1.4.6 Magnetic domains and domain walls

From the SQUID MH loop shown in Fig. 1.17 one can observe two points of external field known as the coercive fields where the magnetisation reduces to zero. Also at zero field, the sample exhibits remanent magnetisation. This is due to the strong exchange energy interaction between spins in a ferromagnet and the magnetic anisotropy, and have discussed in Sec. 1.4.1, and is of the order of magnitude proportional to $k_B T_c$ where $T_c$is the Curie temperature and k_B is the Boltzmann's constant ($8.617 \times 10^{-5} eVK^{-1}$). For a ferromagnetic material with a Curie temperature of 600K this effective field has a value approximately 500 T, which is incredibly high and makes it confusing to explain the zero magnetisation at lower fields. To explain this Weiss postulated the idea of magnetic domains where spon-

taneous magnetisation is differently oriented and may average to zero in the whole sample[165]. These domains were experimentally observed under microscope by Bitter and his technique is known as the Bitter patterning technique[107, 165].

Domains are formed to minimise the free energy of a ferromagnetic material and two neighbouring domains are separated by a transition region defined as the domain wall. The domain walls are needed to reduce the exchange energy rising at the domain borders where the magnetisation abruptly changes its orientation. Within the wall, the magnetisation spatially varies in orientation from one domain to that in the other domain. The width of the domain wall depends on the strength of the magnetic anisotropy, exchange energy, sample thickness, saturation magnetisation[69, 107], and is usually expressed by

$$\sigma = \pi S \sqrt{\frac{2J}{Ka}} \tag{1.38}$$

where J is the value of the exchange integral, S is the spin orientation, K is the magnetocrytalline anisotropy constant, and a is the lattice constant.

There are two broad models of explaining the type and mechanism of domain walls (DW): Bloch model and Neél model [107, 110, 165] and are schematically represented in Fig. 1.28 (a) and (b) which has been adapted from Ref. [166]. In a Bloch DW the magnetisation vector gradually rotates out of the film plane and perpendicular to the normal to DW. To the contrary in a Neél DW, the magnetisation vector gradually rotates in the plane of the film.

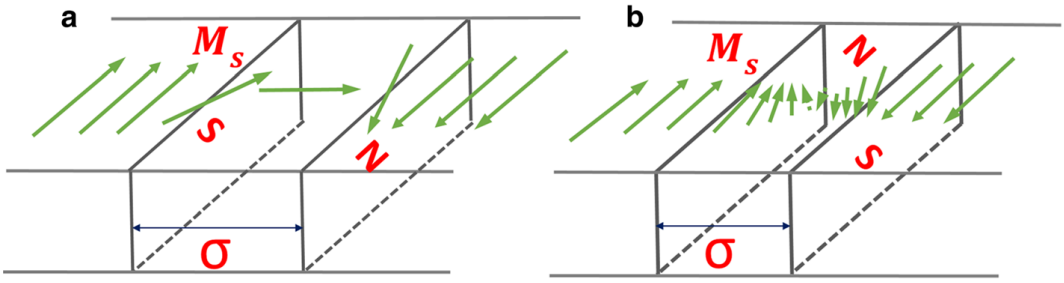

Figure 1.28: Schematic representation of different domain wall types. (a) Neél wall, (b) Bloch wall.

For a thin film with the magnetisation in-plane, it is favourable for the magnetisation to rotate in the film plane than out of the film plane because of extra costs due to the demagnetising energy. Therefore Neél domain walls are preferred in thin films with uniaxial and biaxial anisotropies. They have different subclasses as well like the asymmetric domain walls, vortex domain walls, transverse walls and others

that have been observed in patterned nanostructures[167] and stripes[168], wires[4], where the anisotropy contributes to the domain wall shape and motion[165].

The process of magnetisation reversal is assisted by domain nucleation and domain wall motion. The magnetisation reversal can be intuitively explained by a simple energy landscape model as represented in Fig. 1.29 which is due to the contribution of the several energies discussed previously in this chapter. Following a Stoner Wohlfarth model for coherent rotation , for a given field the resulting spin orientation will be that for which energy will be at local minimum. Now when the field is varied, the spin orientation varies from one local minimum to another due to domain wall unpinning. When the difference between the two energies of neighbouring local minimum is sufficiently larger than the energy of formation of the domain walls, the domain walls rapidly expand and propagate freely across the sample, letting the magnetisation orient to a new position. A detailed discussion is performed in Chapter 5 of the thesis.

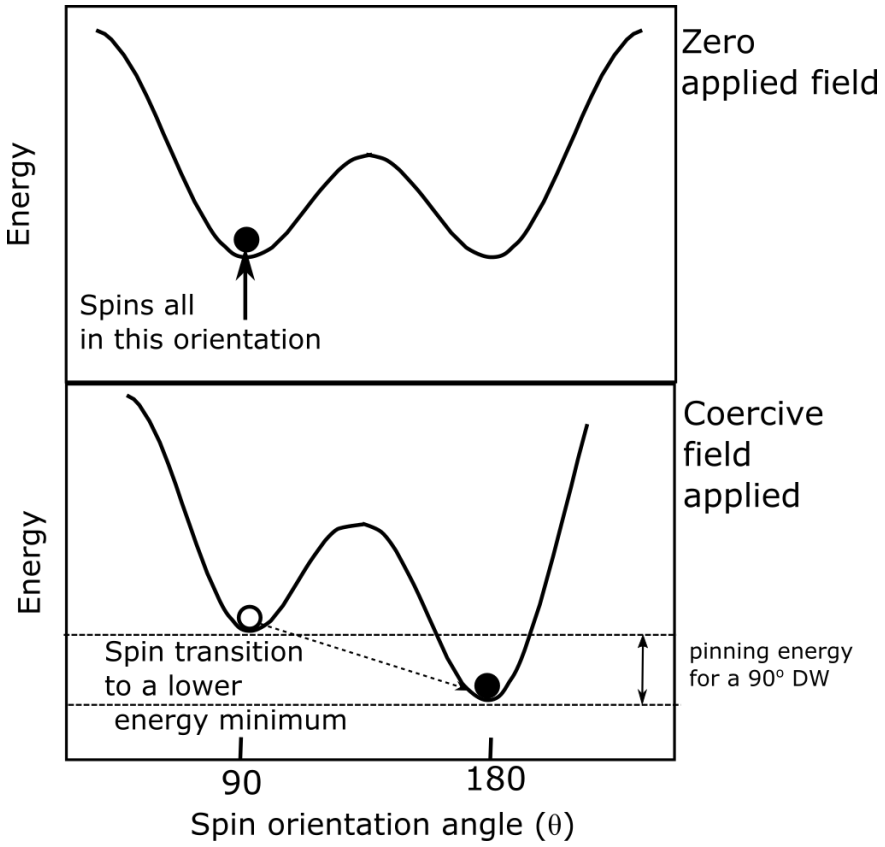

Figure 1.29: Representation of a magnetisation reversal due to domain wall unpinning and expansion.

1.5 Thesis organisation

This thesis comprises six main chapters and two appendices. Chapter 1 outlines the basic concepts and physics of magnetic materials specially the magnetostrictive alloy $Fe_{1-x}Ga_x$. It introduces the key concepts which have been used for the experimental analysis in the later sections of this thesis. Chapter 2 discuses the general experimental techniques and methodology performed for the device fabrication and the experiments. Chapter 3 and chapter 4 discuss the main experimental and modelling work of my PhD study. Chapter 3 describes the characterisation techniques, the ferromagnetic resonance, and SQUID experiments and the methodology to extract the magnetic anisotropies for the ferromagnetic bilayer system. Chapter 4 presents magnetotransport measurements on Hall cross devices in a varying in-plane magnetic field and under mechanical strain. The magnetisation reversal curves are analysed and modelled to understand the effects of strain on the magnetisation reversal processes as well as to extract the magneto-elastic constants of the layers.. Chapter 5 simulates the operation of a memory cell based on the magnetic parameters extracted from chapter 3 and 4. Chapter 6 is the conclusion and the future work , and outlines the broad and interesting future work and scopes for this material.

Appendix A describes the mathematical derivation required towards setting up the longitudinal MOKE magnetometer and the penetration depth calculation. Appendix B presents the strain calibration for the samples used in chapter 4.

Chapter 2

Materials and Techniques

This chapter describes the ferromagnetic samples investigated in this thesis. The experimental and mathematical methods used for measurement and analysis are also described.

2.1 Ferromagnetic bilayers

The samples investigated in this thesis consist of double layers of galfenol separated by a non magnetic layer. Galfenol is an alloy of iron and gallium. A non- magnetic spacer of copper or aluminium is sandwiched between two layers of this alloy of different composition. The structures were grown on GaAs substrates of thickness 150 μm and 350 μm using magnetron sputtering. Table 2.1 details the layers and the nominal compositions of different samples investigated in this thesis.

Sample	Structure (nm)	Substrate
$S419$	GaAs\$Fe_{81}Ga_{19}$(5)\Al (5)\$Fe_{90}Ga_{10}$(5)\Al (5)	150 μm $GaAs(001)$
$S420$	GaAs\$Fe_{81}Ga_{19}$(5)\Al (10)\$Fe_{90}Ga_{10}$(5)\Al (5)	150 μm $GaAs(001)$
$S421$	GaAs\$Fe_{81}Ga_{19}$(5)\Cu (5)\$Fe_{90}Ga_{10}$(5)\Al (5)	150 μm $GaAs(001)$
$S422$	GaAs\$Fe_{81}Ga_{19}$(5)\Cu (10)\$Fe_{90}Ga_{10}$(5)\Al (5)	150 μm $GaAs(001)$

Table 2.1: Summary of the ferromagnetic samples and the nominal compositions of different samples investigated in this thesis. The ferromagnet samples are sputter grown on $GaAs(001)$ substrates with different type and thickness of non magnetic spacer and a 5 nm Al capping to prevent oxidation.

2.1.1 Growth

All the samples in this thesis were grown using the DC magnetron sputtering technique. Before growing, the substrates were prepared by cleaning in 1:1 HCl to water for 120 seconds. After that they were moved into the main chamber of the sputter machine and annealed in vacuum at $550°C$ for one hour and allowed to cool to room temperature. This step ensured that $Fe_{1-x}Ga_x$ grows epitaxially on the substrate following similar works reported in [114] [99]. $Fe_{1-x}Ga_x$ layers were then grown by co-sputtering FeGa target of composition 50:50 alongside a 99.99 % pure Fe target at argon pressure of 1.3×10^{-3} Torr, with the sample rotated at 20 rpm. The sputtering growth rate was in the order of $0.5 \pm 0.04\ nms^{-1}$. During the growth, the thickness of each layer including the non-magnetic spacer and capping layer were monitored by the quartz crystal monitor (QCM) .

Sputtering

Sputtering is a physical vapour deposition technique in which atoms in a solid target material are bombarded by high energy argon ions. The target atoms are then ejected in the chamber and diffuse upwards to form a thin film coating on the substrate, which is rotated to get a uniform coating of the target material. When a DC voltage is placed between the target and the substrate, the neutral argon atoms are ionised and are set to acceleration towards the anode target. The presence of strong magnetic field near the anode area causes the travelling Ar ions to spiral around the magnetic flux lines. This process generates a stable plasma with a high and uniform density of target ions to ensure a higher sputtering yield and faster deposition rates. The spiral motion of the ions also limits the damage to the substrate due to stray particles.

Sputtering is an inexpensive growth technique, with a fast growing rates. Sputter grown $Fe_{1-x}Ga_x$ have previously been reported to grow epitaxially on certain substrates [99][114]. Due to good quality sample growth , low cost and time saving, all the samples were grown using sputtering. The sputtering of the samples was performed using a Mantis QPrep500 ultra high vacuum sputter deposition system at the University of Nottingham. A schematic of the magnetron sputtering process used to grow the samples investigated in the thesis is represented in Fig. 2.1, which presents the process in which the target material is ejected from the target when Ar^+ions are bombarded to it which are regulated by the magnetic field.

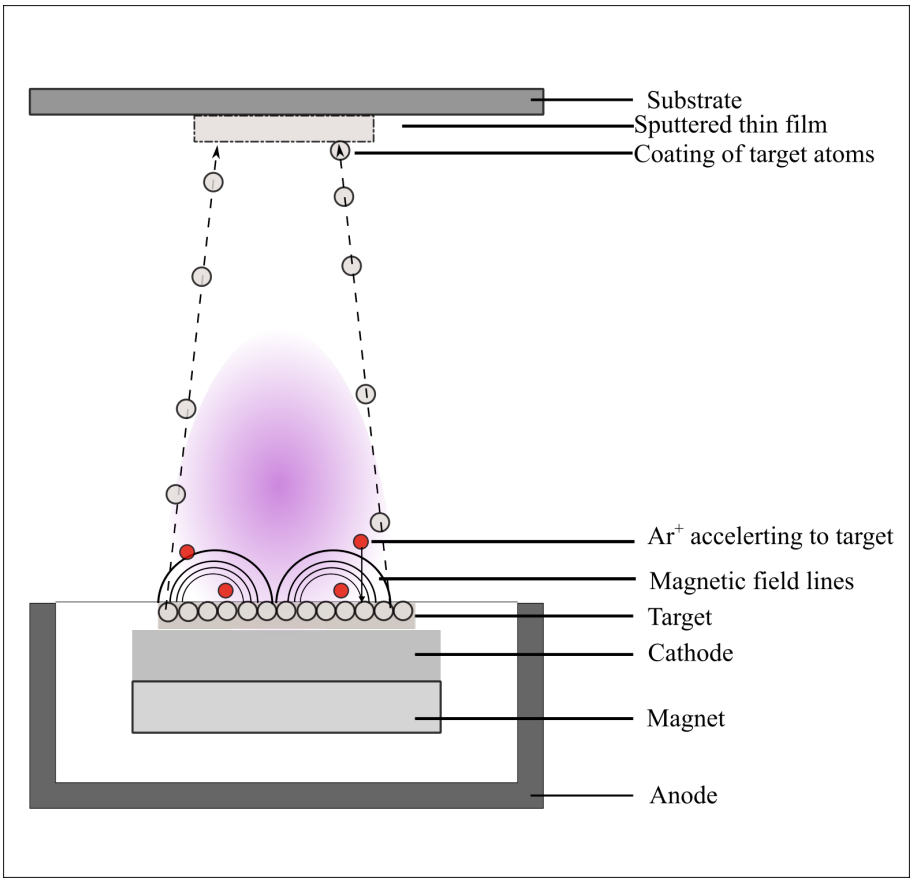

Figure 2.1: Schematic of the magnetron sputtering process showing the basic components of the sputtering system. Ionised Ar^+ ions accelerate and bombard the target metal, releasing atoms which forms layers on the substrate. The electrons and Ar ions form a plasma which is confined by the magnetic field near the target metal. The proximity of the plasma to the magnetic field causes fast and uniform deposition and limits substrate damage.

2.2 Fabrication

2.2.1 Photo-lithography

To prepare samples for magneto-transport measurements, standard photo-lithography techniques were used to pattern devices with lateral dimensions of a few micrometers. A schematic of the device used to perform the magneto-transport measurements is shown in Fig. 2.2. The sample preparation and fabrication were carried out in the clean room facility at the University of Nottingham. Table 2.2 summarises the fabrication and preparation procedure for samples.

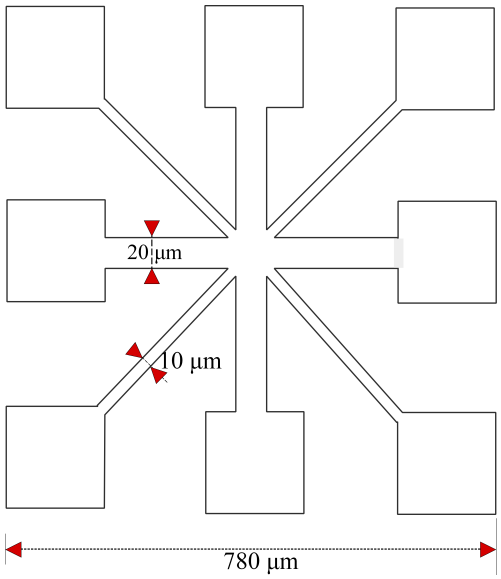

Figure 2.2: Schematic of the device used for the transport measurements. The symmetric Hall bars were processed in the clean room at Nottingham using standard photo-lithography techniques.

Step #	Step name	Process
1	Clean	Acetone, and isopropyl alcohol
2	Scribe	5 ×4 rectangular section
3	Clean	Acetone, and isopropyl alcohol
4	Spin coat	BPRS 150, 4krpm, 30 seconds
5	Bake	Hot plate, $90{\cdot}C$, 120 seconds
6	Expose	UV exposure, 75 Jcm^{-1}, 6 seconds
7	Develop	AZ400K: H_2O (10:70), 6 seconds
8	Etch	Ion milling
9	Clean	Acetone, and isopropyl alcohol
10	Spin coat	BPRS 150, 4krpm, 30 seconds
11	Bake	Hot plate, $90{\cdot}C$, 120 seconds
12	Expose	UV exposure, 75 Jcm^{-1}, 6 seconds
13	Develop	AZ400K: H_2O (10:70), 6 seconds
14	Metallise	Thermal evaporator, Ti (20 nm), Au (100 nm)
15	Lift off	Acetone

Table 2.2: Summary of the steps carried out to perform the fabrication of the device shown in Fig. 2.2 for magneto-transport measurements.

2.2.2 Thermal evaporation

Thermal evaporation is a technique in which pure metals are deposited onto a substrate. The substrate and the metals are placed in a vacuum chamber which is then pumped down to a pressure of the order 2 $\times 10^{-7}$mbar. The metals are placed on a boat which is then heated by passing a high current. Thermally vaporized molecules of the metals strike and deposit onto the substrate surface. For making electrical contacts, 20 nm of Ti and 100 nm of Au were deposited on the devices used for magneto-transport measurements.

2.2.3 Ion milling

In order to etch the fabricated samples discussed in this thesis I employed the technique of ion milling. Ion milling was preferred over the wet chemical etching because it is not layer dependent and allows one to obtain good quality edge definition without significant side wall over and under cut. This technique involves bombarding the sample surface with a beam of Ar^+ ions produced by reversing the polarity of the sputter machine as discussed in [169] using a 630 V bias voltage to the substrate. Due to this reverse bias, Ar^+ would then accelerate towards the substrate instead of the target material causing milling or etching of the substrate.

For ion milling of the samples mentioned in the thesis, when a 630 V bias voltage was applied, a plasma power of $6W$ was produced which had Ar^+ ions accelerated towards the substrate which was rotated at 20 rpm. Fig 2.3 represents a patterned and milled magneto-transport device mounted on a piezoelectric transducer . The bonding wires can be clearly seen as well.

2.2.4 Sample mounting

The samples were prepared and mounted depending on the experimental technique involved. Table 2.3 summarises the sample mounting process with figure 2.4 showing the mounted samples .

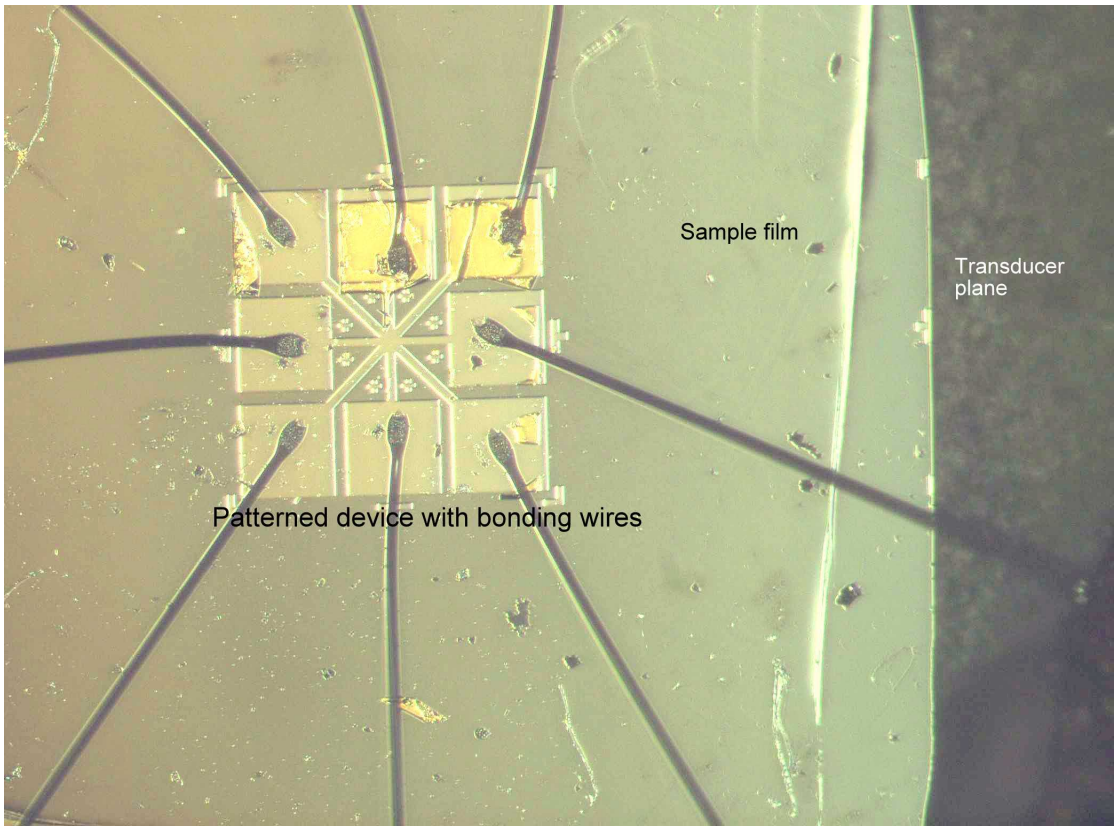

Figure 2.3: Microscopic image of the patterned device mounted on a piezoelectric transducer. The samples were bonded to the transducer using an epoxy resin cured at room temperature such that the uniaxial strain is parallel to the [100]/[010] directions of the substrate.

Technique	Mounting	Process
MOKE	On piezoelectric transducer	Glued using epoxy resin. Cured at room temperature.
Magneto-transport	On piezoelectric transducer	Glued using epoxy resin. Cured at room temperature.
SQUID magnetometer	Silicon rod	Glued using GE varnish
VNA- FMR	Co-planar wave guide	Placed on the waveguide with ferromagnet side touching the transmission axis

Table 2.3: Summary of the sample mounting process for different experimental techniques investigated in this thesis.

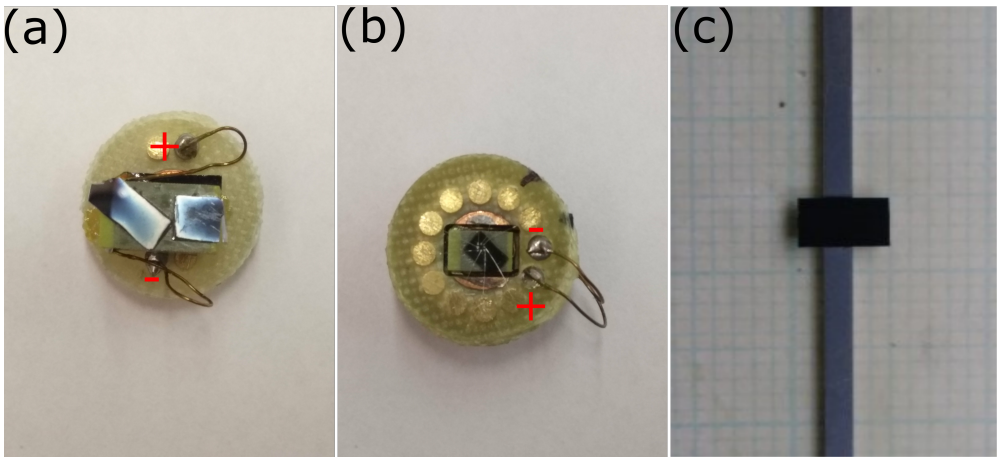

Figure 2.4: Sample mounting for different techniques. (a)For MOKE measurements two samples were bonded to the transducer with the strain parallel and orthogonal to [100] axis. (b) For magneto transport measurements, the processed devices were bonded to the transducers with strain parallel to the [100]/[010] directions. (c) For SQUID measurements, a $4mm \times 3mm$ chip was glued to the sample rod using Ge varnish.

To measure the effect of strain on the magnetisation reversal process, samples S419, S420, S421, and S422 were mounted on piezoelectric transducers using epoxy resin. The transducers used are piezostacks Pst 150/3.5 ×3.5/7 and Pst 150/5 ×5/7 from Piezomechanik GmbH, which produce a homogeneous uniaxial strain within

the volume of the transducer. When operated in a bipolar mode between -30V to +150 V the piezostacks are capable of applying a maximum load force of 800 N and produce uniaxial strain in the measured multilayer in the range of $\pm 2 \times 10^{-4}$ as shown in ref.[68] and in Appendix B . The transducer is covered with a polymer coating on both the sides. The coating on one side of the transducer was removed using polishing paper. It was then cleaned with IPA to remove any dust and making sure the surface is smooth. The transducer was then glued using GE varnish to silicon stacks and to a standard 12 pin header for magneto transport measurements and to a standard 4 pin header for magneto-optical measurements. The transducer was only glued on one edge to allow the transducer to move freely and the strain to transmit and not be restricted because of the GE varnish glue. The wires were clipped and the enamel was removed. The terminals were then soldered to the pins of the header making sure that the positive and negative terminals are noted. The samples were then bonded to the polished side of the transducer, with the [100] crystal direction parallel to the edge of the piezoelectric transducer, using Epotech 70E epoxy resin mixture and cured at room temperature for 1 day. To prevent damage to the sample due to strain which can go up to the order of 10^{-3}, the transducers have been operated between a safe voltage of -30 V to +30 V. When there is voltage across the transducer, a uniaxial strain across the volume of the transducer is generated which is transmitted through the substrate to the device. Not all of this force is transmitted to the top layer of the sample as a significant fraction of it can be attenuated in the epoxy glue and the substrate. Therefore it becomes necessary to determine the transmitted strain experimentally.

Figure 2.5 shows the schematic of the sample mounted on a piezoelectric transducer for magneto-transport measurements and the type of uniaxial strain, tensile and compressive for positive and negative voltage respectively.

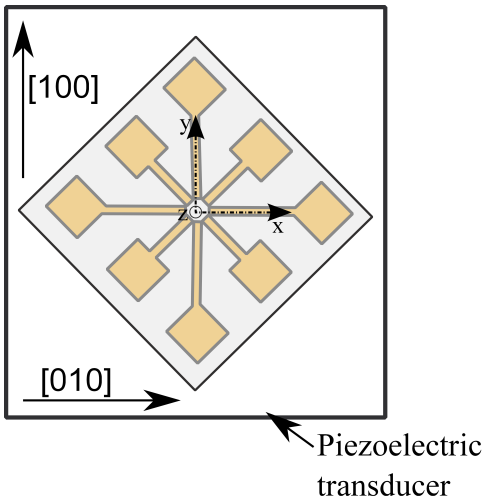

(a) Schematic of a device mounted on the piezoelectric transducer

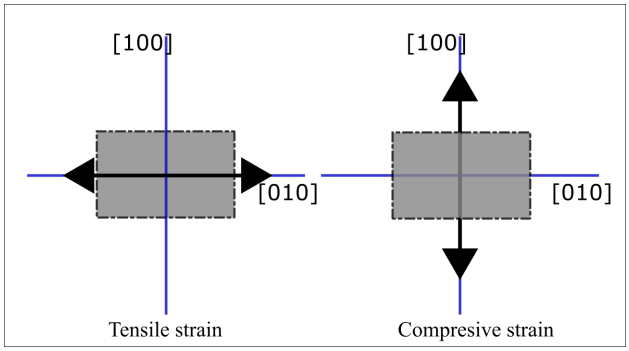

(b) Characteristic of strain for positive and negative voltages

Figure 2.5: Schematic of a magneto transport device on a piezoelectric transducer showing the direction of the uniaxial strain for positive and negative voltage across the transducer. The transducer is represented by the rectangle with the arrows representing the directions of the tensile and compressive strains for positive and negative voltages.

Strain calibration

To deduce the relation between the applied voltage and strain produced in the piezoelectric transducer, magnetotransport measurements were performed. This technique involved measuring the longitudinal resistance and relating the change to the induced strain. The sample was held in an in-plane magnetic field of 0.5 T , sufficiently strong to saturate the magnetisation along the [010] crystal direction, and the change in resistance with strain was recorded. Assuming the initial length of the device to be x_o in the x direction, the following can be deduced:

Initial length of the device in x direction $=x_o$
Final length of the device when strain ϵ_x is applied along x direction $=x_1$
So,

$$\epsilon_x = \frac{x_1 - x_o}{x_o} \tag{2.1}$$

The Poisson's ratio which can be defined as the ratio of transverse strain to the

longitudinal strain is given as :

$$\nu = -\frac{\epsilon_{trans}}{\epsilon_{longitudinal}} = -\frac{\epsilon_y}{\epsilon_x} = -\frac{\epsilon_z}{\epsilon_x} \tag{2.2}$$

The resistance of the device for current along the $x-$ direction can be written as:

$$R = \frac{\rho x}{yz} \tag{2.3}$$

therefore the change in resistance due to strain will be

$$\frac{\Delta R}{R} = \frac{\triangle x}{x} - \frac{\triangle y}{y} - \frac{\triangle z}{z} \tag{2.4}$$

$$\frac{\Delta R}{R} = \epsilon_x - \epsilon_y - \epsilon_z \tag{2.5}$$

Taking the isotropic upper limit of the Poisson's ratio, $\nu = 0.5$

$$\frac{\Delta R}{R} = \epsilon_x(1 + 2\nu) = 2\epsilon_x \tag{2.6}$$

Equation 2.6 gives the relation between the change in longitudinal resistance to the relative strain.

2.3 Measurement techniques and Modelling

The different techniques used in this thesis to understand the material characteristics are discussed in this section. The motivation of employing these techniques was mainly to understand the magnetisation response of the material as a function of external magnetic field and frequency. This magnetisation response is controlled by the anisotropies of the material which depend on the free energy of the magnetic system.

Several experimental techniques have been employed in order to build a complete understanding of the magnetic and structural properties of the multilayer samples. Magneto Optical Kerr Effect (MOKE) magnetometry was performed to understand the magnetic characteristic mainly for the top layer of the structure at different voltages of the piezoelectric transducer. Super Conducting QUantum Interface Device (SQUID) along with the magneto-transport measurements probe the whole of the material structure and give us the magnetic and electric character-

istics respectively. Ferromagnetic resonance studies along with the mathematical modelling were done to obtain the anisotropy constants, and field linewidths for each layer separately and thereby the damping parameters of the materials. High Resolution -Transmission Electron Microscopy (HR-TEM) was done to investigate the structural characterisation of the material in particular the epitaxial crystal quality of the magnetic and spacer layers. Further to this, with the knowledge of material characteristics, modelling of two dimensional memory elements employing strain only to induce change in magnetisation have been investigated.

2.3.1 Magneto Optic Kerr Effect

2.3.1.1 System description

The magneto- optical measurements reported in the thesis were carried out in the static longitudinal MOKE set up as shown in the figure 2.6:

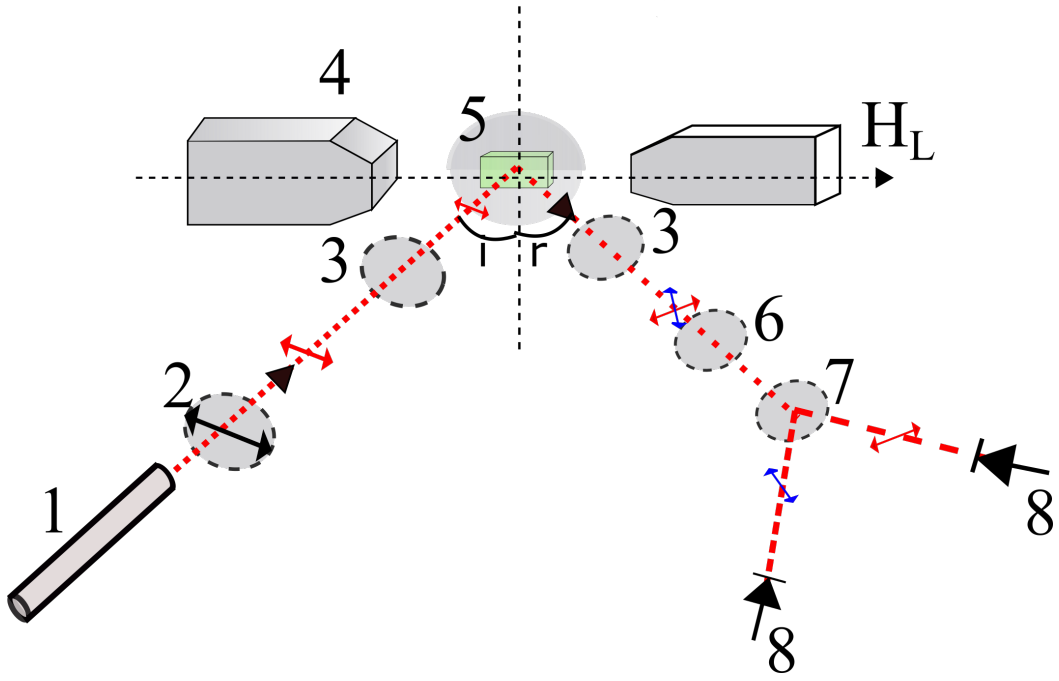

Figure 2.6: Schematic of the MOKE set up showing the different components used for the longitudinal Kerr effect. In the figure the components are: 1(He-Ne Laser), 2 (Polariser), 3 (20mm confocal lenses), 4(Electromagnet poles) , 5(Sample on a standard header), 6($\lambda/2$ wave plate), 7(Wollaston beam splitter), and 8 (Photodiodes). The red dashed line represents the incident and reflected beam at angles i and r respectively. The red arrows indicates $p-$polarisation and blue arrows indicate $s-$ polarisation .

System set up

The amplitude of the parallel and perpendicular components of the light reflected from a magnetic material is related to the parallel and perpendicular components of the incident beam by the Fresnel coefficients[170]

$$E_r = R \cdot E_i \tag{2.7}$$

or,

$$\begin{pmatrix} E_p \\ E_s \end{pmatrix}_r = \begin{pmatrix} r_{pp} & r_{sp} \\ r_{sp} & r_{ss} \end{pmatrix} \begin{pmatrix} E_p \\ E_s \end{pmatrix}_i \tag{2.8}$$

where E_r is the reflected beam, R is the Fresnel coefficient matrix and E_i is the incident beam. For a p polarised incident beam, the reflected beam can be written as following Ref. [171][163] and Appendix A.

$$E_r = E_i \left[\left(m_t^2 r_{pp}^t + m_l^2 r_{pp}^l + m_z^2 r_{pp}^p \right) \hat{p} + \left(m_l^2 r_{sp}^l + m_z^2 r_{sp}^p \right) \hat{s} \right] \tag{2.9}$$

where the unit vectors $\hat{p}$ and $\hat{s}$ are parallel or perpendicular to the incident plane respectively, and $r_{\beta\gamma}^{\alpha}$ are the Fresnel reflection coefficients, due to transverse ($\alpha = t$), longitudinal ($\alpha = l$) , and polar ($\alpha = p$). MOKE effect for electric field components parallel ($\beta = p$ or $\gamma = p$) and perpendicular ($\beta = s$ or $\gamma = s$) to the plane of incidence.

The reflected intensity can then be defined as:

$$I_r = |E_r|^2 \tag{2.10}$$

$$I_r = |E_i|^2 \left[| \left(m_t^2 r_{pp}^t + m_l^2 r_{pp}^l + m_z^2 r_{pp}^p \right) |^2 + | \left(m_l^2 r_{sp}^l + m_z^2 r_{sp}^p \right) |^2 \right] \tag{2.11}$$

For the magneto-optical measurements performed in this thesis, the photodiodes are configured to measure only the longitudinal component of the magnetisation . Therefore the transverse components can be neglected and equation 2.11 can be simplified to

$$I_r = |E_i|^2 [|m_l^2 r_{pp}^l|^2 + |m_l^2 r_{sp}^l|^2] \tag{2.12}$$

Equation 2.12 therefore implies that the reflected beam has two components

compared to the incident beam which has only the p component. A representation of this is shown in figure 2.7.

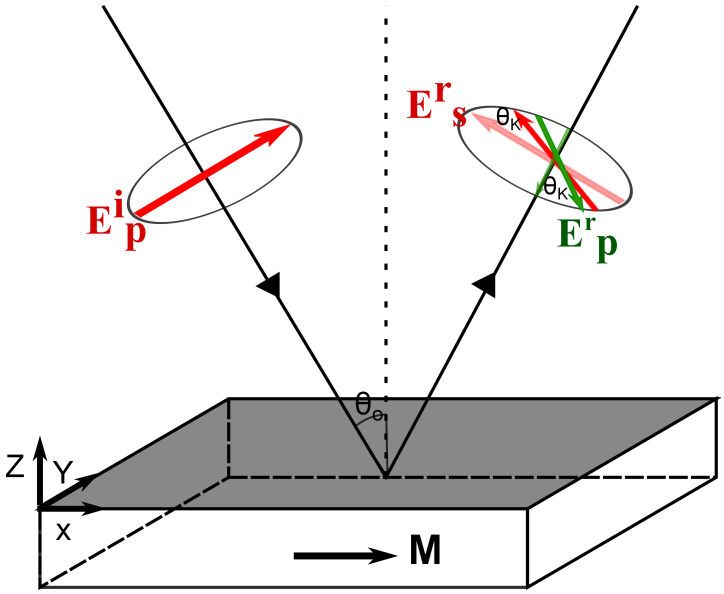

Figure 2.7: Geometry of the MOKE magnetometer measurement showing the incident and reflected light. For an incident $p-$ polarised beam, the reflected beam has a p component and a small s component as well which is the Kerr angle (θ_k).

For longitudinal MOKE configuration, the maximum sensitivity to measure Kerr rotation (θ_k) is by performing a differential measurement of the individual components of the reflected light which is given by

$$\Delta = |E_r|^2 \left(cos^2(\theta_k) - sin^2(\theta_k)\right) \tag{2.13}$$

Therefore the sensitivity is

$$\frac{d\Delta}{d\theta_k} = -2|E_r|^2 sin(2\theta_k)$$

which is maximum for a Kerr rotation angle ($\theta_k = 45°$). Thus it becomes necessary to rotate the plane of the small Kerr rotation angle without changing its polarisation. This was done by using a half-wave plate and a polarising beam splitter. The two components of the reflected beam were rotated by 45° and separated. The difference between the intensity of the p and s component is then given as

$$\Delta = |E_r|^2 \left(cos^2(45° + \theta_k) - sin^2(45° + \theta_k)\right) == -|E_r|^2 sin(2\theta_k) \tag{2.14}$$

and

$$\frac{d\Delta}{d\theta} = -2|E_r|^2 cos(2\theta_k)$$

Following the mathematical derivation stated in Appendix A the Kerr rotation can then be given as:

$$\theta_k = \frac{1}{2} sin^{-1}\left(\frac{I_s - I_p}{I_s + I_p}\right) \tag{2.15}$$

2.3.1.2 Measurement description

For in-plane longitudinal MOKE measurements, the sample was mounted on a piezoelectric transducer . The sample and the transducer were then mounted on a sample holder and hosted between the poles of the electromagnet able to sweep magnetic field between ±0.05 T at a step size of 0.2 mT. A 635 nm He-Ne laser with power output 4 mW was incident on the sample at 45°. The incident beam passed through a polariser to produce a linearly polarised beam with polarisation parallel to the plane of incidence. In some experiments the incident beam was focused to 50 μm by using 20 mm confocal lenses before the sample. The reflected beam was then passed through a $\lambda/2$ wave plate and a polarising beam splitter. The individual components of reflected light were measured using a pair of commercial photo-diodes. The Kerr rotation was then interpreted by using equation 2.15. As previously discussed, Kerr angle is the measure of the ellipticity produced by the change in magnetisation as the magnetic field is varied. The sense of the the magnetisation reversal can be realised by normalising the obtained Kerr angle. The experimental set up to perform the longitudinal magneto-optical measurements and also the magneto-transport measurements has been shown in Fig. 2.8.

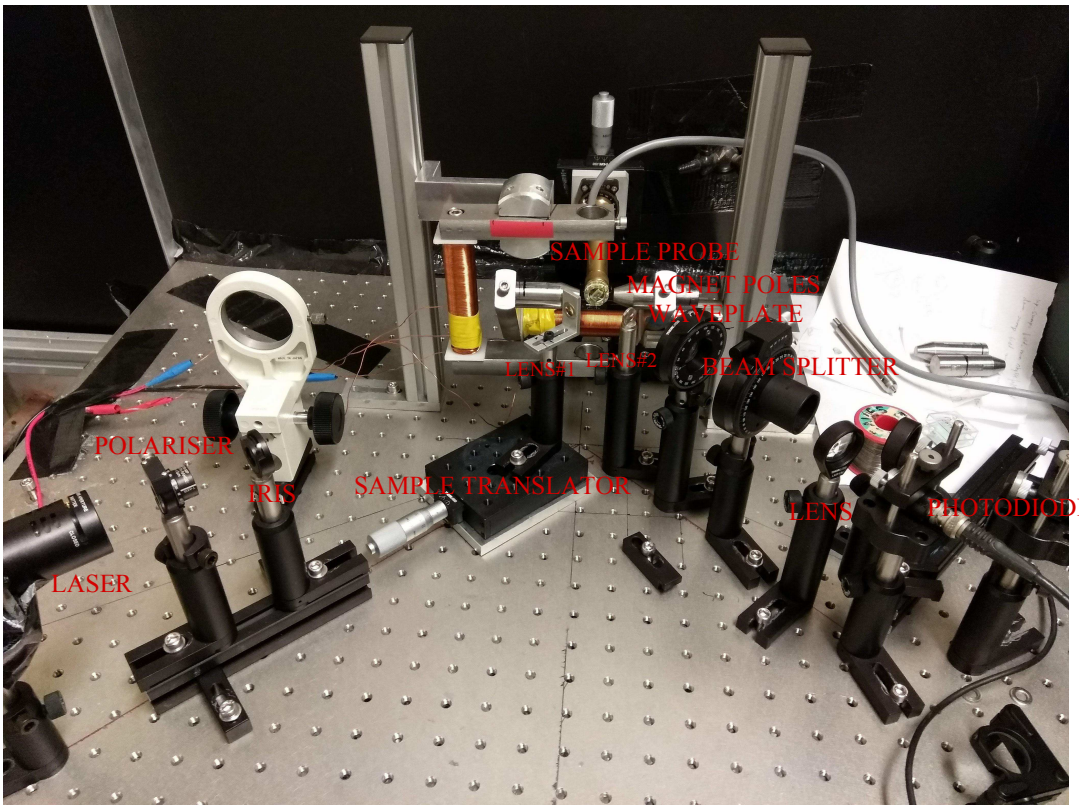

Figure 2.8: Experimental set up employed to perform the magneto-optical and magneto-transport measurements. The red labels indicate the optical and the electrical components which were used for the set up.

An example MOKE graph showing the change in magnetisation of sample S419 when the magnetic field is swept parallel to the $[1\bar{1}0]$ crystal direction at different voltage across the piezoelectric transducer is shown in figure 2.9.

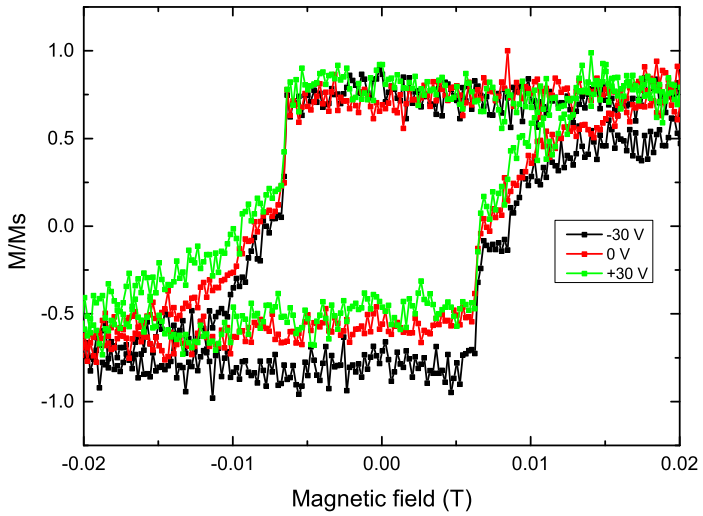

Figure 2.9: Example longitudinal MOKE hysteresis loops for sample S419 showing the magnetisation change of mainly the top layer at different piezoelectric voltages.

The longitudinal MH loop from MOKE as shown in figure 2.9 describes the magnetisation reversal behaviour of a $Fe_{1-x}Ga_x$multilayer sample. Due to the limited penetration depth of the laser, the magnetisation response as seen is limited to only a part of the sample structure and probes mainly the top layer. For a single layer film of iron, the penetration depth was calculated to be 16 nm (See Appendix A). However for multilayer samples taking into account the reflections at the interfaces and different transmission coefficients, the penetration depth is limited to ≈10 nm. Detailed discussion about the MH loops obtained by MOKE is presented in subsequent chapters.

2.3.2 SQUID magnetometry

The SQUID magnetometry measurements discussed in this thesis were performed using a Quantum Design MPMS XL SQUID magnetometer at Institute of Physics, Polish Academy of Sciences, Warsaw. A SuperConducting QUantum Interference Device (SQUID) magnetometer is a very sensitive instrument used to measure the magnetic properties of a material as function of external field[172] . The magnetic field is applied by the superconducting magnet that has a strength between ±1 T and an uniformity of 0.01% over the 4 cm sample space area. The sample is hosted in the central sample space which can be be varied between 2 K to 400 K.

2.3.2.1 System description

A SQUID magnetometer uses the properties of flux quantisation and the DC Josephson effect to sense the magnetisation of a material by using a superconducting ring with Josephson junctions in it. Josephson junctions are made by sandwiching an ultra-thin layer of an insulating material between two layers of superconductors. This superconducting ring of a SQUID magnetometer can contain either one or multiple Josephson junctions.

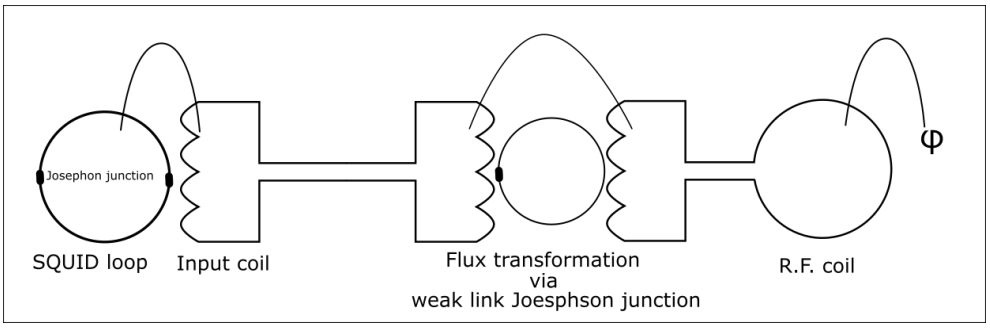

Figure 2.10: Circuit diagram of pick up coils and the sample that are inductively coupled to the Josephson junction and the rf circuit .

The magnetic material is oscillated longitudinally through the detection coils which are inductively coupled to the Josephson junctions as shown in figures 2.10 and 2.11. The sensitivity towards the sample positioning is resolved by the winding of the detection coils. As shown in figure 2.11 the coils at the top and bottom are counter wound to the two coils in the centre. Due to this, any noise picked up by the central coils will be cancelled by the top and bottom coils. Due to the longitudinal oscillation (Fig. 2.11) of the magnetic sample through the superconducting detection coils, the magnetic flux linked to the coil changes, thereby inducing an electric current in the detection coil. As the flux remains quantised, when the current in the detection coil changes a voltage signal is observed in the feedback rf coil (shown in Fig.2.12). This detected signal is then transformed into magnetisation using calibrated measurements. The schematic of the locked loop operation of a rf SQUID showing the input circuit diagram and electronics is shown in Fig.2.12 which has been taken from Ref.[173].

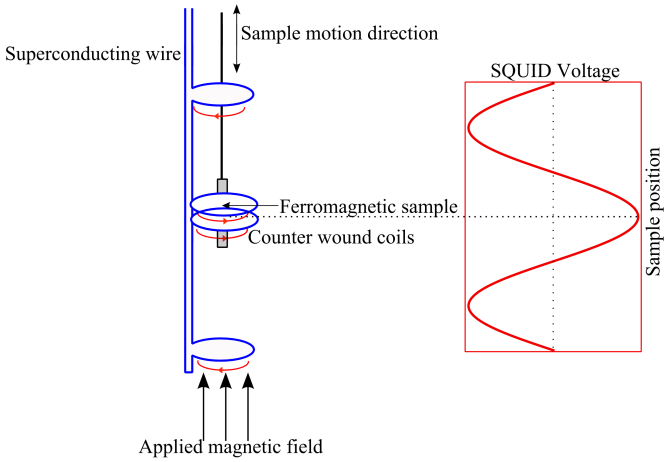

Figure 2.11: Schematic showing the longitudinal oscillation of the magnetic material through a pick up coil which changes the magnetic flux linked to the coil. By flux quantisation, when the current in the detection coil change a voltage signal is observed in the feedback R.F. coil which is then converted into magnetisation signal using calibrated measurements.

The entire detection unit is enclosed in mu metal shield to protect the SQUID from the magnetic field produced by the magnet itself.

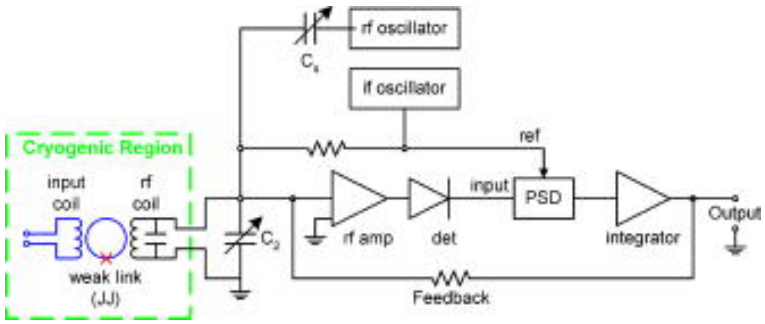

Figure 2.12: Schematic of the locked loop operation of a rf SQUID showing the input circuit diagram and electronics is shown. The input coil is inductively coupled to the pickup coils.

2.3.2.2 Measurement description

Samples for measurement were scribed in dimensions of 4 mm × 3 mm and held to a silicon rod using GE varnish. The silicon rod was then attached to a non-magnetic sample rod, centred within the superconducting coil which is mechanically

driven by a servo motor. The sample was then centred about the detection coil by oscillating the sample sinusoidally using the servo motor. Once centred, the magnetic field was swept between ±0.1 T and corresponding longitudinal moment was recorded by performing measurements in reciprocal sample oscillation (RSO) mode to reduce noise and improve sensitivity. All the superconducting elements of the SQUID magnetometer were immersed in liquid helium, while the central space which hosts the magnetic sample was at room temperature. Figure 2.13 shows an example longitudinal SQUID MH loop for sample S421 along three different crystallographic directions and magnetic field between ±0.1T.

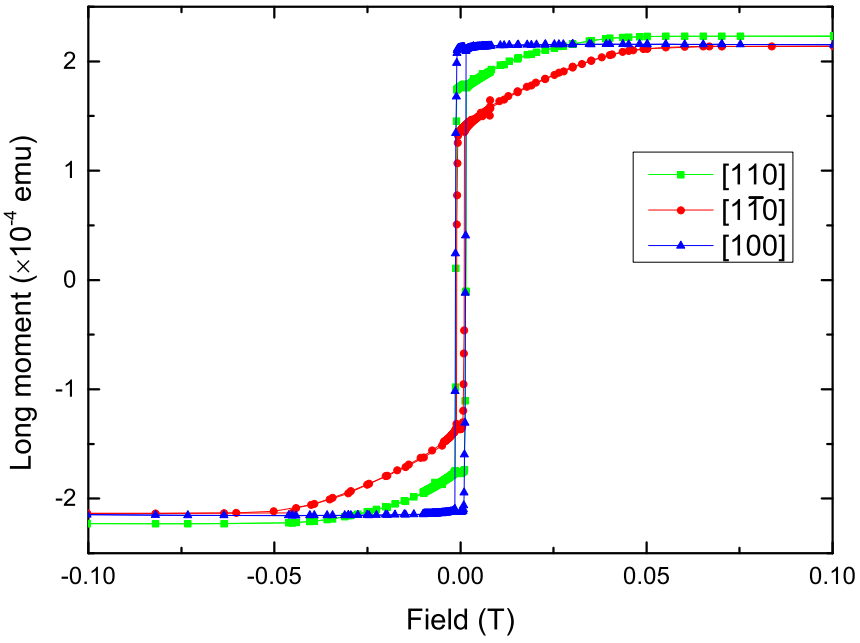

Figure 2.13: Example of a SQUID hysteresis loop for sample S419 representing the net longitudinal magnetic moment of the sample for field swept along different crystal directions: blue ([100]), green ([110]), and red ([1$\bar{1}$0]) directions.

2.3.3 Magneto transport

2.3.3.1 System description

The magneto-transport measurements were performed using the same electromagnet as the MOKE magnetometry measurements. The system comprised the 2 pole electromagnet, a Keithley 2400 current source meter, a Keithley 2400 voltage

source meter, and 2 Keithley 2000 multimeters for measurement of longitudinal (R_{xx}) and transverse (R_{xy}) resistances. The sample was hosted between the poles of the electromagnet as shown in Fig. 2.8 capable of applying field up to ±0.05 T.

2.3.3.2 Measurement description

The magneto transport measurements were performed on devices as shown in Fig. 2.14 .The devices were processed and mounted as discussed in section 2.2. A current of 1×10^{-4} A was passed along the [110] direction and the magnetic field was swept between ± 0.04 T at a step size of of 0.002 T for each angle in the plane of the film between [010] to [0$\bar{1}$0] in intervals of 15°. The magnetic sweep measurements were repeated for voltages across the piezoelectric transducer varied between -30 V to $+30$ V in steps of $+5V$. The corresponding longitudinal and transverse resistances were measured and recorded using a MATLAB code. The code was also used to control the electromagnet and the Keithley source meters and the multimeters. The voltage across the piezoelectric transducer was only incremented when the current measured across would be $<10\mu A$ by charging the capacitor too quickly. This was done such that a large strain is not produced across the transducer too quickly which might damage or crack the magneto-transport device.

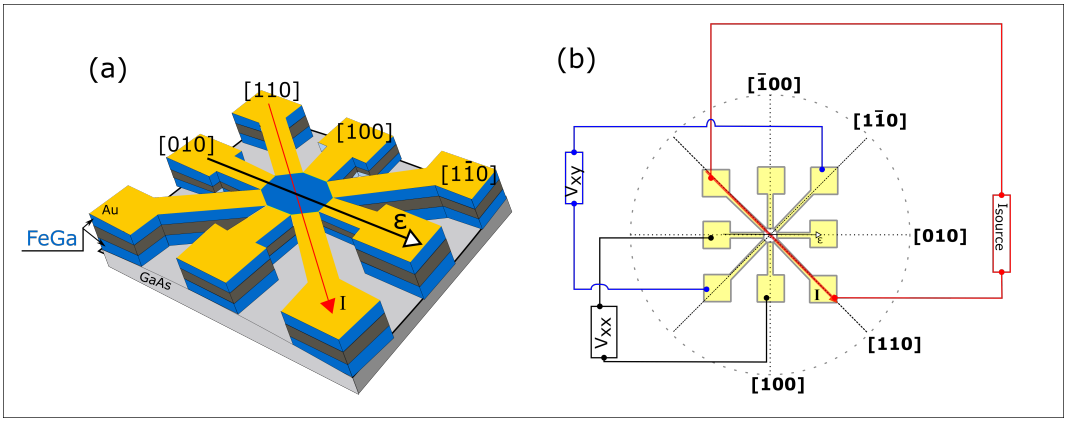

Figure 2.14: Schematic and geometry of the device used for magneto transport measurements. (a) The geometrical pattern of the device showing the directions of current, strain and the ferromagnet layers. (b) Device pattern depicting the direction of current and measurement aspects of longitudinal and transverse resistance.

Fig.2.14 represents the schematic and geometry of the device used for magneto transport measurements, (a) showing the directions of current, strain and the ferromagnet layers, (b) and the measurement geometry for longitudinal and transverse resistance.

Fig. 2.15 shows an example transverse resistance data collected for sample S419, at different piezoelectric voltages while the field is swept parallel to the $[1\bar{1}0]$ crystal direction.

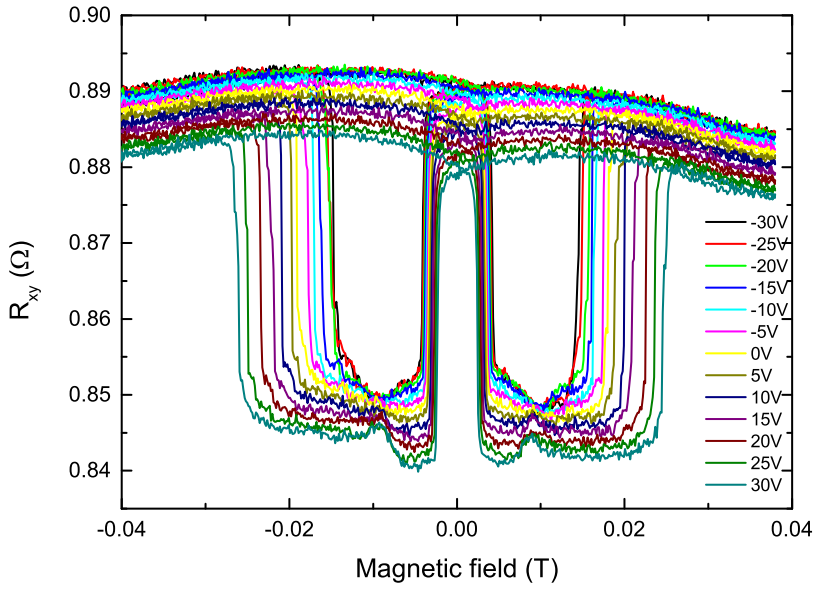

Figure 2.15: Example transverse resistance measured using the magneto transport set up at different piezoelectric voltages for sample S419 with magnetic field varied along the $[1\bar{1}0]$ crystal direction.

2.3.4 Ferromagnetic resonance

As has been discussed previously in Ch. 1, ferromagnetic resonance is a very sensitive technique which is used to probe the static and dynamic properties of magnetic materials. The ferromagnetic resonance experiments (FMR) discussed in this thesis were performed in collaboration with Dr. Stuart Cavill at the University of York, United Kingdom.

2.3.4.1 System description

For the FMR measurements of the samples investigated in my thesis, a broadband vector network analyser based FMR (VNA-FMR) was utilised. The set-up utilises a broadband network analyser (R&S ZNB Vector Network Analyser) to generate and analyse the rf wave, which are directed using non-magnetic sma end-coaxial

cables into the coplanar wave guide which hosts the magnetic sample. The incident microwave signal can be either reflected or/ and transmitted after interacting with the sample. For the case of a VNA set up, the transmitted signal is measured by finding the transmittance, or the ratio of the power of the transmitted to the incident wave.

In a VNA, there are two ports which can produce and analyse the microwave signal. The scattering parameter (S_{ij}) which refers to the scattering power ratio of the incident rf wave generated by i-port, and measured by port j. For the VNA used, the two ports 1 and 2 are used, and the S_{21} signal is used to obtain the FMR spectrum. This spectrum is observed as a Lorentzian line shape[131, 174], and has the maximum value when the frequency of the rf wave matches the natural frequency of the magnetic moments. Fig. 2.16 shows a schematic of a VNA-FMR.

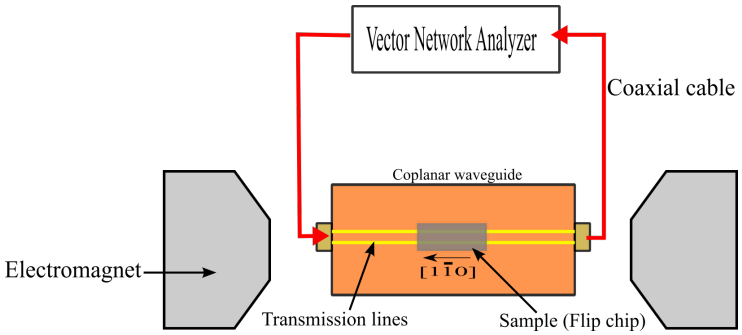

Figure 2.16: Schematic of a VNA-FMR system used to perform the FMR measurements discussed in this thesis.

2.3.4.2 Measurement description

The FMR measurements were conducted at room temperature by employing a coplanar wave guide. To achieve good coupling with the microwave, the bilayer sample was placed top down with the metal face towards the transmission axis (also called as the flip chip method [175, 176]), and then positioned between the poles of the electromagnet. For a fixed frequency ranging between 1 GHz to 20 GHz, the external in-plane magnetic field was varied along different crystal directions of the sample, while measuring the S_{21} signal of the transmission line. Fig. 2.17 shows an example of a measured S_{21} signal at 12 GHz for sample S419 ,when the field was varied along the $[1\bar{1}0]$ crystal direction. The experimentally observed spectra is represented by the black points, and the lines represent the Lorentzian fits which will be discussed in details in Ch. 3 of this thesis.

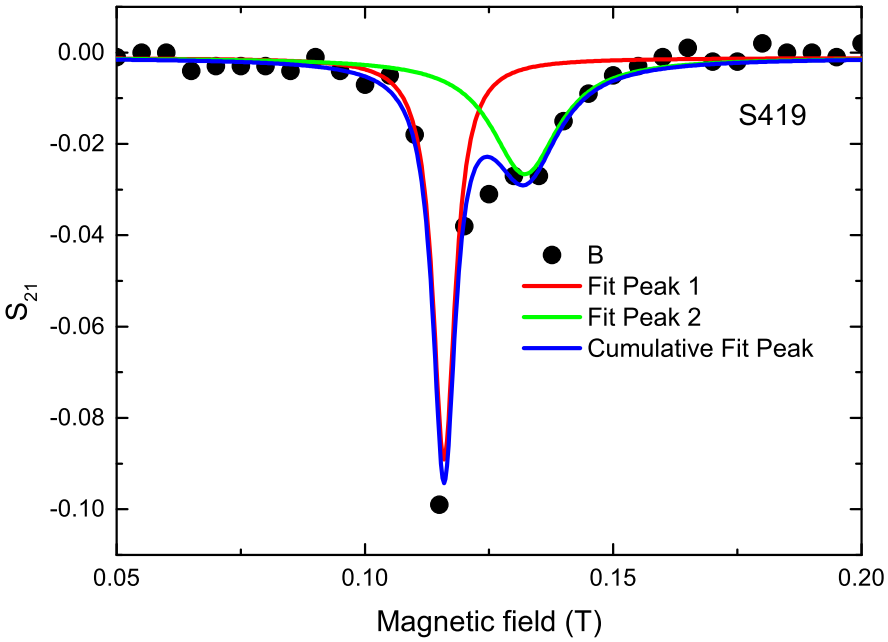

Figure 2.17: S_{21} transmission spectra for sample S419 at 12 GHz, when the magnetic field was varied along the $[1\bar{1}0]$ crystal direction. The experimentally observed spectra is represented by the black points, and the lines represent the Lorentzian fits .

2.3.5 HR-TEM

The High Resolution Transmission Electron Microscope results discussed in the thesis were obtained by FEI TITAN Themis 60-300 Cubed installed at Brno University of Technology, Central European Institute of Technology, Czech Republic. The methods for TEM were performed by Dr. Jan Michalicka, and Dr. Michal Urbanek with the collaboration support from Dr. Martin Veis.

High Resolution TEM is an imaging technique that allows to capture the crystallographic structure of a sample at an atomic scale. Due to its high resolution, it is a very sensitive and valuable technique to investigate morphological properties of materials at high magnifications.

2.3.5.1 System description

A HR- Transmission electron microscope comprises four main components: electron source, electromagnetic lens system, sample holder and the imaging system. The

electron source include a cathode made of tungsten which emits electrons when heated and an anode. The high energy electrons accelerate towards the anode which are then focussed and regulated by the electromagnetic lens system. This system comprising magnetic lens and aperture only allows electrons within a certain energy to pass through. The sample is hosted by the sample holder which can be manipulated in the x-y-z plane. The focussed electron beam bombard the sample and transmit through it to the imaging system which forms a contrast image based on the collected electrons. The image contrast depends on the the interaction of the electrons with the sample which is dependent on the thickness, atomic number and crystal structure of the sample. Fig. 2.18 shows a schematic of a TEM column.

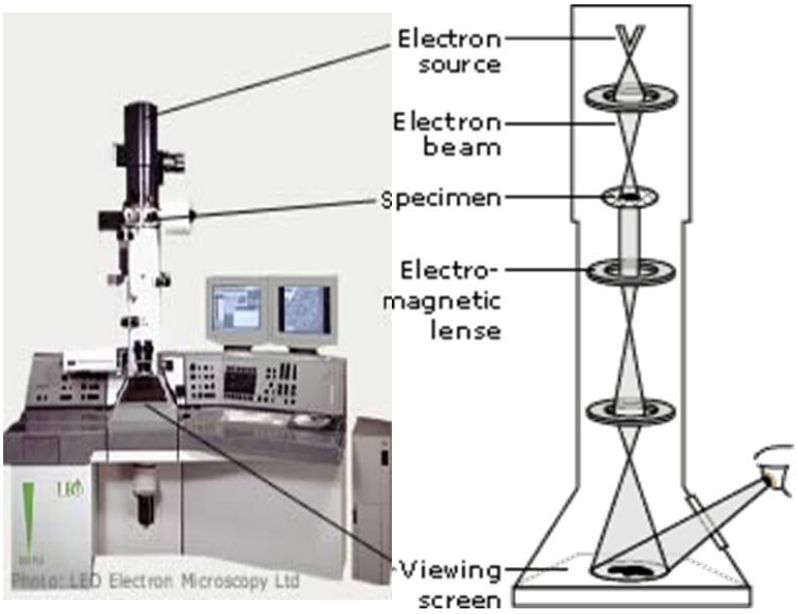

Figure 2.18: Schematic of a Transmission Electron Microscope.(www.nobelprize.org)

2.3.5.2 Measurement description

The samples were performed in form of thin cross sectional lamellae prepared by dual Scanning Electron Microscope with gallium Focussed Ion Beam column. An image C_S-corrector of optic aberrations, which is a part of the used TEM, was aligned for atomic HR-TEM imaging. The atomic structures were revealed in TEM phase contrast, when the crystal of the GaAs substrate was tilted to a low-index zonal axis.

2.3.6 Modelling Ferromagnetic resonance conditions

In order to obtain the magnetic anisotropies and saturation magnetisation of each layer of the bilayer system, the angular resonance conditions at a fixed strength in-plane external field were obtained and modelled for each of the samples described in this thesis. The general conditions for resonance have been obtained in terms of the second derivatives of the total free energy density of magnetisation in an external magnetic field . This approach for the derivation of the resonance condition in terms of minimising the magnetic free energy is known as the Smit, Suhl and Beljers approach. The ferromagnetic resonance frequency [137, 138] and field line-width can be expressed by Eqn. 2.16 and Eqn.2.17.

$$\left(\frac{\omega_{res}}{\gamma}\right)^2 = \frac{1}{M^2 sin^2(\theta_M)}\left[\frac{\partial^2 E}{\partial\theta_M^2}\frac{\partial^2 E}{\partial\phi_M^2} - \left(\frac{\partial^2 E}{\partial\theta_M \partial\phi_M}\right)^2\right]_{\theta_{equilibrium},\phi_{equilibrium}} \tag{2.16}$$

$$\triangle H = \frac{\alpha}{|\partial\omega_{res}/\partial H_{ext}|}\frac{\gamma}{M}\left[\frac{\partial^2 E}{\partial\theta_M^2} + \frac{1}{sin^2\theta_M}\frac{\partial^2 E}{\partial\phi_M^2}\right]_{\theta_{equilibrium},\phi_{equilibrium}} \tag{2.17}$$

where ω_{res} is the angular resonance frequency, γ is the gyromagnetic ratio, M is the magnitude of the magnetisation vector, E is the free energy of magnetisation, α is the damping parameter and θ_M, ϕ_M are the polar angle and azimuthal angles respectively.

For the modelling discussed in this thesis, the two layers of $Fe_{1-x}Ga_x$ are treated as two independent thin films, and the resonance conditions of each layer are treated separately. This section describes the derivation of the general expression of the magnetic anisotropies, the resonance conditions and the field linewidth.

The free energy of each layer of $Fe_{1-x}Ga_x$ in an in-plane external magnetic field is given by Eqn. 2.18 [101, 177, 178], where E_{Zeeman} is the Zeeman contribution to the energy, E_{demaig} is the demagnetising energy. The uniaxial and cubic energy are represented by $E_{uniaxial}$ and E_{cubic} respectively. The different energies have been discussed in Chapter 1 (Sec. 1.4.2) .

$$E = E_{Zeeman} + E_{demag} + E_{uniaxial} + E_{cubic} \tag{2.18}$$

or,

$$E = H_{ext}M_s(sin\theta_M cos(\phi_H - \phi_M)) + M_s^2 cos^2(\theta_M) + \frac{1}{2}H_u M_s sin^2\theta_M cos^2(\phi_M - 45^\circ) + \frac{1}{8}H_c M_s \left(sin^4\theta_M sin^2\phi_M + sin^2 2\theta_M\right)$$

Where H_{ext} is the external applied field, M_s is the saturation magnetisation, H_u is the uniaxial anisotropy field , H_c is the cubic anisotropy field, and the angles are as defined in Fig. 2.19

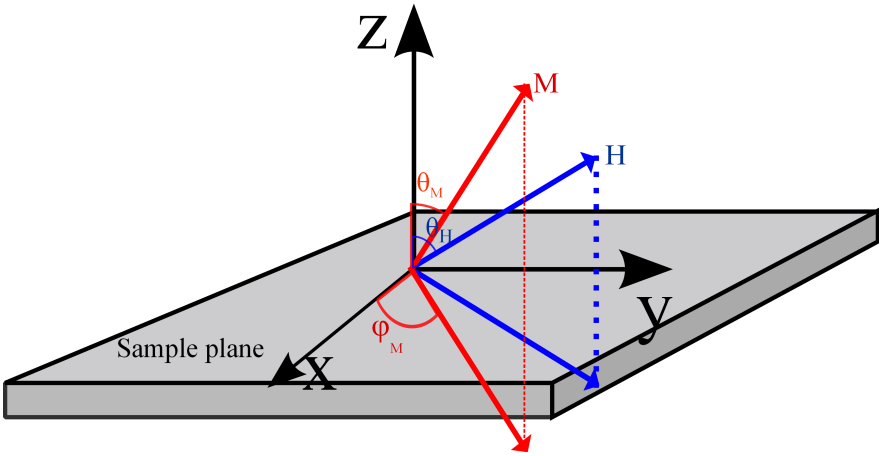

Figure 2.19: Coordinate system for finding the resonance frequency conditions

.

With the polar value of the external field being $\theta_H = 90^o$, the equilibrium conditions ($\frac{\partial E}{\partial \theta_M} = 0$; and $\frac{\partial E}{\partial \phi_M} = 0$) are derived to be

$$\theta_M = 90^\circ,$$

and

$$-H_{ext}M_s(sin(\phi_H - \phi_M)) + \frac{1}{2}H_u M_s sin2(\phi_M - 45^o) + \frac{H_c}{4}M_s sin4\phi_M = 0$$

Therefore, the second derivatives are,

$$\frac{\partial^2 E}{\partial \theta_M^2} = H_{ext}M_s(cos(\phi_H - \phi_M)) + M_{eff}M_s + H_u M_s cos^2(\phi_M - 45^o) + \frac{H_c}{2}M_s\,(1 + cos4\phi_M) \quad (2.19)$$

$$\frac{\partial^2 E}{\partial \phi_M} = H_{ext}M_s(cos(\phi_H - \phi_M)) + H_u M_s cos2(\phi_M - 45^o) + \frac{H_c}{2}M_s cos4\phi_M \quad (2.20)$$

Substituting Eqn..2.19 and 2.20 in Eqn. 2.16 results in

$$\left(\frac{\omega_{res}}{\gamma}\right)^2 = \left[H_{ext}(cos(\phi_H - \phi_M)) + M_{eff} + H_u cos^2(\phi_M - 45^o) + \frac{H_c}{2}\,(1 + cos4\phi_M)\right] \times \left[H_{ext}(cos(\phi_H - \phi_M)) + H_u cos2(\phi_M - 45^o) + \frac{H_c}{2}cos4\phi_M\right] \quad (2.21)$$

The magnetic properties of the layers of $Fe_{1-x}Ga_x$ were then obtained by modelling the angular resonance frequencies at a constant field strength using Eqn. 2.21 and doing a sum of least square fit to the experimental observed angular resonance for each layer. The fit was done keeping the anisotropies and the saturation magnetisation as free parameters. From the obtained values of anisotropy constants, the resonance frequency at a fixed angle was modelled and fit to the experimental variation of the resonance field with frequency to estimate the values of the saturation magnetisation within error bars. This process was iterated several times to have the variation of the estimated parameters restrict within the calculated errors.

The field linewidths of the layers were also calculated using Eqn. 2.22 which is obtained from Eqn. 2.17. Fitting the modelled field linewidth to the experimental linewidth results in the calculation of the intrinsic and extrinsic damping parameters.

$$\triangle H = \frac{2\alpha\omega_{res}}{\gamma}\frac{1}{cos(\phi_H - \phi_M)} \quad (2.22)$$

Fig 2.20 shows the modelled angular resonance frequency at 0.1 T with the experimental resonance frequencies and the field linewidths for sample S421. Th experimental FMR results will be discussed in Ch 3 of this thesis.

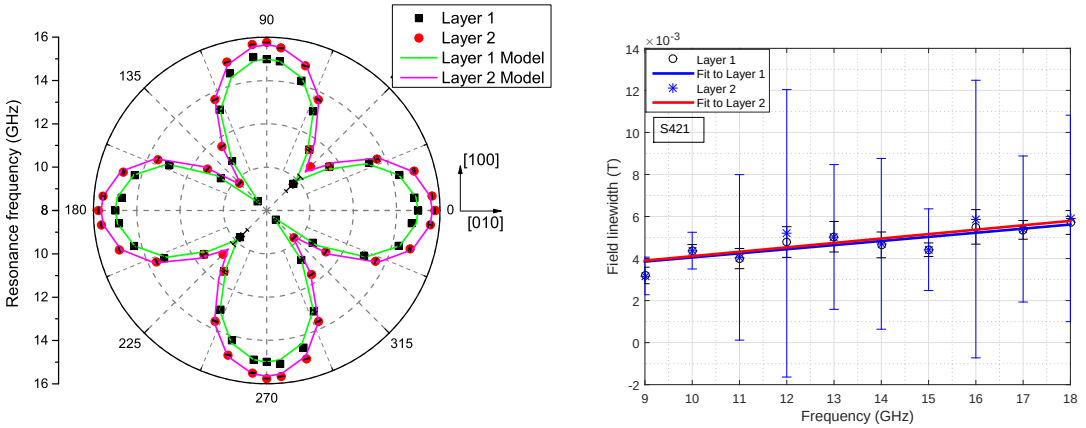

(a) Angular resonance frequency at 0.1 T (b) Modelled and experimental field linewidth

Figure 2.20: Example to show the modelling of the angular dependence of resonance frequency to obtain (a) the magnetic anisotropy and (b) the damping parameters from the field linewidth

2.3.7 Modelling MH loops

Fitting to the FMR data using the model described in section 2.3.6 yields values for the magnetic anisotropy constants and the saturation magnetisation of each magnetic layer. In order to simulate the data obtained by SQUID magnetometry, the magnetisation reversal curves have been simulated by calculating the conditions to minimise the magnetic free energy as a function of external magnetic field. The method is described in this section and the comparison of the fitting of the model to the experimental data in chapters 3 and 4 permits a check of the consistency between the data obtained by SQUID and FMR. It also allows extraction of the domain wall de-pinning energy. [179].

The magnetic free energy is modelled as a function of magnetic field. The direction of the magnetisation is determined to be the angle that represents the minimum of the magnetic free energy. As the external magnetic field changes the angle of the magnetisation is allowed to switch to a neighbouring minimum in energy when the energy difference between the two minima is greater than the parameter E_{DW}, representing the energy to nucleate or to de-pin a domain wall. Therefore, in this model magnetisation reversal proceeds via domain wall motion.

A schematic of this process is shown in Fig. 2.22 for external field 52° away from the [010] crystal direction, where layer 1 (shown in red) is the layer of $Fe_{1-x}Ga_x$ grown on GaAs substrate and layer 2 (blue) is the layer over the spacer and the green circle with the arrow denotes the location of the magnetisation M.

Fig 2.21 shows an example of modelled fit to the SQUID MH loop for sample S421 for external field parallel to the $[1\bar{1}0]$ crystal direction. The modelled curve is fit to the experimental SQUID magnetisation loop by minimising the sum of least squares with E_{DW} as a free parameter for each layer.

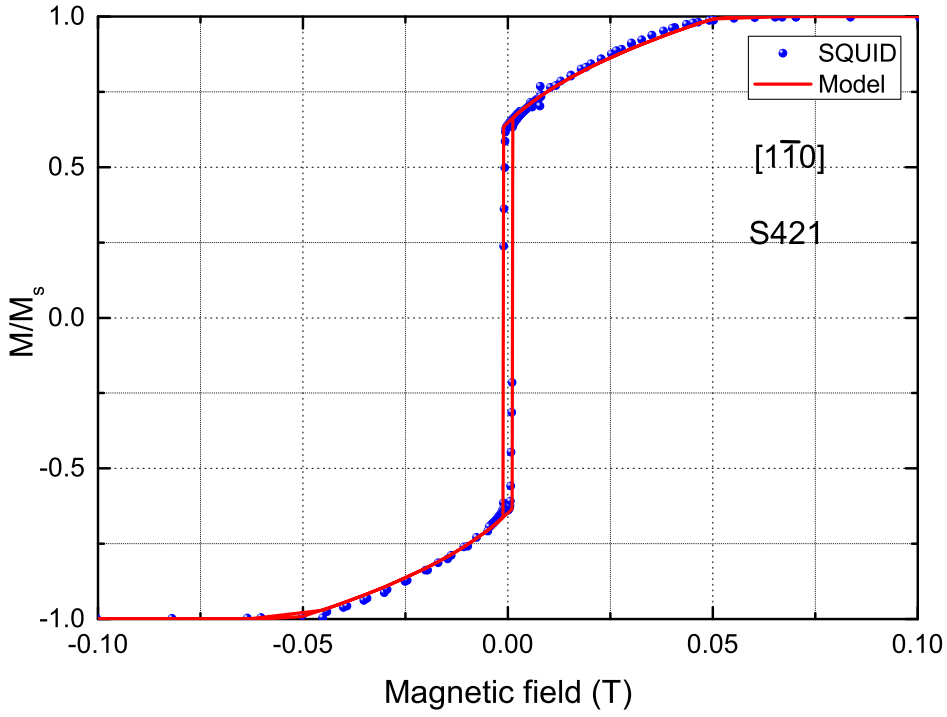

Figure 2.21: Modelled MH loop for SQUID to estimate the values of the E_{DW}. The normalised SQUID MH loop is shown in blue with the modelled MH loop in red.

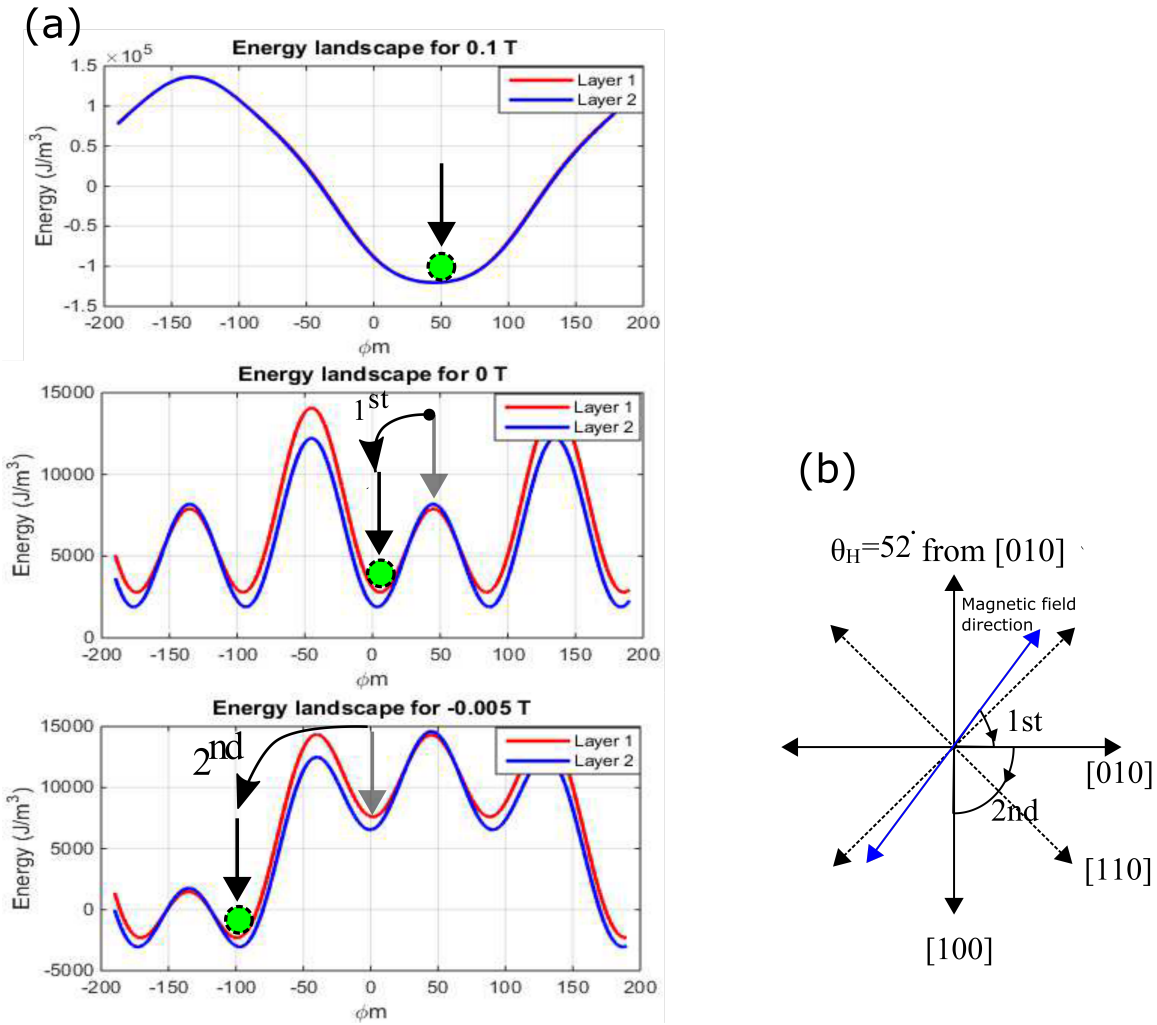

Figure 2.22: Schematic of the energy landscape describing the magnetisation reversal process. (a) Energy landscape for each layer showing the position of the magnetisation at different magnetic field strengths. The green dot with an arrow represents the angle of magnetisation at certain field strength. As the magnetic field is varied, the magnetisation for each layer (red for layer 1, and blue for layer 2) switches or rotates to a different value to align with the easy axis or with the external field which is shown by the schematic in (b).

Chapter 3

Static, dynamic and structural properties of $Fe_{1-x}Ga_x$ bilayer films studied by SQUID, Ferromagnetic resonance and HR-TEM

3.1 Introduction

In this chapter, an investigation of the magnetic properties of $Fe_{1-x}Ga_x$ bilayer films including the magnetocrystalline anisotropies, saturation magnetisation, damping, linewidth, and the morphological properties are described. Ferromagnetic resonance and SQUID magnetometry are two very sensitive and convenient techniques to determine the dynamic and static properties of the multilayer $Fe_{1-x}Ga_x$ layers. The investigated multilayer samples by SQUID and FMR are shown in table 3.1. The individual layers have different Fe content resulting in different values of the magnetisation and anisotropy constants. Ferromagnetic resonance (VNA-FMR) and SQUID magnetometry have been used along with mathematical modelling to determine the static and dynamic properties for each layer in the multilayer structure. For the structural characterisation only the 5 nm thick spacer samples were investigated by HR-TEM technique to resolve the surface interface interaction.

Sample	Nominal Structure (nm)	Substrate
S419	GaAs \ $Fe_{81}Ga_{19}$(5) \ Al (5) \ $Fe_{90}Ga_{10}$(5) \Al (5)	150 μm GaAs (001)
S420	GaAs \ $Fe_{81}Ga_{19}$(5) \ Al (10) \ $Fe_{90}Ga_{10}$(5) \Al (5)	150 μm GaAs (001)
S421	GaAs \ $Fe_{81}Ga_{19}$(5) \ Cu (5) \ $Fe_{90}Ga_{10}$(5) \Al (5)	150 μm GaAs (001)
S422	GaAs \ $Fe_{81}Ga_{19}$(5) \ Cu (10) \ $Fe_{90}Ga_{10}$(5) \Al (5)	150 μm GaAs (001)

Table 3.1: Investigated samples for static and dynamic properties using VNA-FMR and SQUID magnetometry.

3.2 FMR study of dynamic properties

In this section the ferromagnetic resonance experiments and the mathematical analysis to obtain the values of the magnetic parameters of the investigated samples are discussed. The FMR experiments were performed using a VNA-FMR set up in collaboration with Mr. C. Love and Dr. S. Cavill at the University of York, United Kingdom.

3.2.1 Extraction of magnetic anisotropy constants

A vector network analyser based FMR system was used to investigate the dynamic properties of the multilayer galfenol films. Magnetic field was scanned between 0 T and 0.3 T at microwave frequencies ranging from 0 GHz to 20 GHz for each sample along different in-plane directions of magnetic field with respect to the transmission axis parallel to the $[1\bar{1}0]$.

From the FMR measurements at different frequencies and at different angles of a constant in-plane external field, the resonance frequency and the linewidth[180] were extracted for each sample, from the S_{21} spectra . Example spectra are shown in Fig. 3.1. It shows the FMR spectra for a constant field strength of 0.1 T along three different crystal directions : [110], [100], and $[1\bar{1}0]$, for sample S421 . The black circles are the experimental data from the FMR, and the coloured solid lines are the Lorentz fits given by Eqn 3.1:

$$y = y_o + \frac{2A}{\pi}\left(\frac{w}{4\left(f - f_r\right)^2 + w^2}\right) \tag{3.1}$$

where A is the signal area after background subtraction, f is the frequency in

GHz, f_r is the resonance frequency, and w is the linewidth given by the full width at half maximum of the peak.

From the Lorentz fits, the frequency linewidth is the full width at half maximum of the peak, and the resonance frequency is the peak centre. As can be seen in the transmission spectra of the ferromagnetic resonance, the presence of two peaks would indicate a different resonance frequency for each layer. As the layers have nearly similar composition, the resonance frequencies are very near, and hence the spectra have two overlapping modes instead of separate distinct Lorentz features.

For each of the samples, the values of the resonance frequency at different angles of a fixed magnetic field rotated with respect to the [010] direction were then obtained and have been shown by the points in Fig. 3.2 (a) to (d). The red points denote the experimental resonance frequencies for layer 1, while the green points denote the experimental resonance frequencies for layer 2. A similar approach to obtain the resonance frequencies as a function of field magnitude, for the magnetic field applied along the $[1\bar{1}0]$ crystal direction was performed for all the samples.The results are represented in Fig. 3.3 (a) to (d) for both the magnetic layers. The $[1\bar{1}0]$ crystal direction was chosen, as the transmission axis is parallel to this direction, and has a better signal to noise ratio in comparison to the other directions of applied field. This is only for a matter of convenience and the same can be done for any of the crystal directions.

In the angular resonance frequency plots, it is observed that the individual layers have distinct resonance frequencies which is expected because the layers have different iron composition, and hence different net magnetic moment and different values for the anisotropy constants. The angular resonance frequencies exhibit a typical quasi-sinusoidal angular dependence which is a combination of the 2 fold uniaxial component and 4 fold cubic component with lower values for 45° ([110]) and 135°($[1\bar{1}0]$) and higher resonance values for the 0°([010]) and 90°([100]) field directions. The difference in the resonance frequencies between the [110] and $[1\bar{1}0]$ direction is due to the uniaxial anisotropy term .

In order to obtain the magnetic anisotropy constants and the values of the saturation magnetisation, the experimental points were fitted using simulated values of the resonance frequencies for individual layers. The mathematical modelled curves are shown by the red and green dashed lines in the figures 3.2 (a) to (d) and d figures 3.3 (a) to (d). The mathematical fits for the angular variation of resonance frequency and the field variation of the frequency were performed iteratively to minimise the standard error on the anisotropy and the saturation magnetisation

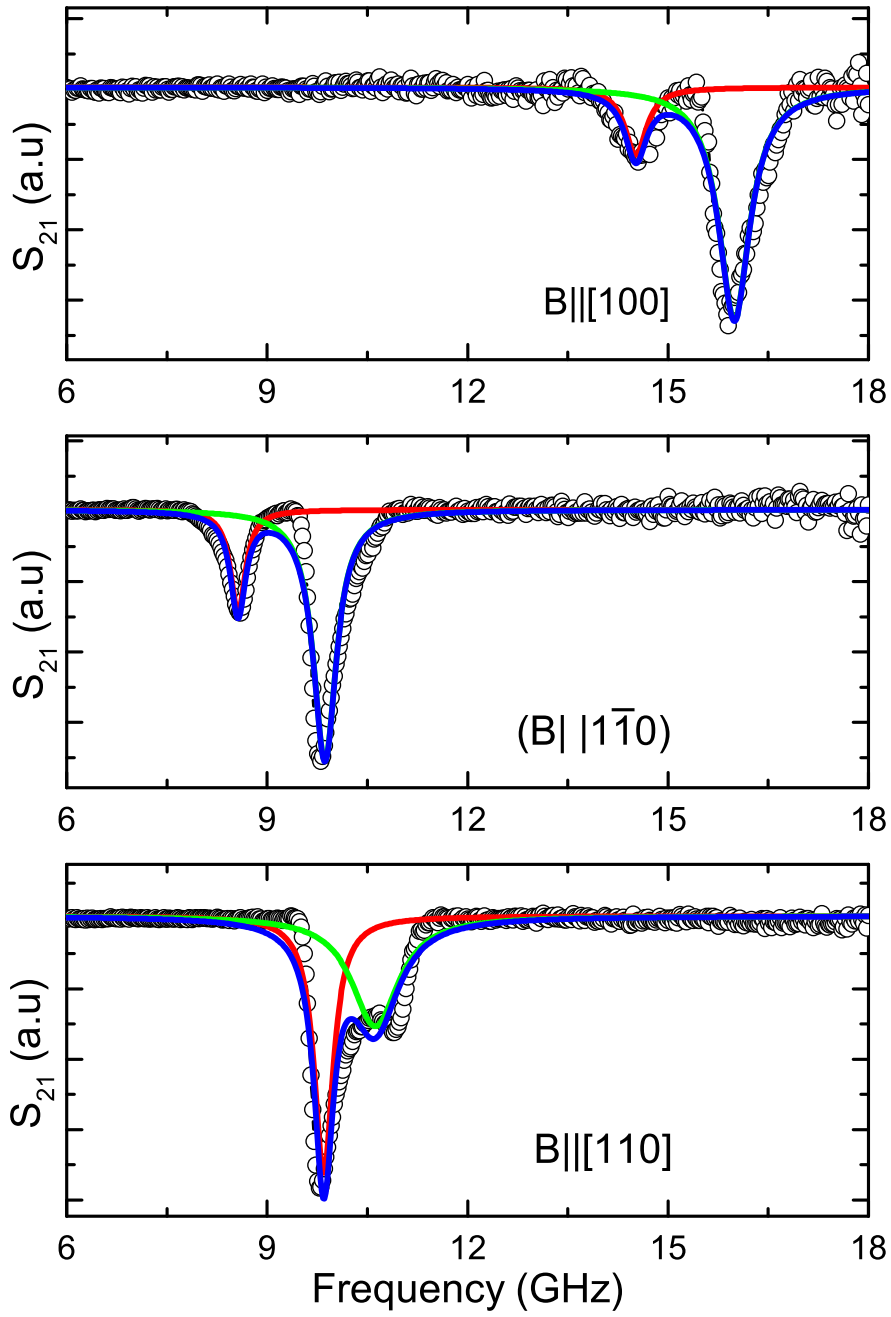

Figure 3.1: FMR spectra for sample S421 at 0.1 T parallel to different crystal directions. The black hollow circles are the experimentally observed FMR spectra, with the Lorentz fit in blue (total), red (layer 1) and green (layer 2) solid lines. The resonance frequency is the peak centre of the fits and the frequency linewidth is the FWHM of the Lorentz fits. As the layers have different Fe concentration along with unique magnetocrystalline anisotropies, the resonance frequencies are different for each layer and vary with field direction.

value. The angular variation of the resonance frequency for all the samples were first fit using sum of least squares and using Eqn.3.2 with the anisotropy fields and saturation magnetisation constant as the free parameters. Eqn. 3.2 relates the resonance frequency to the magnetic anisotropies and was previously discussed in Chapter 2 (see Eqn. 2.21).

$$\left(\frac{\omega_{res}}{\gamma}\right)^2 = \left[H_{ext}(cos(\phi_H - \phi_M)) + M_{eff} + H_u cos^2(\phi_M - 45^o) + \frac{H_c}{2}(1 + cos4\phi_M)\right] \times \left[H_{ext}(cos(\phi_H - \phi_M)) + H_u cos2(\phi_M - 45^o) + \frac{H_c}{2} cos4\phi_M\right] \quad (3.2)$$

Next the field variation of the frequency along the $[1\bar{1}0]$ direction was modelled using the same equation Eqn.3.2, but this time the anisotropy energy terms were fixed parameters and the angle chosen was along the $[1\bar{1}0]$ crystal direction. This fit would give an estimate of the saturation magnetisation, which was reused to fit the angular variation of the resonance frequency to get different values of the anisotropies. This cycle was iterated multiple times till the variation of the values were limited within the error bars. A flowchart depicting the steps of the mathematical modelling is shown in Fig. 3.4.

Example fits to the angular resonance frequency at 0.1 T for samples S419, S420, S421 and S422 are shown in fig 3.2 (a) to (d) respectively. In these plots 0° refers to the [010] crystal direction. The modelled values of the resonance frequencies for each layer are denoted by the dashed lines.

Table 3.2 lists the calculated values of the magnetic anisotropy coefficients and the saturation magnetisation for each layer calculated using the mathematical modelling process as described above.

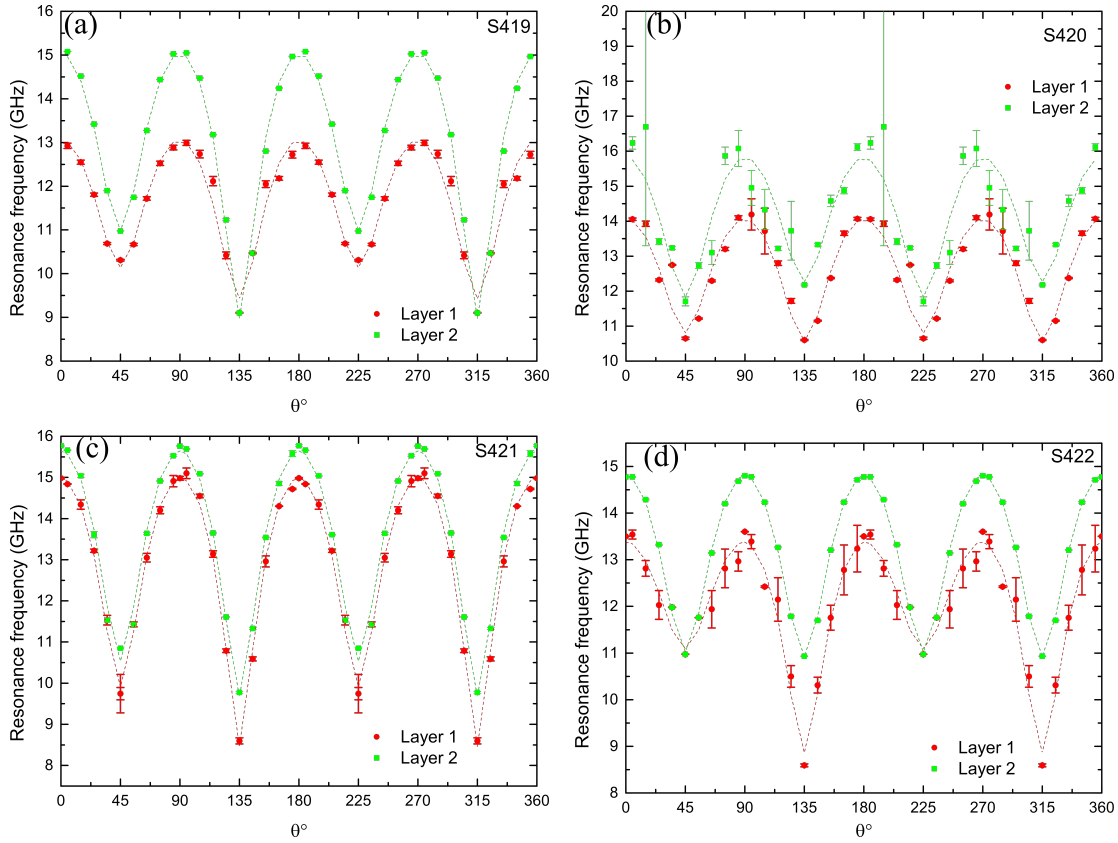

Figure 3.2: Fit to the angular resonance frequency at 0.1 T for samples (a)S419, (b)S420, (c)S421, (d)S422 using Eqn. 3.2. The experimental resonance frequencies for each layers are represented by scattered points : red for layer 1 and green for layer 2, and the dashed lines represents the simulated fits to the experimental points.

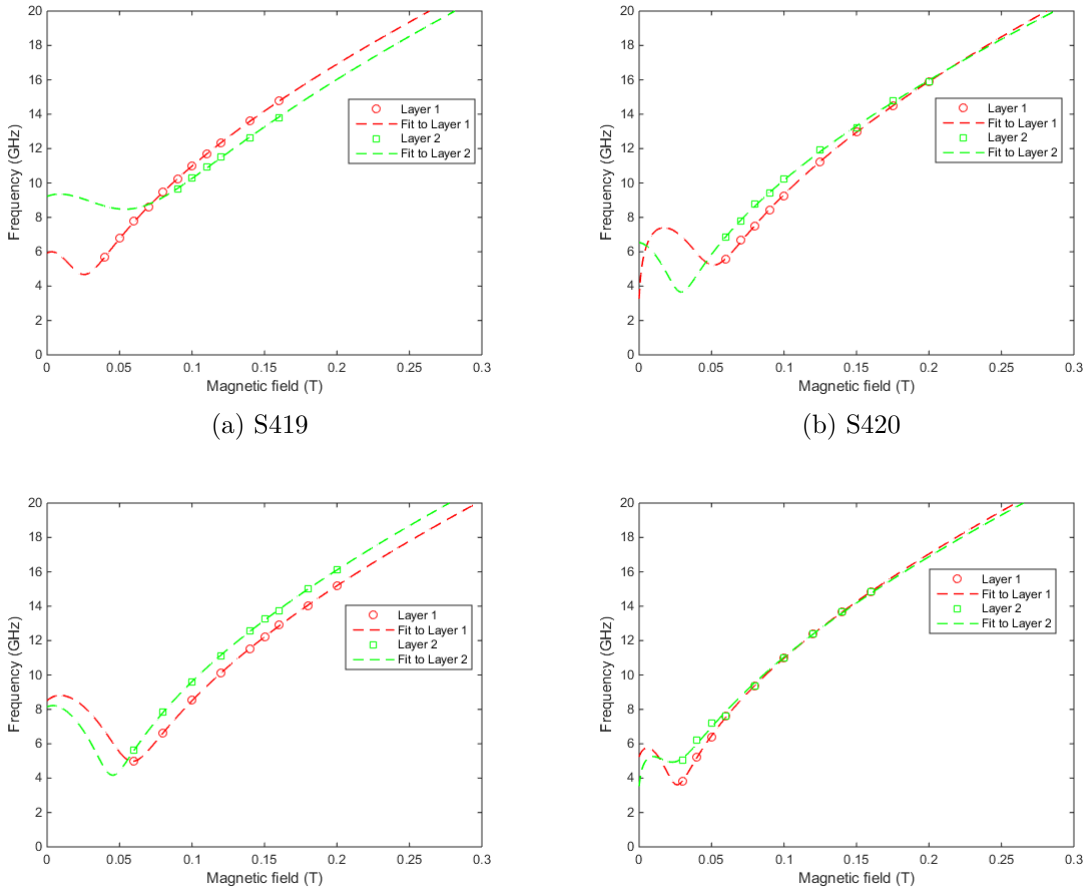

(a) S419 (b) S420

(c) S421 (d) S422

Figure 3.3: Resonance frequency for sample S419 to S422 with magnetic field along $[1\bar{1}0]$ direction.The experimental values for each layers are represented by scattered points : red for layer 1 and green for layer 2, and the dashed lines represents the simulated fits to the experimental points.

Sample	K_u^{layer1} (J/m^3)	K_c^{layer1} (J/m^3)	M_s^{layer1} $\times 10^6 Am^{-1}$	K_u^{layer2} (J/m^3)	K_c^{layer2} (J/m^3)	M_s^{layer2} $\times 10^6 Am^{-1}$
S419	9400 ± 100	29000 ± 400	1.46 ± 0.03	3300 ± 700	18000 ± 200	1.47 ± 0.01
S420	2400 ± 200	23000 ± 200	1.32 ± 0.01	-770.0 ± 100	20000 ± 100	1.51 ± 0.01
S421	6200 ± 10	32000 ± 10	1.42 ± 0.04	4100 ± 500	33000 ± 200	1.49 ± 0.01
S422	11000 ± 100	18000 ± 100	1.45 ± 0.04	500 ± 10	23000 ± 100	1.51 ± 0.01

Table 3.2: Extracted values of the uniaxial and cubic magnetocrystalline anisotropies and saturation magnetisation for each layer of samples S419, S420, S421 and S422 using FMR experiment and mathematical modelling using Eqn.3.2.

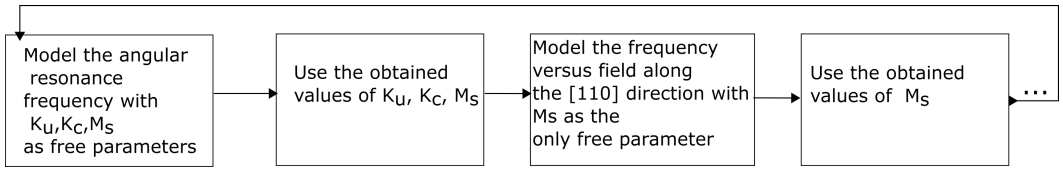

Figure 3.4: Flowchart describing the steps to iterate multiple times to get the values of the magnetic anisotropies and the saturation magnetisation for the samples listed in table 3.1.

The labels layer 1 and layer 2 mentioned in the above figures and table, as mentioned previously represent the layers of the multilayer sample. In order to identify these labels to the actual layers of the multilayer structure, the saturation magnetisation along with the magnetocrystalline anisotropy values can be compared.

The magnetocrystalline anisotropy parameters for each layers are compared quantitatively by using the fractional values of $\frac{K_u^1}{K_c^1}$, $\frac{K_u^2}{K_c^2}$, and $\frac{K_u^1}{K_u^2}$ where 1 and 2 refer to the ferromagnetic layers. These fractions have been listed in Table 3.3 along with net percentage of Fe. The values of Fe % have been calculated using the saturation magnetisation value of pure iron ($1.7 \times 10^6 Am^{-1}$) and finding the ratio $\frac{M_s^{layer1/2}}{M_s^{Fe}}$. The error associated with the ratio of the uniaxial anisotropy and cubic anisotropy is given by[100]:

$$\Delta \frac{K_u}{K_c} = \sqrt{\left(\frac{\Delta K_u}{K_c}\right)^2 + \left(\frac{-K_u \Delta K_c}{K_c^2}\right)^2} \tag{3.3}$$

Sample	Fe % Layer 1	$\frac{K_u}{K_c}$ Layer 1	Fe % Layer 2	$\left\lvert\frac{K_u}{K_c}\right\rvert$ Layer 2
S419	86 ± 2	0.32 ± 0.007	87 ± 1	0.18 ± 0.04
S420	78 ± 1	0.1 ± 0.008	89 ± 1	0.04 ± 0.01
S421	84 ± 2	0.2 ± 0.001	88 ± 1	0.12 ± 0.02
S422	85 ± 2	0.61 ± 0.006	89 ± 1	0.02 ± 0

Table 3.3: Table showing the Fe% in each layer of the grown samples calculated from the saturation magnetisation values obtained from the FMR experiments. The fractions $\frac{K_u^1}{K_c^1}$, $\frac{K_u^2}{K_c^2}$, and $\frac{K_u^1}{K_u^2}$ are used to map the labels to the layers grown on the substrate and the layer grown on the non-magnetic spacer.

From the above table it is seen that since the values of the cubic anisotropy are fairly consistent for the layers the fraction $\frac{K_u}{K_c}$ mostly reflects the variation of the uniaxial anisotropy. Both the fraction are always found to be < 1 which indicates both the fraction K_u/K_c and the absolute values of Ku of the layer 1 is greater than the layer 2. The in plane uniaxial anisotropy has been attributed to the metal-GaAs interface bonds and is inversely proportional to the thickness of the film[181–183]. A higher uniaxial anisotropy value would indicate a more significant anisotropic influence of the ferromagnet-substrate interface bonds while a lower value would indicate that the effect of the interface is weaker. Therefore using this argument it can be realised that layer 1 refers to the bottom layer that is grown on the GaAs substrate while layer 2 with lower K_u values is the top layer grown on the metallic stack. This realisation has been checked for consistency by comparing the M_s values. The saturation magnetisation values of layer 1 for all of the samples are smaller than the values for layer 2. This indicates that the layer labelled 1 has less Fe content compared to layer 2, and is something we planned to grow for samples listed in Table. 3.1. However the Fe content in different samples is not consistent,and this anomaly in the Fe composition could be due to multiple reasons which includes systematic errors in the sputter growth rates due to calibration, interface mixing etc.

3.2.2 Extraction of the dynamic parameters

For the purpose of investigating magnetisation dynamics in thin films, the linewidth and Gilbert damping are commonly used parameters that describe the spin relaxation, spin damping and scattering of the magnetic system.

For the investigated samples the linewidths have been determined from the

Lorentzian fits at 10 GHz for all the samples along the [100] and [1$\bar{1}$0] directions and have been shown in Fig.3.5 (a) to (h) below. In the plots, the black hollow circles are the experimentally observed FMR spectra, with the Lorentz fit in blue (total), red (bottom layer) and green (top layer) solid lines. The frequency linewidth is the FWHM of the Lorentz fits. The values of the linewidths for both the layers are listed in Table 3.4.

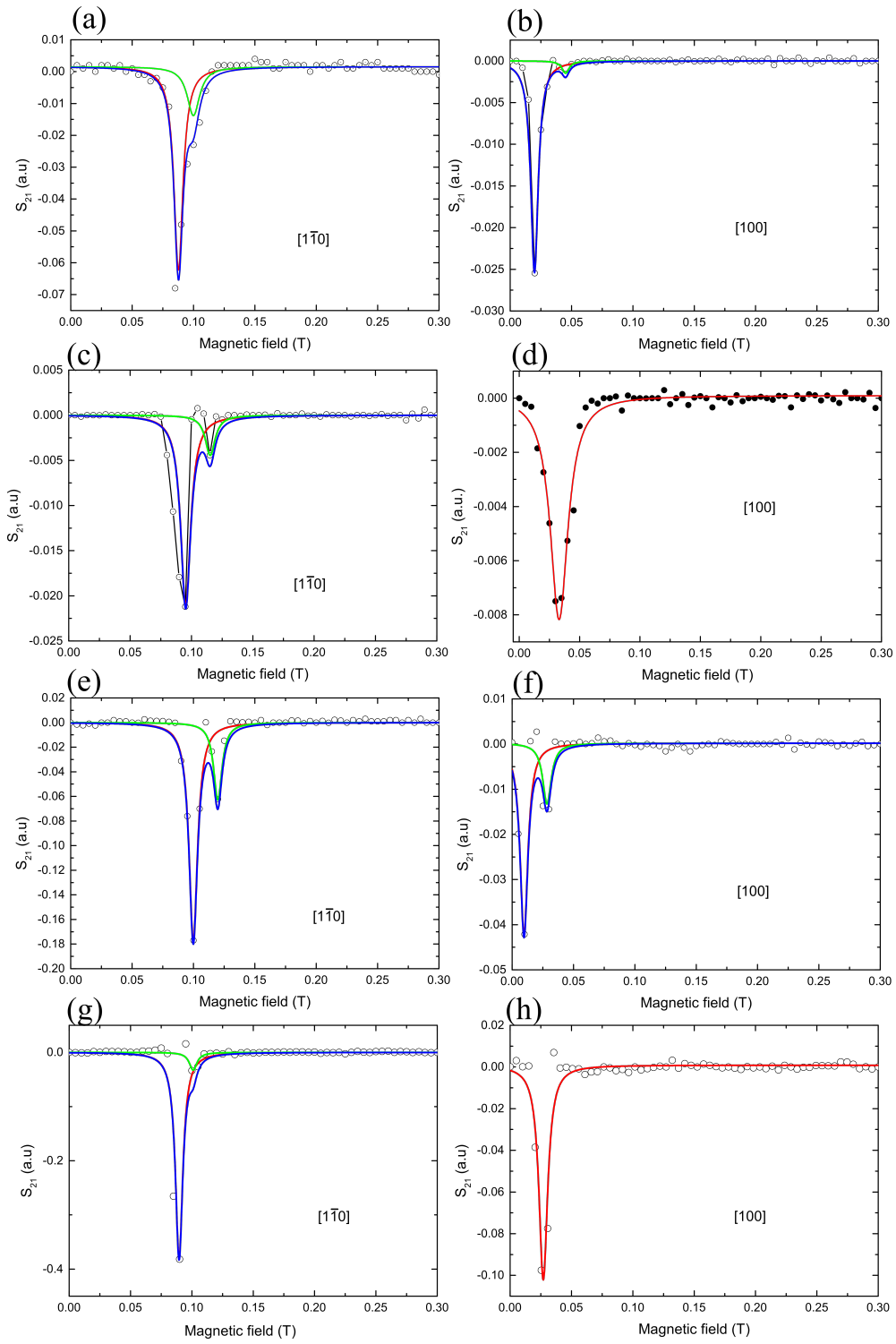

Figure 3.5: FMR spectra for sample numbers S419 (a, b), S420 (c, d), S421 (e, f), S422 (g, h), at 10 GHz frequency along the [1$\bar{1}$0], and [100] crystal directions . The black hollow circles are the experimental observed FMR spectra, with the Lorentz fit in blue (total), red (layer 1) and green (layer 2) solid lines. The frequency linewidth is the FWHM of the Lorentz fits.

Sample	Bottom layer [100] ($\times 10^{-3}T$)	Top layer [100] ($\times 10^{-3}T$)	Bottom layer [1$\bar{1}$0] ($\times 10^{-3}T$)	Top layer [1$\bar{1}$0] ($\times 10^{-3}T$)
S419	4.7 ± 1.9	3.8 ± 1.6	4.5 ± 1.2	5.9 ± 2.7
S420	3.6 ± 0.4	3.6 ± 0.4	4.9 ± 0.9	5.1 ± 2.2
S421	7.6 ± 0.5	8.1 ± 2.2	8.1 ± 2.7	4.2 ± 0.8
S422	4.3 ± 0.5	4.3 ± 0.5	3.7 ± 1.4	3.8 ± 0.2

Table 3.4: Values of the linewidths for the samples calculated from the Lorentzian fits to the FMR spectra at 10 GHz

It is observed that for the 10 nm spacer samples, only one linewidth value is seen when the field is applied along the [100] directions. This is due to a single peak in the S_{21} spectra. It should be because along this direction both the layers have the same resonance frequencies.

An impressive and outstanding feature of these films are the narrow linewidths which are a characteristic of a high quality and weakly damped systems. Previous linewidth measurements at 10 GHz frequency for $Fe_{1-x}Ga_x$ bulk with Ga concentration up to 20% have shown linewidth values of about 40×10^{-3} T [184] and 70×10^{-3} T [185]. MBE grown thin films with 19% Ga have values 7.7×10^{-3} T for [100] and 6.7×10^{-3} T for [1$\bar{1}$0] crystal axes [101]. Sputter grown samples with 20% Ga concentration [102] have reported values of 3.5×10^{-3}T. Such narrow linewidths are crucial for microwave devices employing spin-transfer torque, for example STT-RAM or STT-MRAM. Due to low values of the linewidths the range of dc currents where the oscillator locks to the reference signal can be maximised with increased power output [186].

The Gilbert damping parameter has been calculated and has been shown for all samples in the Fig. 3.6 (a) to (d) for the [100] direction . The points are the values of the field linewidths at different frequencies for all the samples, and the dashed line represents the linear fit following the relation expressed in Eqn. 3.4.

$$\Delta H = \Delta H_o + \frac{2\pi\alpha f}{\gamma} \tag{3.4}$$

where ΔH_o is the extrinsic linewidth and α is the intrinsic damping parameter. and γ is the gyromagnetic ratio with value $1.76 \times 10^{11} s^{-1} T^{-1}$.

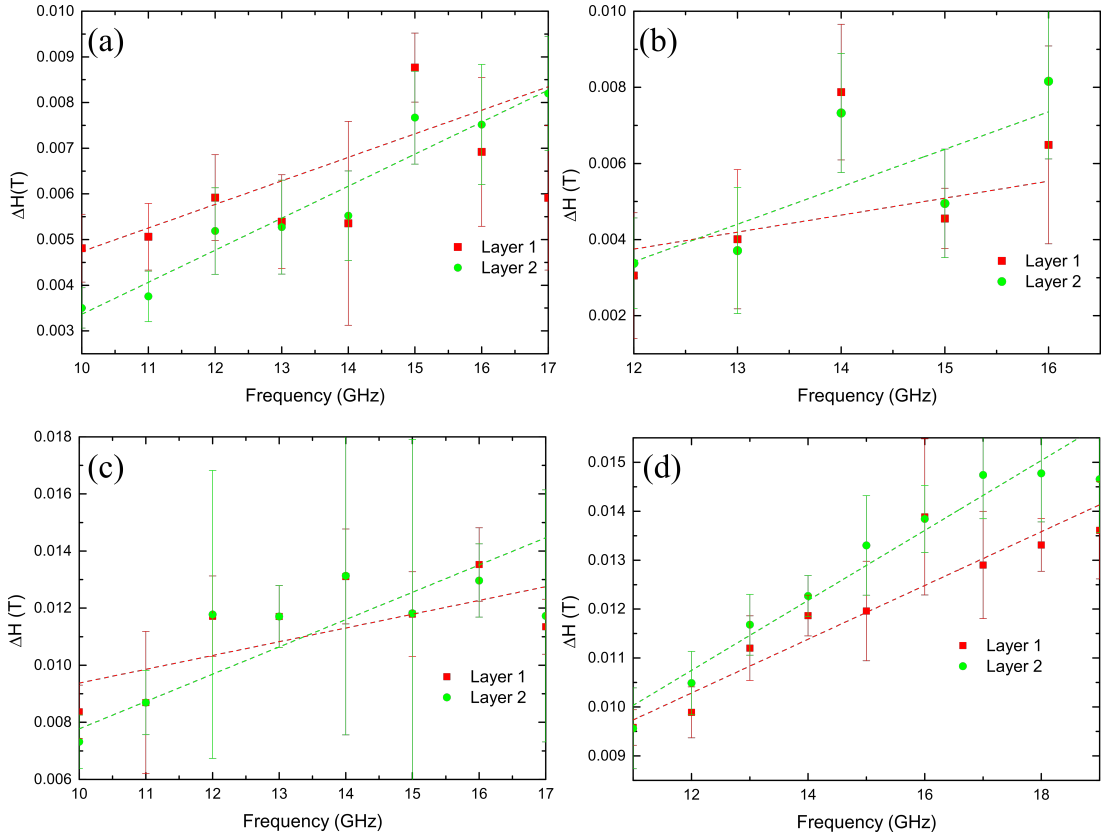

Figure 3.6: Linewidth for samples (a) S419, (b) S420, (c) S421, and (d) S422 with magnetic field along [100] direction.The experimental values for each layers are represented by scattered points : red for layer 1 and green for layer 2, and the dashed lines represents the simulated fits to the experimental points. The intrinsic damping parameter is obtained from the fit.

From the linear fits to the experimental field linewidths for each layer, the intrinsic damping parameter otherwise known as the Gilbert damping factor has been calculated for all the samples and are shown in table 3.5 .

Sample	Bottom layer Gilbert damping	Top layer Gilbert damping
S419	0.019± 0.002	0.015± 0.004
S420	0.028± 0.013	0.013± 0.002
S421	0.027± 0.004	0.013± 0.005
S422	0.020± 0.002	0.016± 0.002

Table 3.5: Table showing the calculated values of intrinsic or the Gilbert damping value for the investigated samples.

The values of the damping parameters for both the layers are of the same order of magnitude to previous reported value of 0.017 by Parkes et al [101] and 0.012 by Kuanr et al [102]. However the values for the bottom layer are significantly higher than for the top layer. It has been reported [102] that the Gilbert damping parameter is affected by Ga concentration in the FeGa samples, and with increase in the concentration of Ga the intrinsic damping term increases. The Gilbert damping parameter may also be influenced by the interfacial effects[187], surface morphology, crystallinity.

3.3 SQUID magnetometry study of static properties

The static magnetic properties of the multilayer samples at zero strain were characterised by Superconducting QUantum Interface Device (SQUID) magnetometry. From previous works done on epitaxial single layer of $Fe_{1-x}Ga_x$ grown on a $GaAs$(001) substrate [68, 100] , it is well established that the net in plane magnetic anisotropy is a combination of an uniaxial anisotropy and a cubic anisotropy. Using the ferromagnetic resonance technique I have calculated the values of these terms, which shows a strong cubic anisotropy for all of the samples. To confirm the values extracted from the ferromagnetic resonance experiments, and to investigate the

magnetisation reversal processes for all the samples, SQUID magnetometry measurements were performed. In this case, the longitudinal moment measured by the SQUID is a measure of the net magnetisation of the samples and serves as a necessary tool to determine the relative easy crystal directions, the net magnetic moment, and the domain wall de-pinning energies. The estimation of the domain wall de-pinning energies referred here onwards as E_{DW} is very useful to predict the switching fields, and to understand the magnetisation reversal process for each layer.

The SQUID magnetometry measurements for the samples are presented in figures 3.7 (a) to (d),which shows the direction of the magnetic field and the measured longitudinal moment as the field is varied along the different crystal directions.

By determining the angles of magnetisation for all three crystal directions, as the field is swept the relative easy and hard axes for magnetisation can be identified by solving the magnetic free energy density equation (Eqn. 3.5).

$$E = -H_{ext}M_s(cos(\phi - \theta)) + K_u sin^2(\theta) + \frac{1}{4}K_c sin^2 2\theta \tag{3.5}$$

where H_{ext} is the external magnetic field applied at an angle θ to the [010] and ϕ is the angle between magnetisation and [010], and K_u, K_c are the uniaxial and cubic anisotropy constants.

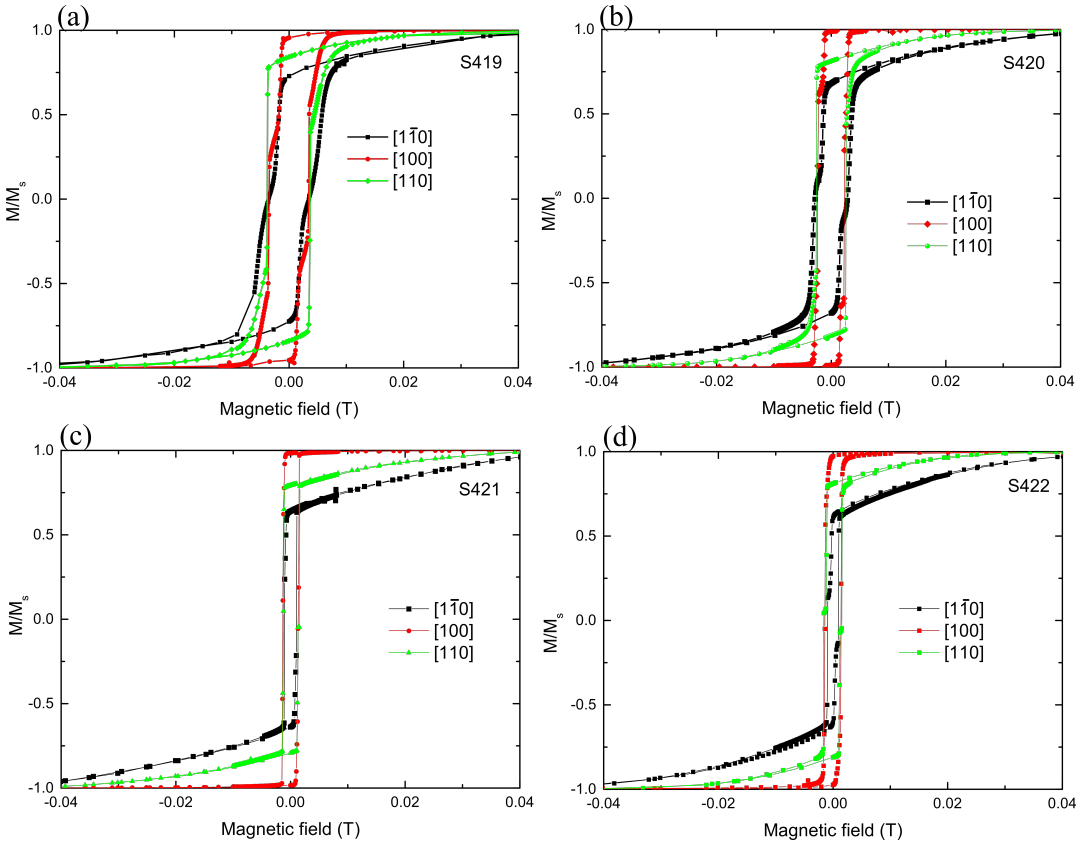

Figure 3.7: SQUID MH loop for samples (a) S419, (b) S420, (c) S421, and (d) S422. The longitudinal magnetic moments for three crystal directions are shown by red ([100]), green ([110]), and black ([1$\bar{1}$0]). Multiple switching fields are seen for all directions which can be attributed to the contribution from each layer of the multilayer structure. The magnetisation reversal is a combination of coherent rotation of the magnetisation and magnetisation switching.

Looking into the experimental SQUID magnetisation loops for all the samples in Fig.3.7 for field sweep along the [100], [110], and [1$\bar{1}$0] crystal directions it is confirmed that the [100] direction is the easy direction compared to the [110] and [1$\bar{1}$0] crystal directions as it needs lesser field to saturate the magnetisation in the field direction compared to the other directions, and also the remanent magnetisation is the highest for this direction. A similar argument holds for the [110] and [1$\bar{1}$0] direction, and it can be concluded that the [110] direction is relatively easier than the [1$\bar{1}$0]. The angular ferromagnetic resonance plots shown in Fig. 3.2 are consistent with this interpretation as the resonance frequency is the highest for [100]/[010] or 0° and is lowest for the [1$\bar{1}$0] or 135°.

Table 3.6 presents the calculated values of the net composition of Fe in the multilayers as calculated from SQUID and compared to the individual Fe% de-

termined by the ferromagnetic resonance experiment. It can be well related that the SQUID measures the average magnetic moment of the two layers and the net measured magnetisation by SQUID is the mean of the magnetic moment of the two layers, within experimental uncertainties. The experimental saturation magnetisation (M_s) in Am^{-1} was calculated by taking the average of the longitudinal moment at 0.05 T for the three crystal directions and dividing it over the volume of the sample. The net iron content in % was found from the fractional value of M_s measured from SQUID with the M_s of Fe which is $1.7 \times 10^6\ Am^{-1}$. It is seen that the net Fe content measured by SQUID is within the estimated values of net Fe% from the FMR.

Sample #	M_s^{SQUID} $\times 10^6 Am^{-1}$	% Fe^{SQUID}	M_s^{layer1} $\times 10^6 Am^{-1}$	$\%Fe^{layer1}$	M_s^{layer2} $\times 10^6 Am^{-1}$	$\%Fe^{layer2}$
S419	1.46±0.05	86 ± 3	1.46±0.03	86 ± 3	1.47±0.01	87 ± 1
S420	1.42±0.05	84 ± 3	1.32±0.01	78 ± 1	1.51±0.01	89 ± 1
S421	1.43±0.04	84 ± 2	1.42±0.04	84 ± 4	1.49±0.01	88 ± 1
S422	1.50±0.01	88 ± 2	1.45±0.04	85 ± 3	1.51±0.01	89 ± 1

Table 3.6: Comparison of the saturation magnetisation and $Fe\%$ for samples S419 to S422 obtained from SQUID measurements and the FMR calculations.

The magnetisation reversal is a combination of coherent rotation which is indicated by gradual change in magnetisation as the field is varied and an abrupt change in magnetisation which would indicate a magnetisation switch over the hard axis energy barrier. As the measured sample is a multilayer with different iron content and with different anisotropy energy values, it is reasonable to accept that the magnetisation reversal will be different for each layer and thereby will be having different switching events. As the SQUID magnetometer measures the net magnetic moment of the entire multilayer sample, it will be measuring the total longitudinal magnetisation from the contributions of both the layers. However as the magnetisation switching fields are different, it will be shown as a superposition of two switching events. The magnetisation reversal (MvH) loops are shown in Fig. 3.8 for all the samples. These figures are the same data as in Fig. 3.7 but repeated again to identify the distinct magnetisation switching events. In this figure the first magnetisation reversal is identified as ΔM_a and denotes the difference in magnetisation before and after the magnetisation switch, and the second reversal is represented as ΔM_b and denotes the magnetisation difference before and after the second switch.

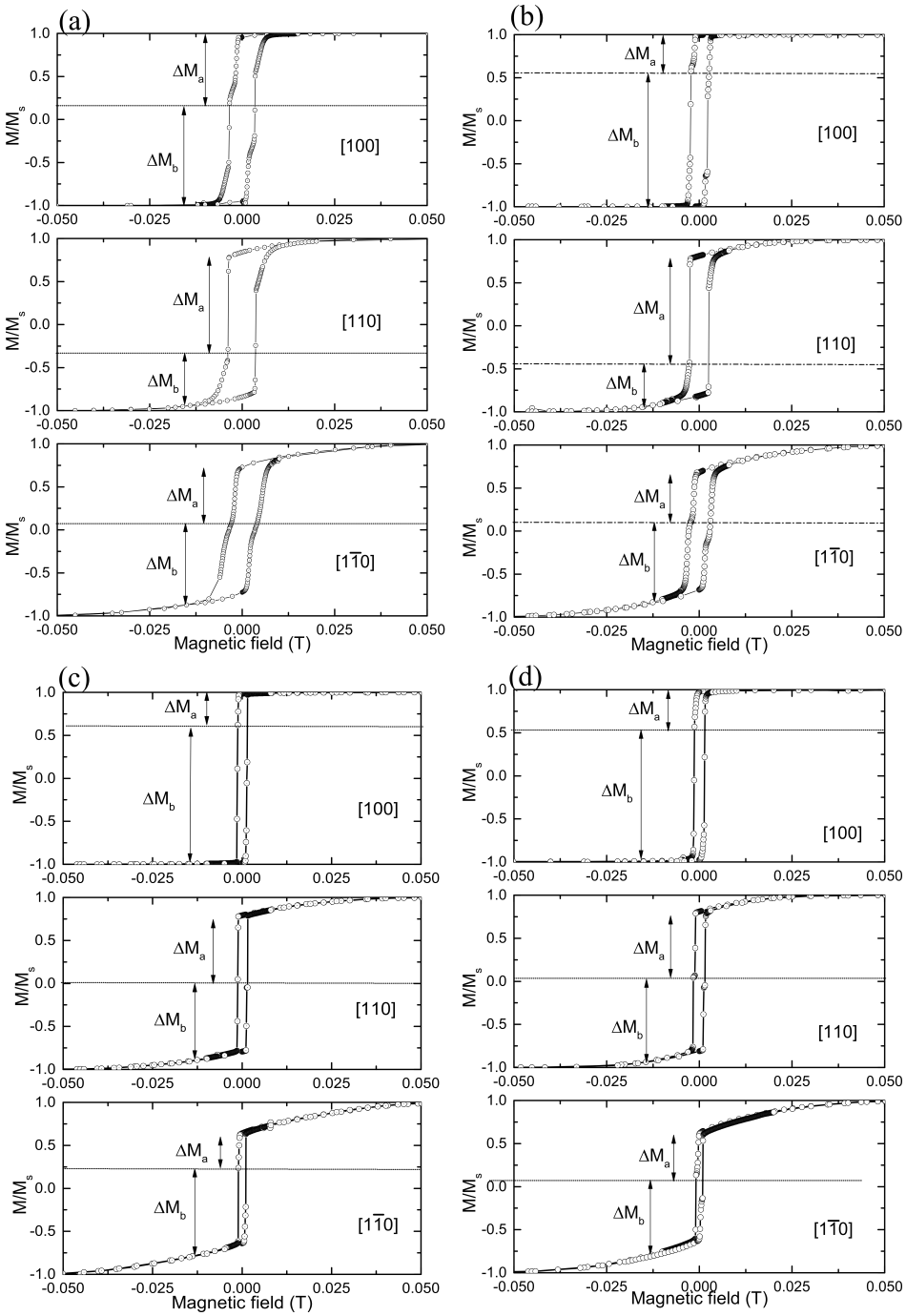

Figure 3.8: SQUID MH loops for the three crystal directions to identify the magnetisation reversal for samples (a) S419, (b) S420, (c) S421, and (d) S422. As the external field is swept from a higher saturating value to a negative value, the first magnetisation reversal is identified as ΔM_a and denotes the difference in magnetisation before and after the magnetisation switch, and the second reversal is represented as ΔM_b and denotes the magnetisation difference before and after the second switch.

The coercive fields for the Al spacer and Cu spacer differ as well ,with the samples S419 and S422 having higher coercive fields than samples S421 and S422. This may be due to different domain wall nucleation energy. In order to check the consistency of the magnetic anisotropy and saturation values calculated from the ferromagnetic resonance and also to calculate the E_{DW} values, MH loops were modelled for each sample by numerically solving the free energy (Eqn.3.5) and performing a sum of least squares fit as the field is varied along the three crystal directions as shown in Fig. 3.9 to Fig. 3.12. The modelled loops are shown by the thick red lines over the scattered experimental points with the inset plots showing the angle of magnetisation with respect to the [010] crystal direction for each field sweeping direction.

It can be seen that the modelled curves, using the parameters for magnetisation and anisotropy energy extracted from ferromagnetic resonance studies, agree very well with the data from SQUID measurements in the regions where the magnetisation rotates coherently and represents a single magnetic domain. In order to model the switching fields, the parameterE_{DW} is varied to achieve a fit to the data over the entire field range. The domain wall de-pinning energies which are responsible for the switching fields were determined from the modelling using least sum of square method at the experimental switching events and have been listed in Table 3.7 for all the samples.

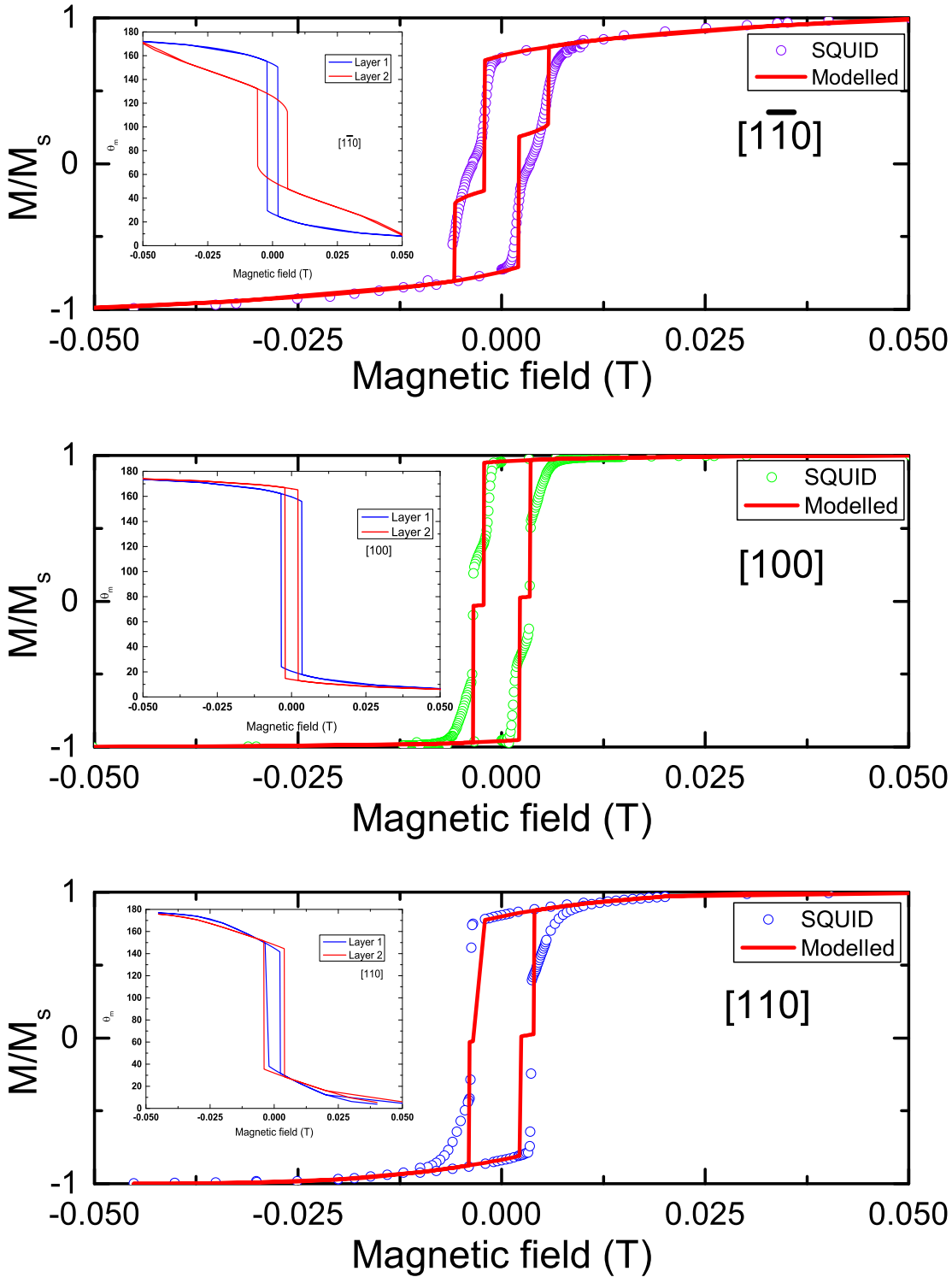

Figure 3.9: MH loop for S419 with the modelled (solid red line) and experimental data (scattered hollow points). The inset shows the angle of magnetisation for each layer as the magnetic field is varied. The modelling of the SQUID data was used to determine the E_{DW}.

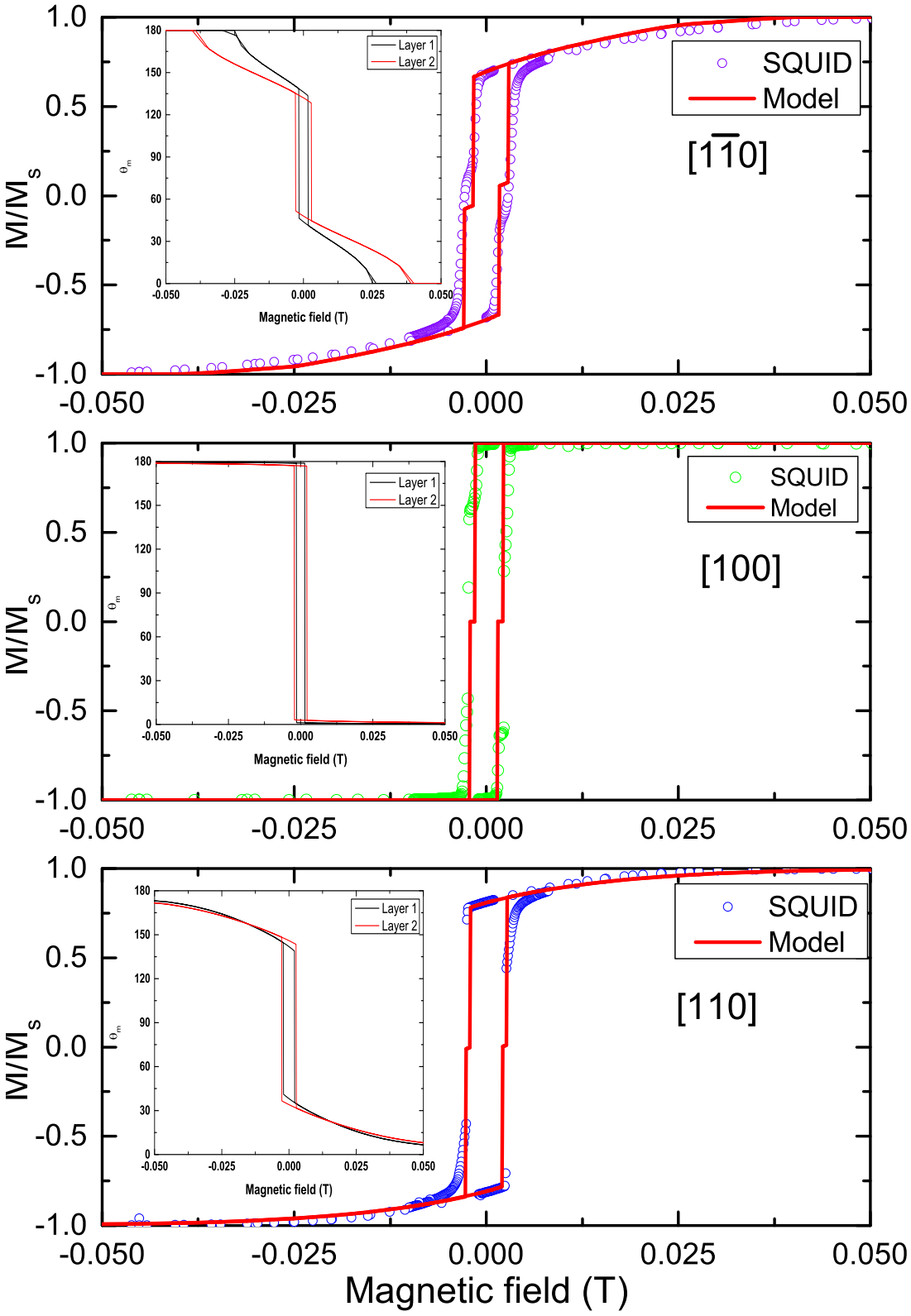

Figure 3.10: MH loop for S420 with the modelled (solid red line) and experimental data (scattered hollow points). The inset shows the angle of magnetisation for each layer as the magnetic field is varied. The modelling of the SQUID data was used to determine the E_{DW} and check the consistency of the parameters extracted from FMR.

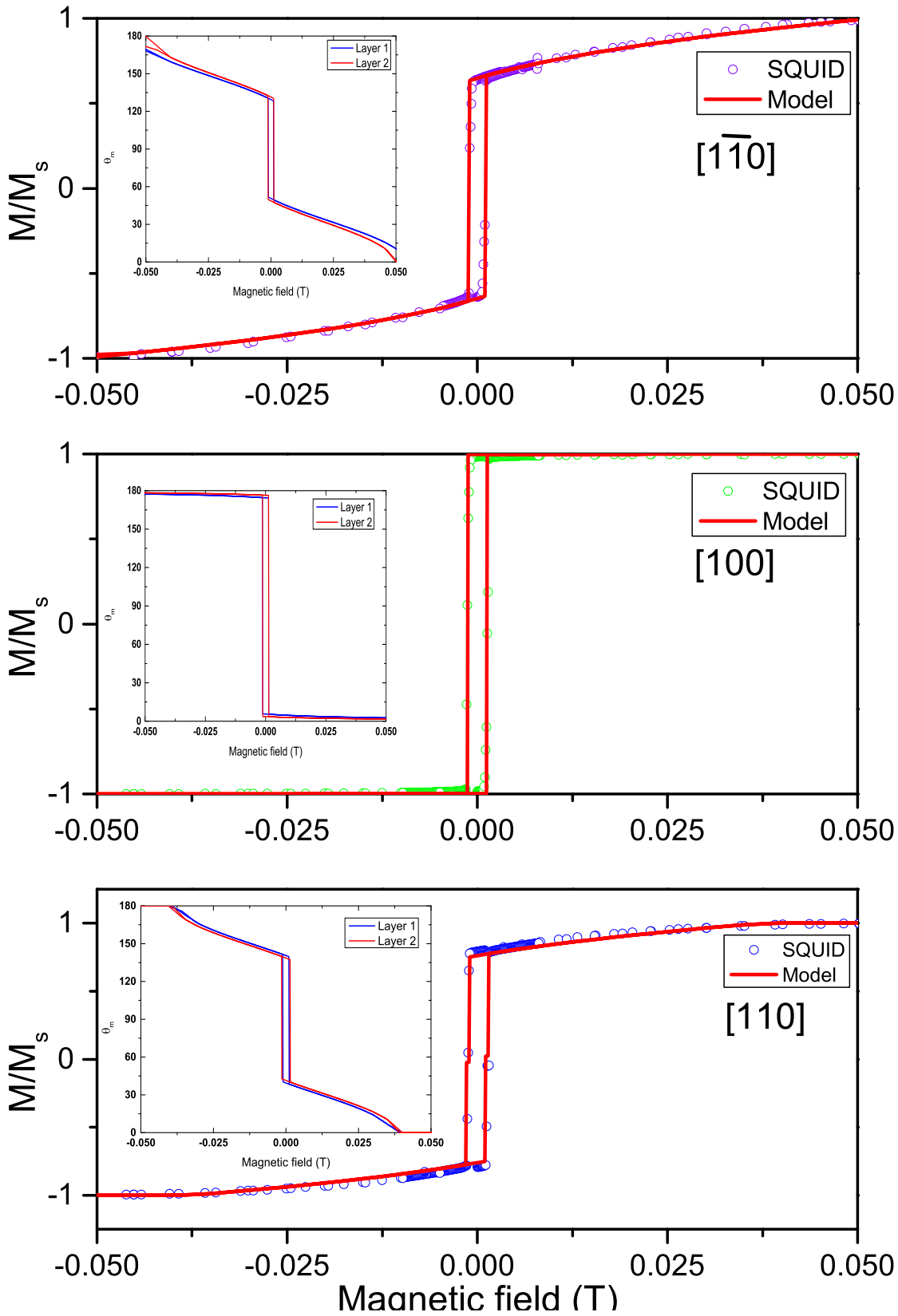

Figure 3.11: MH loop for S421 with the modelled (solid red line) and experimental data (scattered hollow points). The inset shows the angle of magnetisation for each layer as the magnetic field is varied. The modelling of the SQUID data was used to determine the E_{DW}.

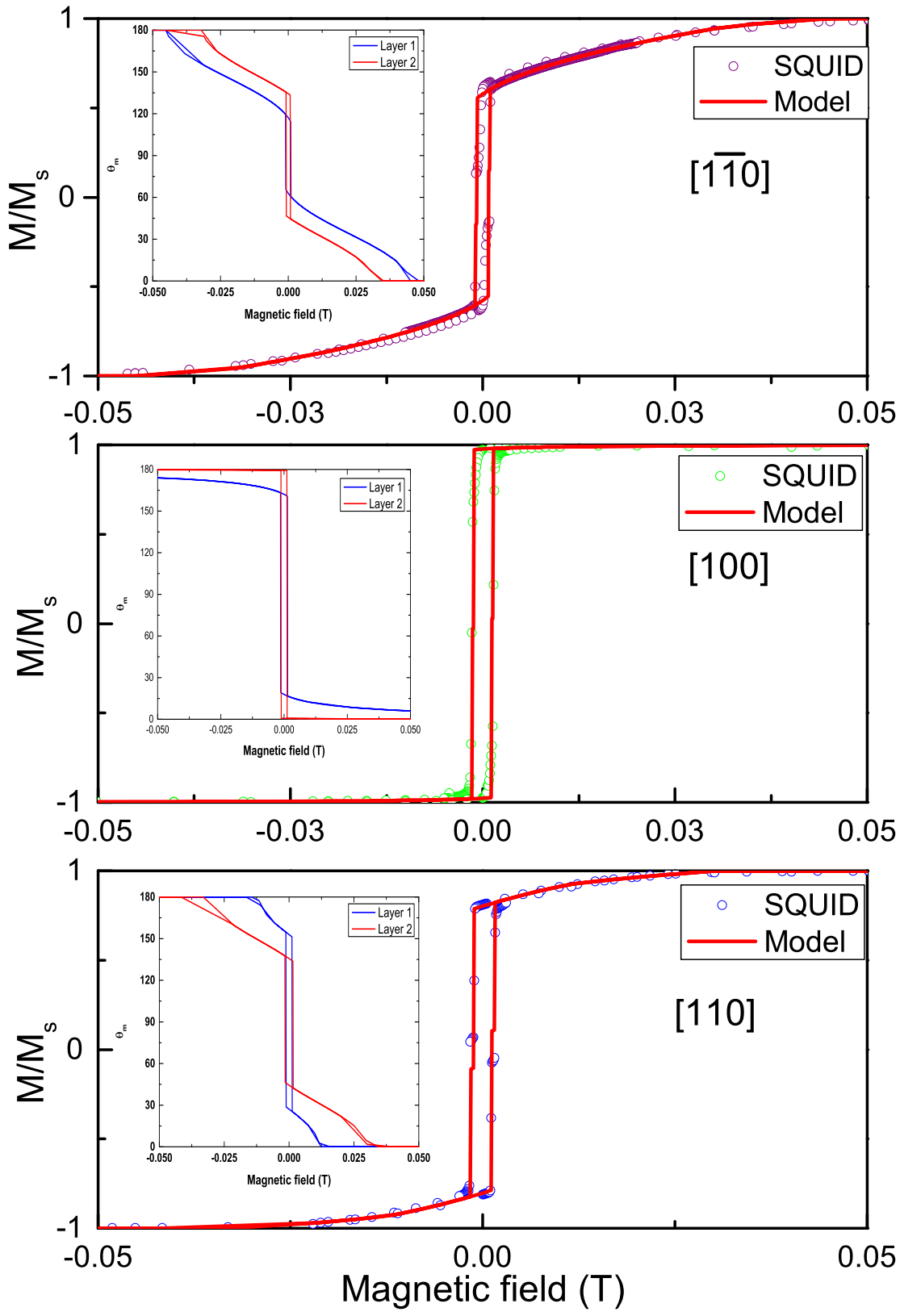

Figure 3.12: MH loop for S422 with the modelled (solid red line) and experimental data (scattered hollow points). The inset shows the angle of magnetisation for each layer as the magnetic field is varied. The modelling of the SQUID data was used to determine the E_{DW}.

From the modelled MH loops and the corresponding angles of magnetisation of each layer shown in inset the magnetisation reversal behaviour can be described. For the [100] directions the sudden change in measured longitudinal magnetisation is due to the 180°switch when the field changes sign and happens at nearly same field strengths for both the layers. For the hard axes, as the field is reduced (i) the magnetisation coherently rotates towards the easy [100] direction then (ii) switches by 90° and (iii) continues coherently rotating towards the field direction along the hard axes.

Sample	Bottom layer (Jm^{-3})	Top layer (Jm^{-3})
S419	6100 ± 1200	9500 ± 3200
S420	4500 ± 1900	5700 ± 4100
S421	3600 ± 100	3700 ± 1000
S422	3300 ± 1200	3300 ± 1100

(a) [100] direction

Sample	Bottom layer (Jm^{-3})	Top layer (Jm^{-3})
S419	5500 ± 2000	10000 ± 7000
S420	4900 ± 1200	5800 ± 2500
S421	2300 ± 1300	3200 ± 1500
S422	2600 ± 2200	3350 ± 2000

(b) [110] direction

Sample	Bottom layer (Jm^{-3})	Top layer (Jm^{-3})
S419	5400 ± 3600	10000 ± 5600
S420	3600 ± 1600	5100 ± 2500
S421	2000 ± 400	2200 ± 1100
S422	1100 ± 600	1500 ± 900

(c) [$1\bar{1}0$] direction

Table 3.7: E_{DW} values for the investigated samples along different field directions.

The values of domain wall energy extracted from fitting to the MvH loops are summarised in Table 3.7. It is observed that these values of the domain wall pinning energies depend on the directions of the applied field and are consistently lower for the bottom layer compared to the top layer. Qualitatively this might be because of different pinning effect for the FeGa/GaAs interface and the FeGa/spacer interface causing distinct domain wall formation. The Cu spacer samples exhibit weak values of E_{DW} compared to the Al spacer samples and are in rough agreement with the previous values of about $\sim 3000\ Jm^{-3}$ reported in Ref. [68, 100]. The high values for the Al spacer can be due to the interface effects but no substantial evidence can be concluded at this point.

3.4 HR-TEM imaging study for sample morphology

To resolve the interface quality and crystallinity, High Resolution (HR) TEM was used to investigate the 5 nm thick spacer samples: S419 and S421. The measurements were performed by Dr. Jan Michalicka, Dr. Ondřej Man, and Dr. Martin Veis at CEITEC Brno University of Technology, Czech Republic.

The HR-TEM image for the sample S419 and S421 are shown in Fig. 3.13 and Fig. 3.14 respectively along with the degree of crystallinity for the individual layers. The samples were grown with an extra layer of Pt for preparation for the HR-TEM. This step is performed in order to protect the magnetic surface from incurring FIB induced damage.

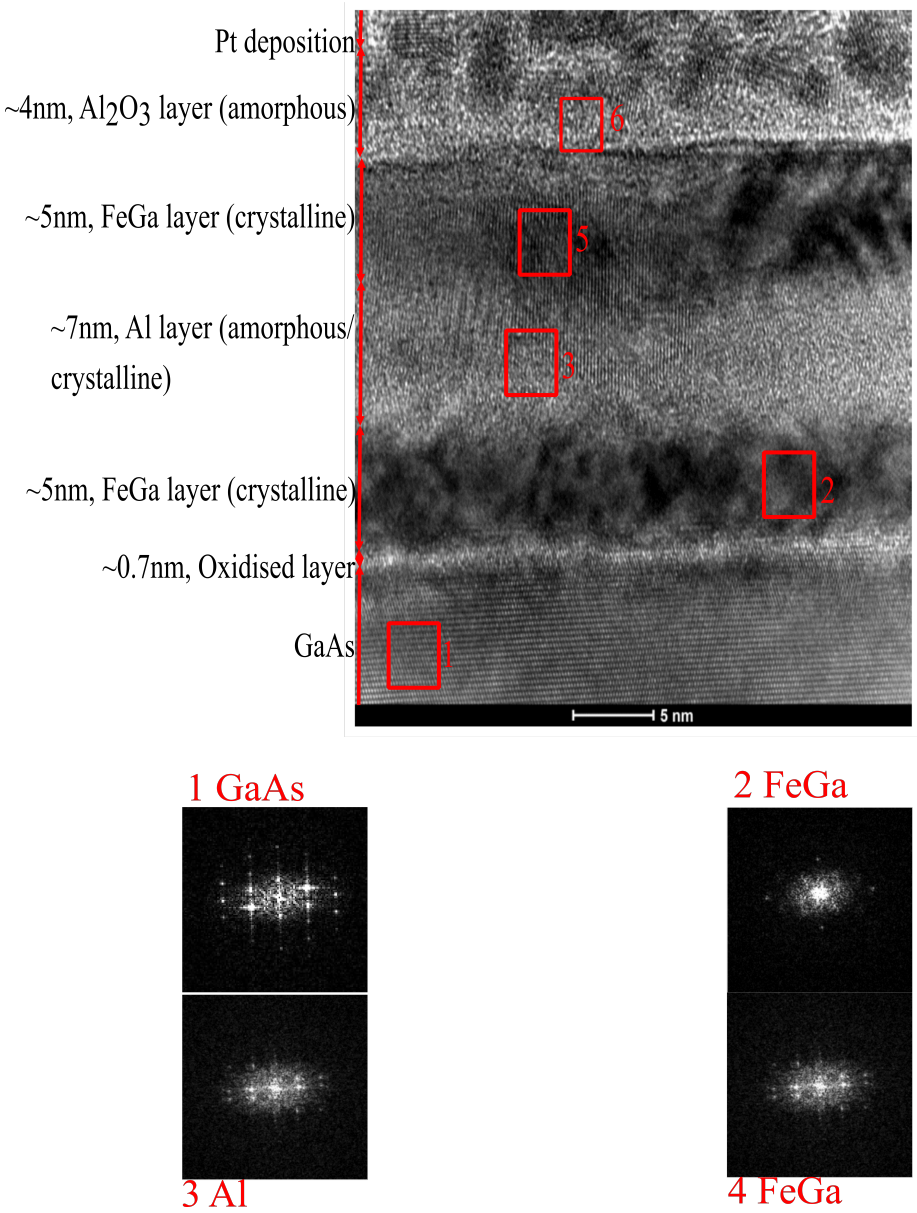

Figure 3.13: HR-TEM image of sample S419 (top) along with the diffraction pattern of each layer (bottom). The labelled layers have been shown as red rectangles in the TEM image.

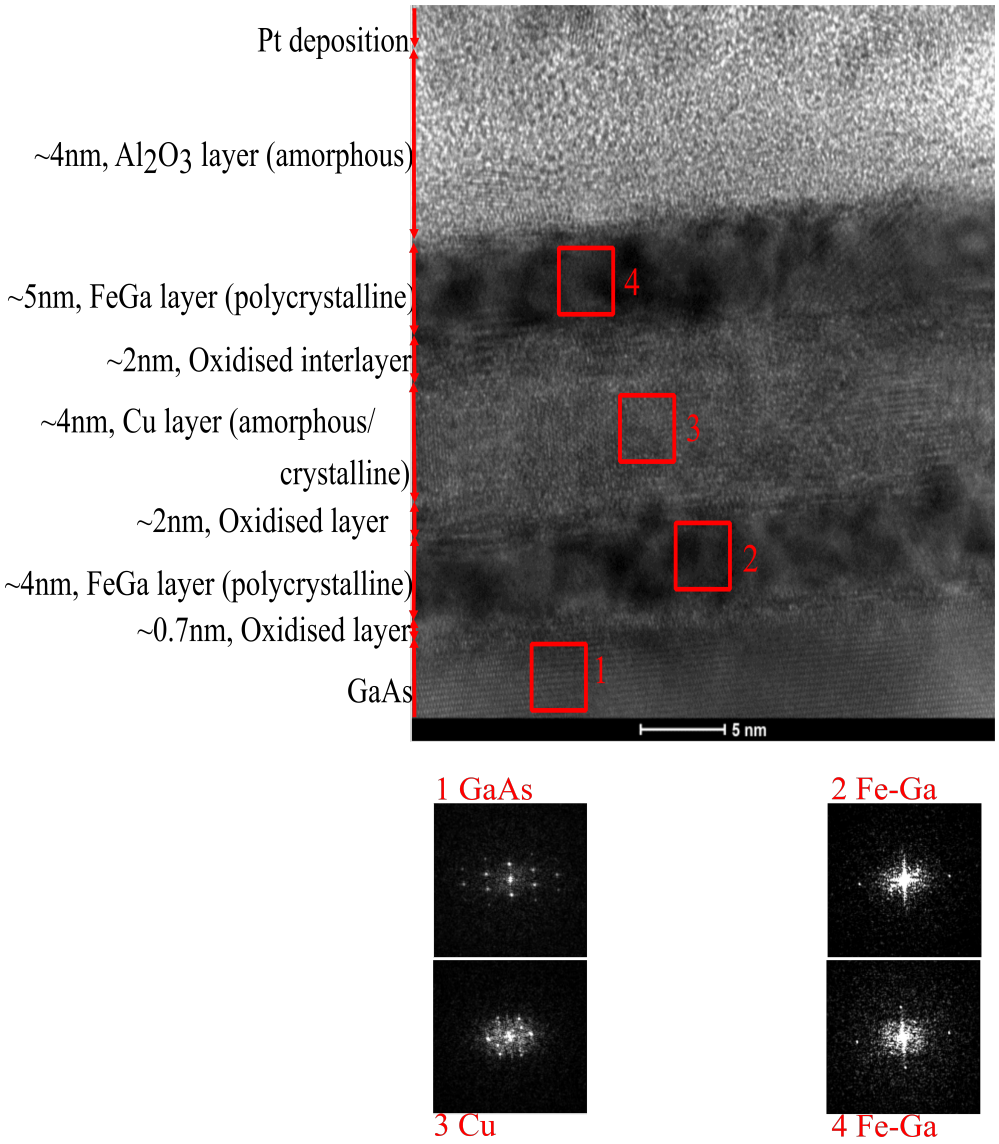

Figure 3.14: HR-TEM image of sample S421 (top) along with the diffraction pattern of each layer (bottom). The labelled layers have been shown as red rectangles in the TEM image.

From the HR-TEM images along with the diffraction pattern for each layer, an observation about the layer morphologies can be performed. It is seen that the degree of crystalline order of the studied samples are distinct to one another. For the Al spacer sample S419, both the $Fe_{1-x}Ga_x$ layers including the spacer layer produce a diffraction image that comprise a pattern of dots at periodic interval, implying the crystalline order of these layers. However, for the Cu spacer sample S421, the generated diffraction pattern for each layer are series of diffusive rings which overlap the spots. Such a pattern can be linked to polycrystalline layers.

It is also seen that for the sample S419, the thickness of the $Fe_{1-x}Ga_x$ are accurate to the grown parameter value of 5 nm each. However the thickness of the spacer is about 7 nm compared to the expected 5 nm. There are also evidence of intermixing between Al and $Fe_{1-x}Ga_x$ of the top layer. For the Cu spacer sample S421, there is no spacer layer-$Fe_{1-x}Ga_x$ layers inter-mixing. The spacer layer has been found to be thinner than the Al sample with an oxidised interlayer. The oxidation of the layers can be attributed to the contamination in the sputter chamber.

It has been known that Ga content along with the crystal morphology and impurities affect the magnetostriction of $Fe_{1-x}Ga_x$layers [64, 81, 84, 188]. As previously discussed in chapter 1, nano-clusters within the bcc lattice structure which distort the crystal into an intermediate tetragonal phase (DO_{22}) are the origin of the enhanced magnetostriction in $Fe_{1-x}Ga_x$. The HR-TEM images are necessary as they indicate that the magnetostriction coefficients in the Al spacer samples will definitely differ from the Cu counterpart due to the crystal morphology and Al intermixing. The effect of the spacer thickness and intermixing will also affect the magnetostriction value along with the spin diffusion length. This is further investigated in Ch. 4 when strain induced magnetisation reversal processes are studied. At this point of the thesis, it is difficult to say which layers are useful for strain dependent magnetisation reversal, whether the crystalline layers or the polycrystalline layers.

3.5 Summary

In summary, the static, dynamic, and structural properties of the sputter grown $Fe_{1-x}Ga_x$ multilayer films on GaAs (001) with Al and Cu spacers were investigated by SQUID magnetometry, FMR and by HR-TEM technique. SQUID and FMR consistently yield values of the magnetisation, the anisotropy constants and domain wall pinning energies for each of the FeGa layers in each sample. The films exhibit a strong cubic anisotropy field and a relatively weaker uniaxial anisotropy term favouring the magnetisation to lie close to the [010]/[100] crystal directions as confirmed by the SQUID MH loops. By comparing the saturation magnetisation for each layer with the net saturation magnetisation measured by SQUID, it can be reasonably assumed that the net magnetic moment is the mean of the individual magnetic moments for each layer. The MvH loops obtained by SQUID magnetometry are consistent with the modelled hysteresis loops using the

anisotropy constants obtained from the FMR measurements.The values of the extracted anisotropy constants are of the same order of magnitude as values obtained previously for thin Fe layers deposited epitaxially onto GaAs, and for MBE grown $Fe_{1-x}Ga_x$ layers on GaAs. It is observed that the uniaxial anisotropy value of the bottom layer is consistently higher than the top layer which is attributed to the interface bonds between the substrate and the ferromagnet. The uniaxial anisotropy term decreases as the thickness of the spacer layer is increased. There is also a dependence of the E_{DW} energy term to the sample's spacer type. The Cu spacer samples exhibit lower values of E_{DW} compared to the Al spacer samples. This may be due to different domain wall pinning energies due to the crystal structure which was investigated by HR-TEM and revealed that the layers were crystalline for the Al spacer sample, while they were polycrystalline for the Cu spacer sample.

All the samples show a narrow linewidth and low Gilbert damping value which makes them an interesting candidate in the applications of microwave spintronic devices with high tunability and power consumption demands. The Gilbert damping values are in close agreement to the previous values of 0.012 to 0.017 (see Ref.[101, 102]), and the values are influenced by the Ga content.

High resolution-TEM imaging was used to realise the layers interfacial morphology and crystal structure. It was observed that the for the Al spacer samples, both the $Fe_{1-x}Ga_x$ layers demonstrated to be crystalline, with intermixing between the Al spacer and the top layer. For the Cu spacer sample, the spacer was found to be thinner than the Al spacer, and the $Fe_{1-x}Ga_x$ layers were polycrystalline in nature with no interfacial intermixing. These crystalline, along with impurity due to mixing affect the magnetostriction coefficients of each layer and the different samples. It has been reported that crystalline samples have enhanced magnetostriction value in the order of $1.6 \times 10^{-7} Jm^{-3}$[189], while polycrystalline $Fe_{1-x}Ga_x$ have weaker magnetostriction value in the order $0.3 \times 10^{-7} Jm^{-3}$[188].

With all the magnetisation parameters, and structural properties investigated in this chapter, these will be used to in the investigations of the effect of strain on the magnetisation reversal process in the next chapter.

Chapter 4

The effects of strain on magnetisation reversal in $Fe_{1-x}Ga_x$ bilayer films

4.1 Introduction

The ability to change the magnetisation of a magnetic material by applying an electric field has been a a topic of interest for designing multi-functional devices mainly for energy efficient data storage and logical processing units. These devices can be realised by designing hybrid structures comprising ferromagnetic films with a high magnetostriction value (Sec. 1.2.2) combined with piezoelectric layers which can generate a strain when a voltage is applied. In these devices, the magnetisation reversal behaviour can be manipulated by applying a voltage induced strain, instead of external magnetic field or electric currents, thereby removing the energy loss due to Joule heating. Also the ability to change the magnetisation by only strain substitutes the need to apply any electrical current and magnetic field resulting in designing smaller and more compact units which scales down the design architecture leading to room for packing more devices. Ferromagnetic films of $Fe_{1-x}Ga_x$ which have a very high magnetostriction coefficient [190] have previously been shown to be very sensitive to strain [68, 100] and manipulation of the magnetisation has been reported by the Spintronics group in Nottingham [68, 99–101, 189] for single layer films.

This chapter investigates the strain mediated modification of the magnetisation reversal in sputter grown bilayer films of $Fe_{1-x}Ga_x$ which were discussed in the last

chapter. The magnetic anisotropy values, saturation magnetisation, and E_{DW} that were calculated from the ferromagnetic resonance experiments and SQUID magnetometry on unstrained layers will be used to understand the magnetisation reversal of the individual magnetic layers for strained samples . The investigations so far have revealed that the layers have different composition of Fe and following Ref.[64] it is reasonable to accept that the bottom layer is more sensitive to strain. This is due to the Ga concentration being closer to that required for the peak in magnetostriction (19%) and also due to its proximity to the strain produced by the piezoelectric transducer itself. A benefit of this kind of multilayer structure is that we can obtain and realise distinctive and independent magnetisation reversal processes in the individual films which can be detected in magnetotransport via the GMR and AMR effects. The cubic magnetocrystalline anisotropy of the layers leads to stable easy axes in each layer which are orthogonal, allowing the possibility to use the structures as multilevel memory elements where the extra spatial dimension improves the storage density.

It is not possible to obtain the absolute value of strain in the devices because a uniaxial strain of order a few 10^{-4} is induced during the device fabrication process, when the epoxy glue cures. A relative magnitude of strain can be calculated using the steps described in Sec.2.2.4 and have been presented in the Appendix B for all the investigated samples. The calculated strains are centred about zero at zero volts on the transducer. These values do not necessarily denote the actual value experienced by the layers and can differ as we will see when we discuss the experiments in the forthcoming sections of this chapter.

The role of strain to manipulate the magnetisation has been investigated by performing magneto-optical and magnetotransport measurements on the bilayer samples. The optical measurements mainly probe the top layer of the hybrid structure owing to the penetration depth limitation of the laser, while the magnetotransport measurements probe the entire structure. By comparing the data from both these techniques, the magnetisation reversal features and processes in each of the the $Fe_{1-x}Ga_x$ layers can be identified.

The schematic of the device used to perform the magneto-optical and magnetotransport measurement is shown in Fig. 4.1. The device has a cross structure with dimensions previously discussed in Sec.2.2. The device was bonded to a piezoelectric transducer using epoxy glue such that a uniaxial strain is along the [010]/[100] crystal axis. For magnetotransport measurements a 1 mA current was passed along the [110] direction while the magnetic field was varied between ± 0.04 T along dif-

ferent in-plane crystal directions and corresponding longitudinal and transverse voltages were measured. For the MOKE measurements the laser beam of spot size about 50 μm was focussed on the central region of the device and the reflected light was measured by the longitudinal MOKE set-up discussed in Sec. 2.3.1.

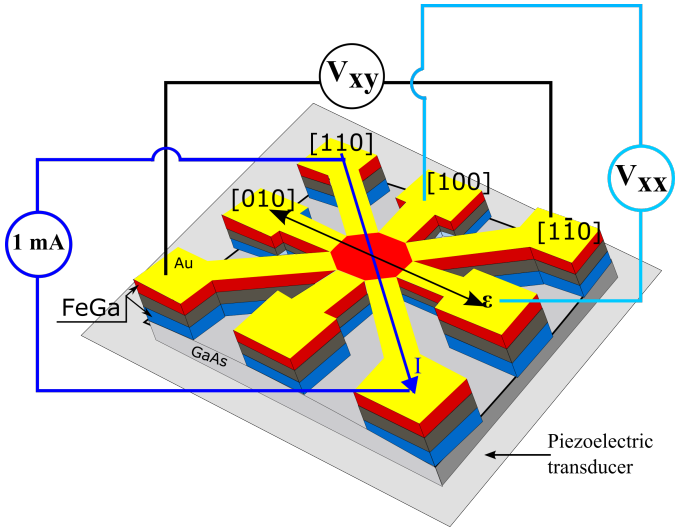

Figure 4.1: Schematic of the device used for magnetotransport and magneto-optical measurements. The samples are grown on GaAs substrates from which devices are processed and then bonded to the piezoelectric transducer using epoxy resin.A DC current of magnitude 1mA was passed along the [110] direction with strain along the [100]/[010] direction. Magnetic field was then varied along different directions with respect to the current direction. For magneto-optical measurements the laser spot was focused on the central region of the cross-structure.

4.2 Magnetotransport and magneto-optical study of strained samples

In this section the magnetotransport and magneto-optical studies performed on the bilayer samples are discussed. By using the magnetisation parameters calculated in Ch.3 the magnetisation processes in each bilayer samples have been simulated which aids in the understanding of the experimental observations. The section is divided into three broad subsections. The first section describes the results for the 5 nm thick spacer layer samples and the second section discusses the results for the 10 nm thick spacer layer samples. Each subsection then discusses the Cu spacer and Al spacer samples of relevant thickness. The third section comparatively discusses the effect of voltage induced strain to alter the magnetic switching fields

for each sample. This section gives a comprehensive comparison of the strain to alter the magnetisation reversal processes when magnetic field is applied along different directions.

The discussion begins with a broad discussion on the 5 nm Cu spacer sample. This sample has been extensively studied as it demonstrated appreciable change in magnetisation reversal process for each layer at different values of strain, along with a big GMR value. The understanding gained from investigating this sample is used to investigate the magnetisation process for the 5 nm Al spacer sample. This sample demonstrated large modification to magnetisation due to strain, however the contribution of each layer could only be understood at a qualitative level from the simulations which were derived from the previous sample because I did not have a reliable measurement of the strain versus voltage characteristics for this sample. The 10 nm samples were similarly qualitatively understood by comparing them with the the 5 nm spacer samples to get a complete understanding of the strain mediated modification to the magnetisation reversal processes in each layer of the investigated bilayer samples. The poor signal to noise ratio for the samples with 10nm spacers made quantitative analysis difficult.

4.2.1 5 nm spacer samples

This section will describe the optical and transport measurements performed on the 5 nm thick spacer samples: S421, and S419 along different in-plane crystal directions. The role of the spacer for the strain mediated magnetisation reversal will be discussed in this section.

4.2.1.1 Sample S421: 5 nm Cu spacer

(i) Magnetic field along easy axis directions

The transverse and longitudinal resistances for the samples are presented in Fig. 4.2 for field applied along the [010] and the [100] crystal axes at voltage values of -30 V and +30 V across the transducer. The transverse resistance plots look very similar to those observed by Parkes et al[99], where he observed large changes in the transverse resistance as the magnetisation switched between the [010]/[100] directions.

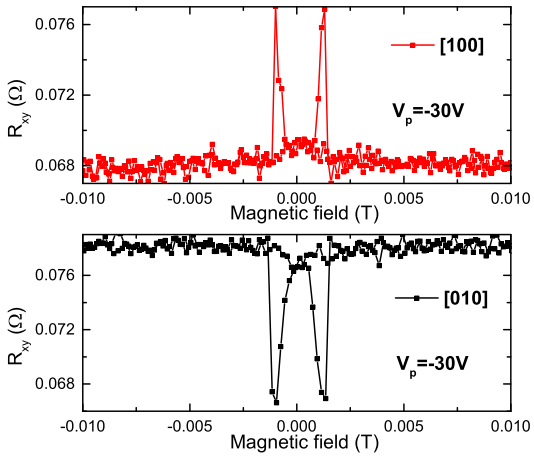

(a) Transverse resistance at -30 V

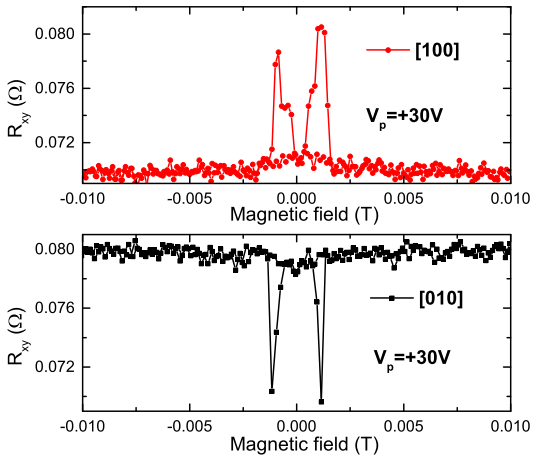

(b) Transverse resistance at +30 V

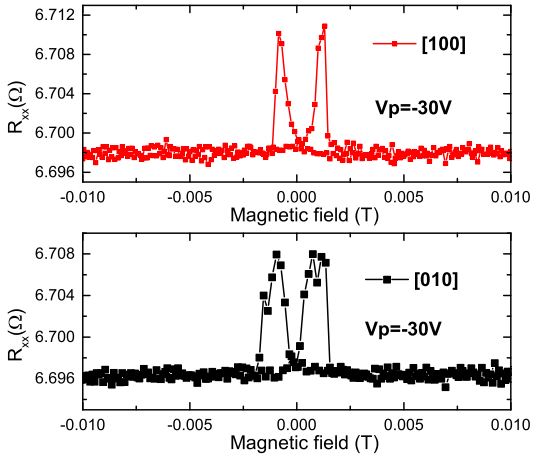

(c) Longitudinal resistance at -30 V

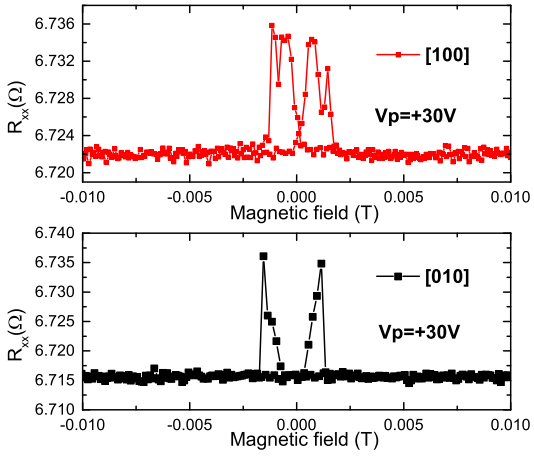

(d) Longitudinal resistance at +30 V

Figure 4.2: Transverse and longitudinal magnetoresistance for the [010] and [100] direction at -30V and +30V across the transducer for sample S421.

The large change in resistance observed in both the transverse and longitudinal resistance indicate the switching of the magnetisation and are very similar to the reported measurements of transverse resistance during magnetisation switching by Parkes et al.[99] and Bowe [100] who observed this large change in resistance due to the 90° switch of magnetisation between the [010]/[100] crystal directions. Their findings stated that if there was a tensile or a compressive strain then the easy axis was manipulated and the magnetisation reversal process for the tensile (+30 V) and compressive (-30 V) were different. For magnetic field swept along the [010]

direction they observed a large change in resistance depicting the 90° switch at tensile strain values and no change in measured resistance for compressive strain values. The opposite dependence on strain was observed for field along the [100] direction, with large change in transverse resistance at compressive strain values and no change for tensile strain values.

However in our measurements it is observed that this large resistance change is observed for both −30 V and +30 V. Even for 5V across the transducer which corresponds to zero strain by the strain calibration method followed in this thesis. (See Appendix B for the plot showing the variation) the transverse resistance shows a large change in resistance at the switching fields. The transverse resistance at approximately zero strain for the [010] and [100] directions are shown in Fig. 4.3 along with the transverse resistances at a series of piezoelectric voltages. The variation of the switching fields with the piezoelectric voltage have also been shown in Fig. 4.4 for both the applied field directions. The magnitude of the variation has been discussed in Sec. 4.2.3.

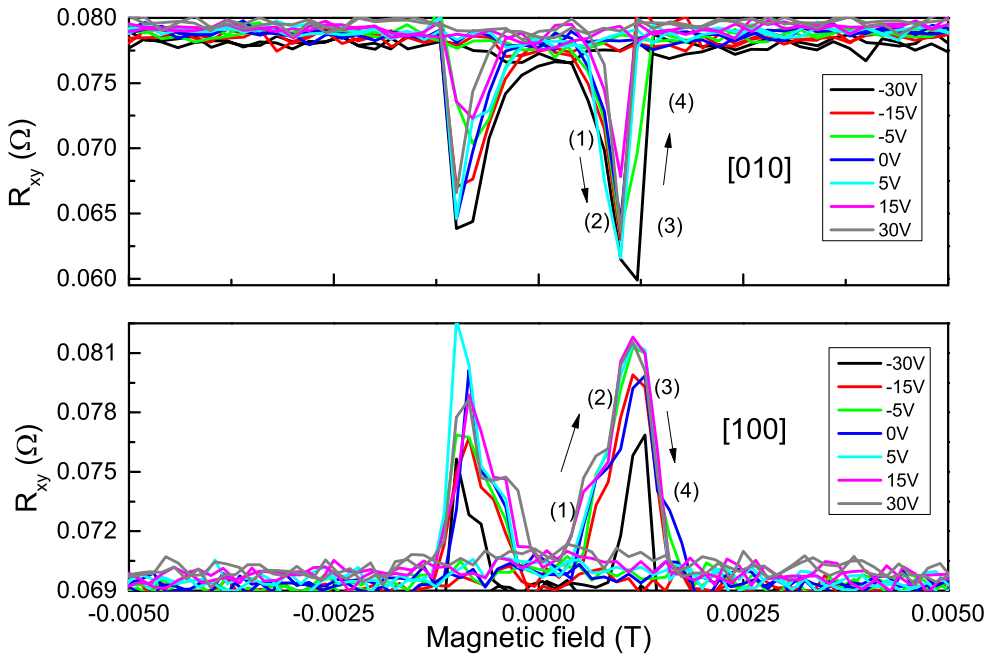

Figure 4.3: Measured transverse resistance for sample S421 for the [010] and [100] directions at different values of piezoelectric voltages. The large change in resistance for all voltages indicate that the measured strain values are not absolute values but relative values about zero voltage.

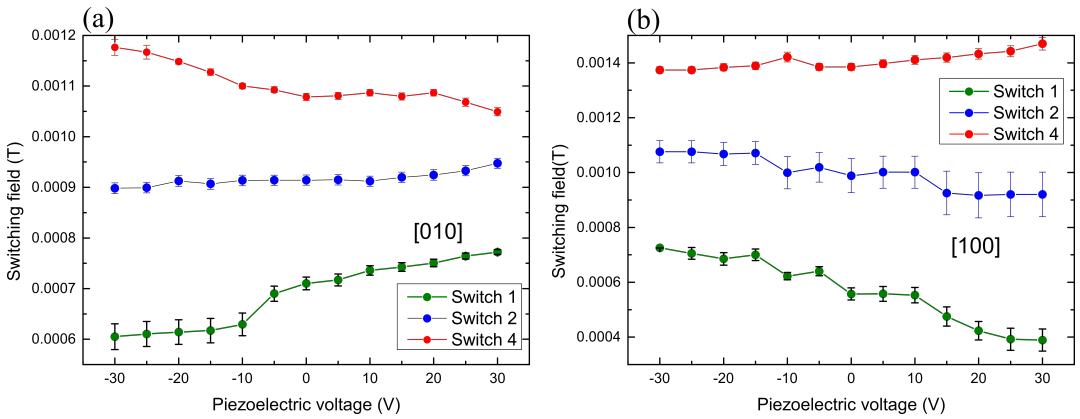

Figure 4.4: Variation of the switching fields for sample S421 when field was applied along the (a) [010], and (b) [100] at different values of piezoelectric voltage.

As can be seen the large resistance change is observed for all piezoelectric voltages.This would indicate that the strain values calculated by measuring the change in resistance gives the relative strain centred about zero and are not the absolute values. For this case it is very difficult to say if it is always tensile in nature or very weak in magnitude. This anomaly in strain values will also explain the magnetisation reversal process which vary from the previously shown SQUID hysteresis loops in Fig. 3.11. For the magnetotransport measurements it is seen that the magnetisation switches by 90° corresponding to the large change in resistance while in the hysteresis loops there is a 180° magnetisation switch at zero strain value. This switch by 90° is only possible when there is an anisotropy along the [100] direction and for this case it is the strain which is always present along this direction. The reason there is always a tensile strain present may be because of the curing process of the epoxy resin which produces an inbuilt strain.

In order to confirm the magnetisation switch by 90° the transverse resistance was modelled and shown in Fig. 4.5 for magnetic field applied along the [010] and the [100] directions. The modelling was done using the anisotropy and saturation values obtained in the previous chapter and performing a least sum of squares fitting at the switching region with strain(ϵ) and the magnetoelastic constant (B) as free parameters. The model only gives a qualitative picture of the magnetisation reversal but does not allow the extraction of the magnetoelastic constants because the absolute value of the strain is not known.. The method of extraction of the value of the magnetoelastic constants will be discussed later in the section by using the gradients of the switching fields with respect to the relative strain.

Fig. 4.5 is provided to show that the model produces the qualitative features

that are observed in the measured transport data. In the plot the blue modelled line represents the transverse resistance when magnetic field is swept from lower saturating value to a positive value and the red represents the sweeping of the magnetic field from the higher saturation field to a lower field value. The labels (1) to (4) denote the magnetisation switching process from one direction to another as the magnetic field changes sign, with labels (1) and (3) for one layer and (2) and (4) for the other layer. As the magnetic field is swept through zero, due to tensile strain along the [100] direction the magnetisation orientation switches by 90° instead of 180°. This magnetisation rotation by 90° is manifested as a large change in the transverse resistance.

The sign of the resistance change due to the AMR is opposite for field sweep along the [010] and the [100] direction. This is because transverse resistance is a $sin(2\theta)$ function where θ is the angle between the magnetisation from the [010] and the direction of current.

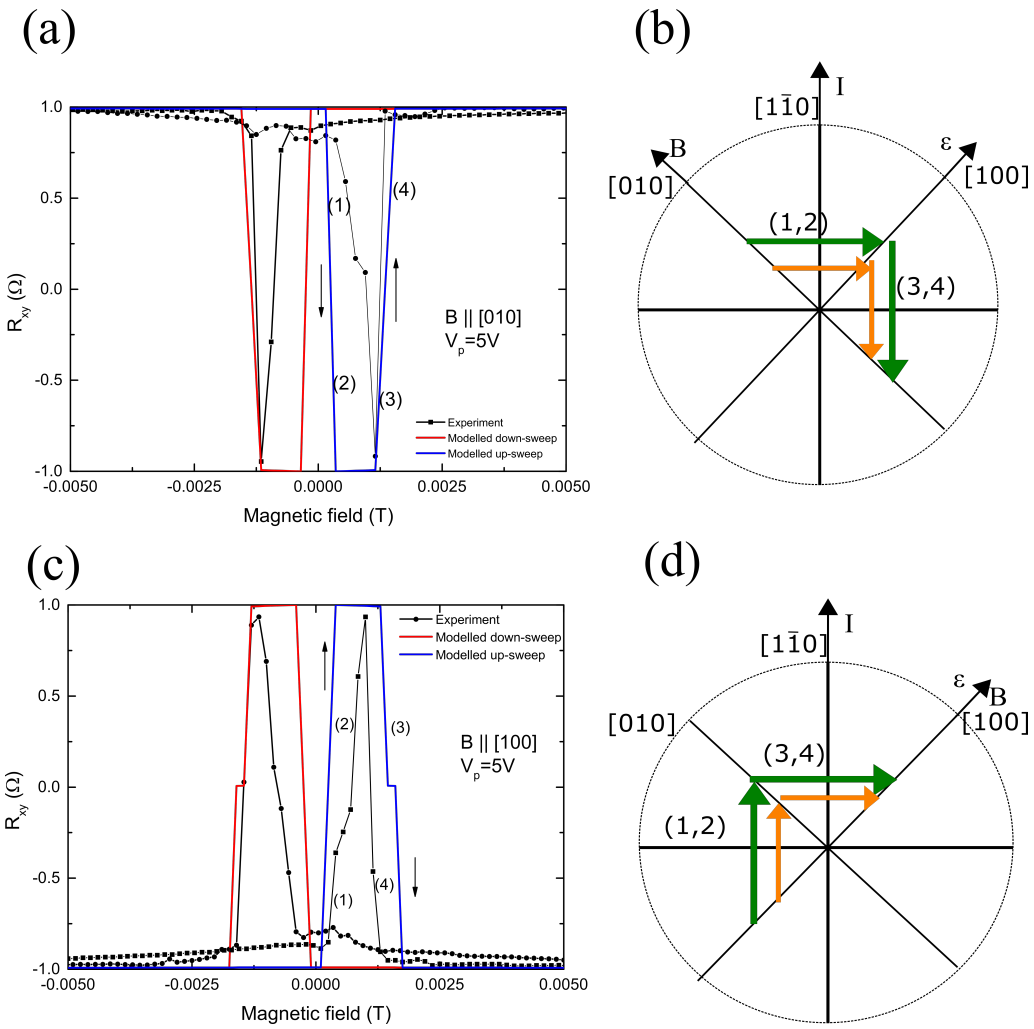

Figure 4.5: Modelled (red and blue lines) and experimental (black lines) normalised transverse resistance for sample S421, with magnetic field applied along the [010] and [100] directions at +5V. The large changes in transverse resistance correspond to a magnetisation switch between the [010]/[100] directions as shown by the adjacent schematic representations. The arrows in the schematic represent the magnetisation switching process for each ferromagnetic layer.

The modelled magnetisation reversal and angles of magnetisation are necessary to explain the large change in resistance in the longitudinal resistance, and also understand the magnetisation reversal of each individual layer when the field is varied. The large change in transverse resistance is accounted for the magnetisation switching between the [010]/[100] easy directions for each layer , and this 90° switch should show no change in the longitudinal resistance schematically shown in Fig. 4.6. However the measured R_{xx} at +5V for the two applied field directions (Fig. 4.7) shows a large change in the resistance of the same order of magnitude and very

similar to the transverse resistance along with features marked by green arrows.

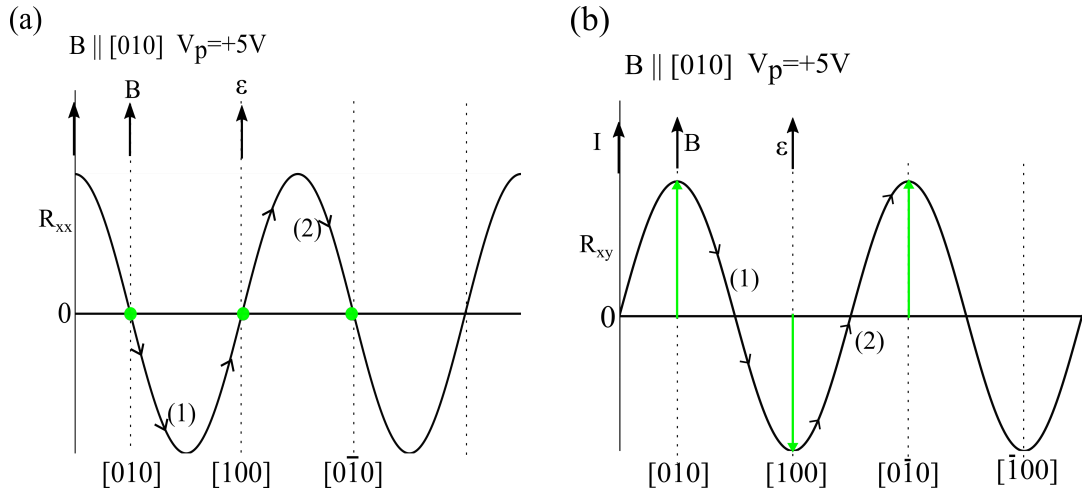

Figure 4.6: Schematic of the variation of the (a) Longitudinal resistance, (b) Transverse resistance due to AMR when field is swept along the [010] and current is along the [1$\bar{1}$0] direction. The green circle and arrow represents the orientation of the magnetisation with respect to the current along the [110] direction. The magnetisation reversal process is represented by the arrows on the curve.

The large change in the longitudinal resistance can be attributed to the independent switching of the magnetisation of the two layers. Independent switching of the magnetisation are very likely to occur since the layers have different values of the magnetocrytalline anisotropies and saturation magnetisation, along with distinct E_{DW} values and magnetostriction coefficients. Due to this independent switching there is a relative angle difference between the magnetisations when they undergo the switches labelled (1) and (3) for layer 1 and switches (2) and (4) for the other layer. This manifests as a GMR contribution to the longitudinal resistance leading to features marked by green arrows in the measured longitudinal resistance shown in Fig. 4.7. This can be explained and verified by comparing the modelled MH loop with the normalised MOKE loop for the two directions as shown in Fig. 4.8 (a) and (b).

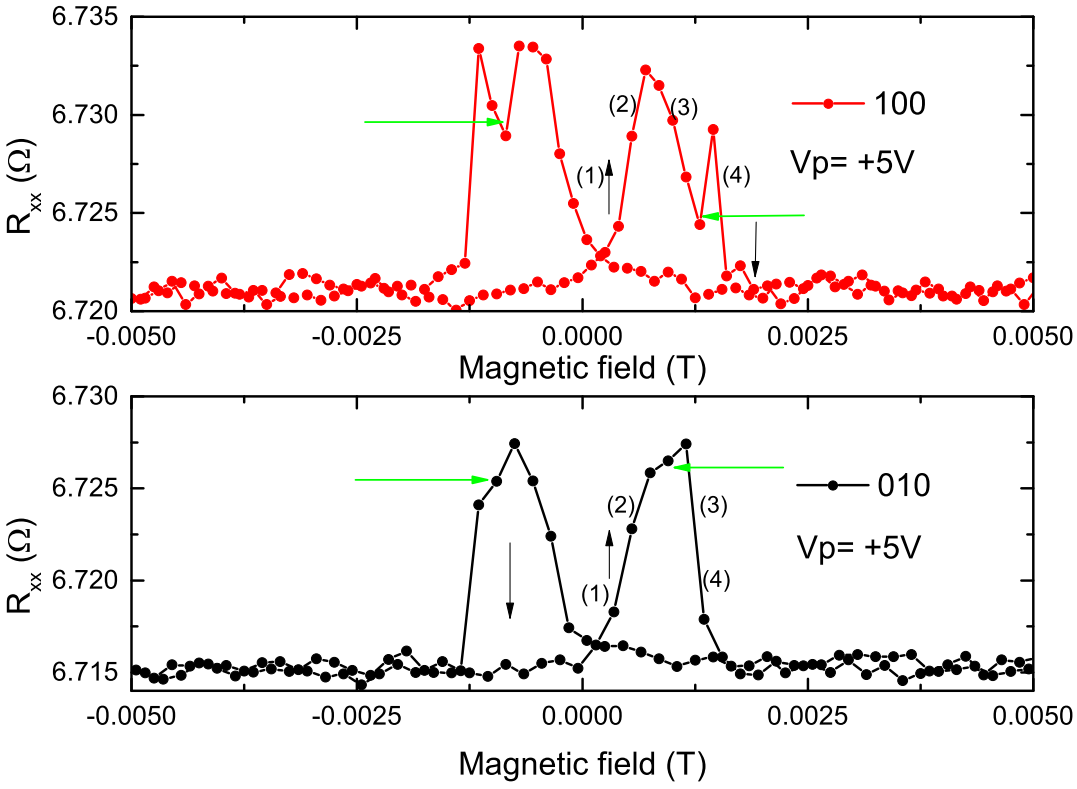

Figure 4.7: Longitudinal resistance for magnetic field applied along the [010] and [100] directions at +5 volts across the transducer for sample S421.

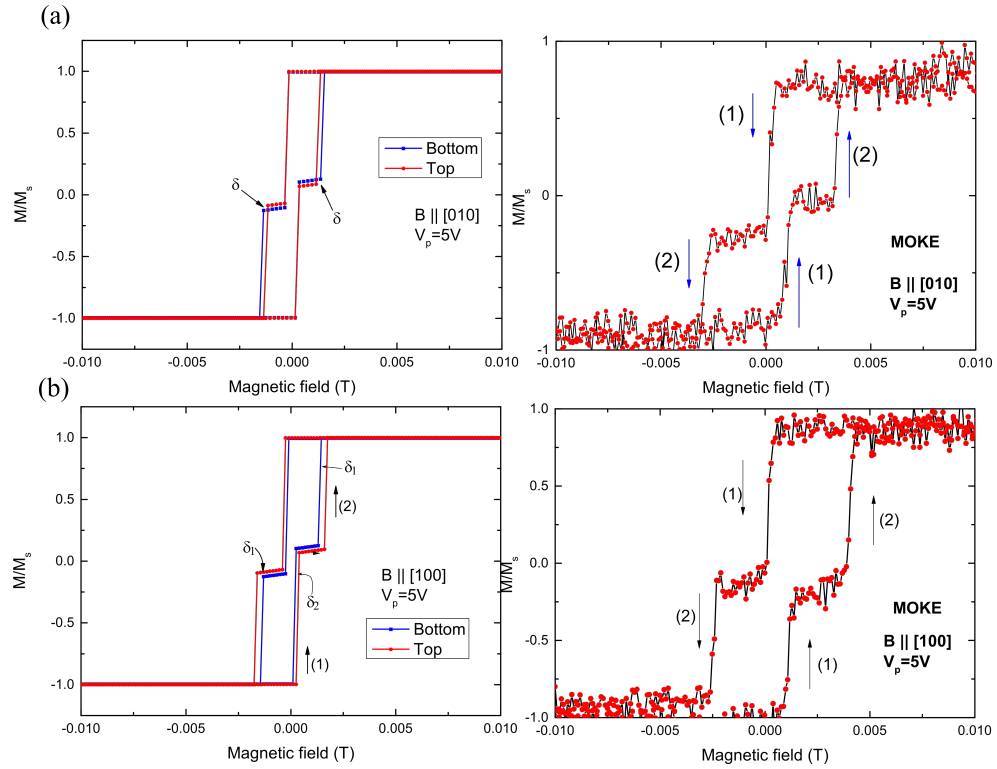

Figure 4.8: Modelled MH loop for sample S421 from transverse resistance and MOKE MH hysteresis loops for field along the (a) [010] direction, and (b) [100] direction.

The MOKE MH loops probe mainly the top layer of the structure due to the laser's penetration depth limitation of approximately 10 nm (Appendix A). The small difference in switching field between the MOKE, modelled and the transport data could be because of localised heating due to the laser. With this assumption, the MOKE MH loops are in reasonable agreement with the modelled loop for the top layer and show a double step jump corresponding to the 90° switch instead of a single switch as was seen in the SQUID MH loop (see Fig. 3.7). The MOKE gives a qualitative measurement of the magnetisation reversal process.

Looking at the modelled MH loops the feature labelled δ indicates the field at which there is a difference in the angle of the magnetisation of the layers. For magnetic field applied along the [010] direction, the top layer switches away from the [100] before the bottom layer , and over that small field range the magnetisations in the two layers are orthogonal to each other. This manifests as a GMR peak. Assuming the amplitude of the GMR is approximately the same as AMR, it is reflected as a large change in resistance of the same order as R_{xy} in the longitudinal resistance.

The [100] direction shows a similar large change in longitudinal resistance which can be accounted for by the same mechanism. However the experiment showed two peaks in the longitudinal resistance. This is very well represented in the model as well where there are two instances of δ : δ_1 and δ_2 for every 90° switch. Due to differences in the magnetostriction and the anisotropies the layers switch at different fields resulting in different relative magnetisation orientations which manifests as double peaks in the measured R_{xx}. The reason there are two δ in this configuration can be ascribed to the easy axes becoming more easy due to the uniaxial strain along this direction. Since this strain affects the individual layers differently one of the layer will switch before the other. The double peaks are more prominent at positive value of voltages than the negative voltage values. This should be due to increased tensile strain for positive voltages which influences the independent magnetisation switching of the individual layers. Fig. 4.9 shows the experimental and a qualitative model of the longitudinal resistance. The longitudinal resistance has been normalised as the absolute magnitude of the AMR and GMR coefficient along with the offset resistance is unknown. The switching fields for the experimental data and the modelled data do not match. The reason will be discussed later in the section when the calculation of the magnetoelastic constants are described.

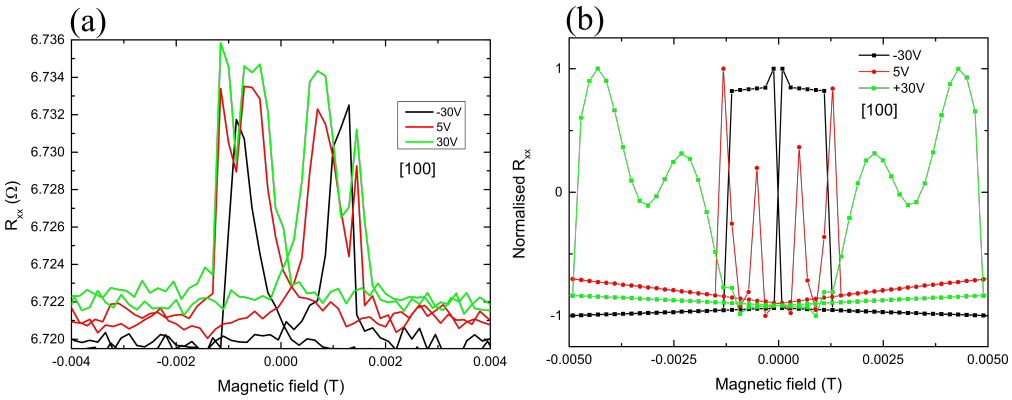

Figure 4.9: (a) Measured and (b) modelled longitudinal resistances at -30 V,+5 V and 0 V for sample S421, when magnetic field is varied along the [100] direction. The variation of the double peak is observed at higher values of positive voltages.

The model qualitatively predicts the independent switching behaviour of the magnetisation for the individual layers at higher tensile values of strain. At lower strain values, the independent switching of the magnetisation is suppressed and the GMR peak which can be attributed to the the double spikes in the longitudinal resistances are small. As the resistance of each layer and the resistance of the

spacer layer has not been considered in the model, the amplitude of the peaks are not similar to the experiment. Due to uncertainty in the strain value in each layer the switching fields do not match to the experiment as well.

(ii) Estimation of the magnetoelastic constants

In this section the estimation of the values of the magnetoelastic constants for the individual $Fe_{1-x}Ga_x$ layers have been performed . As has been shown previously in Fig. 4.3 for field varied along the [010] directions, there are evidences of a step feature in the magnetisation switching process from [010] to [100] direction at different piezoelectric voltages. It has been concluded from the last section that this step features are due to independent magnetisation switching of the layers and are observed as spikes in the measured longitudinal resistances.

In order to estimate the magnetoelastic constant values for each layer the modelling was performed with a starting value of magnetoelastic constants B1=1.5×10^7 Jm^{-3} and B2=$1.6\times10^7 Jm^{-3}$. These values were used as these are the reported values from previous works on single layer Fe-Ga films[68, 100, 189]. By using these magnetoelastic constants, and domain wall de-pinning energy values of 3536 Jm^{-3} and 3736 Jm^{-3} obtained from SQUID magnetometry, the transverse AMR was modelled for a few piezoelectric voltages and shown in Fig. 4.10 below for +5V and +30V.

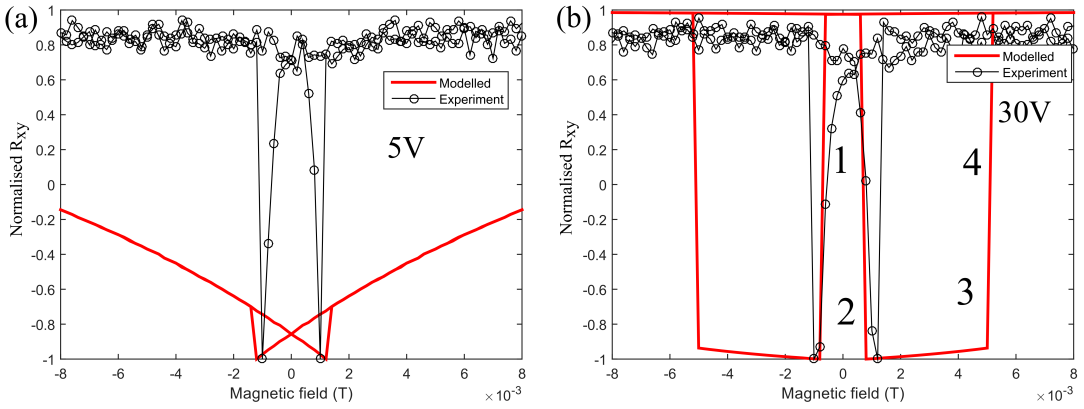

Figure 4.10: Simulated and experimental transverse for sample S421 when magnetic field is varied along the [010] direction at +5V and +30V. The simulation was performed using B1=1.5×10^7 Jm^{-3} and B2=$1.6\times10^7 Jm^{-3}$, and $E_{DW1} = 3536 Jm^{-3}$,$E_{DW2} = 3736 Jm^{-3}$.

It is seen from the figure that the experimental and modelled transverse resist-

ance do not match. At higher value of tensile strain, the magnetisation performs a 90° switch and the model results in a large change of resistance while at lower values of strain the magnetisation doesn't perform a 90° switch and a large resistance is not observed. This is quite useful and the reason for this discrepancy can be classified as below:

(1) The absence in magnetisation switching for the lower voltage value but a 90° switch for +30V shows that the domain wall energies from SQUID are affected by the uniaxial strain.

When the strain is along the [100] easy direction, and the field is varied along [010] direction the magnetisation is oriented along the [010] at higher values of magnetic field. In order to perform a 90° switch towards the [100], the magnetoelastic energy has to overcome the domain wall energy to trigger the switching. For the +30V case the tensile strain is enough to pay for the energy to switch the magnetisation towards the [100], and therefore a large change in resistance is observed in both the experiment and the model.

However at low values of voltage the tensile strain is very low to pull the magnetisation towards the [100] over the domain wall energy barrier. Therefore the model predicts no significantly large change in resistance. But the experiment shows a large change in resistance. To match the model to the experimentally observed large change in resistance, E_{DW} for both the layers was iteratively decreased till a close fit was found. It was observed that at $E_{DW1} = E_{DW2} = 1300\ Jm^{-3}$ the model predicted a large change in resistance and shown in Fig. 4.11.

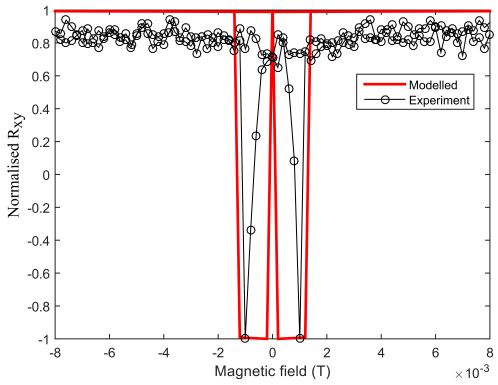

Figure 4.11: Modelled and experimental transverse resistance for field along [010] at +5V for sample S421. For the model to show a large change in resistance due to 90° switch, the domain wall energies was set to 1000 Jm^{-3}.

(2) The magnetoelastic constants values considered for the modelling are high compared to the experimentally investigated sample.

It is also possible that the magnetoelastic constants considered for the modelling are exaggerated values. As can be seen in Fig.4.10 (b) for the +30 V case, the switching fields 3 and 4 which represent the magnetisation switch away from the strain axes direction towards the [010] direction are at higher field values than the experimental switching fields. This can ascribed to the fact that if the magnetoelastic constants are high, the strain anisotropy along the [100] is high and the magnetisation will prefer to be along this direction. In order to cause the magnetisation to switch towards the field direction, a higher field will be required.

This property can be utilised to estimate the measure of the magnetoelastic constants. However it suffers with the limitations like : (a) switch 3 and switch 4 can not be resolved to identify the switching layer, and (b) only limited transducer voltage values to show the switching feature at the measured domain wall energy values. Using the measured strain values of 1.1×10^{-4}, 1.4×10^{-4} and 1.7×10^{-4} for transducer voltages of +20 V, +25 V, and +30 V respectively, and keeping the domain wall energy and magnetoelastic parameters constant the switching fields were estimated and have been shown in Fig. 4.12 along with the experimental switching field values.

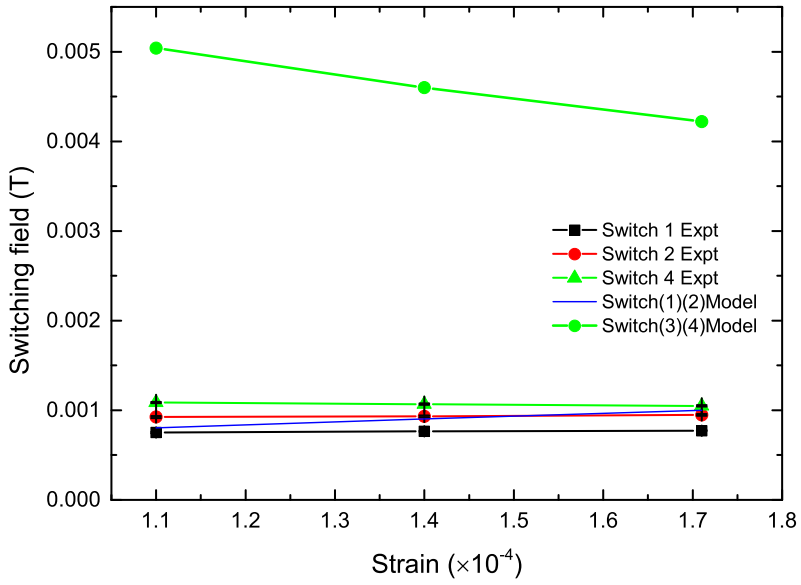

Figure 4.12: Experimental and modelled switching fields (1,2) and (3,4) for sample S421, when the field was varied along [010] direction and the values of the magnetoelastic constants B1 and B2 used were B1=$1.5\times10^7\ Jm^{-3}$ and B2=$1.6\times10^7 Jm^{-3}$

It is observed that the gradient of the modelled switching fields are higher than the gradients of the experimental switching fields. The reason for this are higher strain values or higher values of the magnetoelastic constant.

(3) The absolute strength and nature of the voltage induced strain in each layer is unknown.

As can be seen from the experimentally observed transverse resistance in Fig. 4.3, there is always a large change in resistance corresponding to the magnetisation switch by 90° irrespective of the applied field direction. For the magnetic field along the [100], when the tensile strain is along [100], there should be no magnetisation switch by 90°, however a large change in resistance is observed corresponding to the magnetisation switch from [100] to [010] directions. What this indicates that the strain values calculated by the strain calibration method are not absolute and is probably very weak.

So in conclusion by taking the above discussions into account, it can be said that the experimentally observed resistances showed large change in resistance due to different domain wall de-pinning energies and uncertain magnetoelastic constants

even at lowest and negative values of strain. The strain value in each layer complemented with the magnetoelastic constants, along with the domain wall de-pinning energy of each layer determine the switching fields labelled (1) to (4). A change in one of the parameters is reflected as a change in the other. The uncertainty in determining the absolute value of the strain in each layer along with the domain wall energy makes it complicated to determine the exact values of the magnetoelastic constants. However a similar discussion is outlined in section 4.2.1.1 of the chapter for this same sample, where the magnetoelastic constants for each layers are determined by a qualitative analysis.

(iii) Magnetic field along $[1\bar{1}0]$ hard direction

The electrical and optical behaviour for magnetic field applied along the $[1\bar{1}0]$ direction is now discussed. $[1\bar{1}0]$ is the hard axis of magnetisation as determined by SQUID magnetometry measurements discussed previously where it was also demonstrated that for an unstrained sample the magnetisation rotates coherently towards one of the easy axes and subsequently does a 90° switch. For a tensile strain along the [100] direction it is reasonable to assume that the switching towards the [100] axis for the bottom layer will occur at lower magnetic field value than the top layer, and this difference will contribute towards GMR.

The MOKE MH loop for this direction at +30 V is shown in Fig. 4.13 and compared to the SQUID MH loop for zero strain, to qualitatively understand the magnetisation reversal for mainly the top layer (though there might be some small contributions to the MOKE signal from the bottom layer) . The measurement at +30V is shown because for this voltage the tensile strain should be the maximum. In this plot the alphabetic and numeric labels indicate the magnetisation reversal process, and for consistency the coherent rotation have been labelled alphabetically, and magnetisation switching has been labelled by numbers through out this chapter. The reason the second magnetisation switching have been labelled as 3 will be apparent when we discuss the result in details.

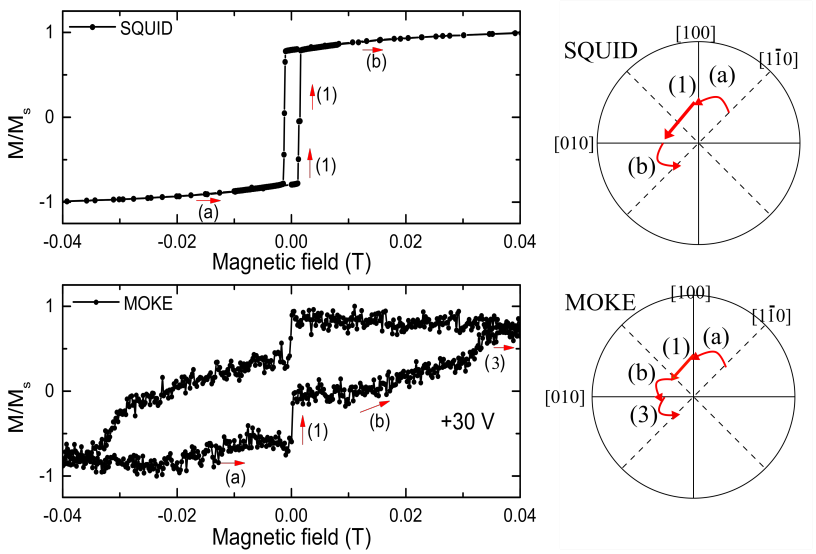

Figure 4.13: Magnetisation MH loop measured for unstrained sample S421 by SQUID magnetometry and at a voltage of +30V on the transducer by MOKE, along with the schematic of the magnetisation reversal process.

From the pictorial representation of the magnetisation reversal shown above for the SQUID and MOKE, it can be seen that for an unstrained sample the magnetisation rotates from the [1$\bar{1}$0] direction towards the easy [100] direction as the magnetic field strength decreases (labelled as a). As the field passes through zero it does a 90° switch (label (1)) and subsequently aligns to the field direction (label (b)). This was previously discussed in Sec. 3.3 when the modelled SQUID MH loop were shown. However when there is a tensile strain present along the [100] direction, as the magnetic field is decreased the magnetisation rotates towards the [100] (label a) , and instead of undergoing a 90° switch coherently orients towards the [010] as a combination of switching (label 1) and rotation (label b), following another switch (labelled (3)) and then orients towards the field direction. This is due to the extra uniaxial magnetoelastic energy along the [100] due to the tensile strain which pulls the magnetisation to stay along this direction, and there is extra energy expense incurred to rotate the magnetisation away from this direction.

It is reasonable to assume that the magnetisation for both the layers behave identically except the fact they will switch at different magnetic field values and this would show additional GMR features. This is observed by performing the magnetotransport measurements. The transverse and longitudinal resistances for this configuration are shown in Fig. 4.14 for piezoelectric voltage of +30V. The modelled transport data has also been superimposed over the experimental data

to show the behaviour of the magnetisation reversal process. Besides this the modelled data also show the contribution of GMR to the net measured longitudinal resistance.

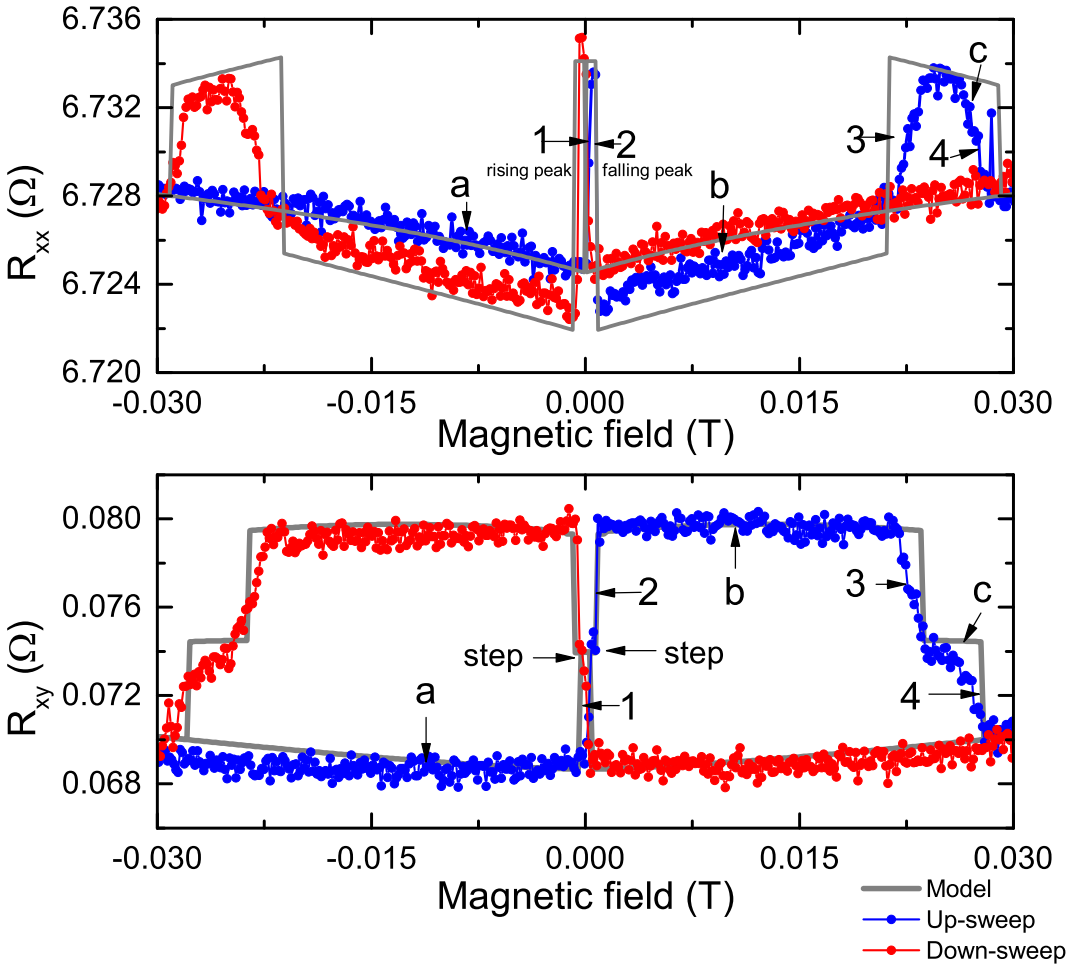

Figure 4.14: Experimental and modelled magnetotransport data for sample S421 when magnetic field was varied along the $[1\bar{1}0]$ direction and at +30 V

Since a very close agreement between the modelled resistances and the experimental data has been achieved, the calculated angles from the simulation are used to explain the magnetisation reversal. These angles of magnetisation are shown in Fig. 4.15 (a) and are with respect to the [100] axis and for the field up-sweep direction with the schematic of the magnetisation reversal in Fig. 4.15 (b) . A very similar explanation holds for the down-sweep direction.

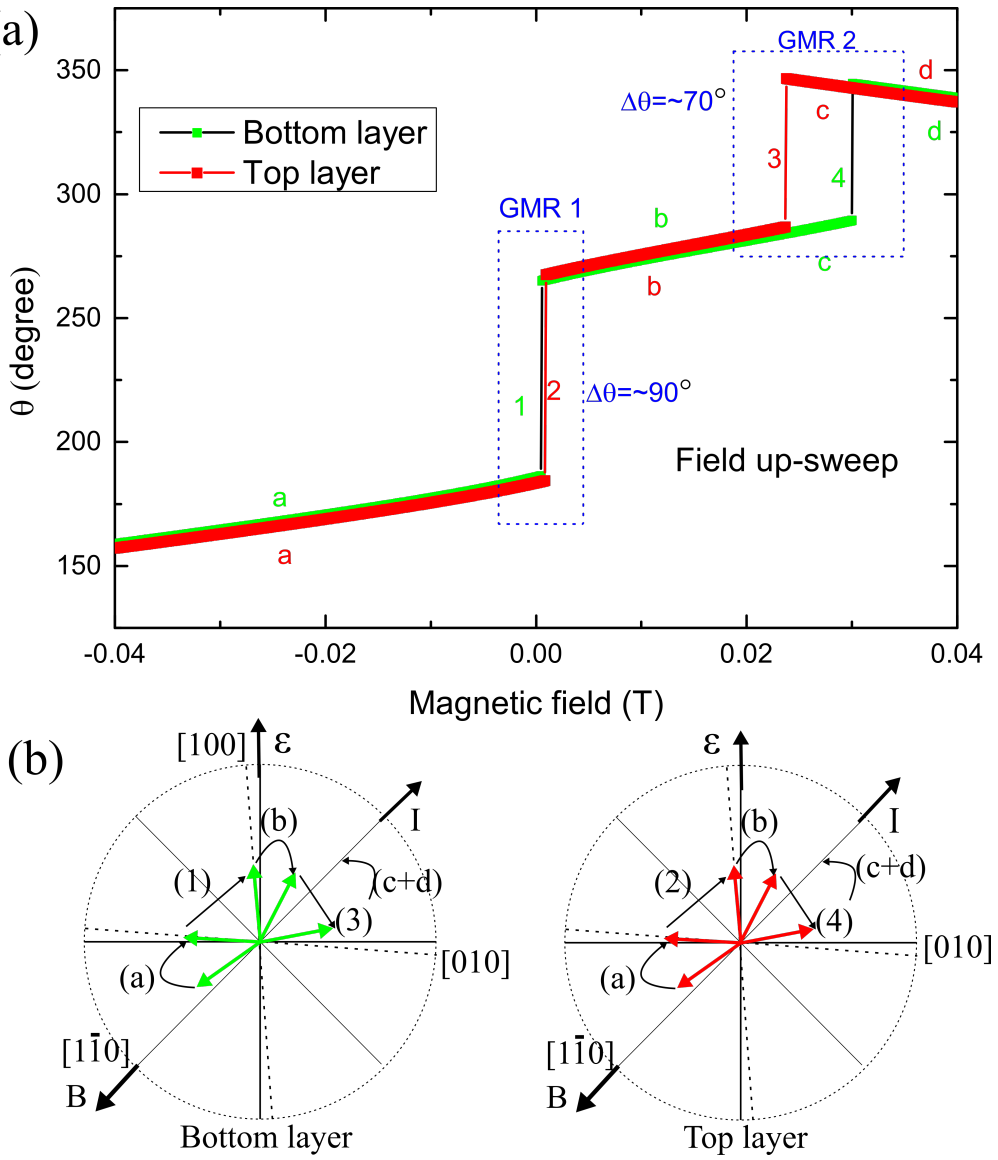

Figure 4.15: (a) Calculated angles of magnetisation for both the $Fe_{1-x}Ga_x$ layers for the down-sweep direction for sample S421. The difference in magnetisation that contribute to GMR have been enclosed in dashed blue rectangles. (b) Schematic of the magnetisation reversal. The green and red arrows represent the magnetisation of the bottom and top layers respectively. The black arrows denote the magnetisation reversal process. The curved black arrows indicate coherent rotation and the straight arrows indicate magnetisation switching over the hard axes. The dashed lines represent the angle offset used to perform the model that predicts the experimental features.

From the figure 4.15 (a) and (b), it is seen as the magnetic field is varied towards the positive saturating value from negative:

(a) The magnetisation for both the layers coherently rotates towards the easy [010] axis.

(1,2) Switches by 90° towards the [100] strain axes direction.

(b) Coherently rotates again towards the field direction along $[1\bar{1}0]$.

(3,4) Does another subsequent switch over $[1\bar{1}0]$ towards the easy axes [010], and then

(d) Aligns along the field about the $[1\bar{1}0]$ direction.

Mapping this reversal to the measured and modelled transverse resistance (see Fig. 4.14 bottom plot) it is observed that due to the coherent rotation (label a) R_{xy} decreases and shows a large change in resistance when the magnetisation switches by 90° (label 1 and 2). As the layers have different switching fields due to different magnetocrytalline anisotropy energy, and magnetoelastic constants, the change in transverse resistance is a combination of the switching of each layer and has a characteristic step. As the field increases the magnetisation continues rotation towards the $[1\bar{1}0]$ direction (label b) which shows a decrease in the transverse resistance again . Due to a tensile strain along the [100] the magnetisation is pulled towards the [100] direction at low field. At high field the magnetisation switches towards the [010] direction resulting in a sudden decrease in resistance for both the layers (identified as 3 and 4 in transport resistance figure) with a similar step due to different switching field (labelled c in transport resistance figure). As the field strength increases the magnetisation rotates back towards the field direction and causes an increase in resistance again as the field strength increases.

A very similar explanation holds for the longitudinal resistance but the contribution of GMR is taken into consideration which can explain the large change in resistance. Switch 1 and 2 of the magnetisations gives a large change in the transverse resistance due to AMR but it should be a small change for the longitudinal resistance as it follows a $cos(2\theta)$ function. However in this field region , which has been enclosed by the blue rectangle (labelled GMR 1) it is seen that the angles of the magnetisation for each layer are nearly 90° apart. This happens because the bottom layer switches first due to high magnetostriction value and is more influenced by the strain compared to the top layer. This difference in angle contributes to the GMR in the net longitudinal resistance. A similar process happens when the magnetisation switches over the second hard axis and have been enclosed in the rectangle labelled as GMR 2. Since the angle difference for GMR 1 is greater

than the angle difference for GMR 2 the peak amplitude is higher for switch labelled (1 and 2). Nevertheless the second GMR peak is broader as the difference in magnetisation is over a wider magnetic field range.

Next we discuss the effect of the voltage induced in-plane strain to change the magnetisation reversal, which will be used to extract the value of the strain induced anisotropy value (K_s) for the individual $Fe_{1-x}Ga_x$ layers. To perform this the transverse resistance at different voltages were used and the modelling was performed using the calculated value of the relative strain to simulate the switching fields which have been labelled in the Fig. 4.16. Fig. 4.16 shows the variation of transverse resistance at different piezoelectric voltage values with the labels 1-4 representing the magnetisation switching events over the hard axes as discussed previously. The variation of the switching fields with the voltage has also been shown.

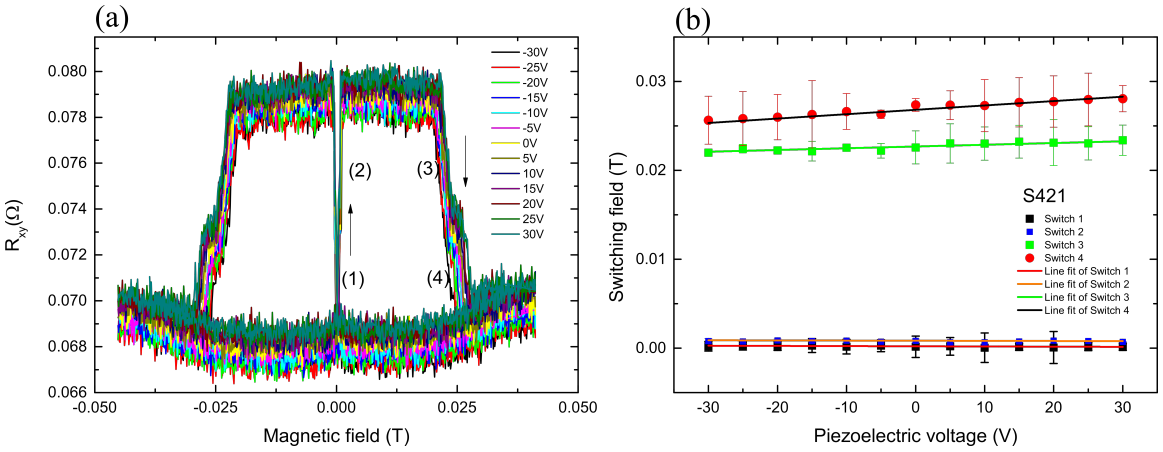

Figure 4.16: (a)Measured transverse resistance at different piezoelectric voltage values for field applied along the $[1\bar{1}0]$ direction for sample S421, along with the (b) variation of the switching fields.

It can be seen that the strain does not affect too much the switching fields labelled 1 and 2. However the switch 3 and 4 show a considerable change when the strain is varied. Hence these magnetisation switching processes will be used in determining the value of the magnetoelastic coefficients for the individual layers.

(iv) Determination of the magnetoelastic constants

In order to calculate the values of the magnetoelastic constants the variation of the switching fields with different voltage induced in-plane strain has been considered. To do that, the identification of the switching events to the layers needs to be

first determined. From Fig. 4.16 it is observed that the switch (1) and (2) do not show considerable change with strain while switch (3) and (4) do. Also the change in switch (4) is greater then the change in switch (3). The lower layer which has a higher composition of Ga and is in proximity to the transducer should be affected more by the strain, than the top layer which feels less strain and has less magnetostriction value. Therefore switch (3) can be mapped to the top layer and switch (4) can be mapped to the bottom layer grown on GaAs.

As the absolute value of the transmitted strain in each layer is unknown, and is always tensile as seen from the experiment, analysis by performing least sum of square fit at the switching field values is not possible. Since the solution for the minimum positions of the free energy involves three independent parameters such as E_{DW}, the uniaxial strain value, and the magnetoelastic constants, the model will not give accurate prediction for the magnetoelastic constants. A similar observation was seen for the estimation of the magnetoelastic constants for field along the [010] direction.

In this section, the analysis for the determination of the magnetoelastic constants has been discussed and is very similar to what was discussed earlier for B || [010] direction. The calculation has been performed by taking into consideration the uncertainty in the absolute value of strain in each layer, and the dependence of the magnetisation switching on the domain wall de-pinning energy. As such this analysis has been carried in different stages as stated below:

Stage 1

The first stage involves checking for the dependence of the magnetisation switching on the magnetoelastic constants, at the calibrated values of strain. In this process, the transverse resistance was modelled for different values of measured strain, and using the domain wall energies of each layer calculated for the unstrained sample by the SQUID measurements in Ch. 3. The first stage of the modelling was performed by using the previously reported values [100, 189] of the magnetoelastic constants at this composition: B1=1.5×10^7 Jm^{-3} and B2=$1.6 \times 10^7 Jm^{-3}$. From the modelled transverse resistance, the switching fields for switch 3 and 4 were obtained and have been shown in Fig. 4.17 by the red and green lines respectively.

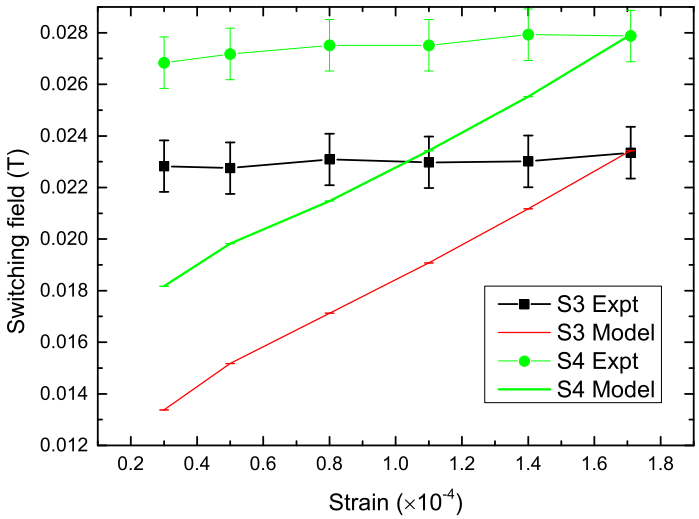

Figure 4.17: Experimental and modelled switching fields (3) and (4) for sample S421 when the values of the magnetoelastic constants B1 and B2 were B1=1.5×10^7 Jm^{-3} and B2=$1.6\times10^7 Jm^{-3}$.

It is seen that the gradient of the modelled values are much greater than the slope of the experimental switching fields. This was due to the high values of the magnetoelastic constants which would make the layers very sensitive to the strain. So to solve this, the magnetoelastic constants need to be altered.

It is known from previous reports that the magnetostriction value is dependent on the Ga concentration and also on the crystal morphology[100, 188]. For this sample it was seen from the FMR and TEM images in Ch. 3, that the layers have lower Ga content compared to the MBE grown sample reported by Parkes[101], and are also polycrystalline. Therefore multiple iterations were performed using different lower values of B1 and B2 until the gradients of the modelled switching fields with respect to strain were the same as the gradients of the experimental switching fields. It was found that at B1=1.4×10^7 Jm^{-3} and B2=$0.45\times10^7 Jm^{-3}$ the modelled switching fields showed the same gradient to the experimentally calculated switching fields. The experimental and modelled normalised transverse resistance for a few piezoelectric voltages have been shown in Fig. 4.18 and the switching fields for these set of modelling have been shown in Fig. 4.19.

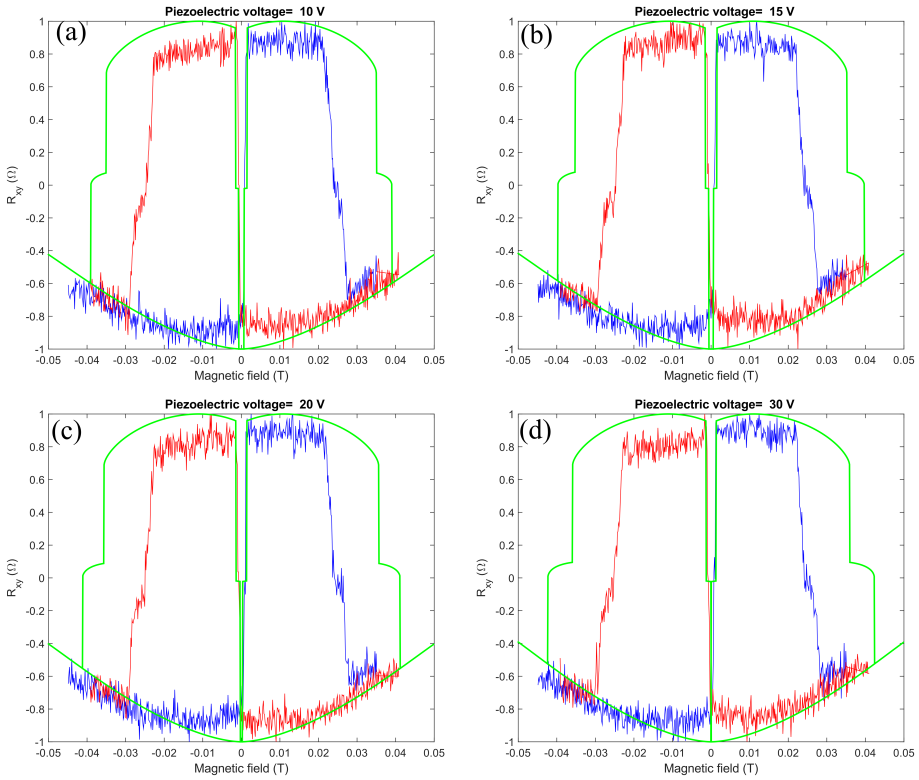

Figure 4.18: Experimental (blue and red) and modelled (green) normalised transverse AMR for sample S421 at piezoelectric voltages of (a) 10V, (b) 15V, (c) 20V and (d) 30V

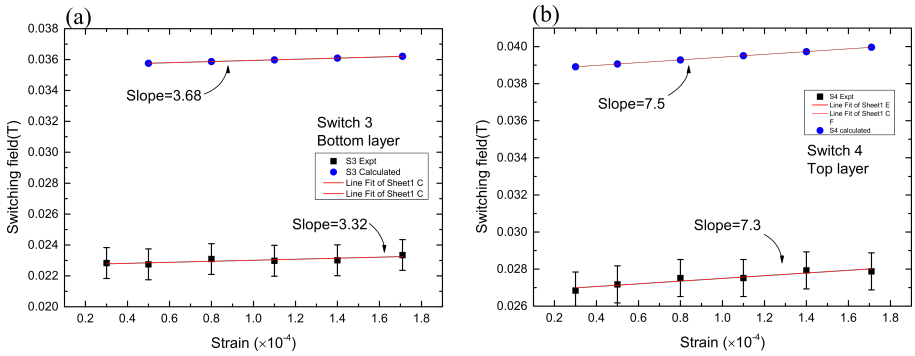

Figure 4.19: Experimental and Modelled switching fields for switch labelled (a) 3 and (b) 4 at calibrated values of strain for sample S421.

As can be seen from Fig. 4.18 and Fig. 4.19, using this set of magnetoelastic constants resulted in switching events which are affected by the strain equivalent to the experimentally measured transverse resistances. However the modelled and experimental switching fields do not match and there is an offset in the switching

fields. This offset may be due to the contribution of the offset in strain value along with the offset in domain wall de-pinning energies. It has already been resolved that the domain wall de-pinning energies are different for the strained sample when the field along [010] was discussed. This has been performed in stage 2.

Stage 2

In this stage of determination of the magnetoelastic constants, the values of the magnetoelastic constants were fixed at B1=$1.4\times10^{7}\ Jm^{-3}$ and B2=$0.45\times10^{7}Jm^{-3}$ to give the same gradient as the experiment. The offset in the switching fields due to different E_{DW} for strained sample was investigated.

For this the switching fields were modelled using constant B1 and B2, and at measured strain values . Only the domain wall de-pinning energy values were changed to plot the transverse resistance. The modelled switching fields at different E_{DW} values have been shown in Fig. 4.20.

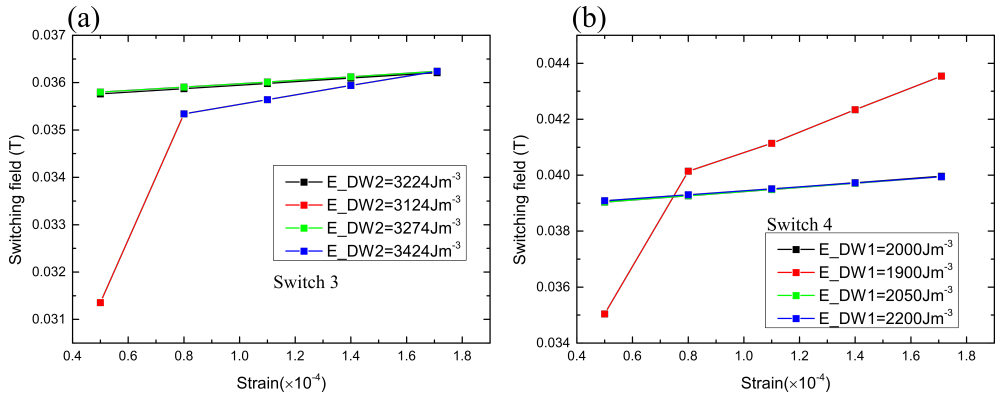

Figure 4.20: Modelled switching fields for switch labelled (a) 3 and (b) 4 at calibrated values of strain for sample S421 using different domain wall de-pinning energies in Jm^{-3}.

It is observed that a slight change in the domain wall energies resulted in switching fields with the same gradients as the experiments but at certain lower bound and upper bound values the model would result in switching fields with different gradients and with a single switch at lower strain values. The single switch is a result of the layer switching by 90° showing a large change in resistance while the top layer switching by 180° causing no change in resistance. This direct 180° switch of the magnetisation is because of a high domain wall depinning energy which doesn't let the magnetisation switch to the strain axes direction. This reversal process is due to the lower effect of the strain induced anisotropy for the top layer than the domain wall depinning energy.

Due to this boundary constraint of the domain wall depinning energy which is dependent on the strain induced anisotropy, the offset in the modelled and experimental switching fields could not be resolved by altering the E_{DW} values. The offset correction has been followed up in stage 3.

Stage 3

In this stage the offset was resolved by changing the uniaxial strain values to qualitatively match the experimental switching fields . An example modelled loop for +30V is shown in Fig. 4.21 where in order to match the switching fields, strain was decreased to 0.61×10^{-4} from 1.71×10^{-4}.

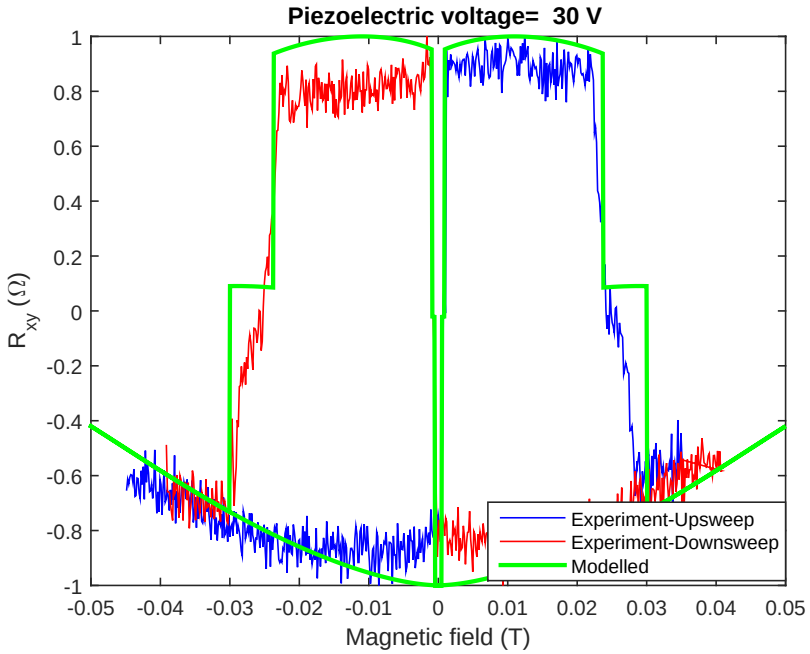

Figure 4.21: Experimental (blue and red) and modelled (green) normalised transverse AMR at +30 V for sample S421. The strain was changed to 0.61×10^{-4} to match the switching fields.

So in conclusion it can be said that the calibrated strain and the calculated domain wall depinning energies are two cooperative contributing effects to the free energy of a single domain model, and compete with each other to decide the orientation of the magnetisation. This antagonistic behaviour has been observed in the stages discussed and can be seen that changing one of the parameter reflects to the other. Without knowing the exact strain value transmitted to the layers which is an experimental limitation in this case the calculation of the exact strain dependent magnetoelastic constant is challenging. The estimated values of

B1=1.4 $\times$ 10^7 Jm^{-3} and B2=0.45 $\times$ $10^7 Jm^{-3}$ may be correct as they reproduce very similar AMR feature with the gradient equal to the experiment and are of the same order of magnitude reported previously to be between 0.3 $\times$ 10^7 Jm^{-3} and 2.0 $\times$ $10^7 Jm^{-3}$ [100, 188, 189]. The shift in the switching fields between the experiment and the modelled transverse AMR can also be due to depinning fields at device boundary, inhomogeneous strain transmission, sample morphology, etc. For the rest of the thesis, these values of magnetoelastic constants have been used to model and understand the magnetisation reversal processes in the remaining samples.

4.2.1.2 Sample S419: 5 nm Al spacer

In this section a similar discussion is performed for the 5 nm Al spacer sample.

(i) Magnetic field along the easy axis directions

Before the magnetotransport results are discussed the relative strain transmitted to the structure will be outlined. To explain this the variation of the transverse resistance with voltage across the transducer has been shown in Fig. 4.22 for the [010] and [100] easy directions along with the change of switching fields in Fig. 4.23. A quantified discussion on the effect of voltage induced strain to the magnetisation has been described in Sec. 4.2.3

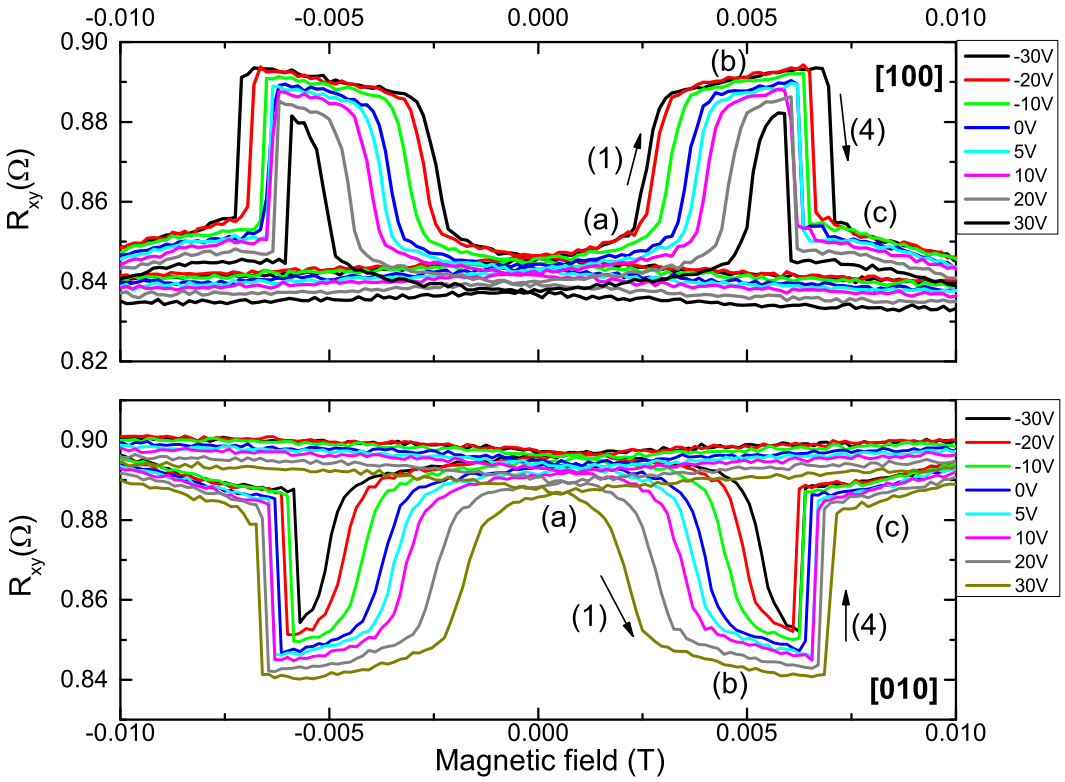

Figure 4.22: Transverse resistance for sample S419 for magnetic field varied along the [010] and [100] directions at different voltages across the transducer.

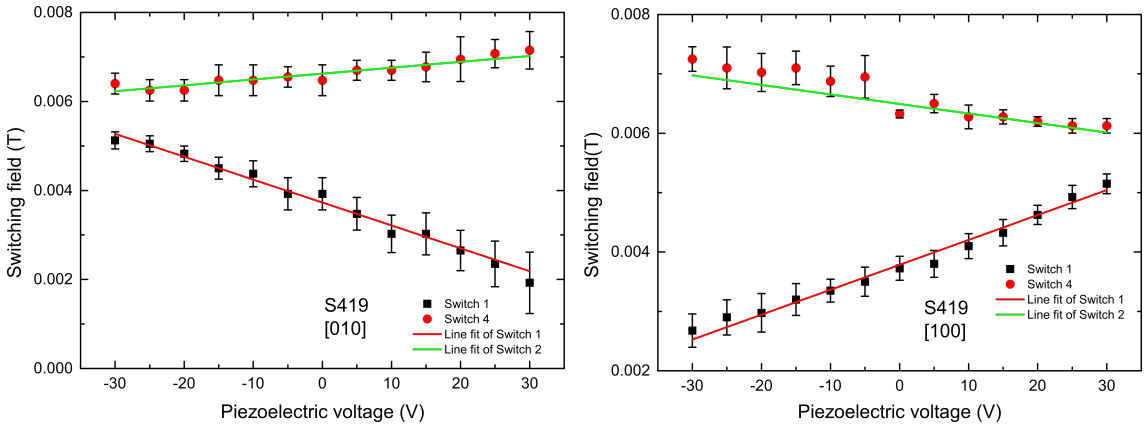

Figure 4.23: Variation of the switching fields with the piezoelectric voltage for sample S419, when the magnetic field was varied along the [010] and [100] directions.

It can be seen that the voltage induced strain very clearly changes the switching fields, labelled as (1) and (4) and thereby controls the magnetisation reversal. However for all the voltages there is the same large change in the measured resist-

ance at the switching fields, even for a 5 V where the calculated strain is zero by the technique described in Sec. 2.2.4. The large change in the transverse resistance is a result of the magnetisation switching by 90° similar to the sample S421 and have been explained previously. The switching by 90° is a contradiction to the 180° switch at zero strain which was measured by SQUID and shown in Fig. 3.9 and is an evidence that there is always a tensile strain present in the structure due to the epoxy glue curing process which could not be avoided for the measurements and that the strain value determined is not the absolute value of strain that is perceived by the two layers but is relative value centred about zero.

The large change in the transverse resistance is very similar to the 90° switch by sample S421, and therefore have been labelled as (1) and (4). However the change is not abrupt which is an indication for a sudden switch and no step features are observed which would indicate the contribution from each layer. This is the reason labels (2) and (3) are dropped, and to a consistent labelling of the magnetisation switching. For this sample the large change in resistance is a combination of coherent rotation and switching over the hard axes. A general pictorial representation of the magnetisation reversal for either field directions are shown in Fig. 4.24 (a) and (b) respectively. In this representation the green arrows represent the magnetisation orientation from [010] and shows the reversal process when the magnetic field is varied. The labels (a), (b), (c), (1), and (4) correspond to the features marked in Fig. 4.22. The sign of AMR is positive for [100] direction case while is negative for the [010] case , and can be reasoned from the schematic very clearly. The switch from [010] to [100] is associated with a decrease in resistance while a switch from the [100] to [010] gives a positive change in resistance.

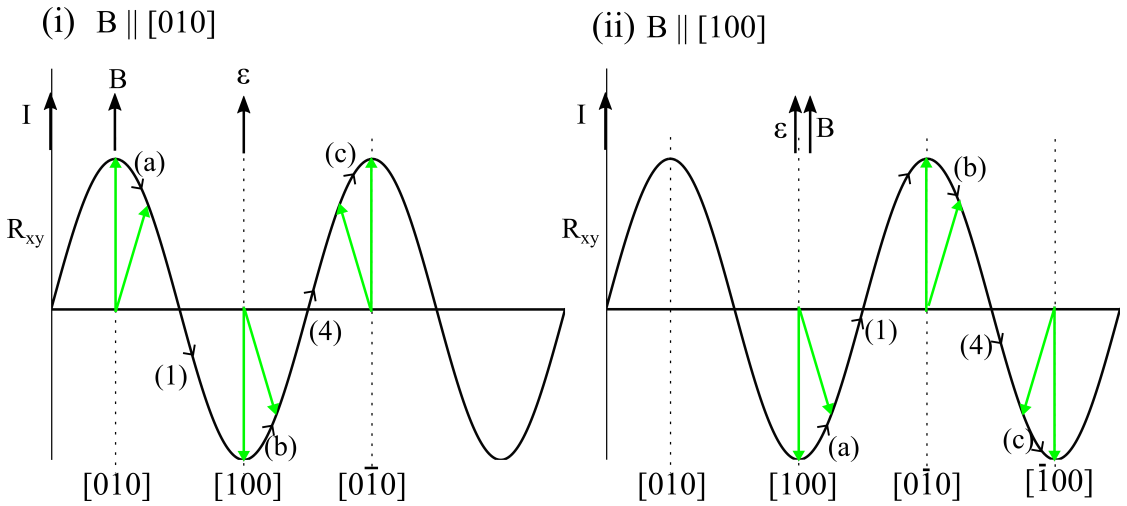

Figure 4.24: Schematic of the magnetisation reversal for magnetic field applied along (i) [010] direction, and (ii) [100] direction. The green arrows represents the magnetisation and the labels correspond to the features identified in Fig. 4.22.

The magnetisation reversal by $\sim 90°$ causes large change in the transverse resistance, and this should not show a large change in the longitudinal resistance. The longitudinal resistances for the [010] and the [100] directions are shown in Fig. 4.25 at different values of piezoelectric voltages.

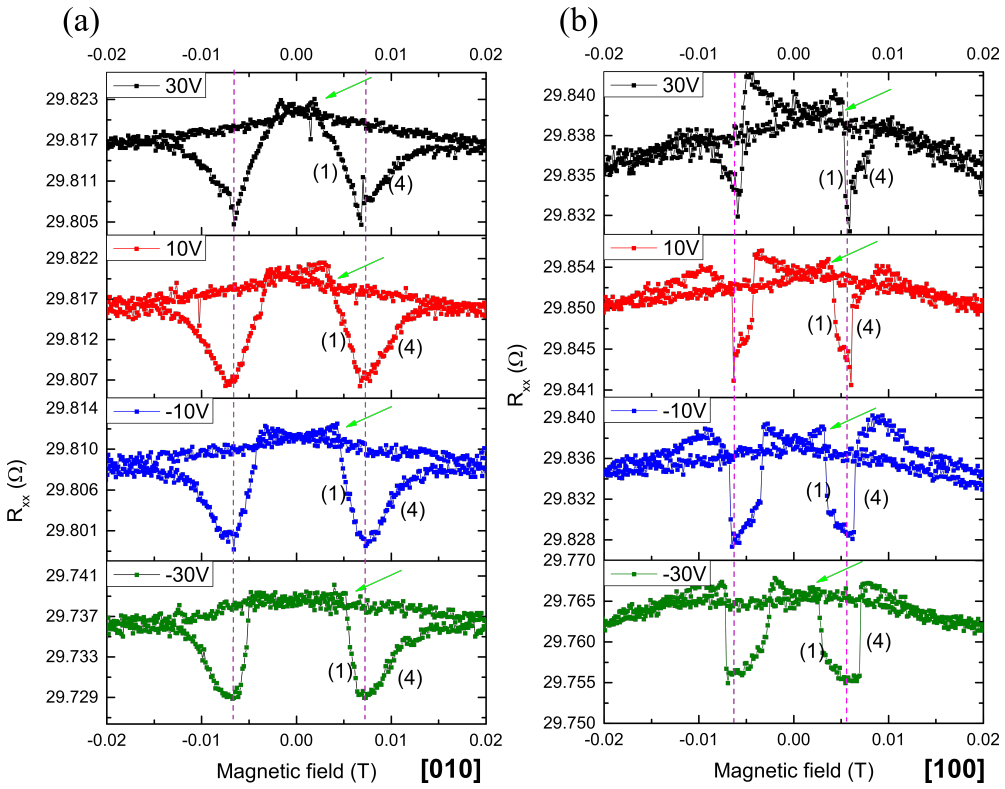

Figure 4.25: Longitudinal resistance for magnetic field along the (a) [010], and (b) [100] direction at different piezoelectric voltages for sample S419. The pink dashed lines represents the switching field corresponding to the transverse resistance and the green arrows represent the tiny GMR feature.

For the measured longitudinal resistance, the resistance decreases linearly as the strength of magnetic field is increased. According to AMR relation there should be no change in resistance. This non zero change in resistance can be attributed to electron-magnon interactions which cause the linear dependence of the resistivity on a high applied field [191], or it can be a manifestation of misalignment in the device with respect to the field. It is observed that the longitudinal resistance shows some change in resistance but it is an order of magnitude lower than the change in the transverse resistance. Unless there is independent switching of magnetisation of the two layers, this change in resistance is purely AMR. For the 90° switch between [010]/[100] the longitudinal change in resistance is tiny as it is a $\cos(2\theta)$ function (θ being the angle between the current and magnetisation from [010]). The measured tiny change can be accounted for by the rotation of the magnetisation, or if there is any independent switching the magnitude of the GMR is very small. Since the GMR can not be negative the tiny feature indicated by green arrows indicate the small GMR contribution to the measured longitudinal resistance. The

magnitude of the GMR will be discussed when the field applied along the $[1\bar{1}0]$ will be presented in the following section. A schematic of the magnetisation reversal that contributes to the AMR part of the longitudinal resistance variation is shown in Fig. 4.26 (i) and (ii), where the green circle represents the magnetisation with respect to the current along the $[1\bar{1}0]$ direction and is at an offset angle due to the misalignment. The switch over the hard axis for either field direction contributes to a tiny change of the longitudinal AMR.

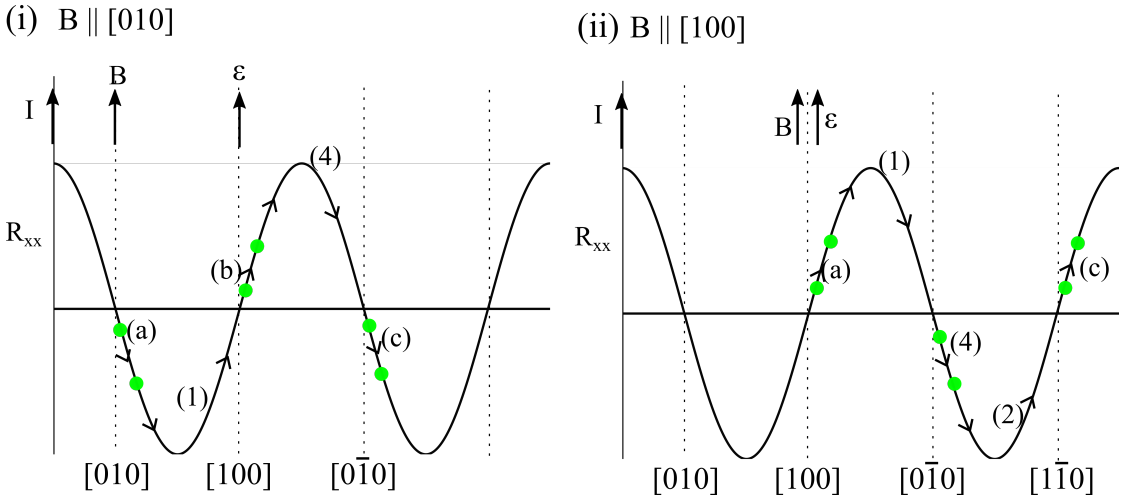

Figure 4.26: Schematic of the magnetisation reversal for sample S419 when magnetic field is varied along (i) [010] direction, and (ii) [100] direction. The green circles represents the magnetisation and the labels correspond to the features identified in Fig. 4.22 and Fig. 4.25.

The 90° switch has been confirmed by MOKE MH loops which were performed at different piezoelectric voltages and shown in Fig. 4.27. The transducer was charged and damaged during this experiment, so only 0 volt is shown for the [100] direction. The MOKE MH loops exhibit a step like magnetisation reversal which is an evidence for 90° switch, unlike the SQUID MH loops which showed a sudden 180° switch (see Fig. 3.8). The switching fields in MOKE do not match to the switching fields in the transport measurements. This may be due to localised heating, laser spot position.

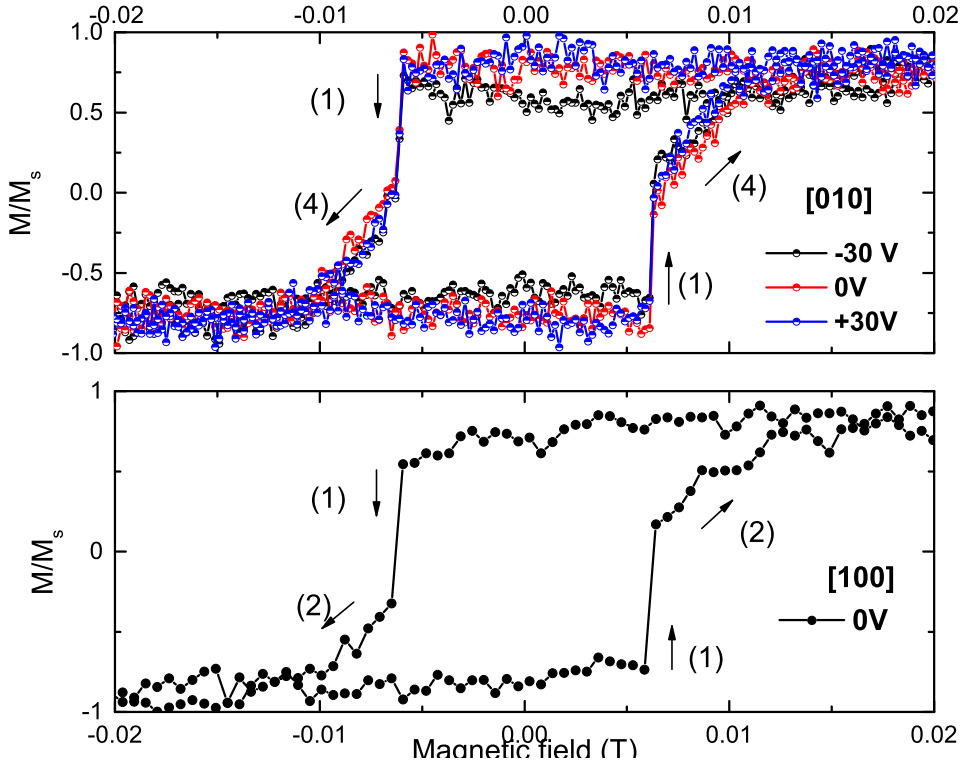

Figure 4.27: MOKE MH loops for sample S419. The magnetic field was applied along the [100] and [010] direction at different voltages across the transducer.

(ii) Magnetic field along $[1\bar{1}0]$ hard direction

The transverse and longitudinal resistance for different piezoelectric voltages for field swept along the $[1\bar{1}0]$ direction is shown in Fig.4.28. The black arrows in R_{xx} show the direction of the applied field and the magenta arrow denotes the peaks in the longitudinal resistance which are at the same switching field as switch (1) and (4) in the transverse resistance.

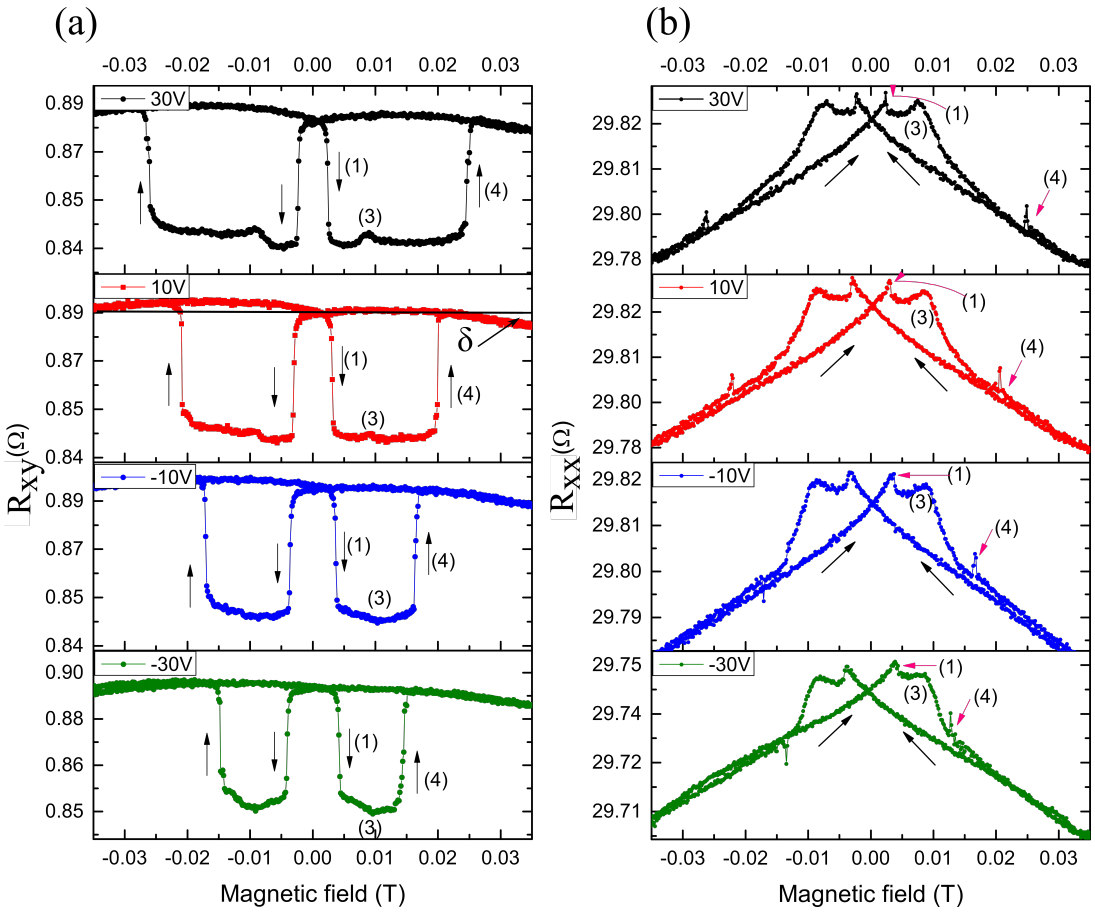

Figure 4.28: (a) Transverse and (b) Longitudinal resistance for sample S419 when the field is varied parallel to the $[1\bar{1}0]$ direction at few piezoelectric voltages.The black arrows show the direction of the applied field and the magenta arrows denote the peak in the longitudinal resistance which are at the same switching field as switch 1 and 4 in the transverse resistance.

There are four main observations from these magnetotransport plots. They are:

(a) Ordinary Hall effect

The transverse resistance for all voltages show a Hall effect contribution which is caused due to offset in the sample position with respect to the magnetic field. It is seen as an offset in the measured transverse resistance and have been labelled as δ for the transverse resistance at +10V.

(b) Different switching fields compared to S421

For field varied along the $[1\bar{1}0]$ direction it is seen that the switching fields for the measured Tr-AMR are different in comparison to Tr-AMR in sample S421.

Sample S421 demonstrated four distinct switching events, two for each layer and were marked with a step feature. However for sample S419 it is seen that there is no step feature that distinguishes the switching events for individual layers, rather there is just one single switch for both the layers manifested as large change in resistance. For consistency in comparison, the switch 1 in this sample is analogous to switch 1 and 2 for sample S421. Switch 3 is for the top layer and switch 4 is for the bottom layer, as was seen for the previous sample.

(c) Effect of strain.

The voltage induced strain is seen to change the magnetic switching field and can be observed from the transverse resistance. Besides the switching field, the strain changes the shape of the transverse resistance curve as well. For lower values of voltages, switch is followed by a gentle V-shaped feature for switch 3 while at higher voltages two separate features are resolved.

For this sample, switch 4 shows a large variation in switching fields so can be reasonably accepted to be because of the bottom layer, and switch 3 shows smaller variations to switching fields and can be mapped to the top ferromagnetic layer which is less sensitive to strain. The variation of the transverse resistance, and the switching fields have been shown again in Fig. 4.29 (a) and (b) respectively to show the effect of strain to modify the switching fields.

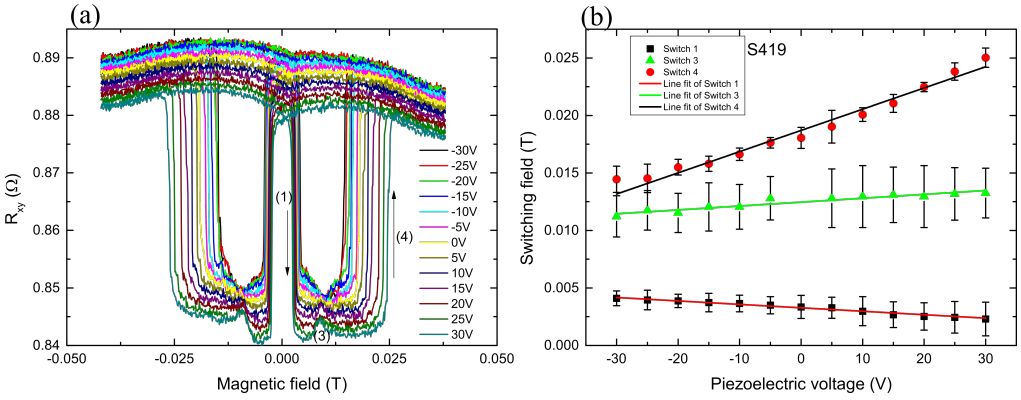

Figure 4.29: (a) Measured transverse resistance, and (b) switching fields for sample S419 at different piezoelectric voltage values when the field is applied along the $[1\bar{1}0]$ direction.

(d) GMR contribution.

The switching fields (1) and (4) in the transverse resistance are reflected as a sudden change with a spike in the longitudinal resistance. This should be due to a relative

angle difference between the magnetisation orientation of the two layers which adds up as a small GMR to the measured longitudinal resistance. The small amplitude may be due to relatively small GMR coefficient.

Before the effect of strain is described it is necessary to qualitatively understand the magnetisation reversal process. To do this the normalised transverse resistance with the Hall resistance subtracted, and the longitudinal resistance at +10 V and -10 volts have been used in conjunction with the modelled R_{xy} and R_{xx} to understand the magnetisation process. The values of the magnetoelastic constants used were the ones previously calculated for sample S421 and only the strain was varied till the switching fields for switch 1 and switch 4 match. The extraction and determination of the elastic coefficients for this sample could not be performed because of the: (a) uncertainty in the absolute strain values in each layer ; (b) the large change in resistances doesn't show a step feature so a perfect mapping to the layers is not possible; (c) for the [010]/[100] directions the magnetisation reversal is a combination of the coherent rotation and hard axes switch while for the $[1\bar{1}0]$ direction, the Tr-AMR shows distinct resistance process at lower and higher values of voltages. With this a consistent analysis could not be performed like the way was performed for sample S421 to extract the magnetoelastic constants.

The modelled and experimental magnetotransport data for +10 V are shown in Fig. 4.30. It can be seen that the model and the experiment are in close agreement at the switching fields labelled 1 and 4. The difference in the field for the second peak or switch 3 can be attributed to the limitations of the model. Some of which are: The model takes into account a single domain configuration. There are chances of some coupling and spacer roughness factors that can affect the experimental behaviour which has not been taken in consideration in the simulation. The uncertainty in the value of strain and the magnetoelastic coefficients can also affect the modelling of the switching events. Also the interfacial surface roughness and Al- doped $Fe_{1-x}Ga_x$ have been known to alter the magnetostriction value as reported in Ref. [81]. This enhanced magnetostriction due to Al mixing along with a crystalline top $Fe_{1-x}Ga_x$ layer will result in a different magnetoelastic constant value rather than $0.45 \times 10^7 Jm^{-3}$ which has been used to model this feature. Due to uncertainty in the estimation of this constants value there is a difference in the modelled and experimental switching field labelled 3.

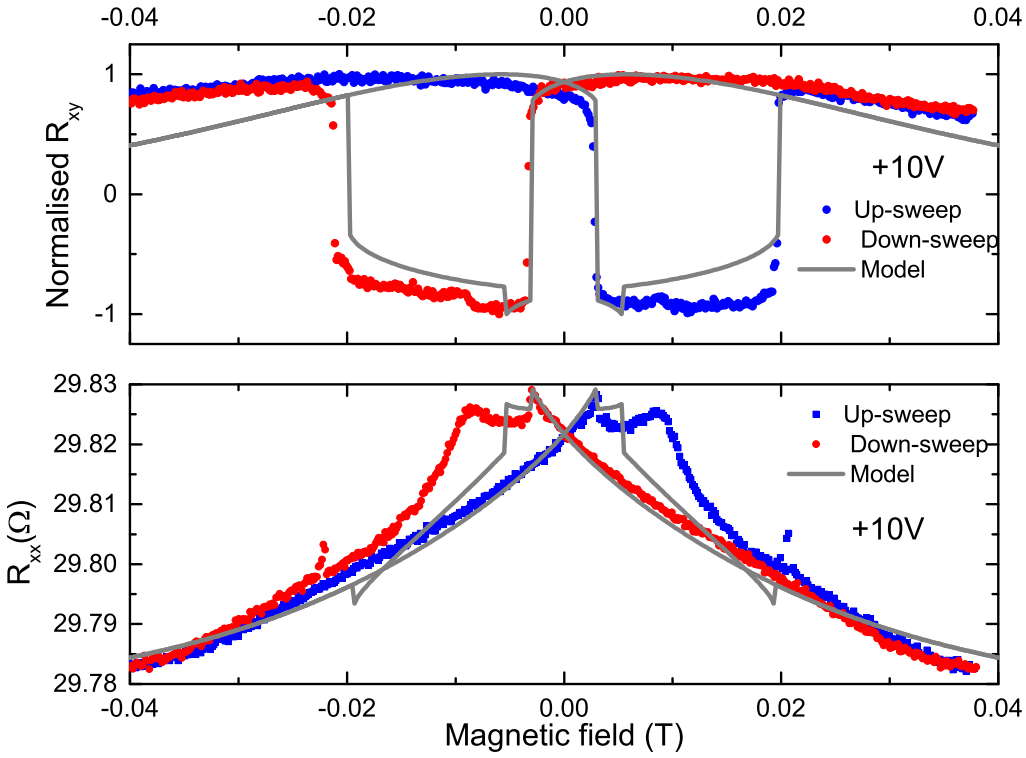

Figure 4.30: Experimental transverse and longitudinal resistance for sample S419 with field along the $[1\bar{1}0]$ direction. with the modelled magnetotransport curves at 10V.

From the model the angle of magnetisation for each layer with respect to the [010] were calculated and shown in Fig. 4.31 (a) for the field up-sweep case along with the pictorial schematic in Fig. 4.31 (b). As it is seen that the magnetisation of each layer have distinct reversal process and have been labelled in the figures. The bottom layer shows a 90° switch instead of a 180° like the top layer and therefore switch 2 is missing for this sample. This 180° is due to the too low transmitted strain or the magnetostriction value is too low and the magnetisation for this layer aligns towards the field direction immediately instead of orienting towards the strain direction along [100]. The field regions that gives rise to a relative magnetisation angle difference which results in GMR has been enclosed by a rectangle. The feature labelled GMR 2 and 3 have a relative angular difference between the magnetisation orientations that causes the spikes in the measured R_{xx}. The feature GMR 1 has a small angle difference and doesn't contribute much to the GMR. It can also be realised that the magnitude of the GMR coefficient is very low unlike sample S421.

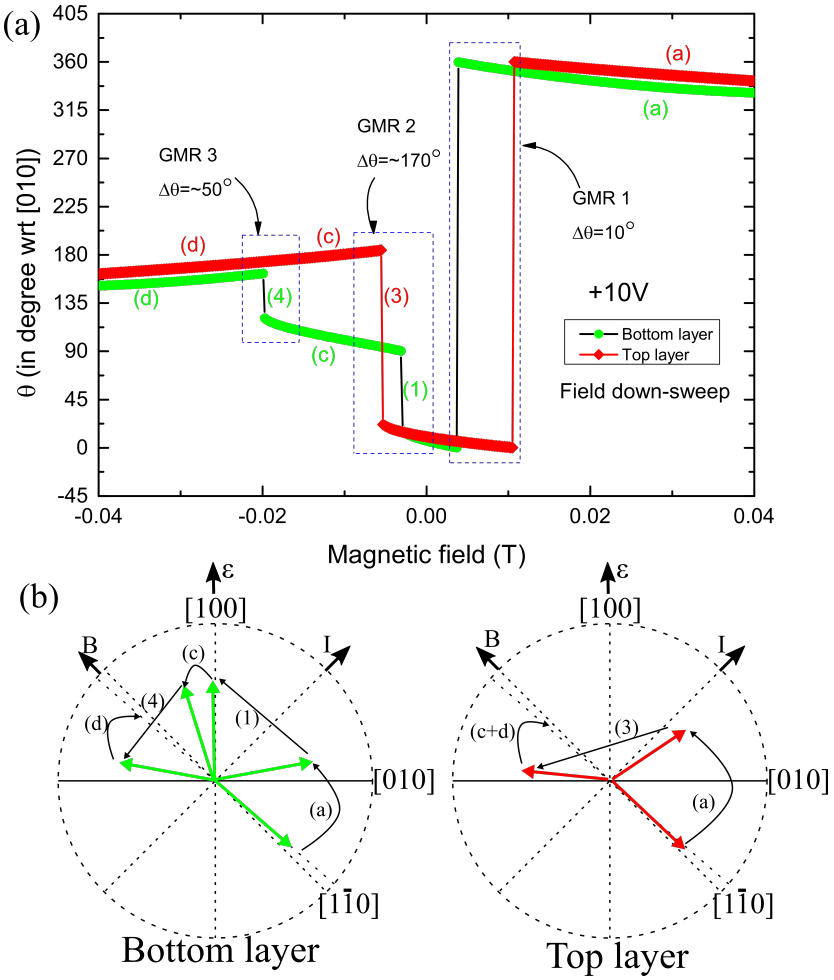

Figure 4.31: (a) Modelled angles of magnetisation for each layer when the field is swept to a negative saturating value with a representative schematic in (b). The piezoelectric transducer is at +10V. In (b) the green and red arrows represent the magnetisation of the bottom and top layers respectively. The black arrows denote the magnetisation reversal process. The curved black arrows indicate coherent rotation and the straight arrows indicate magnetisation switching over the hard axes.

A similar approach to understand the magnetisation reversal at -10 V was performed and is shown in Fig. 4.32 depicting the angles of magnetisation for each layer with respect to the [010] crystal axis and the modelled transverse resistance.

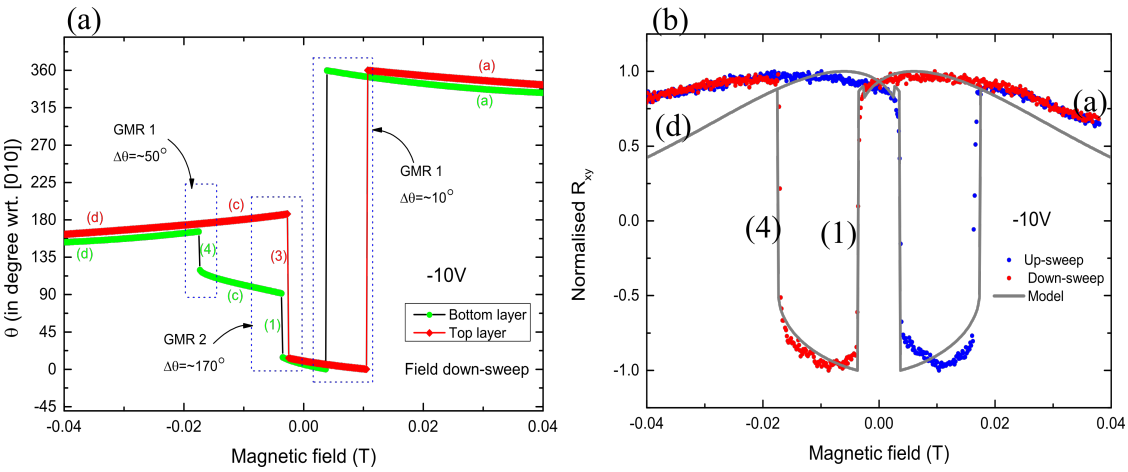

Figure 4.32: (a)Modelled values of the magnetisation with respect to the [010] for field down sweep direction and (b) modelled transverse resistance atV_P=-10V, compared to the experimental data for sample S419

It is observed that the magnetisation reversal is very similar, except the 90°switch labelled as (1) for the bottom layer. Due to very low tensile strain, the top layer switches before the bottom layer, This is because of weaker anisotropy energy of the top layer, while the bottom layer which has a higher uniaxial anisotropy energy would require higher magnetic field to switch over the hard axis.

As mentioned previously, the magnitude of the GMR in this sample is seen to be lower compared to sample S421. This can be associated with the role and thickness of the spacer, the interfacial scattering and the spin diffusion lengths of the spacer and ferromagnetic layer, and spin flipping at the interfaces, impurity scattering etc. From the HR-TEM data it was observed that the thickness of the Cu spacer was 4 nm, and is lower than the thickness of the Al spacer (~ 7 nm). As the thickness of the Cu spacer layer is approximately half of the thickness of the Al spacer layer, the GMR effect may be larger in Cu spacer sample due to shunting of most of the electrons by the thicker Al spacer [192]. Also HR-TEM revealed that there is more interfacial mixing of Fe-Ga with the Al spacer layer than the Cu layer. This can cause interfacial spin mixing effects which further reduces the spin flipping or spin diffusion lengths. Ideally it has been reported that the spin diffusion lengths of Cu is relatively higher than the spin diffusion length of Al [193, 194] but these calculations were performed by using a CPP-GMR configuration. There can be however other reasons which needs further experimental investigation by study of the CIP- GMR effect with varying thickness of the spacer which can fill this gap.

4.2.2 10 nm spacer samples

The magnetotransport and magneto-optical measurements performed for the 10 nm Al and Cu spacer (sample S420 and S422) are described in this section. It is known that the magnitude of GMR is suppressed with the increase in thickness of the spacer layer and nearly vanishes if the spacer layer thickness are much greater than the mean free path of the electrons (of order 10 nm)[107, 158]. From the previous section, the [100]/[010] directions were used to estimate the nature of the voltage induced strain-whether tensile or compressive and the $[1\bar{1}0]$ direction was used to qualitatively estimate the contribution of the GMR to AMR. A similar approach has been used for this section.

4.2.2.1 Sample S422: 10 nm Cu spacer

(i) Magnetic field along easy axis direction

The measured transverse resistance for the [010] and [100] directions at +30V and -30V piezoelectric voltages are shown in Fig. 4.33 (a). It can be seen that unlike the samples discussed previously the transverse resistance for the positive and negative values of the piezoelectric voltages show distinct behaviour. When there is always a tensile strain present in the structure the transverse resistance showed a large change in resistance which corresponded to a 90° switch. However for this sample the transverse resistance for the [010] and [100] directions have different response when the field is varied.

For $V_p = -30V$ there is a large change in resistance for the [010] direction and no appreciable change for the [100] direction. The reverse happens for $V_P = +30V$. There is a large change in R_{xy} for [100] while there is no noticeable change for [010] direction.

The way it can be explained is, at positive voltage there is a large tensile strain along the [100], therefore this direction is relatively easier or more easy than the [010]. When the magnetic field is swept along this more easy [100] direction, the magnetisation is not affected and stays along the [100] axis direction. When the field changes sign the magnetisation does a 180° switch which does not change the transverse AMR. However when the field is varied along the less easy [010], as the field passes through zero, the magnetisation will be forced to orient along the more easy [100] direction due to the pull by the tensile strain. As the field strength along the other direction increases the magnetisation orients along the field direction. This two 90° switch cause large change in the transverse AMR.

The negative voltage case can be explained in a similar fashion, When the voltage is negative there is a compressive strain along the [100], therefore [100] is relatively less easier compared to the axis along [010]. As the field is varied along the easy [010] direction it doesn't get affected and no AMR change is observed too. When the magnetic field is swept along the less easy [100], at zero field strength the magnetisation is pulled by strain to the more easy direction which contributes to the AMR jumps in the measured resistances. The schematics of the magnetisation reversal discussed above are shown in Fig. 4.34 for all the cases which will also explains the sign of the AMR.

The variation of the measured transverse resistance for the [010] and [100] directions along with the switching fields have been shown in Fig.4.35.

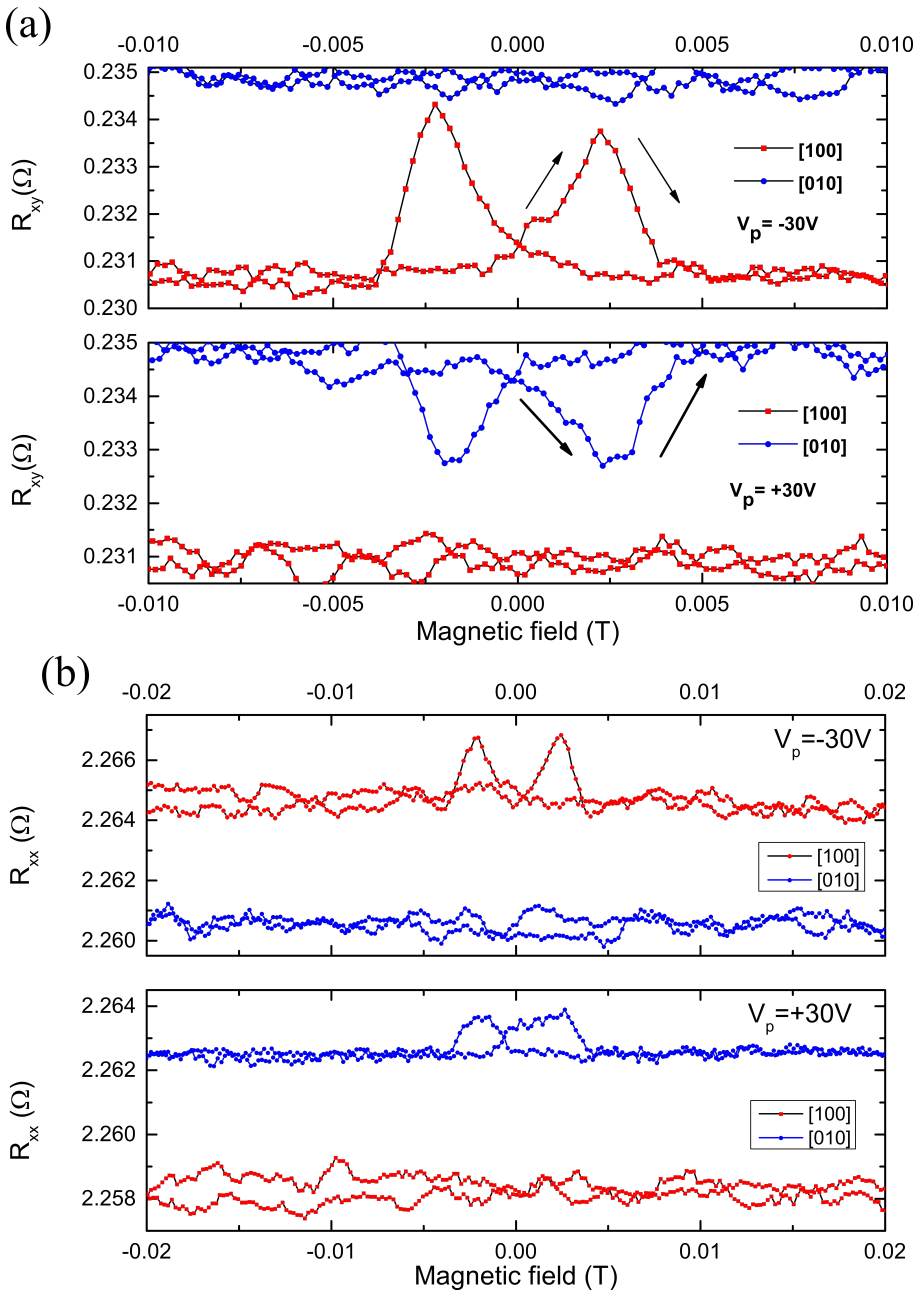

Figure 4.33: (a) Transverse and (b) Longitudinal resistance for sample S422 when the magnetic field was varied along the [010] and [100] directions at +30V and -30V piezoelectric voltages.

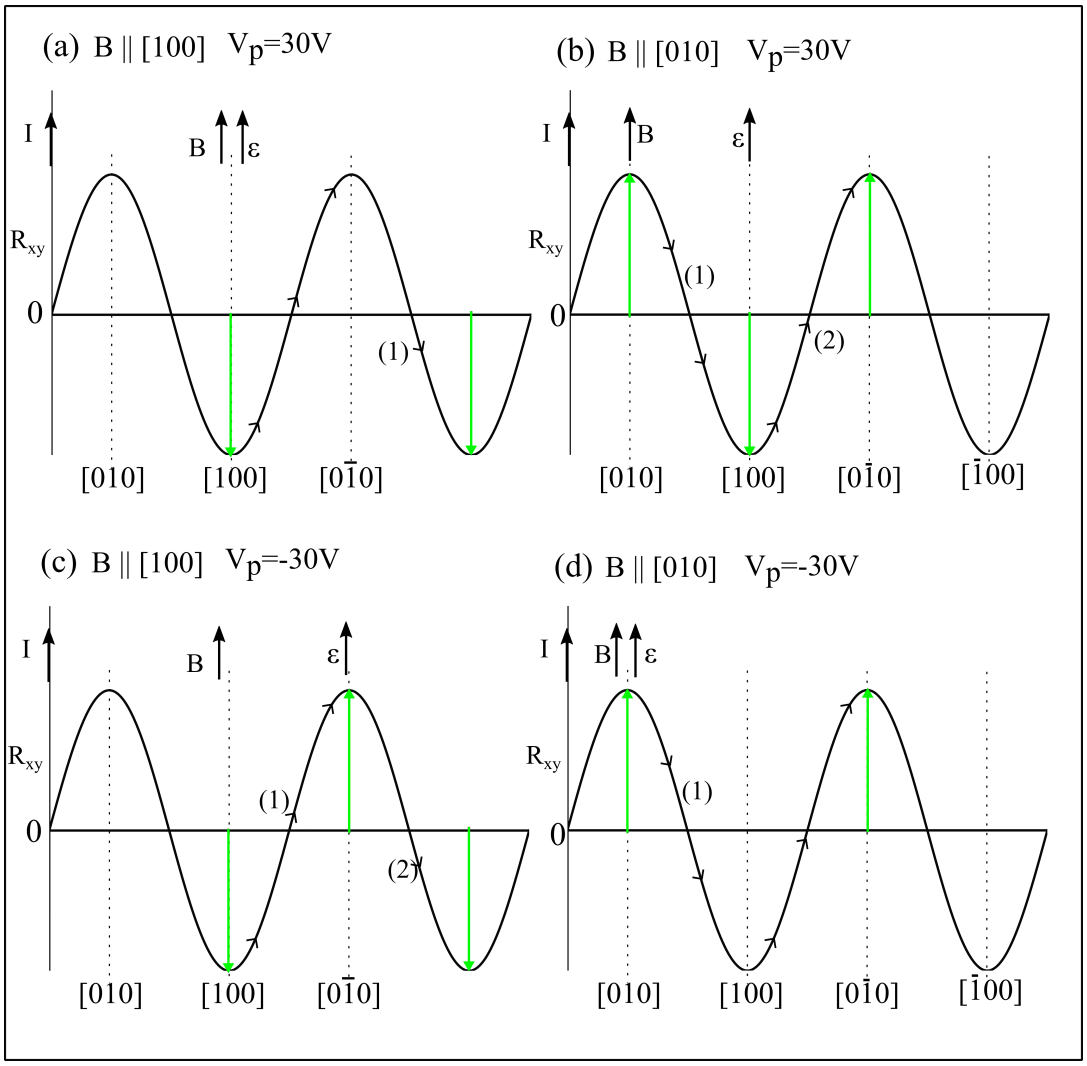

Figure 4.34: Schematic of the magnetisation reversal for sample S422 with magnetic field varied along the [100] and [010] directions at V_p=+30 V and -30 V. The magnetisation is represented by the green arrow, and the transverse resistance is a $sin(2\theta)$ function.

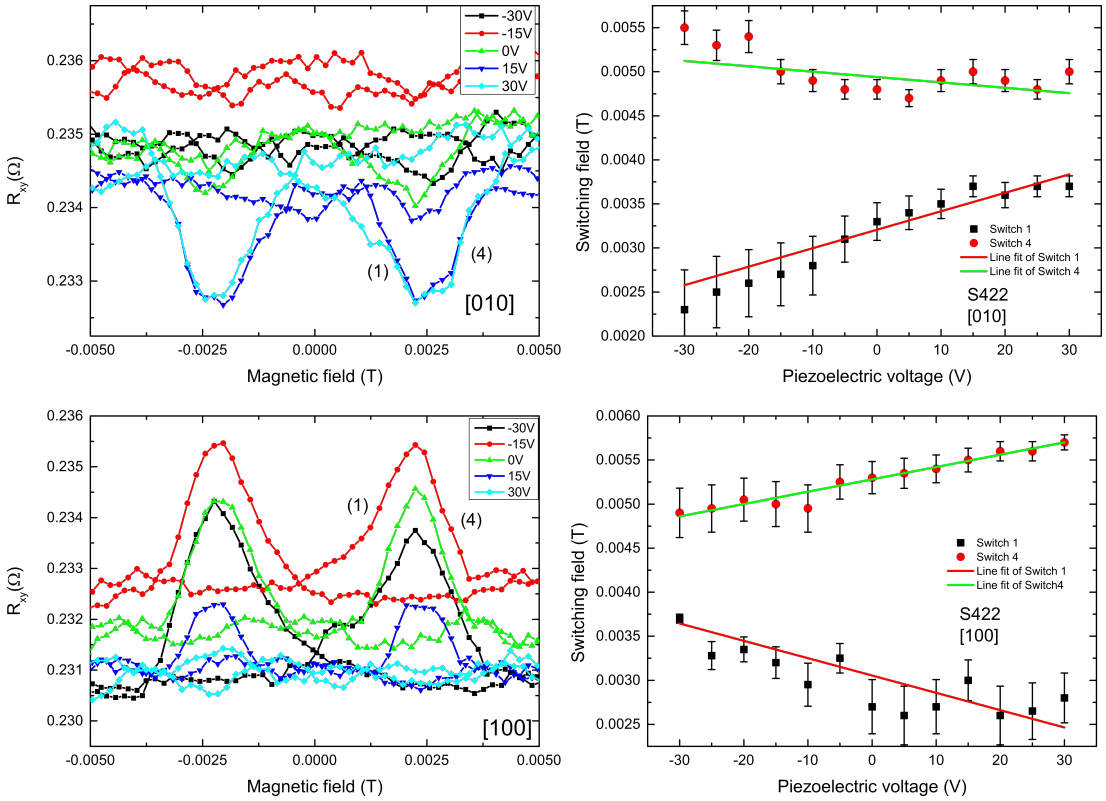

Figure 4.35: Variation of the measured transverse resistance and switching fields with piezoelectric voltage for sample S422, when magnetic field is varied along the [010] and [100] directions

For the crystal directions which showed magnetisation switching, this switch from one less easy axis to another more easy axis does not give a large change in the longitudinal AMR, as the former follows a $cos(2\theta)$ function. However the measured longitudinal resistance shown in Fig. 4.33 (b) demonstrates a change in the resistance of order ($\sim 2\times10^{-3}\Omega$) which is smaller than the change in transverse resistance ($3\times10^{-3}\Omega$). This should be because of the GMR as has been previously seen for sample S421 in Sec. 4.2.1.1 and the magnitude of the GMR is tiny compared to the AMR. Nevertheless this tiny change in resistance along with the offset in the measured longitudinal resistance for either field directions can be attributed to another factor as well which is coherent rotation of the magnetisation due to device misalignment and electron-magnon diffusion [191].When field is varied along the easy axes, the magnetisation of this layer would rotate by a small value before switching by 90° and can cause some additional resistance to the measured R_{xx} and seen as the offset resistance between the [010] and [100] directions at each voltage value. This has been schematically represented in Fig. 4.36 .

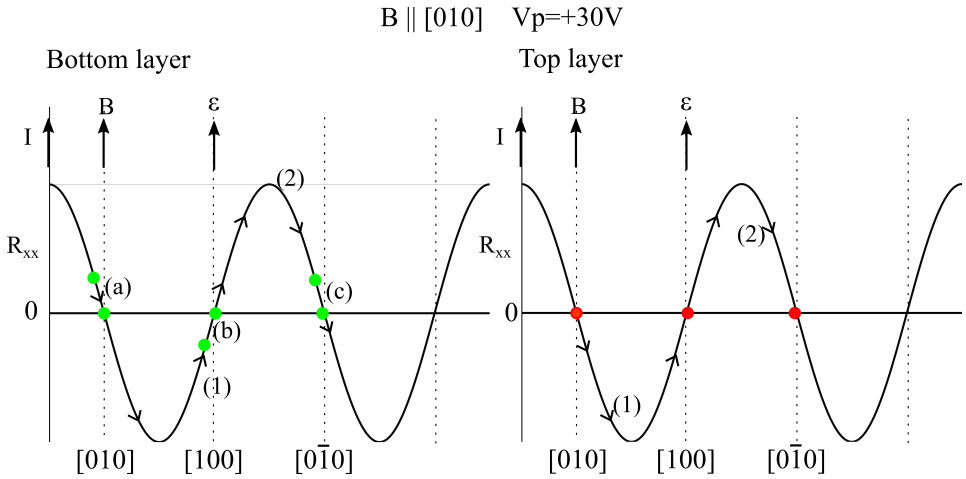

Figure 4.36: Schematic of the magnetisation reversal for sample S422 showing the change in the longitudinal resistance. The magnetisations for the bottom layer is indicated by green circle and for the top layer by red circle. It can be seen that due to rotation of the magnetisation of the bottom layer the longitudinal resistance is not zero when the magnetisation switches.

MOKE MH loops performed along the [100] direction at different piezoelectric voltages confirm the nature of the uniaxial strain- tensile or compressive at different voltage, and its effect on the magnetisation reversal. It can be seen from Fig. 4.37 that at +30 V there is a double step in the loop confirming a 90° switch while the MH loops at -30 V has no evidence of a step and is a 180° reversal.

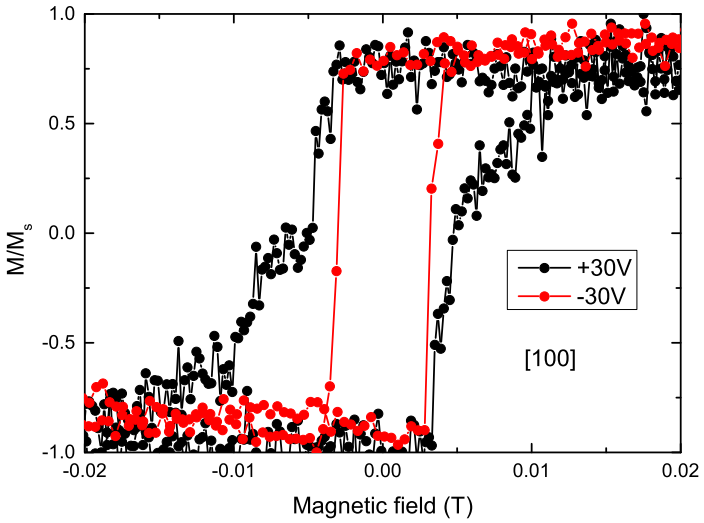

Figure 4.37: Measured MOKE MH loop for sample S422 when magnetic field was varied along the [100] direction at V_p= +30V and -30V

(ii) Magnetic field along $[1\bar{1}0]$ hard direction

The transverse and longitudinal measurements performed for magnetic field along the hard $[1\bar{1}0]$ directions are shown in Fig. 4.38 for a few piezoelectric voltages. In the transverse resistance the labels indicate the magnetisation switching processes identical to those observed for sample S421 in Fig. 4.14. The blue curve represents the field up-sweep while the red curve is the field up-sweep direction.

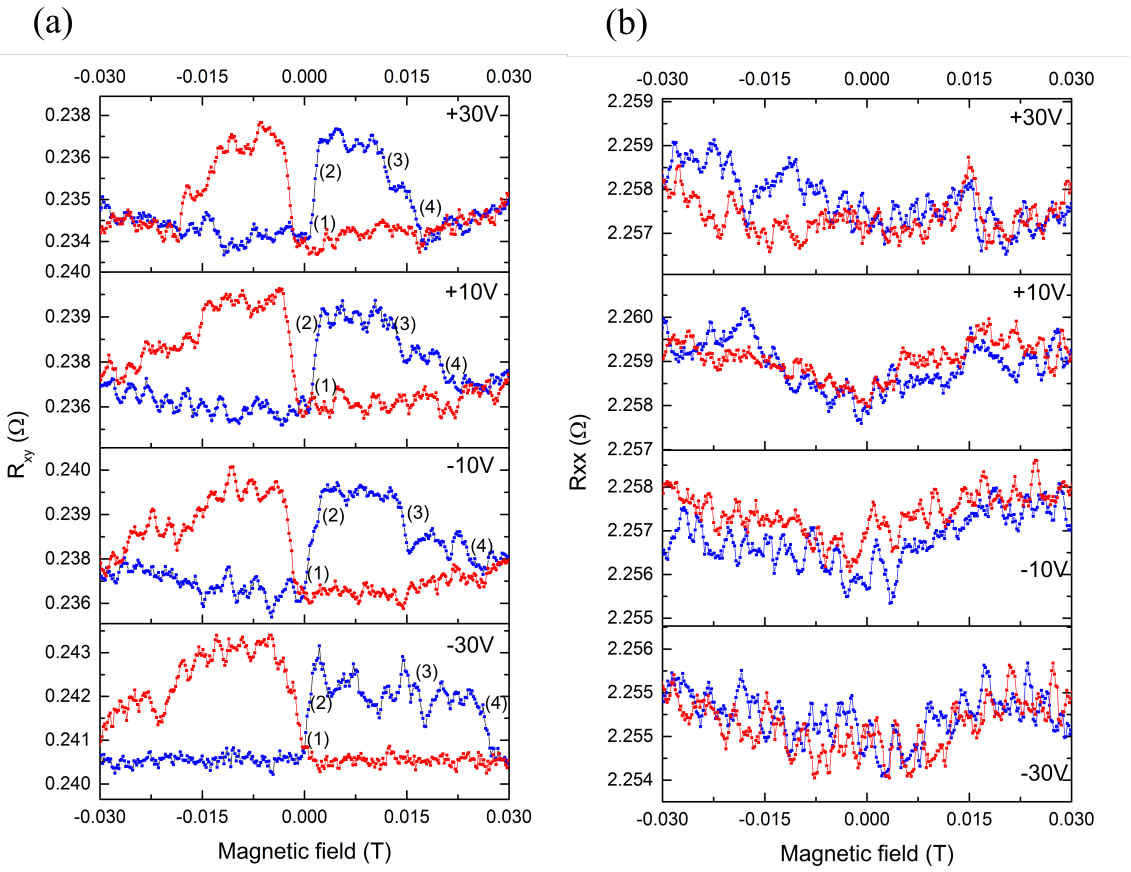

Figure 4.38: (a) Transverse and (b) Longitudinal magnetoresistance for field swept along the [1$\bar{1}$0] direction at different piezoelectric voltages for sample S422.

It is seen that the transverse resistance has a very similar characteristic as has been discussed before for sample S421 (Sec. 4.2.1.1) and the magnetisation reversal can be considered in a very similar process. Interestingly, the longitudinal resistance does not show any considerable large change in resistance except a lot of noise and a somewhat symmetric feature about the zero magnetic field value. Considering the field-down sweep case, it is observed that as the field strength decreases the resistance decreases and after the field changes sign the resistance starts increasing. This trend can be identified to the rotation of the magnetisation from the field direction to/ away the easy axes of the sample. The 90° switches do not make any observable contribution to the measured AMR component of R_{xx}. It was observed that there were very large peaks at the switching fields for sample S421, which were purely due to GMR. Since the GMR value for this sample is very small which is caused by the shunting of the current by the thicker spacer we do not observe any appreciable change in resistance, except the poor signal to noise .

The values of the magnetoelastic constants could not be obtained due to noisy strain calibration data (See Appendix B) and uncertainty of the absolute value of strain in each layer. It is not possible to determine the value of the strain dependent magnetoelastic constants. The variation of the measured transverse resistance showing the change to the switching fields have been shown in Fig. 4.39.

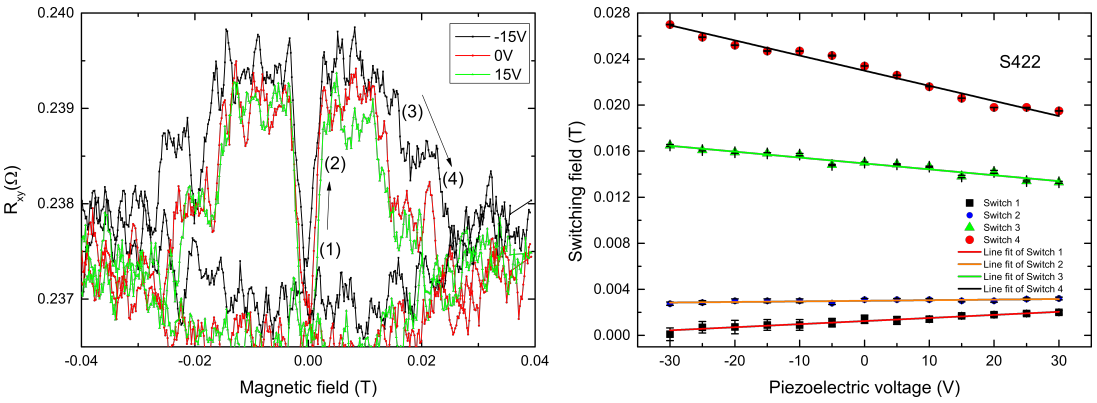

Figure 4.39: Variation of the switching fields with piezoelectric voltage for sample S422 when field is varied along the $[1\bar{1}0]$ direction.

4.2.2.2 Sample S420: 10 nm Al spacer

(i) Magnetic field along easy axis direction

The discussion for this sample follows the similar procedure as the previous samples. The normalised transverse resistance for the [010] and [100] directions shown in Fig. 4.40 demonstrate a large change in the AMR due to the 90° switch over the hard axis. The presence of peaks for all values of voltage suggests that the voltage induced strain is always tensile in nature like samples S419, and S421. The resistances have been normalised and the background resistance have been subtracted that could affect the judgement of the magnetoresistance feature. This was done only for this sample, as the measured resistance was very noisy due to bonding straight onto the sample. This was due to a fault in the thermal evaporator during the fabrication process.

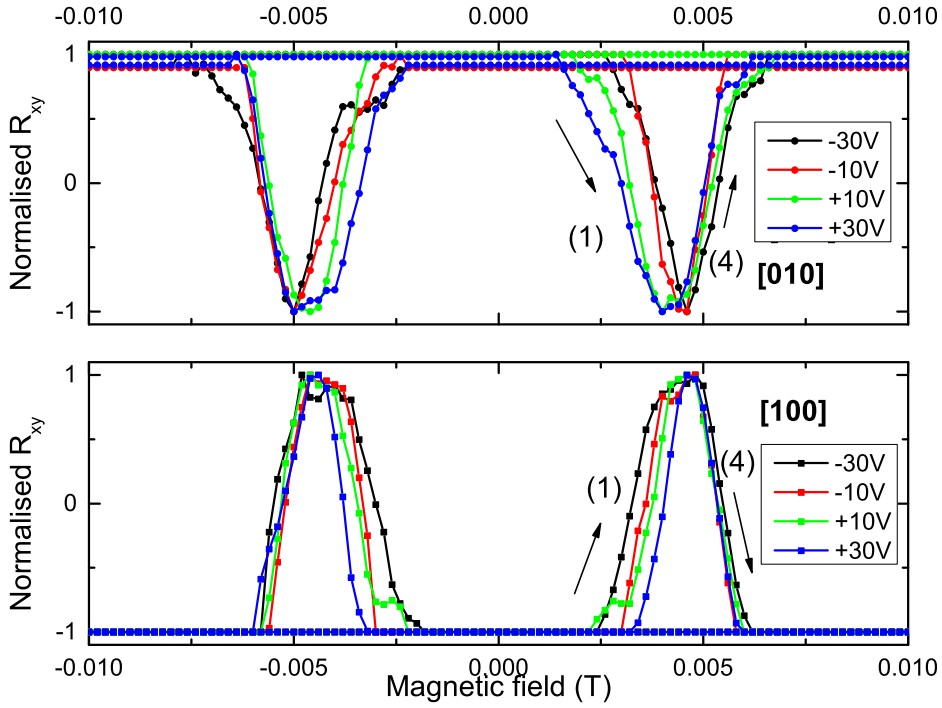

Figure 4.40: Transverse AMR for the [100] and [010] directions at different voltages across the transducer for sample S420.

As the thickness of the spacer layer is quite large the GMR value is extremely small and there are no sharp changes in the longitudinal resistance at any values of voltage. The 90° switches do not contribute to the longitudinal AMR. The longitudinal resistances at different voltage have been processed to remove the experimental noise by performing a moving point average over a 4 point window, and have been shown for the [010] and [100] directions in Fig. 4.41 just as an evidence to show that there is no observed GMR effect in this sample. The offset in the resistance is due to the transmitted strain which alters the resistance.

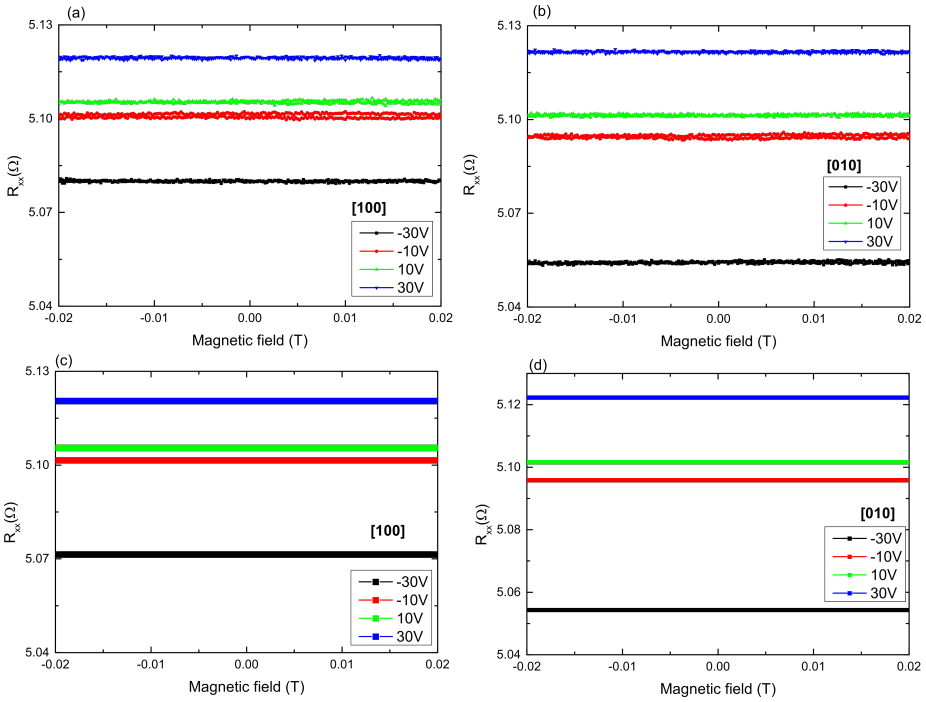

Figure 4.41: Measured longitudinal resistance for sample S420 when magnetic field is along [010] and [100] directions. (a,b) Raw, and (c,d) smoothed data showing no contribution of any GMR due to thick spacer layer.

The normalised MOKE MH loops are shown for the [010] and [100] direction in Fig. 4.42. It shows no significant change to the coercivity due to strain and also no step are observed at the switching events like the 5 nm spacer samples. This should be because the top layer is unaffected as most of the strain is blocked by the underlying layers and the substrate. A 180° switch is observed . However the Tr-AMR data showed changes to the switching fields with strain and has been shown in Fig. 4.43 . These switching fields are because of the 90° switch of the bottom layer. Therefore it is reasonable to state that the measured large change in transverse resistance for the [010] and [100] directions was only due to the 90° switch of the bottom layer. Even though there would be a relative angle difference between the magnetisation orientations of the top and bottom layer, no GMR was observed due to a spacer layer which is thick compared to the spin diffusion length.

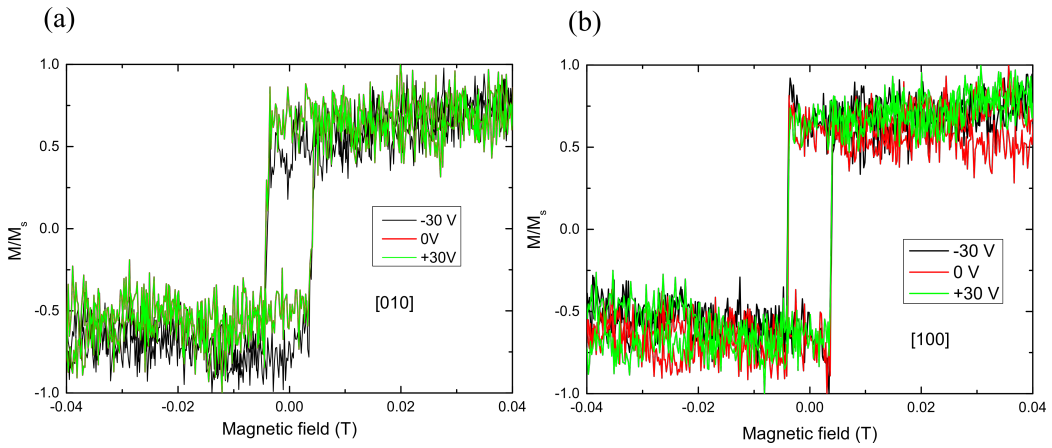

Figure 4.42: MOKE MH loops for the (a) [010] and (b) [100] directions. The strain does not have any effect on the coercivity of the top layer magnetisation.

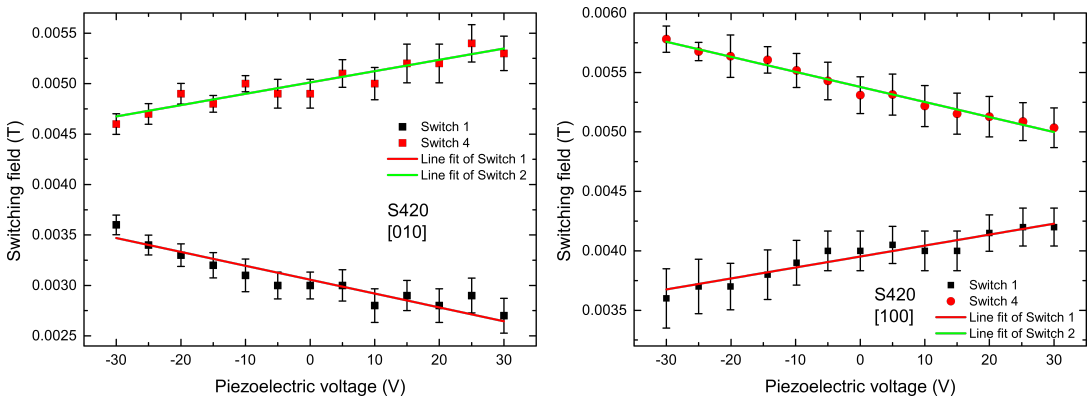

Figure 4.43: Variation of the switching fields labelled 1 and 4 with piezoelectric voltages for sample S420, when magnetic field was varied along the [010] and [100] axes.

(ii) Magnetic field along $[1\bar{1}0]$ hard direction

The field sweep for the hard $[1\bar{1}0]$ crystal direction has been performed and the measured transverse and longitudinal resistance have been illustrated in Fig. 4.44. The alphabetic labels in the figure describe the reversal process discussed here in the text and the numeric labels indicate the sudden switching process manifested as large change in resistances. The transverse resistance shows the identical feature like the previously described samples S421 and S422, and represents the magnetisation reversal process which can be summarised when the field is swept from a lower saturating value to a higher positive value as below :

(a) As the field strength decreases the magnetisation is pulled by the uniaxial

magnetic anisotropy along the [100] and rotates away from the [1$\bar{1}$0] towards the easy [100] direction. This causes increase in the transverse resistance and decrease in the longitudinal resistance.

(b) As the field changes sign, the magnetisation does a 90° switch towards the [010] direction. This causes a large change in transverse resistance but no significant change to the longitudinal resistance. Since the GMR value is tiny no large change in longitudinal resistance is observed.

(c) The magnetisation then rotates for a certain angle and then switches towards the [100] but is not oriented along the [100]. This combination of reversal decreases the R_{xy} and increases the R_{xx}.

(d) The magnetisation then realigns towards the field direction along the [1$\bar{1}$0] which causes further decrease in transverse resistance and increase in the longitudinal resistance.

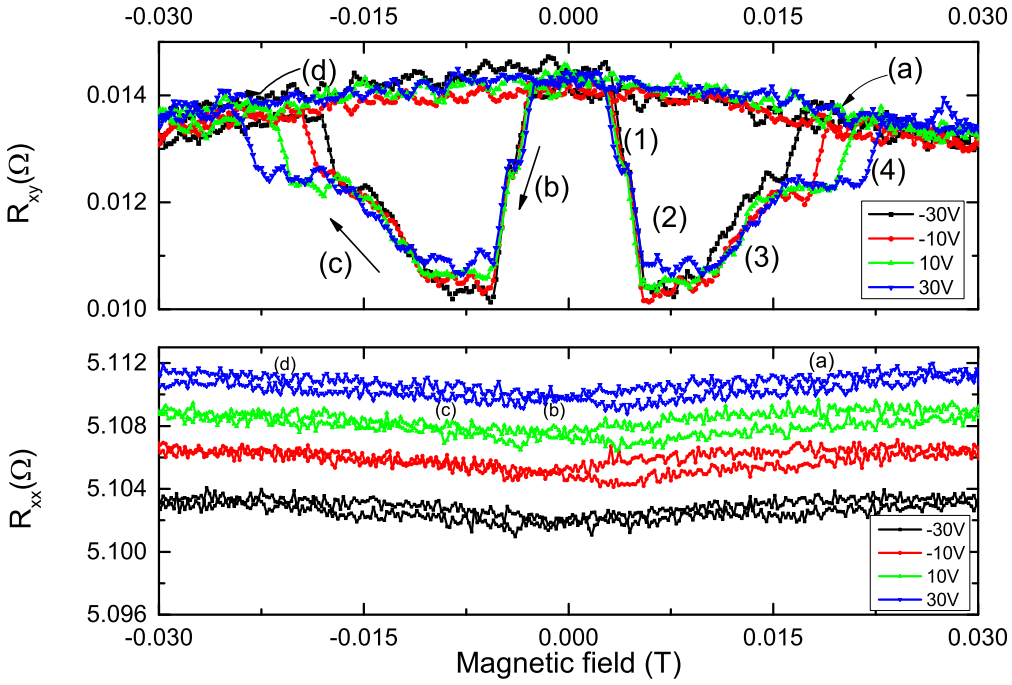

Figure 4.44: Measured transverse and longitudinal resistance for sample S420 with field varied along [1$\bar{1}$0] direction. Due to negligible GMR contribution R_{xx} is purely AMR and shows no large change in resistance. The labels in the figure have been discussed in the text.

As can be seen the voltage induced strain affects the switching fields, with switch 4 being affected the most. It is reasonable to assume that this switch corresponded to the magnetisation switching for the bottom layer grown on the GaAs substrate. The variation of the switching field with voltage calculated from the transverse resistance data has been shown in Fig. 4.45.

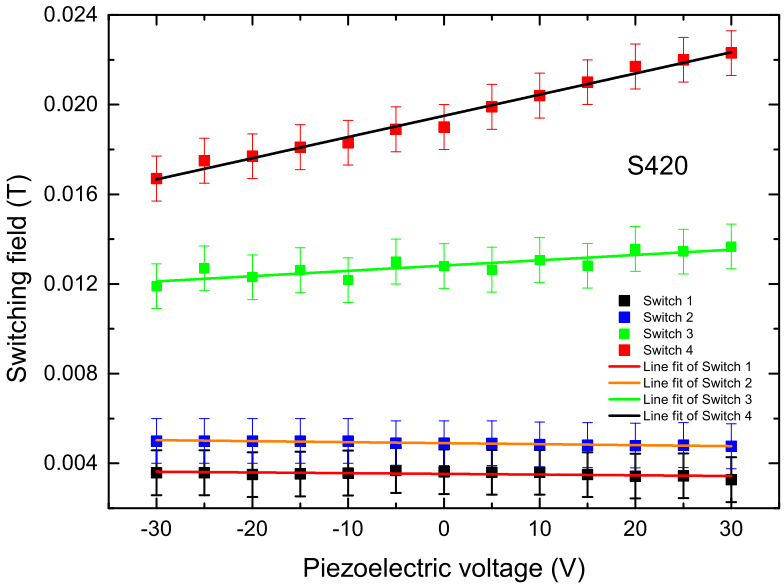

Figure 4.45: Variation of the switching fields with piezoelectric voltages for sample S420, when magnetic field was varied along the $[1\bar{1}0]$ axes.

4.2.3 Effect of voltage induced strain to the magnetisation switching fields

In this section a comparative analysis is discussed about the effect of the voltage induced uniaxial strain on the switching fields. The variations of the switching fields with the piezoelectric voltage were already shown when the individual samples were discussed for different field orientations. Here a quantitative calculation is performed for all the samples is performed. The variation of the switching fields have been plotted against the piezoelectric voltage for each field directions for individual samples and a linear fit is performed, the gradient of which gives the magnitude of the effect of strain to alter the magnetisation reversal processes. The switching fields were calculated by taking the mean value of the magnetic field before and after the switching event from the transverse resistance data. The error

bars are the normalised difference between the mean value and the lower switching field value.

(i) Magnetic field varied along the [010]/[100] directions.

The variation of the switching fields with the voltage across the transducer, when magnetic field was varied along the [010]/[100] crystal directions for all the investigated samples are shown in Fig.4.46. The scattered points in the figure denote the experimentally calculated values of the switching fields and the line is the linear fit to get the gradient of the switching fields. The gradients have been listed in Table 4.1 for all the samples.

Sample	Direction	Switch 1 ($\times 10^{-5} TV^{-1}$)	Switch 2 ($\times 10^{-5} TV^{-1}$)	Switch 3 ($\times 10^{-5} TV^{-1}$)	Switch 4 ($\times 10^{-5} TV^{-1}$)
S419	[010]	-5.2 ± 0.2			1.3 ± 0.2
	[100]	4.2 ± 0.2			-1.6 ± 0.3
S420	[010]	-1.4 ± 0.1			1.1 ± 0.2
	[100]	0.9 ± 0.1			-1.3 ± 0.1
S421	[010]	-0.5 ± 0.3	-0.3 ± 0.1		0.2 ± 0.1
	[100]	0.2 ± 0.1	-0.6 ± 0.1		-0.8 ± 0.2
S422	[010]	2.1 ± 0.2			-1.1 ± 0.3
	[100]	-1.9 ± 0.3			1.4 ± 0.1

Table 4.1: Gradient of the line fits to the switching fields for the [010] and [100] direction for the investigated samples. The blank spaces represents that the independent switching could not be resolved, and doesn't indicate the absence of the switching.

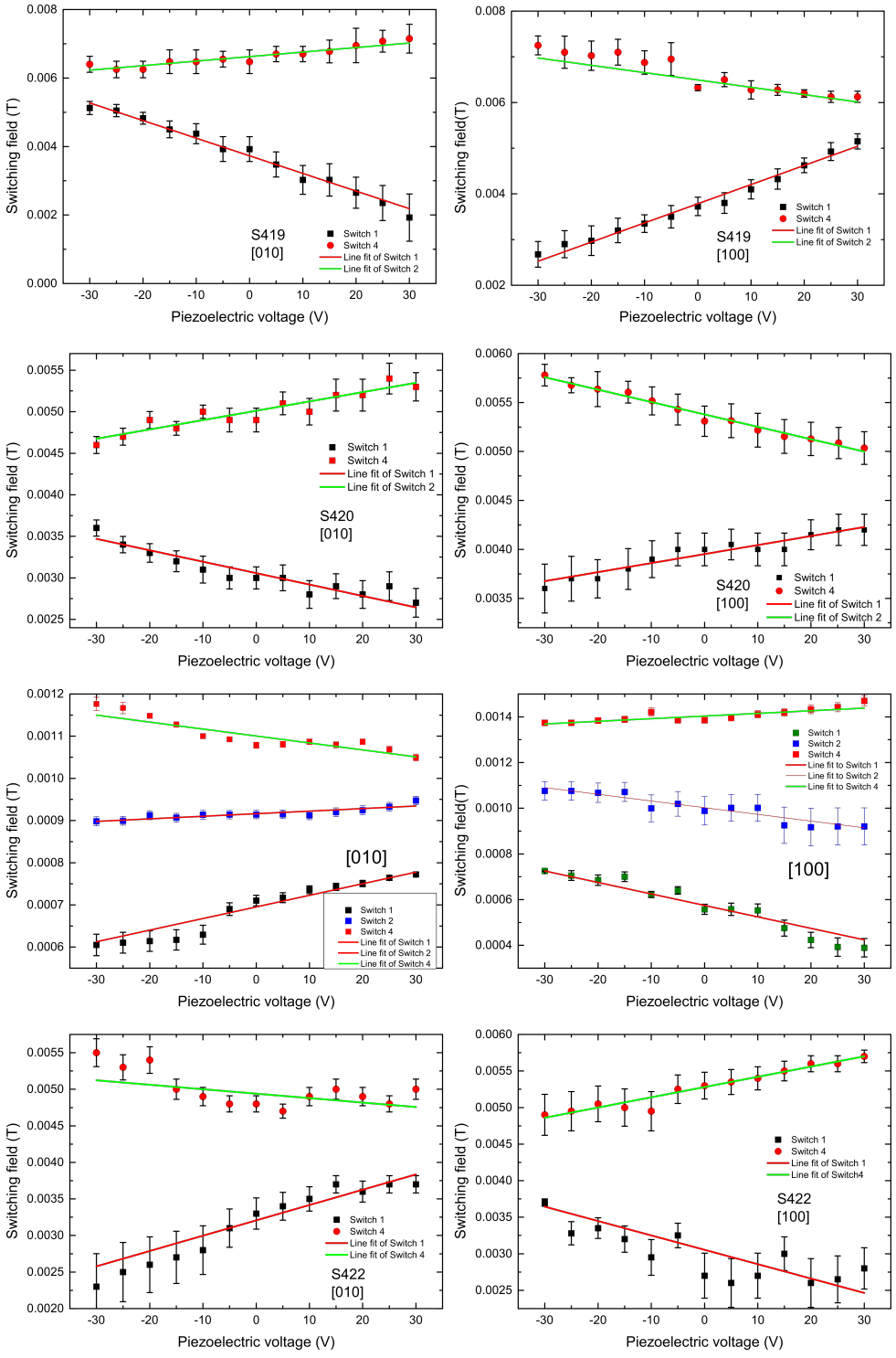

Figure 4.46: Experimentally calculated switching fields for magnetic field along the [010] and [100] directions at different values of voltage across the transducer along with the line fits for all the investigated samples .

It is seen that most of the samples except sample S421, only showed two switching events corresponding to the 90° magnetisation switching. This is due to the limited resolution of the experiment which did not pick up the independent switching of the magnetisation. However for sample S421, the independent switching for the layers were observed at least for one of the switching process. The blank spaces in the table represents that the independent switching could not be resolved, and does not indicate the absence of the switching.

Qualitatively it can be seen that for all the samples except sample S422, when magnetic field is along [010] direction the gradient of switch 1 (and 2) is negative while the gradient is positive for switch 4. Similarly when field is varied along the [100] crystal direction, the gradient of switch 1 (and 2) is positive, while it is negative for switch 4. This is due to the fact that for the case of [010] direction, switch 1 (and 2) is the magnetisation reversal from the [010] towards the [100] and switch 4 is the reversal from [100] to [010]. At high values of voltages the tensile strain is higher along the [100] than when the voltage is lower, therefore it will need lower magnetic field to cause switch 1, but because of this it needs a stronger field to switch the magnetic field to cause switch 4. The [100] case can be explained similarly. It will need higher fields to switch the magnetisation away from the [100] when the voltage is high but lower fields to switch the magnetisation towards it.

Quantitatively it is seen that the absolute gradients are higher for the Al spacer samples compared to the Cu spacer sample except for sample S422, where it has already been established in Sec. 4.2.2.1 that the strain is either tensile or compressive in nature. Possible reasons for this are the enhanced magnetostriction due to Fe-Ga-Al mixing[81], and crystalline nature of both the ferromagnetic layers as seen by TEM images discussed in Ch. 3. The crystallinity may cause distinct magnetostriction values which are order higher than the magnetostriction value for polycrystalline samples as reported by Dean et al[188]. It may be also due to different strength of the transmitted strain in each sample which can be accounted to the sample mounting process.

The inverse behaviour of the switching fields sample S422 compared to other samples will be discussed following the observations for magnetic field along the $[1\bar{1}0]$ direction.

(ii) Magnetic field varied along the $[1\bar{1}0]$ direction.

The variation of the switching fields at different piezoelectric voltages for field varied along the $[1\bar{1}0]$ crystal direction, for all the investigated samples is described in this section. It was seen in the previous sections that for field along this direction there

were distinct magnetisation process due to independent magnetisation reversal of the individual $Fe_{1-x}Ga_x$ layers. This features were labelled (1) to (4) and denoted magnetisation switching over the hard axes for each layer (See Fig.4.16, 4.28, 4.38, and 4.44). For samples S421, 22, and 23 the measured transverse resistances had comparable features, except for sample S419 where the switch 3 was not very consistent at different piezoelectric voltages.

Fig. 4.47 shows the variation of the measured switching fields along with the linear fit for all the samples along the $[1\bar{1}0]$ direction. The gradient values have been listed in Table 4.2 .

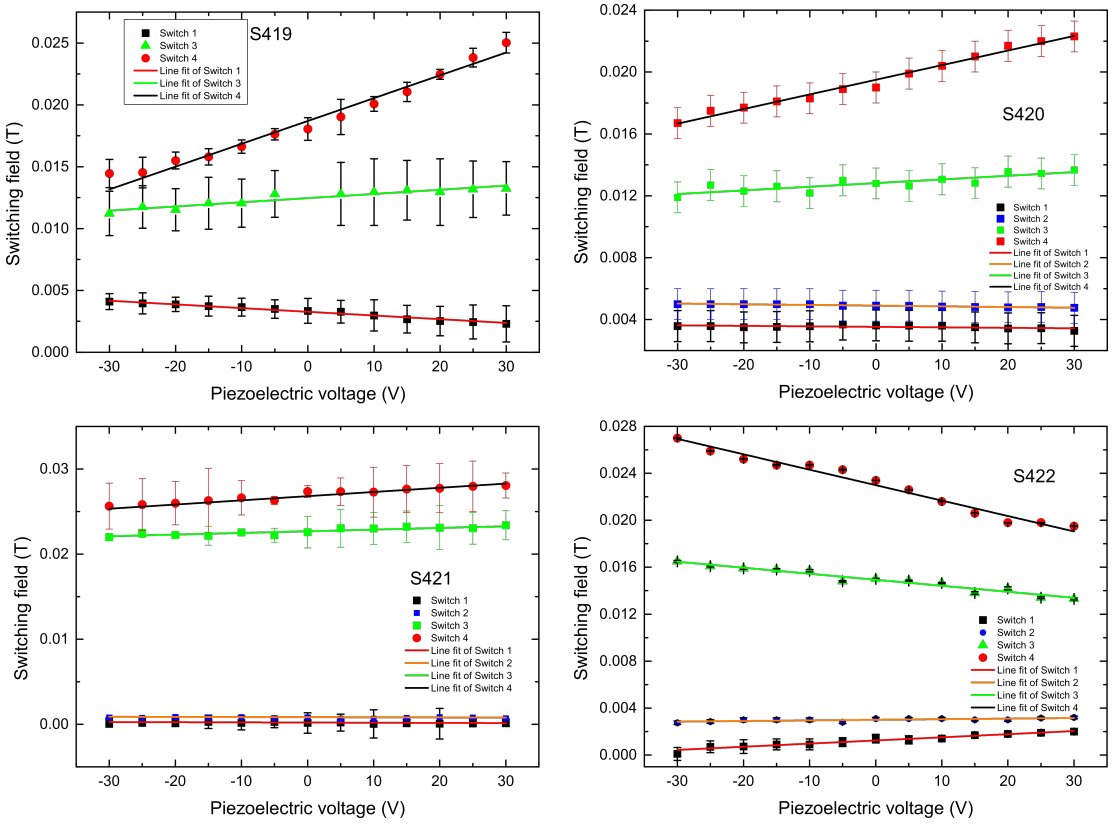

Figure 4.47: Experimentally calculated switching fields for magnetic field along the $[1\bar{1}0]$ crystal axes at different values of voltage across the transducer along with the line fits for all the investigated samples .

Sample	Switch 1 ($\times 10^{-5} TV^{-1}$)	Switch 2 ($\times 10^{-5} TV^{-1}$)	Switch 3 ($\times 10^{-5} TV^{-1}$)	Switch 4 ($\times 10^{-5} TV^{-1}$)
S419	-3.0 ± 0.2		3.4 ± 0.4	18.4 ± 0.7
S420	-0.32 ± 0.01	-0.45 ± 0.04	2.4 ± 0.3	9.5 ± 0.3
S421	-0.21 ± 0.06	-0.24 ± 0.1	1.9 ± 0.4	4.9 ± 0.9
S422	2.7 ± 0.2	0.5 ± 0.1	-5.1 ± 0.4	-13.1 ± 0.6

Table 4.2: Gradient of the line fits to the switching fields for magnetic field along $[1\bar{1}0]$ direction for all the investigated samples.

As can be observed from the above plots and table, the switching fields labelled as 1 to 4 show very similar behaviour for all the samples except for sample S422. However the gradients are different for corresponding switches in each samples, that being due to different strength of the transmitted strain and perhaps distinct magnetostriction value as was discussed previously for the [100]/[010] directions. For the first three plots, it is seen that the switch labelled 1 and 2 are not much affected by the strain compared to switch 3 and 4. It is due to the cooperative competition between the magnetic field and the uniaxial strain to decide the minimum of the magnetic free energy. Switch 1 and 2 are due to the magnetisation switching towards the strain direction and switch 3 and 4 are due to the magnetisation switch away from the strain axes direction for each layer. As the voltage increases, the tensile strength along the [100] increases as well, and therefore it will need less magnetic field to cause switch 1 and 2. But it will incur extra energy costs to align the magnetisation away from the strain and therefore need higher magnetic fields to cause switch 3 and 4.

However the gradients are opposite for sample S422 in this field configuration as well, similar when the field was applied along the [100]/[010] directions. This would mean that at positive voltages the tensile strain is along the [010] direction instead of [100] which could be due to during the device mounting on the piezoelectric transducer.

4.3 Summary

In summary the magnetisation reversal processes for $Fe_{1-x}Ga_x$ samples under the influence of an uniaxial strain are studied using magneto-optical and magnetotransport measurements. By using the values of the magnetic anisotropy and saturation magnetisation extracted from the FMR experiments, the magnetisation reversal

processes were modelled. The magnetisation reversal processes were found to be qualitatively the same for all samples and gave rise to changes in the longitudinal and transverse resistances that were due to either the AMR or the GMR or both. The model aids to the experimental observations of the manipulation of the magnetisation by the voltage induced uniaxial strain. Magnetotransport and magneto-optical measurements were performed on the bilayer $Fe_{1-x}Ga_x$ samples that were studied and described in Ch. 3. It was observed that the 5 nm thick spacer samples demonstrated a significant contribution of GMR to the measured longitudinal resistance, while this contribution was negligible for the 10 nm thick spacer samples. The GMR was due to the different magnetisation state of each layer, or in other words due to different magnetisation orientation of each layer which resulted in a relative angular difference between the magnetisations. The magnetisations in the different FeGa layers reversed at different fields due to the fact that the layers have different magnetocrystalline anisotropy energies and different magnetostriction coefficients.

The magnetisation reversal process for all the samples was investigated with the magnetic field varied along different crystal directions. For the [010]/[100] directions the large change in transverse MR has been understood to be the magnetisation switch corresponding to [010]→ [100] and vice versa. For the hard $[1\bar{1}0]$ directions the magnetisation reversal is a combination of rotation towards the applied field direction and two switches over the hard axes. However the Al spacer samples showed a high response to strain compared to the Cu spacer samples. The change in the switching fields for the Al samples have been observed to be larger than the Cu samples. The Cu samples demonstrated a higher GMR contribution. The higher strain response is possibly due to enhanced magnetostriction value because of the crystalline nature of both the top and bottom layers as shown by HR-TEM. Dean [188] had reported that the structural property determines the magnetostriction value, and for polycrystalline $Fe_{1-x}Ga_x$ samples $\frac{3}{2}\lambda_{100} \approx 0.3 \times 10^7 Jm^{-3}$, while for crystalline samples the magnetostriction values can be as high as $2.1 \times 10^7 Jm^{-3}$. The higher GMR in Cu samples compared to Al spacer sample is due to thicker and more resistive Al layer which has interfacial imperfections and intermixing effects which reduce the mean spin diffusion length. The effect of strain to the switching fields is higher for the 5 nm spacer sample than the 10 nm spacer samples, due to attenuation of most of the transmitted strain by the substrate, and the ferromagnetic- spacer layer.

It was noticed that the curing process of the epoxy mixture leads to an inbuilt

strain in the hybrid structures which creates a tensile strain to be always present in the hybrid structure. Sweeping the voltage to a negative value does not produce a compressive strain. Therefore changing the voltage leads to different and may be low tensile strain that alters the magnetisation switching fields, except sample S422 where the voltage at +30 V and -30 V demonstrated manipulation of the easy axis from the [010] to [100] and vice versa. Due to this inaccuracy in determination of the absolute strain values in each layer for all the samples, the calculation for the exact values of the magnetoelastic constants is not possible. However for sample S421 the determined values of $1.4 \times 10^{-7} Jm^{-3}$ and $0.46 \times 10^{-7} Jm^{-3}$ for the bottom and top layer resulted in switching fields variation at different calibrated strain whose gradient were equal to the experimental switching fields. Keeping this values fixed and changing the domain wall depinning energy resulted in match of the switching fields for one of the layers. Therefore to an approximation these calculated values were able to replicate the experimental features, however due to insufficient knowledge of the absolute strain in each layer the switching fields do not match. The same values were used for the 5 nm Al spacer sample as well and the modelled data qualitatively explained the experimental features. However for the 10 nm spacer samples the strain variation was too noisy to draw any quantitative conclusion. The inability to calculate the exact magnetoelastic coefficients can be attributed to (a) absolute strain estimate in each layer, (b) depinning effects at device boundaries, (c) resistance contribution of each layer, (d) enhanced magnetostriction due to spacer.

Nonetheless the values of the coefficient for the bottom layer ($1.4 \times 10^{-7} Jm^{-3}$) is found to be of the same order as has been reported previously to be $1.5 \times 10^{7} Jm^{-3}$[101], $1.6 \times 10^{7} Jm^{-3}$[100]. The significant reduction in the magnetostriction value for the top layer may be associated with the reduced Ga content, polycrystalline nature of the layer and the associated non- uniformities in the layer and have been reported earlier to be $0.3 \times 10^{7} J/m^{3}$ for sputter grown polycrystalline FeGa samples on Si substrate[188].

The mechanism of the magnetisation reversal along with the values of the magnetoelastic coefficients will be used in the next chapter to simulate the operating parameters for a strain mediated non-volatile memory cell.

Chapter 5

Design parameters for a stress operated magnetic memory device

5.1 Introduction

In this chapter, the design and operating parameters for a stress mediated magnetic memory cell are proposed. The manipulation of the magnetisation on the basis of energy efficiency, rate of reversal and processing times, degree of reversal, and repeatability of the process are topics of interest for the development of novel logical and magnetic memory storage devices. The architecture using electrical current or magnetic field to locally alter the magnetisation state in magnetic random access memory, has a major drawback of spatial localisation of the field and the effects such as Joule heating, low energy efficiency and lower processing times. As shown in the last chapter, strain can lead to change in the coercivity of the magnetisation for a single domain particle. The voltage induced in-plane uniaxial strain alters the magnetisation process of the bilayers which is manifested as the change in switching fields. It is therefore reasonable to state that selective orientation of the magnetisation of individual ferromagnetic layers by proper application of an in-plane strain is possible.

By using the magnetic anisotropy values, saturation magnetisation and magneto-elastic coefficients calculated from the experiments and modelling in the previous chapters (3 and 4), the magnetisation variation for a hybrid structure under the influence of an in-plane uniaxial strain has been discussed in this chapter. The proposed memory structure comprises arrays of bilayer films of $Fe_{1-x}Ga_x$ separated by thin non-magnetic spacers and bonded to a large piezoelectric transducer which can produce a significantly large in-plane strain as illustrated in Fig. 5.1.

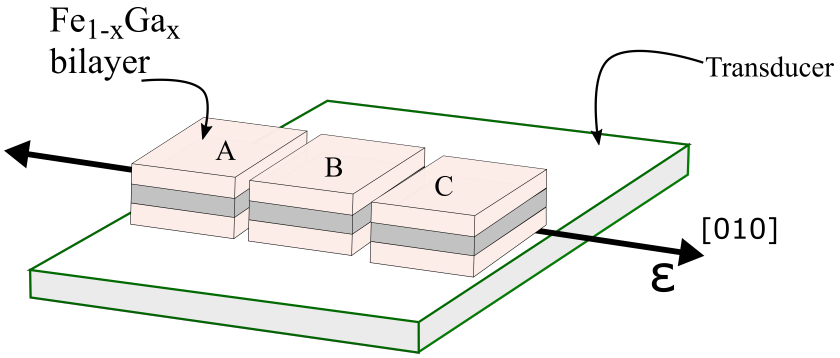

Figure 5.1: Stress operated magnetic memory representation.

5.2 Functionality

A single hybrid ferromagnetic bilayer structure has a distinct magnetic free energy landscape for each layer which has contributions from the magnetocrystalline anisotropy energy along with the magnetoelastic energy. The presence of easy and hard axes of magnetisation which can be manipulated by strain, leads to the understanding that the magnetisation orientation can be controlled by strain only. In order to demonstrate the performance of this memory cell, the operating parameters for a single structure are described. This involves solving the free energy equation (Eqn. 5.1) where θ is the angle between the magnetisation and the [010] and ϕ is the angle between the magnetic field and [010], using a MATLAB routine.

$$E = -H_{ext}M_s cos(\phi - \theta) + K_u sin^2(\theta) + \frac{1}{4}K_c sin^2 2\theta + B\epsilon sin^2\theta \qquad (5.1)$$

H_{ext} is a weak in-plane magnetic field which is applied externally to disturb the magnetisation from the easy axis so that the sweeping strain is able to manipulate the magnetisation orientation. The MATLAB routine then finds the minimum energy conditions for the magnetisation orientation θ , $dE/d\theta = 0$ and $d^2E/d\theta^2 > 0$ for each value of strain as it is swept from a positive value to a negative value and vice versa. A positive strain means a tensile strain along the [100], while a negative strain specifies a compressive strain along the [100] shown in Fig. 5.2. At sufficient strength of strain, it will be possible to orient the magnetisation towards the strain direction and then re-orient it back at the opposite sign of strain.

As the samples have different magnetocrystalline anisotropies, saturation magnetisation and magnetostriction values, the free energy of each layer at a specific strain will yield different values of the magnetisation direction. This, when solved to get the angles of magnetisation for each layer, will result in different values of

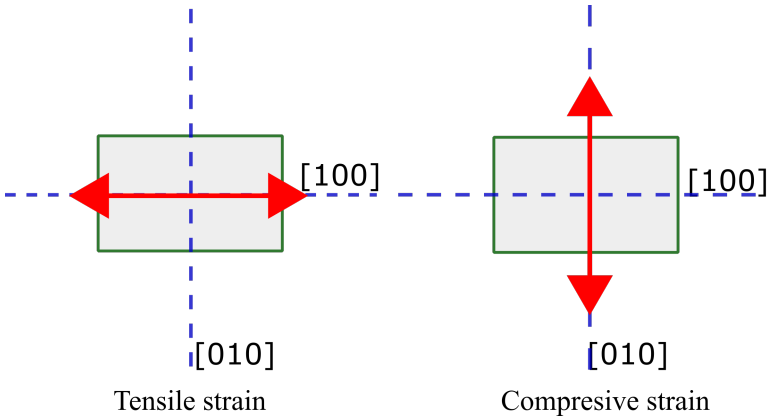

Figure 5.2: Nomenclature to define the positive and negative strain. A positive strain means a tensile strain along the [100] while a negative strain specifies a compressive strain along the [100] as represented by the red arrows.

the angle with respect to the [010] crystal direction.

The basic functionality is henceforth to determine the strain required to manifest a 90° switch of the magnetisation in the absence of any field sweep. It was observed in the previously discussed experiments that when the strain is tensile or compressive in nature the switching fields can be manipulated by the strain which alters the anisotropy energy. For sufficiently large strain, this can in principle change the direction of the easy axes. Though an effective switching field alteration is observed the system suffers with the following drawbacks:

- These results were observed for field sweep measurements. The proposed memory cell should ideally perform the strain manipulation of magnetisation at no external field applied.
- The gradient of the switching fields variation with respect to voltage is not the same for each sample. This is ascribed to inhomogeneity in the produced strain and in built strain during the curing process.
- The magnitude of strain produced is too small to induce rotation of the magnetisation direction in the absence of an applied field,(see Appendix B) due to the attenuation of the transmitted strain.

However this observation is very encouraging as it serves as an indication that these bilayer samples demonstrate a degree of control over the magnetisation direction due to tensile and compressive strain.

5.3 Modelling of strain mediated memory

Before the strain dependent magnetisation reversal is studied, the factors that influence the orientation of the magnetisation are described.

5.3.1 Strain: Strength and orientation

It will be shown in this chapter that the transducer should be able to produce an in-plane uniaxial strain of magnitude at least $\pm 0.3 \times 10^{-3}$ along the [100] direction. The [100] direction is chosen as the preferred strain direction as it is the easy axis determined by SQUID magnetometry and the magnetostriction is highest along this direction : $\frac{3}{2}\lambda_{100} = 395 \times 10^{-6}$[81].

5.3.2 Operation of strain mediated bilayer memory cell

By using the Matlab code the free energy of magnetisation for individual $Fe_{1-x}Ga_x$ layers was solved at different values of oriented magnetic field with the strain varied along the [100] crystal direction. The angle of the magnetisations for each layer were calculated and have been shown in Fig. 5.3 with respect to [010].

It is seen that by varying the strain the magnetisation angle for each layer has been modified. For some cases the magnetisation switches by approximately 90° and in some cases there is only a small rotation of the magnetisation orientation. This process can be divided into two broad sections depending on the direction of applied field.

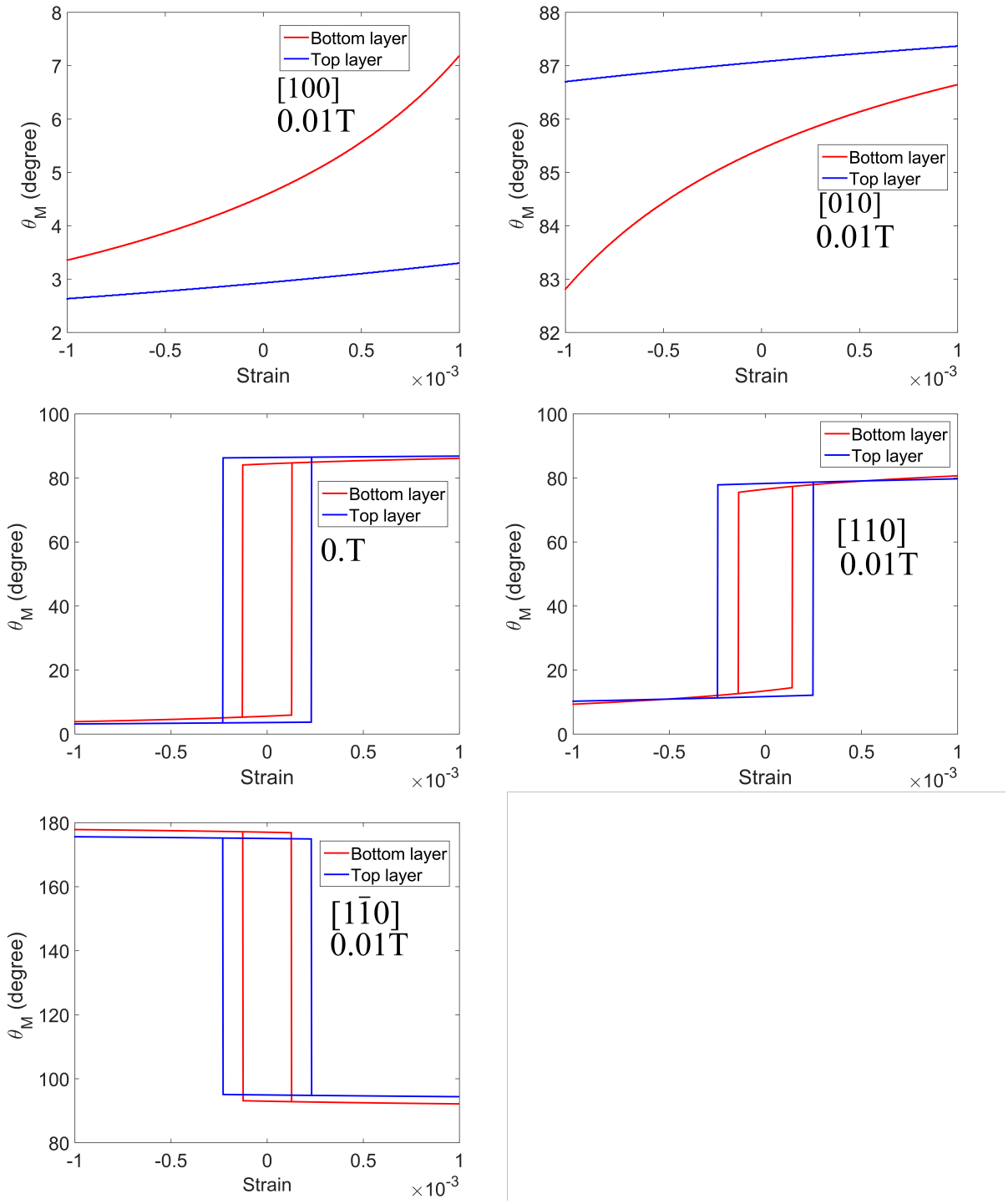

Figure 5.3: Calculated magnetisation angle with respect to the [010] crystal axes for the bottom (red) and top ferromagnetic layers (blue) when a uniaxial strain of magnitude $\pm 10^{-3}$ is varied along the [100] direction at different magnetic field strength and orientations.

1. Magnetic field along the [010]/[100] crystal directions.

This includes cases when (i) a magnetic field of strength 0.01 T is applied along the [010]/[100] crystal directions, and (ii) when no magnetic field is applied. The process of the magnetisation reversal is explained by showing the energy landscape at various strain values.

(i) At a constant field strength of 0.01 T.

For this scenario the energy variation for the [010] and [100] directions are shown in Fig. 5.4 for the bottom and top Fe-Ga layers. The energy landscape reveals that when a magnetic field of 0.01 T is applied, the magnetisation of the individual layers are oriented along the field direction irrespective of the value of strain. So it does not matter what the value of strain, the magnetisation will prefer to be in the minimum position and will not switch.

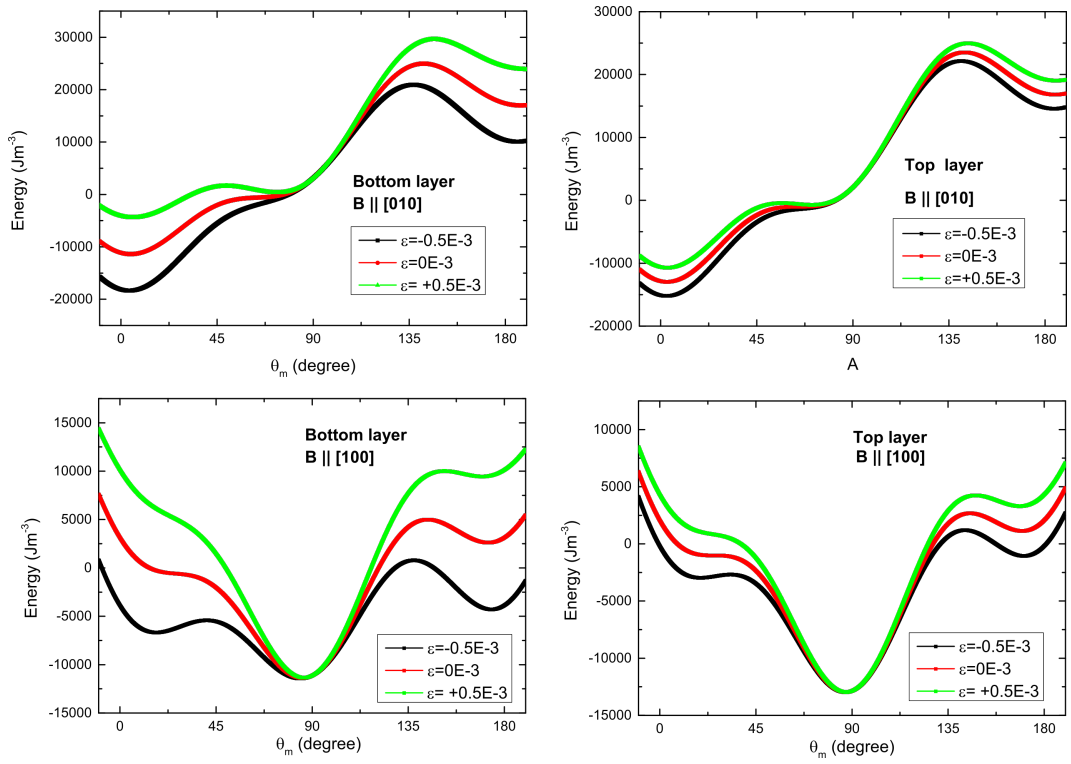

Figure 5.4: Energy landscape for individual Fe-Ga layers at different values of uniaxial strain when 0.01 T field is applied along the [010] and [100] directions. In the energy landscape plots, 0° refers to the [010] crystal direction.

(ii) At zero external field.

In this case the magnetisation has to overcome the magnetocrystalline and magnetoelastic energies to be able to perform a 90° magnetisation switch. It has

been shown in Fig. 5.3 that the magnetisation switches by 90° on sweeping the strain at zero field. The energy landscape for this configuration causing the 90° magnetisation switch has been presented in Fig. 5.5.

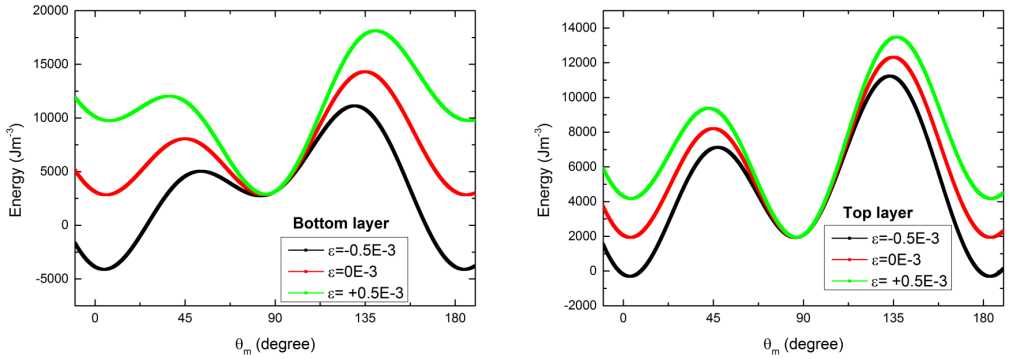

Figure 5.5: Energy landscape for individual Fe-Ga layers at different values of uniaxial strain when there is no external field applied. In the energy landscape plots, 0° refers to the [010] crystal direction.

The magnetisation reorientation by 90° depends on the relative depths of the minima in the energy landscape of the magnetic free energy. In order to qualitatively understand the magnetisation switching process the energy landscape is shown in Fig. 5.6. For magnetisation in state (a) to be oriented to state (b) it has to cross over the energy barrier (E_B) which hinders the transition. In order to overcome this, the domain wall nucleation must be assisted by external methods like thermal heating, small time varying magnetic field or stress at an offset angle, or an out-of plane excursion that will toggle the magnetisation to precess and overcome the large energy barrier When the difference in the energies between the two adjacent minima (local and global) is greater than the domain wall pinning energy, the magnetisation will switch to the state (b), $|E_a - E_b| \geq E_{DW}$.

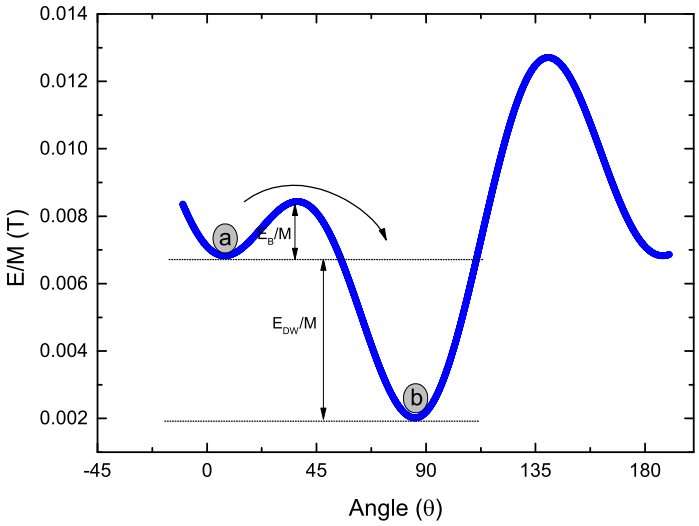

Figure 5.6: Schematic of the energy barrier and E_{DW} defining the magnetisation orientation.

For this case when the magnetic field is zero and at sufficient values of strain, the difference in the energy between the minima at [010] and the minima at [100] is greater than the domain wall de-pinning energy obtained from SQUID, and therefore a 90° orientation of magnetisation occurs.

2. Magnetic field along the [110]/[1$\bar{1}$0] crystal directions.

For the case of magnetic field along the [110] and [1$\bar{1}$0] directions, it was seen that the magnetisation switched by close to 90° in either case. The energy landscapes for these directions have been shown in Fig. 5.7 and can be seen are identical. However the magnetisation angles as the strain is varied are different. For field along [1$\bar{1}$0] direction , a $\sim$ 90° switch has been simulated. However for field along the [110] the angle switch is <90°.

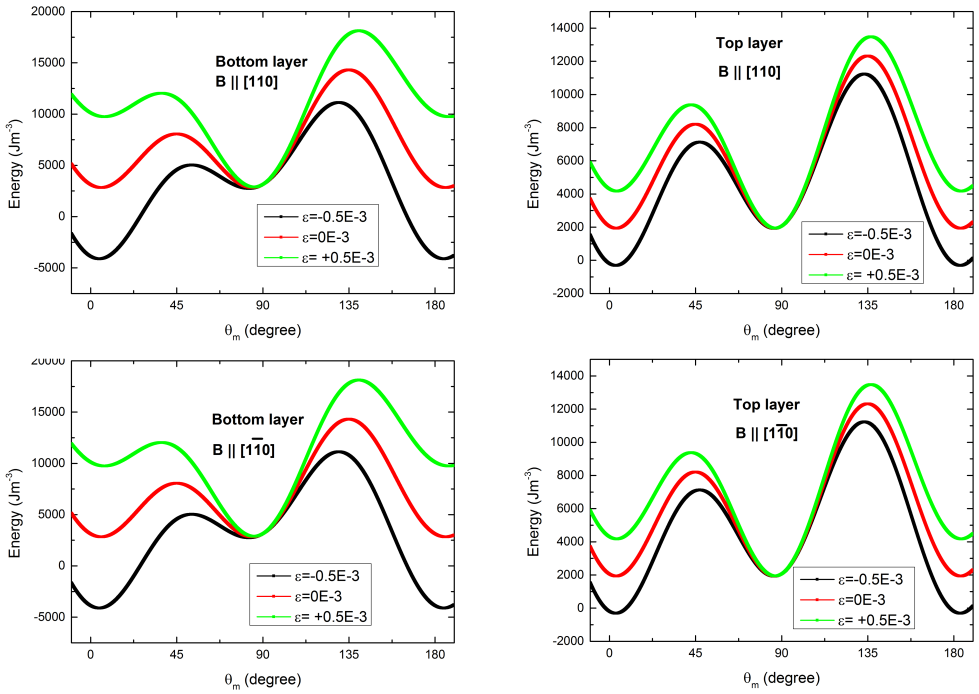

Figure 5.7: Energy landscape for individual Fe-Ga layers at different values of uniaxial strain when a 0.01 T field is applied along the [110] and [1$\bar{1}$0] directions. In the energy landscape plots, 0° refers to the [010] crystal direction and 90°denotes the [100] crystal axis.

The difference in the switching of the magnetisation angle as seen in Fig. 5.3 can be ascribed to the following reasons: (i) the initial field direction. For the [110] case at high values of tensile strain the magnetisation is along the [100] direction. Now when the strain becomes compressive, in absence of any field, the minimum of the energy should be along the [010], but due to the weak field the minimum is offset to a different value. However when the field is along the [1$\bar{1}$0] the minima occurs closer to the 180° due to the cooperation by the magnetic field applied at 135°. (ii) the uniaxial anisotropy term also plays a role as it breaks the symmetry between the [110] and [1$\bar{1}$0] as was seen from the SQUID MH loops in Ch. 3. This higher uniaxial term causes the difference in the relative angle difference for field along the [110] and [1$\bar{1}$0] directions.

Now then it is established that by applying an in-plane uniaxial strain it is possible to switch the magnetisation by 90° and vice versa, and this can be achieved by either applying a weak external field or no field at all.

For the purpose of using the bilayer cell as a non-volatile memory cell, the zero

magnetic field case is considered. The variation of the magnetisation angles for each layer with the varying strain is shown again for this case in Fig. 5.8

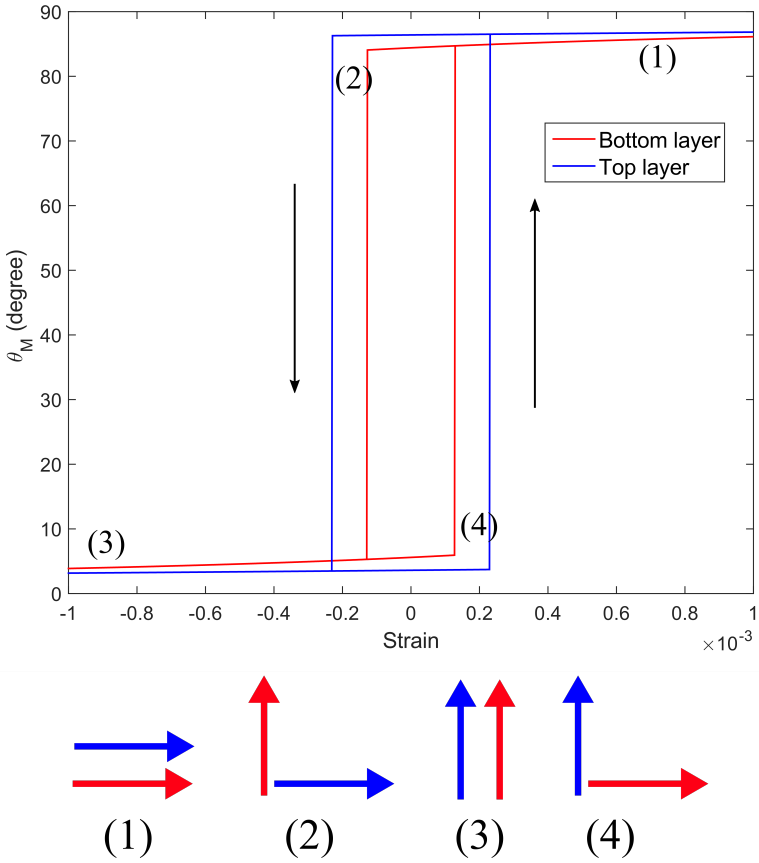

Figure 5.8: Modelled angles of magnetisation for H=0 case, when 90° switch is observed for both the layers. The different magnetocrystalline anisotropies and magnetoelastic constants lead to different switching strain values. This leads to four different states of magnetisation which have been labelled as (1) to (4). Horizontal arrows represent magnetisation towards the strain axis [100], while vertical arrows represents magnetisations oriented along [010] crystal direction.

As shown in Fig. 5.8, the magnetisation of the hybrid cell can have four different states labelled (1) to (4) and can be described a s such:

(1) When the strain is at a high tensile value, the magnetisation of both the layers are oriented along the [100] strain direction.

(2) As the strain changes to a compressive along [100], the bottom layer switches by 90° towards the [010], while the top layer stays along the [100]. This

creates a mutual angle difference in the magnetisations due to orthogonal orientations of the magnetisations.

(3) As the strength of the compressive strain increases, the top layer's magnetisation orients along the [010].

(4) When the strain changes to tensile values, the bottom layer switches first towards the strain direction due to higher magnetoelastic constant causing another orthogonal state. This is followed by parallel configuration again **(1)** at higher tensile strain values.

For the stacked multilayer system, the different magnetisation states can be represented by binary states, for example, $|0>$ for magnetisation parallel to the [010] and $|1>$ for magnetisation parallel to the [100]. Therefore the distinct four states can be written as: $|1,1>$, $|0,1>$,$|0,0>$, and $|1,0>$ for the states labelled (1) to (4) respectively. In order to use these multiple magnetisation states as a memory element the reading mechanism must be able to resolve these independent magnetisation states.

For the prototype cell, the read out approach can be performed by using the transverse AMR . A Hall bar can be fabricated on the bilayer with a constant current along the $[1\bar{1}0]$ direction. Since the cell demonstrates four distinct states, each with different orientations of the magnetisation, the resistance for each of the state will be different. Therefore the read out must be able to measure the resistance of the individual layers and not just of the entire structure. In order to perform this, the fabricated Hall bar must have contact pads to each of the ferromagnetic layers which should be selectively etched, and the spacer can be an insulator like MgO. MgO is an invaluable TMR spacer layer and has been extensively studied and been reported to increase the magnetoresistance up to 604% at room temperature[195, 196].

A schematic of the proposed unit memory cell mounted on a transducer is shown in Fig 5.9(a) where contacts are fabricated on individual magnetic layer to measure the AMR. The resistance can then be converted to normalised magnetisation by following the AMR equation stated in Eqn. 1.32 and shown in Fig. 5.9 (b) along with the four different magnetisation states. It is noted that even when the writing strain is zero, the cell remains in an orthogonal state, keeping the memory non-volatile.

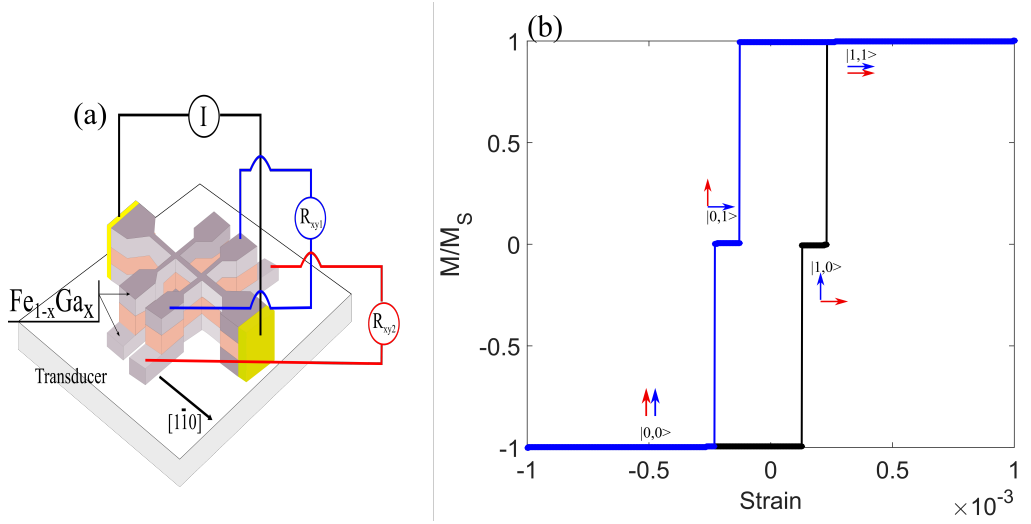

Figure 5.9: (a) Schematic of the prototype memory cell with a processed Hall bar. A dc current is passed along the [1$\bar{1}$0] direction with tensile strain along the [100] direction generated by the transducer. The transverse resistance is measured for each layer independently. (b) Modelled magnetisation loop calculated from net transverse resistance depicting four different magnetisation states.

In order to be used as a memory cell, an array of similar Hall bars can be processed and mounted on a ferroelectric layer [197] such as PMN-PT. PMN-PT have been widely used for voltage control of magnetisation due to the ultra high piezoelectric response allowing an effective manipulation of the magnetisation [198, 199]. For our proposed memory cell, the PMN-PT layer can be etched into an array of mesa structures. To the top of each of these mesa structures, the processed Hall bars made out of the bilayer $Fe_{1-x}Ga_x$ can be mounted or grown. The top of each of the mesa structures also has a gold electrode to which an electric field is applied to locally apply an in-plane strain to the bilayer sample. Thus by using a shift-register like mechanism the strain in individual PMN-PT mesa structures can be produced and thus the magnetisation orientation in individual Hall bars can be manipulated to give the four states configuration. A representative schematic of the proposed cell has been illustrated in Fig. 5.10.

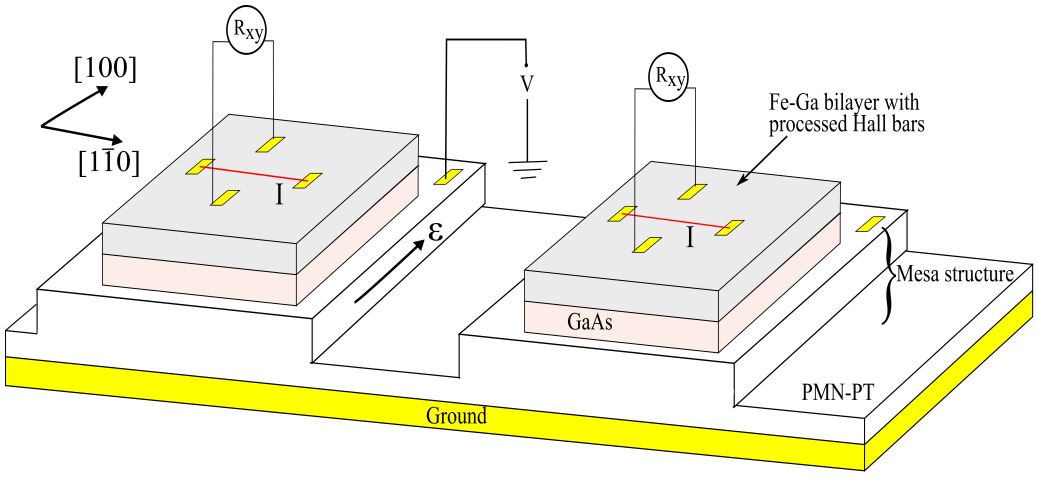

Figure 5.10: Schematic of the memory cell using an array of Fe-Ga bilayer mounted on PMN-PT mesa structures. Each PMN-PT structure can be polarised by poling it with an electric field, which in turn creates a local in-plane strain along the [100] crystal direction. A current is passed along the [1$\bar{1}$0] direction and corresponding planar resistance is measured.

As it is discussed that the uniaxial anisotropic strain manipulates the magnetisation and leads to the multiple independent magnetisation state, therefore the most energy efficient way of producing such strain is by applying an electric field to the piezoelectric material which is coupled to the memory cell by magnetoelastic coupling. The energy of the operation will then depend on the piezoelectric energy density for the used ferroelectric transducer and its crystal cut direction. This operational energy calculation for PMN/PT relaxor has been investigated in recent reports [200, 201] and has been to be in the order of $1.5 \times 10^4\ Jm^{-3}$.

5.4 Summary

In summary, in this chapter a stackable bilayer memory cell composed of $Fe_{1-x}Ga_x$ layers showing multi-level states was described. This multi-state configuration allowed for three dimensional, non-volatile memory integration without the application of any external magnetic field. The voltage induced strain in individual PMN-PT structures modulates the magnetisation orientation of individual ferromagnetic layers by magnetoelastic coupling. The third dimension can be used to stack more ferromagnetic layers thus improving the number of individual bits or magnetisation states, provided the strain is transmitted to the topmost layer effectively.

Since the modulation of the magnetisation states are performed by strain only,

it replaces traditional writing process such as external magnetic fields and electrical currents, thereby minimising energy losses due to Joule heating and spatial localisation of the field which may be destructive. The modelled results showing magnetisation switch by 90° and vice versa and highlight the importance of strain control of magnetisation and its profound potential application. In order to realise a strain mediated memory, array of such bilayers can be grown on mesa structures of piezoelectric materials in which the strain can be varied locally. By reading the magnetoresistance of the individual layers separately using either incorporating destructive techniques, or by growing the ferromagnetic layers on an insulating MgO spacer barrier, the magnetisation state of each layer can be realised. Thus, by applying a voltage of alternating sign, which generates strains of alternating signs, the magnetisation in each layer can be toggled between high/low-resistance states. The demonstration of highly effective voltage manipulation of magnetic bilayer via localized strains paves the way towards deterministic 90° magnetisation switching, and represents a key step towards realizing realistic strain-based MRAM with write energy of few tens of a J/bit provided the piezoelectric properties scale to a few nm thickness of the order 20 nm.

Chapter 6

Conclusion

This thesis incorporated a combination of magneto-optical, SQUID magnetometry, magneto-transport, ferromagnetic resonance, HR-TEM along with numerical modelling techniques to investigate the magnetisation properties, both static and dynamic for bilayer films of $Fe_{1-x}Ga_x$ separated by a non- magnetic spacer layer. This extensive study leads to the concept of a strain mediated magnetic memory cell where the magnetisation can be manipulated in both the ferromagnetic layers by applying a uniaxial strain across the volume of the hybrid sample.

Chapter 3 investigated the static and dynamic magnetisation properties of the unstrained bilayer samples which included determination of the magnetocrystalline anisotropies, saturation magnetisation, Gilbert damping and field linewidth values. The angular variation of the resonance frequency for each layer as measured by FMR were used in conjunction with numerical methods to work out the values of the values for magnetocrystalline anisotropies along with saturation magnetisation values. The determined quantities were then used to model M-H hysteresis loops which were a good fit to the SQUID hysteresis loops, indicating the consistency of the calculated values. The combination of the angular resonance frequency along with SQUID magnetometry showed that all the bilayer samples exhibited a cubic magnetocrystalline anisotropy favouring the [010]/[100] crystal directions and a weaker uniaxial anisotropy favouring the [110] hard direction. The determined values of the magnetocrystalline anisotropies depicted a consistent cubic anisotropy for both the layers and all the samples, while the uniaxial anisotropy for the layer grown on GaAs was higher than the lower grown on the metallic stack. This was due to the anisotropic influence of the interface bonds between the GaAs substrate-ferromagnet layer which got weaker with sample and spacer thickness.

The SQUID M-H loops for all the samples were used in combination with the

modelled magnetisation loops to determine the values of the domain wall energies for each layer. It was noticed that the domain wall energies were distinct for each layer and were dependent on the direction of applied field variation. The domain wall energies for the layer grown on GaAs substrate were found to be to be consistently lower than the layer grown on the metallic stack. Qualitatively this may be due to unique pinning effect of the GaAs substrate- ferromagnet layer, and ferromagnet-metal, and other interstitial effects resulting in different domain wall expansion process. the field dependence of the domain wall energies should be because of the the role of magnetocrystalline anisotropies that over the mechanism of domain wall nucleation and expansion. The calculated values of the magnetocrystalline anisotropies along with the domain wall energies for all the bilayer samples were comparable to that for MBE and sputter grown single layer films of $Fe_{1-x}Ga_x$ grown on GaAs [68, 100].

In order to determine the Gilbert damping parameter and the the field linewidth value, FMR was performed on the bilayer samples at different GHz frequencies. The determined values of the Gilbert or intrinsic damping for both the layers were comparable to previous reported values for single layer galfenol films with varying Ga concentration [102]. The bilayer samples showed narrow linewidths with small Gilbert damping values. The linewidth has been calculated to be about 9 times smaller than previous reported values for bulk and thin films [184, 185] and about the same comparable value for MBE gown $Fe_{81}Ga_{19}$ single layer [101].

The structural characterisation by HR-TEM imaging technique for the 5 nm thick spacer samples were also described in Ch. 3. The high resolution TEM images conducted in collaboration with Brno University of technology investigated crystal morphology of each layer. The imaging results presented also showed the good epitaxial and single-crystal growth of both the $Fe_{1-x}Ga_x$ for Al spacer sample, while a polycrystalline structure of both the layers for the Cu spacer sample. The Al spacer sample also revealed intermixing of the spacer metal diffused into the ferromagnetic layers. This intermixing effects along with crystalline structure have been reported to enhance the magnetostriction constant of $Fe_{1-x}Ga_x$[188]. Further HR-TEM imaging needs to be performed to detrmine a relation between the spacer type and thickness on the structure of the ferromagnetic layers.

The magnetostrictive property of the bilayers were studied in Ch.4 by performing magneto- optical and magnetotransport measurements on piezoelectric-ferromagnetic hybrid structures. The voltage induced strain resulted in the manipulation of the magnetic easy axes which was manifested as change in switching

fields. The response of the layers for all all the samples were different to the voltage induced strain. This was due to the fact the individual layers in the samples had different magnetocrystalline anisotropies, and magnetoelastic coefficients but most importantly the strength and nature of the transmitted strain was distinct. For the 10 nm thick spacer samples it was observed that most of the strain was attenuated by the substrate and the ferromagnetic- spacer layer. It was also observed that the curing of the epoxy glue used to mount the bilayer samples onto the transducer caused an in-built tensile strain along the [100] crystal direction which was always present no matter what the applied voltage was except for sample S422. For samples S419 to S421, the tensile strain caused changes in the magnetic switching fields as the voltage across the transducer was varied. For sample S422 a positive and negative voltage produced a tensile and compressive strain along the [100], which resulted in the manipulation of the magnetic easy axes.

By using the values of the magnetocrystalline anisotropies and domain wall energies calculated in Ch. 3, simulations were performed by solving the magnetisation free energy to model the transverse and longitudinal resistances along with M-H loops. From these it was realised that the applied uniaxial strain influences the magnetisation free energy by adding an extra magnetoelastic energy term. For field applied along the [100]/[010] easy axes directions it was experimentally observed that the measured resistance showed a large change in resistance which was due to a 90° magnetisation switch over the hard axes. A similar 90° switch was also observed by longitudinal MOKE measurements which only probed the top layer of the sample due to the penetration depth limitation of the laser. This switch was different from the 180° observed for unstrained samples by SQUID magnetometry. This demonstration of strain mediated switching of 90° magnetisation direction is important for its potential applicability to technology and had been discussed in Ch. 5.

Due to this uniaxial strain it has been shown in Ch. 3 that the magnetisation reversal in each layer were independent. This relative difference between the magnetisation orientations resulted in measured resistances which were a combination of individual layer resistance. This independent magnetisation reversal was measured as GMR contribution to the longitudinal resistance. The GMR effect was only shown by the 5 nm thick spacer samples and vanished for 10 nm thick spacer samples, as the spacer thickness were comparable to the mean free path of electrons [107] and most of the electrons are shunted by the thicker and more resistive spacer. It was also observed that the magnitude of GMR was greater in Cu

than Al spacer samples. This was more likely due to the thicker Al spacer sample as revealed by TEM imaging. The interfacial mixing of Fe-Ga with the Al spacer may cause interfacial spin mixing effects which further reduces the spin flipping or spin diffusion lengths and can reduce the magnitude of GMR. However further experimental investigations should be performed to conclude a definitive relation between the magnitude of the GMR to the type and thickness of the spacer.

Using the simulation at the switching field regions, the magnetoelastic constants for individual layers were calculated for sample S421 and was found to be comparable to previous reported values for single layer crystalline and polycrystalline samples [101, 188, 189]. These calculated values of magnetoelastic constants were able to replicate the experimental magnetotransport features, however due to insufficient knowledge of the absolute strain in each layer, and de-pinning effects at the sample edges the switching fields did not match very well. The values of the magnetoelastic constants for the rest of the sample were assumed to be the same, and using this values a good qualitative judgement of the magnetisation feature was possible. This results demonstrated that the the magnetotransport and magneto-optical measurements are excellent techniques to determine the magnetisation properties of the magnetostrictive bilayer films.

In Ch. 5 a design and operating parameters for a stress mediated magnetic memory cell was proposed. It outlined mathematical modelling of a single domain device by using the values of the magnetocrystalline anisotropy energies and magnetostriction values of each layer calculated in the previous chapters. This proposed device has an ability to show a strain controlled non volatile 90° magnetisation switching over the hard axes. The extension to more than one layer improves the storage density and also demonstrates a four-state memory application. Having the magnetisation switch by strain minimises the eddy losses incurred due to localised electric and magnetic field. A proposed archtecture of an array of bilayer samples grown on PMN-PT substrate was dicussed to locally alter the magnetisation state of each unit cell.

The strain control of magnetisation is an area with promising future towards development of devices suitable for applications in information storage and logical processing. The narrow linewidth and low Gilbert damping values makes them an interesting candidate in the applications of microwave spintronic devices with high tunability and power consumption demands. This two independent properties have been observed in sputter grown films which make them more useful due to the economics and time constraint. There are a number of areas that could be

developed from the work in this thesis. Some of them can be attempts to improve the magnetoresistance ratio by incorporating different spacer layer, traditionally Cr, and by changing the composition of thickness and composition of the layers to measure different magnetisation resonance properties. Another viable spacer material can be MgO, which can be used to increase the TMR and as well as to read out the individual layer magnetoresistances. Sophisticated growing techniques of array of these bilayers on piezoelectric materials at different crystal cuts, with selective etching processes can be realised and will be a key step towards realising realistic strain-based MRAM with write energy of few tens of a J/bit provided the piezoelectric properties scale to the thickness of the grown layers. It will be interesting to see if a strain mediated non-volatile memory device can be developed which can experimentally demonstrate the independent magnetisation reversal.

References

[1] DennisE Speliotis. Magnetic recording beyond the first 100 years. *Journal of Magnetism and Magnetic Materials*, 193(1):29–35, 1999.

[2] RW Wood and D Petersen. Viterbi detection of class iv partial response on a magnetic recording channel. *IEEE Transactions on Communications*, 34(5):454–461, 1986.

[3] Dan A Allwood, Gang Xiong, CC Faulkner, D Atkinson, D Petit, and RP Cowburn. Magnetic domain-wall logic. *Science*, 309(5741):1688–1692, 2005.

[4] Stuart SP Parkin, Masamitsu Hayashi, and Luc Thomas. Magnetic domain-wall racetrack memory. *Science*, 320(5873):190–194, 2008.

[5] Grünberg Binasch, Peter Grünberg, F Saurenbach, and W Zinn. Enhanced magnetoresistance in layered magnetic structures with antiferromagnetic interlayer exchange. *Physical review B*, 39(7):4828, 1989.

[6] Albert Fert. Nobel lecture: Origin, development, and future of spintronics. *Reviews of Modern Physics*, 80(4):1517, 2008.

[7] Peter A Grünberg. Nobel lecture: From spin waves to giant magnetoresistance and beyond. *Reviews of Modern Physics*, 80(4):1531, 2008.

[8] Igor Žutić, Jaroslav Fabian, and S Das Sarma. Spintronics: Fundamentals and applications. *Reviews of modern physics*, 76(2):323, 2004.

[9] SA Wolf, DD Awschalom, RA Buhrman, JM Daughton, S Von Molnar, ML Roukes, A Yu Chtchelkanova, and DM Treger. Spintronics: a spin-based electronics vision for the future. *Science*, 294(5546):1488–1495, 2001.

[10] Russell P Cowburn. Spintronics: Change of direction. *Nature materials*, 6(4):255–256, 2007.

[11] The Royal Society. *The electrical conductivity of transition metals*, volume 153, 1936.

[12] William Thomson. On the electro-dynamic qualities of metals:–effects of magnetization on the electric conductivity of nickel and of iron. *Proceedings of the Royal Society of London*, 8:546–550, 1856.

[13] Bernard Dieny, Bruce A Gurney, Steven E Lambert, Daniele Mauri, Stuart SP Parkin, Virgil S Speriosu, and Dennis R Wilhoit. Magnetoresistive sensor based on the spin valve effect, April 27 1993. US Patent 5,206,590.

[14] Michel Julliere. Tunneling between ferromagnetic films. *Physics letters A*, 54(3):225–226, 1975.

[15] Shinji Yuasa, Taro Nagahama, Akio Fukushima, Yoshishige Suzuki, and Koji Ando. Giant room-temperature magnetoresistance in single-crystal fe/mgo/fe magnetic tunnel junctions. *Nature materials*, 3(12):868, 2004.

[16] Claude Chappert, Albert Fert, and Frédéric Nguyen Van Dau. The emergence of spin electronics in data storage. *Nature materials*, 6(11):813, 2007.

[17] JM Daughton. Magnetic tunneling applied to memory. *Journal of Applied Physics*, 81(8):3758–3763, 1997.

[18] John C Slonczewski. Current-driven excitation of magnetic multilayers. *Journal of Magnetism and Magnetic Materials*, 159(1-2):L1–L7, 1996.

[19] Julie Grollier, Vincent Cros, A Hamzic, Jean-Marie George, Henri Jaffrès, Albert Fert, Giancarlo Faini, J Ben Youssef, and H Legall. Spin-polarized current induced switching in co/cu/co pillars. *Applied Physics Letters*, 78(23):3663–3665, 2001.

[20] L Berger. Emission of spin waves by a magnetic multilayer traversed by a current. *Physical Review B*, 54(13):9353, 1996.

[21] E Chen, D Apalkov, Z Diao, A Driskill-Smith, D Druist, D Lottis, V Nikitin, X Tang, S Watts, S Wang, et al. Advances and future prospects of spin-transfer torque random access memory. *IEEE Transactions on Magnetics*, 46(6):1873–1878, 2010.

[22] Yiming Huai. Spin-transfer torque mram (stt-mram): Challenges and prospects. *AAPPS bulletin*, 18(6):33–40, 2008.

[23] M Hosomi, H Yamagishi, T Yamamoto, K Bessho, Y Higo, K Yamane, H Yamada, M Shoji, H Hachino, C Fukumoto, et al. A novel nonvolatile memory with spin torque transfer magnetization switching: Spin-ram. In *Electron Devices Meeting, 2005. IEDM Technical Digest. IEEE International*, pages 459–462. IEEE, 2005.

[24] Takayuki Kawahara, Riichiro Takemura, Katsuya Miura, Jun Hayakawa, Shoji Ikeda, Y Lee, Ryutaro Sasaki, Yasushi Goto, Kenchi Ito, Toshiyasu Meguro, et al. 2mb spin-transfer torque ram (spram) with bit-by-bit bidirectional current write and parallelizing-direction current read. In *Solid-State Circuits Conference, 2007. ISSCC 2007. Digest of Technical Papers. IEEE International*, pages 480–617. IEEE, 2007.

[25] BN Engel, J Akerman, B Butcher, RW Dave, M DeHerrera, M Durlam, G Grynkewich, J Janesky, SV Pietambaram, ND Rizzo, et al. A 4-mb toggle mram based on a novel bit and switching method. *IEEE Transactions on Magnetics*, 41(1):132–136, 2005.

[26] YunSeung Shin. Non-volatile memory technologies for beyond 2010. In *VLSI Circuits, 2005. Digest of Technical Papers. 2005 Symposium on*, pages 156–159. IEEE, 2005.

[27] Stuart Parkin and See-Hun Yang. Memory on the racetrack. *Nature nanotechnology*, 10(3):195–198, 2015.

[28] Luc Thomas, See-Hun Yang, Kwang-Su Ryu, Brian Hughes, Charles Rettner, Ding-Shuo Wang, Ching-Hsiang Tsai, Kuei-Hung Shen, and Stuart SP Parkin. Racetrack memory: a high-performance, low-cost, non-volatile memory based on magnetic domain walls. In *Electron Devices Meeting (IEDM), 2011 IEEE International*, pages 24–2. IEEE, 2011.

[29] Andrew D Kent and Daniel C Worledge. A new spin on magnetic memories. *Nature nanotechnology*, 10(3):187–191, 2015.

[30] Wei Han, Roland K Kawakami, Martin Gmitra, and Jaroslav Fabian. Graphene spintronics. *Nature nanotechnology*, 9(10):794–807, 2014.

[31] Lapo Bogani and Wolfgang Wernsdorfer. Molecular spintronics using single-molecule magnets. *Nature materials*, 7(3):179, 2008.

[32] V Alek Dediu, Luis E Hueso, Ilaria Bergenti, and Carlo Taliani. Spin routes in organic semiconductors. *Nature materials*, 8(9):707, 2009.

[33] Tomas Jungwirth, X Marti, P Wadley, and J Wunderlich. Antiferromagnetic spintronics. *arXiv preprint arXiv:1509.05296*, 2015.

[34] AH MacDonald and M Tsoi. Antiferromagnetic metal spintronics. *Philosophical Transactions of the Royal Society of London A: Mathematical, Physical and Engineering Sciences*, 369(1948):3098–3114, 2011.

[35] Peter Wadley, Bryn Howells, J Železnỳ, Carl Andrews, Victoria Hills, Richard P Campion, Vit Novák, K Olejník, F Maccherozzi, SS Dhesi, et al. Electrical switching of an antiferromagnet. *Science*, 351(6273):587–590, 2016.

[36] DJ Thouless, Mahito Kohmoto, MP Nightingale, and M Den Nijs. Quantized hall conductance in a two-dimensional periodic potential. *Physical Review Letters*, 49(6):405, 1982.

[37] Edgar Ascher, Harry Rieder, Hans Schmid, and H Stössel. Some properties of ferromagnetoelectric nickel-iodine boracite, ni3b7o13i. *Journal of Applied Physics*, 37(3):1404–1405, 1966.

[38] S Methfessel. Potential applications of magnetic rare earth compunds. *IEEE Transactions on Magnetics*, 1(3):144–155, 1965.

[39] Tomasz Dietl. Ferromagnetic semiconductors. *Semiconductor Science and Technology*, 17(4):377, 2002.

[40] Tomasz Dietl. A ten-year perspective on dilute magnetic semiconductors and oxides. *Nature materials*, 9(12):965–974, 2010.

[41] H Ohno, D Chiba, F Matsukura, T Omlya, et al. Electric-field control of ferromagnetism. *Nature*, 408(6815):944, 2000.

[42] Martin Weisheit, Sebastian Fähler, Alain Marty, Yves Souche, Christiane Poinsignon, and Dominique Givord. Electric field-induced modification of magnetism in thin-film ferromagnets. *Science*, 315(5810):349–351, 2007.

[43] M Endo, S Kanai, S Ikeda, F Matsukura, and H Ohno. Electric-field effects on thickness dependent magnetic anisotropy of sputtered mgo/co 40 fe 40 b 20/ta structures. *Applied Physics Letters*, 96(21):212503, 2010.

[44] T Maruyama, Y Shiota, T Nozaki, K Ohta, N Toda, M Mizuguchi, AA Tulapurkar, T Shinjo, M Shiraishi, S Mizukami, et al. Large voltage-induced magnetic anisotropy change in a few atomic layers of iron. *Nature nanotechnology*, 4(3):158–161, 2009.

[45] Wei-Gang Wang, Mingen Li, Stephen Hageman, and CL Chien. Electric-field-assisted switching in magnetic tunnel junctions. *Nature materials*, 11(1):64, 2012.

[46] Jian Zhu, JA Katine, Graham E Rowlands, Yu-Jin Chen, Zheng Duan, Juan G Alzate, Pramey Upadhyaya, Juergen Langer, Pedram Khalili Amiri, Kang L Wang, et al. Voltage-induced ferromagnetic resonance in magnetic tunnel junctions. *Physical review letters*, 108(19):197203, 2012.

[47] Shashank Priya, Rashed Islam, Shuxiang Dong, and D Viehland. Recent advancements in magnetoelectric particulate and laminate composites. *Journal of Electroceramics*, 19(1):149–166, 2007.

[48] Wilma Eerenstein, ND Mathur, and James F Scott. Multiferroic and magnetoelectric materials. *nature*, 442(7104):759, 2006.

[49] R Grössinger, Giap V Duong, and R Sato-Turtelli. The physics of magnetoelectric composites. *Journal of Magnetism and magnetic materials*, 320(14):1972–1977, 2008.

[50] Z-M Dang, Y Shen, and C-W Nan. Dielectric behavior of three-phase percolative ni–batio 3/polyvinylidene fluoride composites. *Applied Physics Letters*, 81(25):4814–4816, 2002.

[51] Shuxiang Dong, Jinrong Cheng, JF Li, and D Viehland. Enhanced magnetoelectric effects in laminate composites of terfenol-d/pb (zr, ti) o 3 under resonant drive. *Applied Physics Letters*, 83(23):4812–4814, 2003.

[52] Manfred Fiebig. Revival of the magnetoelectric effect. *Journal of Physics D: Applied Physics*, 38(8):R123, 2005.

[53] SL Kadam, KK Patankar, VL Mathe, MB Kothale, RB Kale, and BK Chougule. Electrical properties and magnetoelectric effect in ni 0.75 co 0.25 fe 2 o 4+ ba 0.8 pb 0.2 tio 3 composites. *Materials chemistry and physics*, 78(3):684–690, 2003.

[54] MB Kothale, KK Patankar, SL Kadam, VL Mathe, AV Rao, and BK Chougule. Dielectric behaviour and magnetoelectric effect in copper–cobalt ferrite+ barium lead titanate composites. *Materials Chemistry and Physics*, 77(3):691–696, 2003.

[55] Jun Yi Zhai, Ning Cai, Li Liu, Yuan Hua Lin, and Ce Wen Nan. Dielectric behavior and magnetoelectric properties of lead zirconate titanate/co-ferrite particulate composites. *Materials Science and Engineering: B*, 99(1):329–331, 2003.

[56] D Chiba, M Sawicki, Y Nishitani, Y Nakatani, F Matsukura, and H Ohno. Magnetization vector manipulation by electric fields. *Nature*, 455(7212):515, 2008.

[57] Mason Overby, Alexander Chernyshov, Leonid P Rokhinson, X Liu, and JK Furdyna. Gamnas-based hybrid multiferroic memory device. *Applied Physics Letters*, 92(19):192501, 2008.

[58] AW Rushforth, E De Ranieri, J Zemen, J Wunderlich, KW Edmonds, CS King, E Ahmad, RP Campion, CT Foxon, BL Gallagher, et al. Voltage control of magnetocrystalline anisotropy in ferromagnetic-semiconductor-piezoelectric hybrid structures. *Physical Review B*, 78(8):085314, 2008.

[59] AE Clark. Magnetostrictive rare earth-fe 2 compounds. *Handbook of ferromagnetic materials*, 1:531–589, 1980.

[60] Ce-Wen Nan, MI Bichurin, Shuxiang Dong, D Viehland, and G Srinivasan. Multiferroic magnetoelectric composites: historical perspective, status, and future directions. *Journal of Applied Physics*, 103(3):1, 2008.

[61] Etienne du Tremolet De Lacheisserie, Damien Gignoux, and Michel Schlenker. *Magnetism: II-Materials and Applications*. Springer Science & Business Media, 2012.

[62] RA Kellogg, AM Russell, TA Lograsso, AB Flatau, AE Clark, and M Wun-Fogle. Tensile properties of magnetostrictive iron–gallium alloys. *Acta Materialia*, 52(17):5043–5050, 2004.

[63] Arthur E Clark, Marilyn Wun-Fogle, James B Restorff, Thomas A Lograsso, and James R Cullen. Effect of quenching on the magnetostriction on fe/sub

1-x/ga/sub x/(0.13 x< 0.21). *IEEE Transactions on Magnetics*, 37(4):2678–2680, 2001.

[64] AE Clark, KB Hathaway, M Wun-Fogle, JB Restorff, Thomas A Lograsso, VM Keppens, G Petculescu, and RA Taylor. Extraordinary magnetoelasticity and lattice softening in bcc fe-ga alloys. *Journal of Applied Physics*, 93(10):8621–8623, 2003.

[65] Zhangxian Deng and Marcelo J Dapino. Characterization and finite element modeling of galfenol minor flux density loops. *Journal of Intelligent Material Systems and Structures*, 26(1):47–55, 2015.

[66] PR Downey and AB Flatau. Magnetoelastic bending of galfenol for sensor applications. *Journal of Applied Physics*, 97(10):10R505, 2005.

[67] RA Kellogg. *Development and modeling of iron-gallium alloys.* PhD thesis, Iowa State University, 2005.

[68] Duncan Edward Parkes. *Strain control of ferromagnetic thin films and devices*. PhD thesis, University of Nottingham, 2016.

[69] Bernard Dennis Cullity and Chad D Graham. *Introduction to magnetic materials*. John Wiley & Sons, 2011.

[70] EW Lee and MA Asgar. The magnetostriction of nickel. In *Proceedings of the Royal Society of London A: Mathematical, Physical and Engineering Sciences*, volume 326, pages 73–85. The Royal Society, 1971.

[71] RC Hall. Single crystal anisotropy and magnetostriction constants of several ferromagnetic materials including alloys of nife, sife, alfe, coni, and cofe. *Journal of Applied Physics*, 30(6):816–819, 1959.

[72] RM Bozorth and JG Walker. Magnetic crystal anisotropy and magnetostriction of iron-nickel alloys. *Physical Review*, 89(3):624, 1953.

[73] Mark B Moffett, Arthur E Clark, Marilyn Wun-Fogle, Jan Linberg, Joseph P Teter, and Elizabeth A McLaughlin. Characterization of terfenol-d for magnetostrictive transducers. *The Journal of the Acoustical Society of America*, 89(3):1448–1455, 1991.

[74] AV Scherbakov, AS Salasyuk, AV Akimov, X Liu, M Bombeck, C Brüggemann, DR Yakovlev, VF Sapega, JK Furdyna, and M Bayer. Coherent magnetization precession in ferromagnetic (ga, mn) as induced by picosecond acoustic pulses. *Physical review letters*, 105(11):117204, 2010.

[75] Ji-Wan Kim, Mircea Vomir, and Jean-Yves Bigot. Ultrafast magnetoacoustics in nickel films. *Physical review letters*, 109(16):166601, 2012.

[76] JV Jäger, AV Scherbakov, TL Linnik, DR Yakovlev, M Wang, P Wadley, V Holy, SA Cavill, AV Akimov, AW Rushforth, et al. Picosecond inverse magnetostriction in galfenol thin films. *Applied Physics Letters*, 103(3):032409, 2013.

[77] JV Jäger, AV Scherbakov, BA Glavin, AS Salasyuk, RP Campion, AW Rushforth, DR Yakovlev, Andrey V Akimov, and M Bayer. Resonant driving of magnetization precession in a ferromagnetic layer by coherent monochromatic phonons. *Physical Review B*, 92(2):020404, 2015.

[78] AV Scherbakov, M Bombeck, JV Jäger, AS Salasyuk, TL Linnik, VE Gusev, DR Yakovlev, AV Akimov, and M Bayer. Picosecond opto-acoustic interferometry and polarimetry in high-index gaas. *Optics express*, 21(14):16473–16485, 2013.

[79] Jayasimha Atulasimha and Alison B Flatau. A review of magnetostrictive iron–gallium alloys. *Smart Materials and Structures*, 20(4):043001, 2011.

[80] JB Restorff, M Wun-Fogle, AE Clark, Thomas A Lograsso, AR Ross, and Deborah L Schlagel. Magnetostriction of ternary fe–ga–x alloys (x= ni, mo, sn, al). *Journal of applied physics*, 91(10):8225–8227, 2002.

[81] EM Summers, TA Lograsso, and M Wun-Fogle. Magnetostriction of binary and ternary fe–ga alloys. *Journal of Materials Science*, 42(23):9582–9594, 2007.

[82] RC Hall. Single-crystal magnetic anisotropy and magnetostriction studies in iron-base alloys. *Journal of Applied Physics*, 31(6):1037–1038, 1960.

[83] CG McKamey, JH DeVan, PF Tortorelli, and VK Sikka. A review of recent developments in fe 3 al-based alloys. *Journal of Materials Research*, 6(8):1779–1805, 1991.

[84] JX Cao, YN Zhang, WJ Ouyang, and RQ Wu. Large magnetostriction of fe 1- x ge x and its electronic origin: Density functional study. *Physical Review B*, 80(10):104414, 2009.

[85] Y Du, Mianliang Huang, S Chang, Deborah L Schlagel, Thomas A Lograsso, and Robert J McQueeney. Relation between ga ordering and magnetostriction of fe-ga alloys studied by x-ray diffuse scattering. *Physical Review B*, 81(5):054432, 2010.

[86] G Petculescu, KL Ledet, Mianliang Huang, Thomas A Lograsso, YN Zhang, RQ Wu, M Wun-Fogle, JB Restorff, AE Clark, and KB Hathaway. Magnetostriction, elasticity, and d03 phase stability in fe–ga and fe–ga–ge alloys. *Journal of Applied Physics*, 109(7):07A904, 2011.

[87] Hui Wang, YN Zhang, Teng Yang, ZD Zhang, LZ Sun, and RQ Wu. Ab initio studies of the effect of nanoclusters on magnetostriction of fe 1- x ga x alloys. *Applied Physics Letters*, 97(26):262505, 2010.

[88] YN Zhang, JX Cao, and RQ Wu. Rigid band model for prediction of magnetostriction of iron-gallium alloys. *Applied Physics Letters*, 96(6):062508, 2010.

[89] Q Xing, Y Du, RJ McQueeney, and TA Lograsso. Structural investigations of fe–ga alloys: Phase relations and magnetostrictive behavior. *Acta Materialia*, 56(16):4536–4546, 2008.

[90] Hu Cao, Peter M Gehring, Christopher P Devreugd, JA Rodriguez-Rivera, J Li, and D Viehland. Role of nanoscale precipitates on the enhanced magnetostriction of heat-treated galfenol (fe 1- x ga x) alloys. *Physical review letters*, 102(12):127201, 2009.

[91] Matthew Paul Ruffoni, S Pascarelli, R Grössinger, R Sato Turtelli, C Bormio-Nunes, and RF Pettifer. Direct measurement of intrinsic atomic scale magnetostriction. *Physical review letters*, 101(14):147202, 2008.

[92] AG Khachaturyan and D Viehland. Structurally heterogeneous model of extrinsic magnetostriction for fe-ga and similar magnetic alloys: Part i. decomposition and confined displacive transformation. *Metallurgical and Materials Transactions A*, 38(13):2308–2316, 2007.

[93] Wei-Feng Rao and Armen G Khachaturyan. Phase field theory of proper displacive phase transformations: Structural anisotropy and directional flexibility, a vector model, and the transformation kinetics. *Acta Materialia*, 59(11):4494–4503, 2011.

[94] Wei-Feng Rao, Manfred Wuttig, and Armen G Khachaturyan. Giant nonhysteretic responses of two-phase nanostructured alloys. *Physical review letters*, 106(10):105703, 2011.

[95] Yangkun He, Chengbao Jiang, Wei Wu, Bin Wang, Huiping Duan, Hui Wang, Tianli Zhang, Jingmin Wang, Jinghua Liu, Zaoli Zhang, et al. Giant heterogeneous magnetostriction in fe–ga alloys: Effect of trace element doping. *Acta Materialia*, 109:177–186, 2016.

[96] TA Lograsso, AR Ross, DL Schlagel, AE Clark, and M Wun-Fogle. Structural transformations in quenched fe–ga alloys. *Journal of Alloys and Compounds*, 350(1):95–101, 2003.

[97] G Petculescu, KB Hathaway, Thomas A Lograsso, M Wun-Fogle, and AE Clark. Magnetic field dependence of galfenol elastic properties. *Journal of Applied Physics*, 97(10):10M315, 2005.

[98] Manfred Wuttig, Liyang Dai, and James Cullen. Elasticity and magnetoelasticity of fe–ga solid solutions. *Applied Physics Letters*, 80(7):1135–1137, 2002.

[99] DE Parkes, SA Cavill, AT Hindmarch, P Wadley, F McGee, CR Staddon, KW Edmonds, RP Campion, BL Gallagher, and AW Rushforth. Non-volatile voltage control of magnetization and magnetic domain walls in magnetostrictive epitaxial thin films. *Applied Physics Letters*, 101(7):072402, 2012.

[100] Stuart Robert Bowe. *Magnetisation dynamics in magnetostrictive nanostructures*. PhD thesis, University of Nottingham, United Kingdom, 2017.

[101] DE Parkes, LR Shelford, P Wadley, V Holỳ, M Wang, AT Hindmarch, G Van Der Laan, RP Campion, KW Edmonds, SA Cavill, et al. Magnetostrictive thin films for microwave spintronics. *Scientific reports*, 3, 2013.

[102] Bijoy K Kuanr, RE Camley, Z Celinski, Adam McClure, and Yves Idzerda. Single crystal fe1- xgax thin films for monolithic microwave devices. *Journal of Applied Physics*, 115(17):17C112, 2014.

[103] Yasushi Endo, Takumi Sakai, Takamichi Miyazaki, and Yutaka Shimada. Effect of film thickness on the high frequency magnetic properties of polycrystalline fe- ga films. *IEEE Transactions on Magnetics*, 2017.

[104] Rodrigo Arias and DL Mills. Extrinsic contributions to the ferromagnetic resonance response of ultrathin films. *Physical review B*, 60(10):7395, 1999.

[105] Samuele Fin, R Tomasello, D Bisero, M Marangolo, M Sacchi, Horia Popescu, M Eddrief, C Hepburn, Giovanni Finocchio, M Carpentieri, et al. In-plane rotation of magnetic stripe domains in fe 1- x ga x thin films. *Physical Review B*, 92(22):224411, 2015.

[106] Charles Kittel. Physical theory of ferromagnetic domains. *Reviews of modern Physics*, 21(4):541, 1949.

[107] Robert C O'handley. *Modern magnetic materials: principles and applications*. Wiley, 2000.

[108] NF Mott and KWH Stevens. The band structure of the transition metals. *Philosophical Magazine*, 2(23):1364–1386, 1957.

[109] JC Slater. Ferromagnetism and the band theory. *Reviews of Modern Physics*, 25(1):199, 1953.

[110] Stephen Blundell. Magnetism in condensed matter, 2003.

[111] JH Wolfe, RK Kawakami, WL Ling, ZQ Qiu, Rodrigo Arias, and DL Mills. Roughness induced in plane uniaxial anisotropy in ultrathin fe films. *Journal of magnetism and magnetic materials*, 232(1):36–45, 2001.

[112] Mathias Getzlaff. *Fundamentals of magnetism*. Springer Science & Business Media, 2007.

[113] PG Evans and MJ Dapino. Efficient model for field-induced magnetization and magnetostriction of galfenol. *Journal of Applied Physics*, 105(11):113901, 2009.

[114] G Wastlbauer and JAC Bland*. Structural and magnetic properties of ultrathin epitaxial fe films on gaas (001) and related semiconductor substrates. *Advances in physics*, 54(2):137–219, 2005.

[115] Soshin Chikazumi and Chad D Graham. *Physics of Ferromagnetism 2e*, volume 94. Oxford University Press on Demand, 2009.

[116] D Sander. The correlation between mechanical stress and magnetic anisotropy in ultrathin films. *Reports on Progress in Physics*, 62(5):809, 1999.

[117] A Javed, NA Morley, and MRJ Gibbs. Structure, magnetic and magnetostrictive properties of as-deposited fe–ga thin films. *Journal of Magnetism and Magnetic Materials*, 321(18):2877–2882, 2009.

[118] Ming Liu, Ogheneyunume Obi, Zhuhua Cai, Jing Lou, Guomin Yang, Katherine S Ziemer, and Nian X Sun. Electrical tuning of magnetism in fe 3 o 4/pzn–pt multiferroic heterostructures derived by reactive magnetron sputtering. *Journal of Applied Physics*, 107(7):073916, 2010.

[119] Ming Liu and Nian X Sun. Voltage control of magnetism in multiferroic heterostructures. *Phil. Trans. R. Soc. A*, 372(2009):20120439, 2014.

[120] John MD Coey. *Magnetism and magnetic materials*. Cambridge University Press, 2010.

[121] AE Berkowitz, JR Mitchell, MJ Carey, AP Young, Shufeng Zhang, FE Spada, FT Parker, A Hutten, and G Thomas. Giant magnetoresistance in heterogeneous cu-co alloys. *Physical Review Letters*, 68(25):3745, 1992.

[122] Lev Davidovich Landau, JS Bell, MJ Kearsley, LP Pitaevskii, EM Lifshitz, and JB Sykes. *Electrodynamics of continuous media*, volume 8. elsevier, 2013.

[123] M Lakshmanan. The fascinating world of the landau–lifshitz–gilbert equation: an overview. *Philosophical Transactions of the Royal Society of London A: Mathematical, Physical and Engineering Sciences*, 369(1939):1280–1300, 2011.

[124] K Lenz, H Wende, W Kuch, K Baberschke, K Nagy, and A Jánossy. Two-magnon scattering and viscous gilbert damping in ultrathin ferromagnets. *Physical Review B*, 73(14):144424, 2006.

[125] Georg Woltersdorf, Matthias Buess, B Heinrich, and CH Back. Time resolved magnetization dynamics of ultrathin fe (001) films: Spin-pumping and two-magnon scattering. *Physical review letters*, 95(3):037401, 2005.

[126] Lawrence F Shampine, Ian Gladwell, and Skip Thompson. *Solving ODEs with matlab*. Cambridge University Press, 2003.

[127] Bretislav Heinrich and J Anthony C Bland. *Ultrathin Magnetic Structures II*, volume 1. Springer, 1994.

[128] C Bilzer, T Devolder, P Crozat, C Chappert, S Cardoso, and PP Freitas. Vector network analyzer ferromagnetic resonance of thin films on coplanar waveguides: Comparison of different evaluation methods. *Journal of applied physics*, 101(7):074505, 2007.

[129] Janusz Dubowik and Hubert Głowiński. Broad-band ferromagnetic resonance in thin magnetic films and nanostructures. *Current Topics in Biophysics*, 33:43–45, 2010.

[130] Sangita S Kalarickal, Pavol Krivosik, Mingzhong Wu, Carl E Patton, Michael L Schneider, Pavel Kabos, Thomas J Silva, and John P Nibarger. Ferromagnetic resonance linewidth in metallic thin films: Comparison of measurement methods. *Journal of Applied Physics*, 99(9):093909, 2006.

[131] Michael Farle. Ferromagnetic resonance of ultrathin metallic layers. *Reports on Progress in Physics*, 61(7):755, 1998.

[132] LR Walker. Magnetostatic modes in ferromagnetic resonance. *Physical Review*, 105(2):390, 1957.

[133] Charles Kittel. On the theory of ferromagnetic resonance absorption. *Physical Review*, 73(2):155, 1948.

[134] Charles Kittel. Interpretation of anomalous larmor frequencies in ferromagnetic resonance experiment. *Physical Review*, 71(4):270, 1947.

[135] P-G De Gennes, C Kittel, and AM Portis. Theory of ferromagnetic resonance in rare earth garnets. ii. line widths. *Physical Review*, 116(2):323, 1959.

[136] J Smith and HG Beljers. Philips res. rep. 10, 113 (1955); h. suhl. *Phys. Rev*, 97:555, 1955.

[137] J Smit and HG Beljers. Ferromagnetic resonance absorption in bafe12o19, a highly anisotropic crystal. *Philips Res. Rep*, 10(113):31, 1955.

[138] H Suhl. Ferromagnetic resonance in nickel ferrite between one and two kilomegacycles. *Physical Review*, 97(2):555, 1955.

[139] Maciej Kasperski and Henryk Puszkarski. On the interpretation of the angular dependence of the fmr spectrum in heterogeneous ferromagnetic thin films. *arXiv preprint arXiv:1208.6573*, 2012.

[140] SV Vonsovskii. *Ferromagnetic Resonance: The Phenomenon of Resonant Absorption of a High-Frequency Magnetic Field in Ferromagnetic Substances*, volume 4. Elsevier, 2013.

[141] Teruya Shinjo. *Nanomagnetism and spintronics*. Elsevier, 2013.

[142] IA Campbell and A Fert. Transport properties of ferromagnets. *Handbook of Ferromagnetic Materials*, 3:747–804, 1982.

[143] A Fert and IA Campbell. Transport properties of ferromagnetic transition metals. *Le Journal de Physique Colloques*, 32(C1):C1–46, 1971.

[144] A Fert and IA Campbell. Electrical resistivity of ferromagnetic nickel and iron based alloys. *Journal of Physics F: Metal Physics*, 6(5):849, 1976.

[145] Augustus Matthiessen and Carl Vogt. On the influence of temperature on the electric conducting-power of alloys. *Philosophical Transactions of the Royal Society of London*, 154:167–200, 1864.

[146] T McGuire and RL Potter. Anisotropic magnetoresistance in ferromagnetic 3d alloys. *IEEE Transactions on Magnetics*, 11(4):1018–1038, 1975.

[147] Robert I Potter. Magnetoresistance anisotropy in ferromagnetic nicu alloys. *Physical review B*, 10(11):4626, 1974.

[148] J Smit. Magnetoresistance of ferromagnetic metals and alloys at low temperatures. *Physica*, 17(6):612–627, 1951.

[149] IA Campbell, A Fert, and O Jaoul. The spontaneous resistivity anisotropy in ni-based alloys. *Journal of Physics C: Solid State Physics*, 3(1S):S95, 1970.

[150] Denny D Tang and Yuan-Jen Lee. *Magnetic memory: fundamentals and technology*. Cambridge University Press, 2010.

[151] Mario Norberto Baibich, Jean Marc Broto, Albert Fert, F Nguyen Van Dau, Frédéric Petroff, P Etienne, G Creuzet, A Friederich, and J Chazelas. Giant magnetoresistance of (001) fe/(001) cr magnetic superlattices. *Physical review letters*, 61(21):2472, 1988.

[152] J Barnas, A Fuss, RE Camley, P Grunberg, and W Zinn. Novel magnetoresistance effect in layered magnetic structures: Theory and experiment. *Physical Review B*, 42(13):8110, 1990.

[153] RE Camley and RL Stamps. Magnetic multilayers: spin configurations, excitations and giant magnetoresistance. *Journal of Physics: Condensed Matter*, 5(23):3727, 1993.

[154] Robert E Camley and J Barnaś. Theory of giant magnetoresistance effects in magnetic layered structures with antiferromagnetic coupling. *Physical review letters*, 63(6):664, 1989.

[155] Peter M Levy, Shufeng Zhang, and Albert Fert. Electrical conductivity of magnetic multilayered structures. *Physical review letters*, 65(13):1643, 1990.

[156] WP Pratt Jr, S-F Lee, JM Slaughter, R Loloee, PA Schroeder, and J Bass. Perpendicular giant magnetoresistances of ag/co multilayers. *Physical Review Letters*, 66(23):3060, 1991.

[157] T Valet and A Fert. Theory of the perpendicular magnetoresistance in magnetic multilayers. *Physical Review B*, 48(10):7099, 1993.

[158] Bernard Dieny, Virgil S Speriosu, Stuart SP Parkin, Bruce A Gurney, Dennis R Wilhoit, and Daniele Mauri. Giant magnetoresistive in soft ferromagnetic multilayers. *Physical Review B*, 43(1):1297, 1991.

[159] Joachim Stöhr and Hans Christoph Siegmann. *Magnetism: from fundamentals to nanoscale dynamics*, volume 152. Springer Science & Business Media, 2007.

[160] Exum Percival Lewis. *The Effects of a Magnetic Field on Radiation-Memoirs by Faraday Kerr and Zeeman*. Read Books Ltd, 2013.

[161] Petros N Argyres. Theory of the faraday and kerr effects in ferromagnetics. *Physical Review*, 97(2):334, 1955.

[162] Robert P Hunt. Magneto-optic scattering from thin solid films. *Journal of Applied Physics*, 38(4):1652–1671, 1967.

[163] DA Allwood, Gang Xiong, MD Cooke, and RP Cowburn. Magneto-optical kerr effect analysis of magnetic nanostructures. *Journal of Physics D: Applied Physics*, 36(18):2175, 2003.

[164] J Zak, ER Moog, C Liu, and SD Bader. Fundamental magneto-optics. *Journal of applied physics*, 68(8):4203–4207, 1990.

[165] Alex Hubert and Rudolf Schäfer. *Magnetic domains: the analysis of magnetic microstructures*. Springer Science & Business Media, 2008.

[166] Juanying Jiao, Tao Wang, Tianyong Ma, Ying Wang, and Fashen Li. Achievement of diverse domain structures in soft magnetic thin film through adjusting intrinsic magnetocrystalline anisotropy. *Nanoscale research letters*, 12(1):21, 2017.

[167] Mathias Kläui. Head-to-head domain walls in magnetic nanostructures. *Journal of Physics: Condensed Matter*, 20(31):313001, 2008.

[168] AB Kashuba and Valery L Pokrovsky. Stripe domain structures in a thin ferromagnetic film. *Physical Review B*, 48(14):10335, 1993.

[169] A. T. Hindmarch, D. E. Parkes and A. W. Rushforth. Fabrication of metallic magnetic nanostructures by argon ion milling using a reversed-polarity planar magnetron ion source. *Vacuum*, 86(10):1600–1604, 2012.

[170] JM Florczak and E Dan Dahlberg. Detecting two magnetization components by the magneto-optical kerr effect. *Journal of Applied Physics*, 67(12):7520–7525, 1990.

[171] JM Teixeira, R Lusche, J Ventura, R Fermento, F Carpinteiro, JP Araujo, JB Sousa, S Cardoso, and PP Freitas. Versatile, high sensitivity, and automatized angular dependent vectorial kerr magnetometer for the analysis of nanostructured materials. *Review of Scientific Instruments*, 82(4):043902, 2011.

[172] K Gramm, L Lundgren, and O Beckman. Squid magnetometer for mangetization measurements. *Physica Scripta*, 13(2):93, 1976.

[173] RL Fagaly. Superconducting quantum interference device instruments and applications. *Review of scientific instruments*, 77(10):101101, 2006.

[174] JC Sankey, PM Braganca, AGF Garcia, IN Krivorotov, RA Buhrman, and DC Ralph. Spin-transfer-driven ferromagnetic resonance of individual nanomagnets. *Physical review letters*, 96(22):227601, 2006.

[175] GBG Stenning, LR Shelford, SA Cavill, F Hoffmann, M Haertinger, T Hesjedal, G Woltersdorf, GJ Bowden, SA Gregory, CH Back, et al. Magnetization dynamics in an exchange-coupled nife/cofe bilayer studied by x-ray detected ferromagnetic resonance. *New Journal of Physics*, 17(1):013019, 2015.

[176] J-ML Beaujour, W Chen, K Krycka, C-C Kao, JZ Sun, and AD Kent. Ferromagnetic resonance study of sputtered co| ni multilayers. *The European Physical Journal B-Condensed Matter and Complex Systems*, 59(4):475–483, 2007.

[177] Xinyu Liu and Jacek K Furdyna. Ferromagnetic resonance in ga1- xmnxas dilute magnetic semiconductors. *Journal of Physics: Condensed Matter*, 18(13):R245, 2006.

[178] Edmund C Stoner and EP Wohlfarth. A mechanism of magnetic hysteresis in heterogeneous alloys. *Philosophical Transactions of the Royal Society of London A: Mathematical, Physical and Engineering Sciences*, 240(826):599–642, 1948.

[179] Z Ge, WL Lim, S Shen, YY Zhou, X Liu, JK Furdyna, and M Dobrowolska. Magnetization reversal in (ga, mn) as/ mn o exchange-biased structures: Investigation by planar hall effect. *Physical Review B*, 75(1):014407, 2007.

[180] Daniel C Ralph and Mark D Stiles. Spin transfer torques. *Journal of Magnetism and Magnetic Materials*, 320(7):1190–1216, 2008.

[181] M Brockmann, M Zölfl, S Miethaner, and G Bayreuther. In-plane volume and interface magnetic anisotropies in epitaxial fe films on gaas (001). *Journal of magnetism and magnetic materials*, 198:384–386, 1999.

[182] Günther Bayreuther, Jörg Premper, Matthias Sperl, and Dirk Sander. Uniaxial magnetic anisotropy in fe/gaas (001): Role of magnetoelastic interactions. *Physical Review B*, 86(5):054418, 2012.

[183] M Gester, C Daboo, RJ Hicken, SJ Gray, A Ercole, and JA C Bland. Continuous evolution of the in-plane magnetic anisotropies with thickness in epitaxial fe films. *Journal of applied physics*, 80(1):347–355, 1996.

[184] A Butera, J Gómez, JL Weston, and JA Barnard. Growth and magnetic characterization of epitaxial fe 81 ga 19/ mgo (100) thin films. *Journal of applied physics*, 98(3):033901, 2005.

[185] Jing Lou, RE Insignares, Zhuhua Cai, Katherine S Ziemer, Ming Liu, and Nian X Sun. Soft magnetism, magnetostriction, and microwave properties of fegab thin films. *Applied Physics Letters*, 91(18):182504, 2007.

[186] Shehzaad Kaka, Matthew R Pufall, William H Rippard, Thomas J Silva, Stephen E Russek, and Jordan A Katine. Mutual phase-locking of microwave spin torque nano-oscillators. In *Magnetics Conference, 2006. INTERMAG 2006. IEEE International*, pages 2–2. IEEE, 2006.

[187] Daniel B Gopman, Vimal Sampath, Hasnain Ahmad, Supriyo Bandyopadhyay, and Jayasimha Atulasimha. Static and dynamic magnetic properties of sputtered fe-ga thin films. *IEEE Transactions on Magnetics*, 2017.

[188] Julian Dean, MT Bryan, NA Morley, G Hrkac, A Javed, MRJ Gibbs, and DA Allwood. Numerical study of the effective magnetocrystalline anisotropy and magnetostriction in polycrystalline fega films. *Journal of Applied Physics*, 110(4):043902, 2011.

[189] RP Beardsley, DE Parkes, J Zemen, S Bowe, KW Edmonds, C Reardon, F Maccherozzi, I Isakov, PA Warburton, RP Campion, et al. Effect of lithographically-induced strain relaxation on the magnetic domain configuration in microfabricated epitaxially grown fe81ga19. *Scientific Reports*, 7:42107, 2017.

[190] Jayasimha Atulasimha, Alison B Flatau, and James R Cullen. Analysis of the effect of gallium content on the magnetomechanical behavior of single-crystal fega alloys using an energy-based model. *Smart Materials and Structures*, 17(2):025027, 2008.

[191] VD Nguyen, L Vila, P Laczkowski, A Marty, T Faivre, and JP Attané. Detection of domain-wall position and magnetization reversal in nanostructures

using the magnon contribution to the resistivity. *Physical review letters*, 107(13):136605, 2011.

[192] Daniel Gall. Electron mean free path in elemental metals. *Journal of Applied Physics*, 119(8):085101, 2016.

[193] Jack Bass and William P Pratt Jr. Spin-diffusion lengths in metals and alloys, and spin-flipping at metal/metal interfaces: an experimentalist's critical review. *Journal of Physics. Condensed Matter*, 19(18):183201, 2007.

[194] Evgeny Y Tsymbal and Igor Zutic. *Handbook of spin transport and magnetism*. CRC press, 2011.

[195] M Bowen, V Cros, F Petroff, Albert Fert, C Martınez Boubeta, José Luis Costa-Krämer, José Virgilio Anguita, Alfonso Cebollada, F Briones, JM De Teresa, et al. Large magnetoresistance in fe/mgo/feco (001) epitaxial tunnel junctions on gaas (001). *Applied Physics Letters*, 79(11):1655–1657, 2001.

[196] S Ikeda, J Hayakawa, Y Ashizawa, YM Lee, K Miura, H Hasegawa, M Tsunoda, F Matsukura, and H Ohno. Tunnel magnetoresistance of 604% at 300 k by suppression of ta diffusion in co fe b/ mg o/ co fe b pseudo-spin-valves annealed at high temperature. *Applied Physics Letters*, 93(8):082508, 2008.

[197] Cheng Song, Bin Cui, Fan Li, Xiangjun Zhou, and Feng Pan. Recent progress in voltage control of magnetism: Materials, mechanisms, and performance. *Progress in Materials Science*, 2017.

[198] SH Baek, J Park, DM Kim, Vladimir A Aksyuk, RR Das, SD Bu, DA Felker, J Lettieri, V Vaithyanathan, SSN Bharadwaja, et al. Giant piezoelectricity on si for hyperactive mems. *Science*, 334(6058):958–961, 2011.

[199] Ya Gao, Jiamian Hu, Li Shu, and CW Nan. Strain-mediated voltage control of magnetism in multiferroic ni77fe23/pb (mg1/3nb2/3) 0.7 ti0. 3o3 heterostructure. *Applied Physics Letters*, 104(14):142908, 2014.

[200] Alexey Klimov, Nicolas Tiercelin, Yannick Dusch, Stefano Giordano, Théo Mathurin, Philippe Pernod, Vladimir Preobrazhensky, Anton Churbanov, and Sergei Nikitov. Magnetoelectric write and read operations in a stress-mediated multiferroic memory cell. *Applied Physics Letters*, 110(22):222401, 2017.

[201] Zhengyang Zhao, Mahdi Jamali, Noel D'Souza, Delin Zhang, Supriyo Bandyopadhyay, Jayasimha Atulasimha, and Jian-Ping Wang. Giant voltage manipulation of mgo-based magnetic tunnel junctions via localized anisotropic strain: A potential pathway to ultra-energy-efficient memory technology. *Applied Physics Letters*, 109(9):092403, 2016.

[202] Dongqi Li, M Freitag, J Pearson, ZQ Qiu, and SD Bader. Magnetic phases of ultrathin fe grown on cu (100) as epitaxial wedges. *Physical review letters*, 72(19):3112, 1994.

Appendix A

MOKE

Penetration depth calculation

Assuming that the layer is perfectly polarised and there is no optical attenuation due to the optical components and any back scattering the penetration for the Al and Cu spacer samples can be calculated as below:

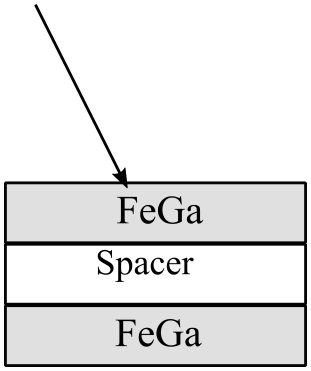

Figure A.1: Schematic of the multilayer samples for calculation of penetration depth of the laser

Aluminium spacer samples

- Layer 1

  Wavelength of incident light: λ_1= 635 nm

  Corresponding energy : 1.953 eV

  η for Iron at this energy: 2.88

  κ for Iron at this energy: 3.05

  Hence wavelength λ_2 in the 1^{st} layer : 635nm/η_{iron} = 220.48 nm

Characteristic length through 1^{st} layer : $\lambda_1 \times 4\pi\kappa = 16.57$ nm .

- Layer 2

  Wavelength of incident light : $\lambda_2 = 220.48$ nm

  Corresponding energy: 1.95 eV

  η for Aluminium at this energy: 1.63

  κ for Aluminium at this energy: 7.82

  Characteristic length through 2^{nd} layer: $\lambda_2 \times 4\pi\kappa = 2.24$ nm.

  Conclusion: For Aluminium spacer samples, laser will not be able to penetrate into the third layer.

Copper spacer samples

- Layer 1

  Wavelength of incident light: $\lambda_1 = 635$ nm

  Corresponding energy : 1.953 eV

  η for Iron at this energy: 2.88

  κ for Iron at this energy: 3.05

  Hence wavelength λ_2 in the 1^{st} layer : $635\text{nm}/\eta_{iron} = 220.48$ nm

  Characteristic length through 1^{st} layer : $\lambda_1 \times 4\pi\kappa = 16.57$ nm .

- Layer 2

  Wavelength of incident light : $\lambda_2 = 220.48$ nm

  Corresponding energy: 1.95 eV

  η for Aluminium at this energy: 1.09

  κ for Aluminium at this energy: 13.43

  Characteristic length through 2^{nd} layer: $\lambda_2 \times 4\pi\kappa = 5.47$ nm.

  Conclusion: For Copper spacer samples, we find that the second characteristic length l_2 is 5.5 nm. Therefore, if we have 5nm spacer, laser penetrates just into the 3rd layer of FeGa. But for 10 nm spacer, laser can not penetrate to the third layer.

Experimental evidence

In order to validate this assumption within limits longitudinal MOKE were performed on Fe samples sputter grown on GaAs(001) substrates of different thickness. The samples were grown by Stuart Bowe for his PhD thesis (Ref. **(author?)** [100]). The MOKE measurements are shown in Fig. A.2

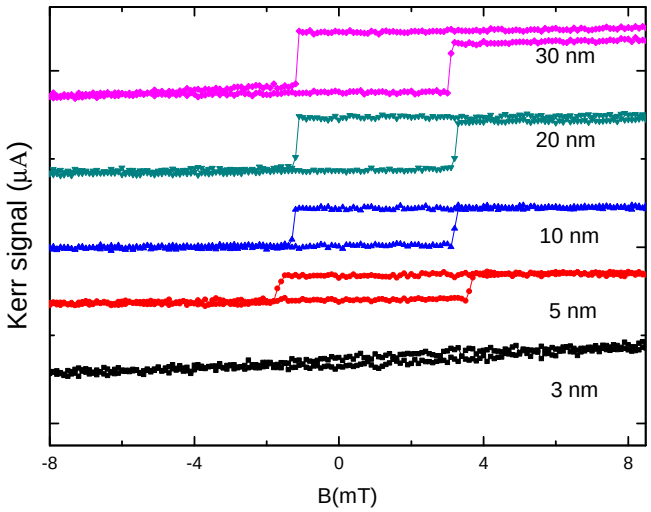

Figure A.2: Longitudinal MOKE measurements performed on Fe samples of various thickness.

By finding the amplitude of the measured signal for different thickness the critical thickness limit was obtained to be ~10.5 nm

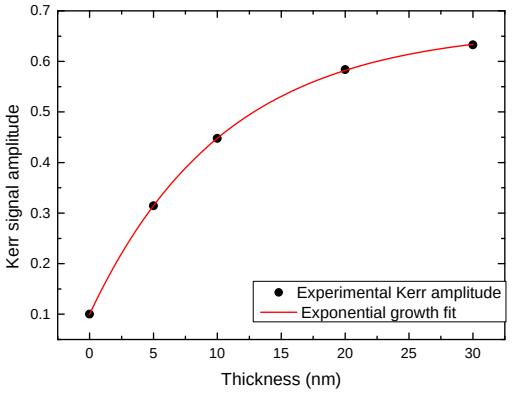

Figure A.3: Variation of the Kerr signal amplitude with thickness of the Fe film

The Kerr signal reflected from a magnetic sample depends on the thickness of the sample. For longitudinal geometry, the Kerr signal is given by the following equation **(author?)** [202] :

$$\phi = \frac{4\pi\eta}{\lambda(1-\eta^2)} Q d\theta \tag{A.1}$$

Where Q is the magneto-optical constant, ϑ is the angle of incidence; d is the thickness of the magnetic sample.

Reflection beam in terms of Fresnel coefficients

The amplitude of the parallel and perpendicular components of the light reflected from a magnetic material is related to the parallel and perpendicular components of the incident beam by the Fresnel coefficients

$$E_r = \Re \cdot E_i \tag{A.2}$$

or,

$$\begin{pmatrix} E_p \\ E_s \end{pmatrix}_r = \begin{pmatrix} r_{pp} & r_{sp} \\ r_{sp} & r_{ss} \end{pmatrix} \begin{pmatrix} E_p \\ E_s \end{pmatrix}_i \tag{A.3}$$

where E_r is the reflected beam, $\Re$ is the Fresnel coefficient matrix and E_i is the incident beam and can be expressed as:

$$\Re = m_t^2 r^x \left[\frac{Q}{m_x}\right] + m_l^2 r^y \left[\frac{Q}{m_y}\right] + m_p^2 r^z \left[\frac{Q}{m_z}\right] \tag{A.4}$$

where $m_t = M_t/M$, $m_l = M_l/M$, and $m_p = M_p/M$.

Appendix B

Strain calibration for various samples.

The calculated values of strain at different voltage across the piezoelectric transducers have been shown here for the samples (a)S419, (b) S420, (c)S421, and (d) S422.

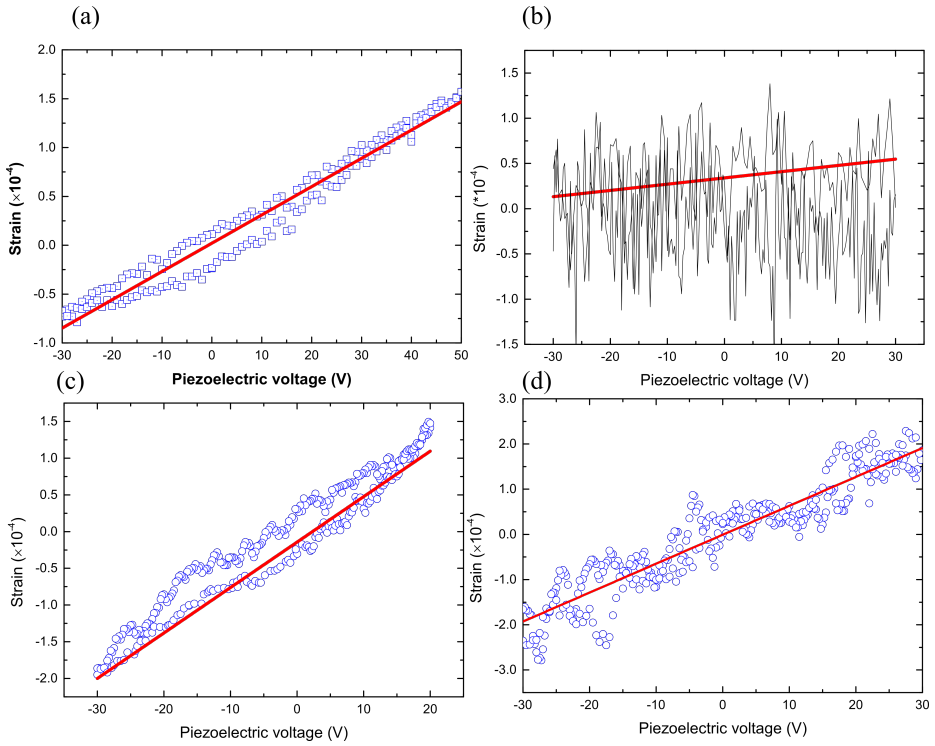

Figure B.1: Calibrated strain values for all the samples.